

Copyright

by

Robert Andrew Wittenmyer

2008

The Dissertation Committee for Robert Andrew Wittenmyer  
certifies that this is the approved version of the following dissertation:

## **A Search for Multi-Planet Systems**

Committee:

---

William D. Cochran, Supervisor

---

Edward L. Robinson, Supervisor

---

Michael Endl

---

Don Winget

---

Neal Evans

---

Hal Levison

# **A Search for Multi-Planet Systems**

by

**Robert Andrew Wittenmyer, B.A.; M.A.; M.S.**

## **Dissertation**

Presented to the Faculty of the Graduate School of

The University of Texas at Austin

in Partial Fulfillment

of the Requirements

for the Degree of

**Doctor of Philosophy**

**The University of Texas at Austin**

May 2008

My wife Gretchen deserves a Nobel Prize for putting up with the zombie that I became this year during the job-search and thesis-writing phases. I would like to raise a pint for my friends in the department who were there for me, in the job search and the final weeks of frenzied writing: Sehyun Hwang, Yuki Watanabe, Masa Shoji, Liubin Pan, Ivan Ramirez, Eder Martioli, Jennifer Sobeck, and Keith Nelson. For my fellow footballers Carlos Martinez, Tom Mumee, Blake Ewing, and Casey Decker, thank you for countless hours of sanity-restoring fun on the soccer field.

I am grateful to the HET TAC for their generous allocation of telescope time for this project. This research has made use of NASA's Astrophysics Data System (ADS), and the SIMBAD database, operated at CDS, Strasbourg, France. The GaussFit model and technical assistance with GaussFit were kindly provided by Barbara McArthur. Much of the computing for the dynamical simulations used the Lonestar cluster at the Texas Advanced Computing Center, as part of the time allocated to Volker Bromm. Additional computing resources were made available by Chris Wilkinson at the Department of Astronomy.

# A Search for Multi-Planet Systems

Publication No. \_\_\_\_\_

Robert Andrew Wittenmyer, Ph.D.  
The University of Texas at Austin, 2008

Supervisor: William D. Cochran  
Co-Supervisor: Edward L. Robinson

I report the results of a three-year intensive radial-velocity survey of 22 planet-host stars in search of the low-amplitude ( $K \sim 5\text{-}10 \text{ m s}^{-1}$ ) signals from additional planets which may be “hiding” in the residuals of the known planet orbital solution. On average, more than 40 radial-velocity observations were obtained for each target using the High-Resolution Spectrograph at the 9.2m Hobby-Eberly Telescope (HET). These high-precision data can be used to rule out additional planets in some of these systems to a detection limit of  $M \sin i \sim 10\text{-}20$  Earth masses at  $a = 0.05$  AU. Jupiter-mass planets can be excluded at the 99% level for orbital separations  $a < 2$  AU. No additional planets are evident, and our data do not confirm

the planets HD 20367b, HD 74156d, and 47 UMa c. Test particle simulations of these systems with the SWIFT N-body integrator reveal the regions where additional planets could reside in stable orbits. Further simulations with Saturn-mass bodies in these regions are also performed. We note a lack of short-period giant planets in any of these 22 systems, despite dynamical feasibility. The frequency of inner giant planets may be much lower than what was expected based on early discoveries of such objects in systems containing jovian-mass planets. Terrestrial-mass planets may be present in these systems but as yet undetectable. These results suggest that planet formation and migration processes do not favor systems containing both “hot” and “cold” Jupiters. Hence, as detection methods become sensitive to terrestrial-mass planets, systems with architectures like our own Solar system may yet be commonplace.

# Contents

<b>Abstract</b>	<b>v</b>
<b>List of Tables</b>	<b>x</b>
<b>List of Figures</b>	<b>xiv</b>
<b>Chapter 1 Introduction</b>	<b>1</b>
1.1 Extrasolar Planet Detection . . . . .	1
1.1.1 A Brief History of Radial Velocity Planet Detection . . . . .	2
1.2 The Architecture of Planetary Systems . . . . .	4
1.3 A Search for Multi-Planet Systems . . . . .	9
<b>Chapter 2 Observations and Stellar Characteristics</b>	<b>12</b>
2.1 Target Selection . . . . .	12
2.2 Observational Techniques . . . . .	17
2.2.1 Hobby-Eberly Telescope . . . . .	17
2.2.2 HET/HRS Error Budget . . . . .	18
2.2.3 Harlan J. Smith Telescope . . . . .	23
<b>Chapter 3 The Search for New Planets</b>	<b>29</b>
3.1 Orbit Fitting and Period Search . . . . .	29
3.2 Genetic Algorithm . . . . .	68
<b>Chapter 4 Candidates: Further Tests</b>	<b>78</b>
4.1 Methods . . . . .	78
4.1.1 Phasing the Residuals . . . . .	78

4.1.2	Examining Each Data Set Separately . . . . .	79
4.1.3	Comparing Velocity Computation Codes . . . . .	79
4.1.4	Fitting a Multi-Keplerian Model . . . . .	80
4.1.5	Dynamical Simulations . . . . .	80
4.1.6	Photometric Monitoring . . . . .	81
4.2	Applications . . . . .	81
4.2.1	HD 19994 . . . . .	81
4.2.2	HD 20367 . . . . .	82
4.2.3	HD 23596 . . . . .	82
4.2.4	HD 28185 . . . . .	84
4.2.5	HD 38529 . . . . .	84
4.2.6	HD 74156 . . . . .	89
4.2.7	47 UMa . . . . .	95
4.2.8	HD 128311 . . . . .	99
4.2.9	HD 178911B . . . . .	99
<b>Chapter 5 Detection Limits</b>		<b>104</b>
5.1	Constant Stars from the the McDonald Observatory Planet Search .	105
5.1.1	Observational Data Presented Here . . . . .	105
5.1.2	Merging the Data . . . . .	106
5.1.3	Periodogram Analysis . . . . .	107
5.1.4	Determination of Companion Limits . . . . .	108
5.1.5	Results and Discussion . . . . .	111
5.2	Planet Hosts . . . . .	114
5.3	Lessons Learned . . . . .	134
<b>Chapter 6 Dynamical Simulations</b>		<b>149</b>
6.1	Massless Test Particles . . . . .	149
6.1.1	Numerical Methods . . . . .	149
6.1.2	Results and Discussion . . . . .	150
6.2	Massive Body Simulations . . . . .	158
6.2.1	Numerical Methods . . . . .	159
6.2.2	Eccentric Orbits . . . . .	161
6.2.3	Mutual Inclinations . . . . .	162



<b>Chapter 7</b>	<b>Conclusions</b>	<b>163</b>
7.1	Where are they? . . . . .	163
7.1.1	Biases in the Sample . . . . .	164
7.1.2	Fundamental Differences . . . . .	165
7.1.3	Observing Strategy . . . . .	168
7.1.4	Just Unlucky . . . . .	169
7.1.5	Swarms of Earths . . . . .	170
7.2	Broader Implications for Planetary Systems . . . . .	171
7.3	Future Investigations . . . . .	173
7.3.1	Other Approaches to Detection Limits . . . . .	174
7.3.2	Test Particles in Inclined Orbits . . . . .	174
7.3.3	A Full Treatment of Massive Bodies . . . . .	176
<b>Appendix A</b>	<b>HET Radial-Velocity Data</b>	<b>177</b>
<b>Appendix B</b>	<b>2.7m Radial-Velocity Data</b>	<b>235</b>
	<b>Bibliography</b>	<b>244</b>
	<b>Vita</b>	<b>257</b>

# List of Tables

2.1	Stellar Parameters . . . . .	13
2.2	Summary of Published Radial-Velocity Data I. . . . .	14
2.3	Summary of Published Radial-Velocity Data II. . . . .	15
2.3	Summary of Published Radial-Velocity Data II. . . . .	16
2.4	HET/HRS Exposure Times . . . . .	19
2.5	Determination of HET/HRS Jitter . . . . .	21
2.5	Determination of HET/HRS Jitter . . . . .	22
2.5	Determination of HET/HRS Jitter . . . . .	23
2.6	HET/HRS Jitter for Planet Hosts . . . . .	27
3.1	47 UMa Orbital Solutions . . . . .	52
3.2	Keplerian Orbital Solutions . . . . .	65
3.3	Summary of Radial-Velocity Data . . . . .	66
3.3	Summary of Radial-Velocity Data . . . . .	67
3.3	Summary of Radial-Velocity Data . . . . .	68
3.4	Results of Periodogram Analysis . . . . .	69
3.5	Planet Parameters Found by Genetic Algorithm . . . . .	71
4.1	Periodogram Analysis for HD 74156 . . . . .	95
5.1	Target List and Stellar Parameters . . . . .	115
5.2	Summary of Observations . . . . .	116
5.3	Radial-Velocity Orbital Solution for 70 Oph A . . . . .	116
5.4	Results of Periodogram Analysis . . . . .	117
5.5	Minimum-Mass Companion Limits . . . . .	126
5.6	Minimum-Mass Companion Limits . . . . .	137

5.7	Statistics of Detection Limits . . . . .	139
7.1	Comparison of Stellar Characteristics . . . . .	164
7.2	Statistics of Single and Multiple Planet Systems . . . . .	166
7.3	K-S Tests on Single and Multiple Planet Systems . . . . .	166
7.4	Inclinations for Undetectable Saturn-Mass Planets . . . . .	170
A.1	HET Radial Velocities for HD 3651 . . . . .	178
A.1	HET Radial Velocities for HD 3651 . . . . .	179
A.1	HET Radial Velocities for HD 3651 . . . . .	180
A.2	HET Radial Velocities for HD 8574 . . . . .	181
A.2	HET Radial Velocities for HD 8574 . . . . .	182
A.3	HET Radial Velocities for HD 10697 . . . . .	183
A.3	HET Radial Velocities for HD 10697 . . . . .	184
A.4	HET Radial Velocities for HD 19994 . . . . .	184
A.4	HET Radial Velocities for HD 19994 . . . . .	185
A.4	HET Radial Velocities for HD 19994 . . . . .	186
A.4	HET Radial Velocities for HD 19994 . . . . .	187
A.4	HET Radial Velocities for HD 19994 . . . . .	188
A.5	HET Radial Velocities for HD 20367 . . . . .	188
A.6	HET Radial Velocities for HD 23596 . . . . .	189
A.6	HET Radial Velocities for HD 23596 . . . . .	190
A.7	HET Radial Velocities for HD 28185 . . . . .	191
A.8	HET Radial Velocities for HD 38529 . . . . .	192
A.8	HET Radial Velocities for HD 38529 . . . . .	193
A.8	HET Radial Velocities for HD 38529 . . . . .	194
A.8	HET Radial Velocities for HD 38529 . . . . .	195
A.8	HET Radial Velocities for HD 38529 . . . . .	196
A.8	HET Radial Velocities for HD 38529 . . . . .	197
A.9	HET Radial Velocities for HD 40979 . . . . .	198
A.9	HET Radial Velocities for HD 40979 . . . . .	199
A.9	HET Radial Velocities for HD 40979 . . . . .	200
A.10	HET Radial Velocities for HD 72659 . . . . .	201
A.10	HET Radial Velocities for HD 72659 . . . . .	202
A.11	HET Radial Velocities for HD 74156 . . . . .	203

A.11 HET Radial Velocities for HD 74156 . . . . .	204
A.11 HET Radial Velocities for HD 74156 . . . . .	205
A.11 HET Radial Velocities for HD 74156 . . . . .	206
A.11 HET Radial Velocities for HD 74156 . . . . .	207
A.11 HET Radial Velocities for HD 74156 . . . . .	208
A.11 HET Radial Velocities for HD 74156 . . . . .	209
A.12 HET Radial Velocities for HD 80606 . . . . .	209
A.13 HET Radial Velocities for HD 89744 . . . . .	210
A.13 HET Radial Velocities for HD 89744 . . . . .	211
A.13 HET Radial Velocities for HD 89744 . . . . .	212
A.14 HET Radial Velocities for 47 UMa . . . . .	213
A.14 HET Radial Velocities for 47 UMa . . . . .	214
A.14 HET Radial Velocities for 47 UMa . . . . .	215
A.14 HET Radial Velocities for 47 UMa . . . . .	216
A.14 HET Radial Velocities for 47 UMa . . . . .	217
A.14 HET Radial Velocities for 47 UMa . . . . .	218
A.14 HET Radial Velocities for 47 UMa . . . . .	219
A.15 HET Radial Velocities for HD 106252 . . . . .	220
A.15 HET Radial Velocities for HD 106252 . . . . .	221
A.16 HET Radial Velocities for HD 108874 . . . . .	221
A.16 HET Radial Velocities for HD 108874 . . . . .	222
A.17 HET Radial Velocities for HD 114783 . . . . .	222
A.18 HET Radial Velocities for HD 128311 . . . . .	223
A.18 HET Radial Velocities for HD 128311 . . . . .	224
A.18 HET Radial Velocities for HD 128311 . . . . .	225
A.18 HET Radial Velocities for HD 128311 . . . . .	226
A.18 HET Radial Velocities for HD 128311 . . . . .	227
A.19 HET Radial Velocities for HD 130322 . . . . .	227
A.20 HET Radial Velocities for HD 136118 . . . . .	228
A.20 HET Radial Velocities for HD 136118 . . . . .	229
A.20 HET Radial Velocities for HD 136118 . . . . .	230
A.20 HET Radial Velocities for HD 136118 . . . . .	231
A.21 HET Radial Velocities for HD 178911B . . . . .	232
A.21 HET Radial Velocities for HD 178911B . . . . .	233

A.22 HET Radial Velocities for HD 190228 . . . . .	233
A.22 HET Radial Velocities for HD 190228 . . . . .	234
B.1 2.7m Radial Velocities for HD 3651 . . . . .	235
B.2 2.7m Radial Velocities for HD 8574 . . . . .	236
B.3 2.7m Radial Velocities for HD 10697 . . . . .	237
B.4 2.7m Radial Velocities for HD 19994 . . . . .	237
B.5 2.7m Radial Velocities for HD 20367 . . . . .	238
B.6 2.7m Radial Velocities for HD 23596 . . . . .	238
B.7 2.7m Radial Velocities for HD 28185 . . . . .	239
B.8 2.7m Radial Velocities for HD 38529 . . . . .	239
B.9 2.7m Radial Velocities for HD 40979 . . . . .	239
B.10 2.7m Radial Velocities for HD 72659 . . . . .	240
B.11 2.7m Radial Velocities for HD 89744 . . . . .	240
B.12 2.7m Radial Velocities for 47 UMa . . . . .	241
B.13 2.7m Radial Velocities for HD 106252 . . . . .	242
B.14 2.7m Radial Velocities for HD 130322 . . . . .	242
B.15 2.7m Radial Velocities for HD 136118 . . . . .	242
B.16 2.7m Radial Velocities for HD 178911B . . . . .	242
B.17 2.7m Radial Velocities for HD 190228 . . . . .	243

# List of Figures

1.1	Extrasolar planet period distribution. . . . .	5
1.2	Eccentricity distribution. . . . .	7
1.3	Exoplanet mass function . . . . .	8
2.1	Internal errors and rms for HET/HRS stars . . . . .	23
2.2	Velocity jitter distribution for HET/HRS . . . . .	24
2.3	Excess scatter versus S/N . . . . .	25
2.4	HET/HRS velocity jitter vs. (B-V) . . . . .	26
3.1	HD 3651b fit and residuals . . . . .	32
3.2	HD 8574b fit and residuals . . . . .	33
3.3	HD 3651 and HD 8574 residuals periodograms . . . . .	33
3.4	HD 10697b fit and residuals . . . . .	34
3.5	HD 19994 fit and residuals . . . . .	34
3.6	HD 10697 and HD 19994 residuals periodograms . . . . .	35
3.7	HD 20367 RADIAL periodograms . . . . .	36
3.8	HD 20367 AUSTRAL periodograms . . . . .	36
3.9	HD 20367b fit and residuals . . . . .	37
3.10	HD 20367 residuals periodogram . . . . .	38
3.11	Phased fit for HD 20367b . . . . .	39
3.12	HD 23596 fit and residuals . . . . .	40
3.13	HD 28185b fit and residuals . . . . .	40
3.14	HD 23596 and HD 28185 residuals periodograms . . . . .	41
3.15	HD 38529b and c fits . . . . .	41
3.16	HD 38529 residuals . . . . .	42

3.17	HD 40979–RADIAL results . . . . .	44
3.18	HD 40979–AUSTRAL results . . . . .	44
3.19	HD 38529 and HD 40979 residuals periodograms . . . . .	45
3.20	HD 72659b fit and residuals . . . . .	45
3.21	HD 74156b and c fits . . . . .	46
3.22	HD 74156 residuals . . . . .	47
3.23	HD 72659 and HD 74156 residuals periodograms . . . . .	48
3.24	HD 80606 fit and residuals . . . . .	48
3.25	HD 89744 fit and residuals . . . . .	49
3.26	HD 80606 and HD 89744 residuals periodograms . . . . .	49
3.27	47 UMa–1-planet fit and residuals . . . . .	52
3.28	47 UMa–2-planet fit and residuals . . . . .	53
3.29	47 UMa residuals periodograms . . . . .	53
3.30	HD 106252 fit and residuals . . . . .	54
3.31	HD 108874b and c fits . . . . .	54
3.32	HD 108874 residuals . . . . .	55
3.33	HD 106252 and HD 108874 residuals periodograms . . . . .	56
3.34	HD 114783 fit and residuals . . . . .	57
3.35	HD 114783 residuals periodograms . . . . .	57
3.36	HD 128311b and c fits . . . . .	58
3.37	HD 128311 residuals . . . . .	59
3.38	HD 130322 fit and residuals . . . . .	60
3.39	HD 128311 and HD 130322 residuals periodograms . . . . .	61
3.40	HD 136118b fit and residuals . . . . .	62
3.41	HD 178911Bb fit and residuals . . . . .	62
3.42	HD 136118 and HD 178911B residuals periodograms . . . . .	63
3.43	HD 190228b fit and residuals . . . . .	63
3.44	HD 190228b residuals periodograms . . . . .	64
3.45	HD 3651 and HD 8574 genetic algorithm results . . . . .	72
3.46	HD 10697 and HD 19994 genetic algorithm results . . . . .	72
3.47	HD 23596 and HD 38529 genetic algorithm results . . . . .	73
3.48	HD 40979 and HD 72659 genetic algorithm results . . . . .	73
3.49	HD 74156 and HD 80606 genetic algorithm results . . . . .	74
3.50	HD 89744 and 47 UMa genetic algorithm results . . . . .	74

3.51	HD 106252 and HD 108874 genetic algorithm results . . . . .	75
3.52	HD 114783 and HD 130322 genetic algorithm results . . . . .	75
3.53	HD 136118 and HD 178911B genetic algorithm results . . . . .	76
3.54	HD 190228 genetic algorithm results . . . . .	77
4.1	Phased residuals for HD 19994 . . . . .	83
4.2	HD 19994 periodograms . . . . .	84
4.3	AUSTRAL periodogram for HD 19994 . . . . .	85
4.4	HD 20367 rotation period . . . . .	86
4.5	HD 23596 residuals . . . . .	86
4.6	HD 28185 residuals . . . . .	87
4.7	Phased residuals for HD 38529 . . . . .	88
4.8	HD 38529 periodograms . . . . .	89
4.9	AUSTRAL residuals for HD 38529 . . . . .	90
4.10	HD 74156 phased residuals and $3\sigma$ clipped periodogram . . . . .	92
4.11	HD 74156 periodograms . . . . .	92
4.12	AUSTRAL results for HD 74156 . . . . .	93
4.13	HD 74156 residuals phased to 346 days . . . . .	94
4.14	Comparison of velocities for HD 74156 . . . . .	94
4.15	Phased residuals for 47 UMa . . . . .	96
4.16	47 UMa periodograms . . . . .	97
4.17	47 UMa periodograms . . . . .	97
4.18	AUSTRAL results for 47 UMa . . . . .	98
4.19	Phased residuals for HD 178911B . . . . .	101
4.20	HD 178911B periodograms . . . . .	102
4.21	HD 178911B periodograms . . . . .	102
4.22	AUSTRAL results for HD 178911B . . . . .	103
5.1	Quadratic fits to $\mu$ Her data (left panel) and $\xi$ Boo A (right panel). . . . .	108
5.2	70 Oph A binary orbital solution . . . . .	109
5.3	Effect of eccentricity on limit determinations . . . . .	112
5.4	Detection limits for $\eta$ Cas, $\tau$ Cet, $\theta$ Per, and $\iota$ Per . . . . .	118
5.5	Same as Fig. 5.4, but for $\alpha$ For, $\kappa^1$ Cet, $\delta$ Eri, and $o^2$ Eri. . . . .	119
5.6	Same as Fig. 5.4, for $\pi^3$ Ori, $\lambda$ Aur, $\theta$ UMa, and 36 UMa. . . . .	120
5.7	Same as Fig. 5.4, for $\beta$ Vir, $\beta$ Com, 61 Vir, and $\xi$ Boo A. . . . .	121



5.8	Same as Fig. 5.4, for $\lambda$ Ser, $\gamma$ Ser, 36 Oph A, and $\mu$ Her. . . . .	122
5.9	Same as Fig. 5.4, for 70 Oph A, $\sigma$ Dra, 16 Cyg A, and $\beta$ Aql. . . . .	123
5.10	Same as Fig. 5.4, for 31 Aql, $\gamma^2$ Del, $\eta$ Cep, and 61 Cyg A. . . . .	124
5.11	Same as Fig. 5.4, for 61 Cyg B, HR 8832, and $\iota$ Psc. . . . .	125
5.12	Histogram of detection limits . . . . .	127
5.13	Detection limits on simulated data . . . . .	128
5.14	Limits for HD 3651 . . . . .	130
5.15	Limits for HD 8574 and HD 10697 . . . . .	130
5.16	Limits for HD 19994 and HD 23596 . . . . .	131
5.17	Limits for HD 28185 and HD 38529 . . . . .	132
5.18	Limits for HD 40979 and HD 72659 . . . . .	132
5.19	Limits for HD 74156 and HD 80606 . . . . .	133
5.20	Limits for HD 89744 and 47 UMa . . . . .	134
5.21	Limits for HD 106252 and HD 108874 . . . . .	135
5.22	Limits for HD 114783 and HD 128311 . . . . .	135
5.23	Limits for HD 130322 and HD 136118 . . . . .	136
5.24	Limits for HD 178911B and HD 190228 . . . . .	136
5.25	Histogram of detection limits . . . . .	140
5.26	Factors determining the quality of limits . . . . .	141
5.27	A model for detection limits quality . . . . .	142
5.28	Stellar characteristics and limits quality . . . . .	143
5.29	Stellar characteristics and limits quality . . . . .	144
5.30	Comparison of detection-limit methods . . . . .	146
5.31	Comparison of different recovery criteria . . . . .	148
6.1	Test particle results for HD 3651 and HD 8574 . . . . .	153
6.2	Test particle results for HD 10697 and HD 19994 . . . . .	154
6.3	Test particle results for HD 23596 and HD 28185 . . . . .	154
6.4	Test particle results for HD 38529 and HD 40979 . . . . .	155
6.5	Test particle results for HD 72659 and HD 74156 . . . . .	155
6.6	Test particle results for HD 80606 and HD 89744 . . . . .	156
6.7	Test particle results for 47 UMa and HD 106252 . . . . .	156
6.8	Test particle results for HD 108874 and HD 114783 . . . . .	157
6.9	Test particle results for HD 130322 and HD 136118 . . . . .	157

6.10	Test particle results for HD 178911B and HD 190228 . . . . .	158
6.11	Survival time of Saturn-mass planets in the HD 108874 system on initially circular orbits. . . . .	160
6.12	Effect of apsidal alignment on stability . . . . .	161
6.13	Test systems with mutual inclinations . . . . .	162
7.1	Mass-separation distribution. . . . .	167
7.2	Planet multiplicity versus stellar parameters. . . . .	168
7.3	Using $\Delta\chi^2_\nu > 3$ as a detection-limit metric. . . . .	175

# Chapter 1

## Introduction

### 1.1 Extrasolar Planet Detection

For centuries, scientists and philosophers have pondered the question: Is our Solar system unique? How common are planets, planetary systems, and Earth-like planets? It is only recently that we are able to characterize extrasolar planetary systems in quantity and with sufficient accuracy to make progress toward solving this age-old dilemma. Some important issues related to this larger question of uniqueness are the following: How common are multiple-planet systems? Do most planetary systems have several gas giant planets? What is the dependency of planetary system architecture on stellar parameters?

As of 2008 February, 270 planets are known to orbit stars other than the Sun. These have been discovered by a combination of pulsar timing, gravitational microlensing, transit, and radial-velocity methods; the vast majority of currently known planets have been discovered by the radial-velocity method. Wolszczan & Frail (1992) reported the detection of two terrestrial-mass planets orbiting the millisecond pulsar PSR1257 + 12. These objects were discovered by extremely precise measurements of the pulses. Variations in the timing of the pulsations of V 391 Peg were also used to infer a planetary companion (Silvotti et al. 2007). Gravitational microlensing (Mao & Paczynski 1991) has also been used to detect planets: when the host star passes in front of a background star, the background star appears to grow brighter. Unseen planets can cause additional brightening before or after the main lensing event. Recently, a 2-planet system resembling the Jupiter-Saturn

architecture has been discovered by microlensing (Gaudi et al. 2008). The transit method, whereby a planet passing in front of its host star induces a 0.1 – 1% dip in observed flux, is coming into its own as an effective way of discovering planets. Of the 35 known transiting planets, 18 of them were discovered in 2007 alone. The first transiting planet, HD 209458b (Charbonneau et al. 2000; Henry et al. 2000), was a previously known radial-velocity planet. From a transit, one can measure the radius of the planet, orbital inclination, and stellar limb darkening (Brown et al. 2001). The transit of a giant planet also affords the opportunity to observe starlight that has passed through the planet’s atmosphere, imprinting absorption lines onto the spectrum. In this way, the atmospheric composition can be probed. Deming et al. (2005) used Keck NIRSPEC observations of the transmission spectrum of HD 209458b to place upper limits on CO absorption, and to test theories explaining the weakness of sodium absorption found by Charbonneau et al. (2002). Redfield et al. (2008) have recently achieved the first ground-based detection of an extrasolar planet atmosphere by observing multiple transits of HD 189733b with the HET. Seager et al. (2007) point out that transmission spectroscopy could be used to differentiate carbon planets from silicate or icy bodies. Spitzer Space Telescope observations of the transiting hot Neptune GJ 436b (Gillon et al. 2007a) have been used to estimate its radius  $R_p = 4.19_{-0.16}^{+0.21} R_{\oplus}$ . These observations, combined with the models of Seager et al. (2007), showed that GJ 436b is likely a water-dominated planet with a substantial gaseous envelope (Gillon et al. 2007b; Deming et al. 2007). While transiting planets provide extremely interesting data about those planets, the radial velocity method is the “workhorse” in terms of new planet detections. Responsible for more than 90% of the confirmed extrasolar planet discoveries so far, the Doppler method remains by far the most effective means of detecting new planetary systems, and is the technique employed in this work.

### 1.1.1 A Brief History of Radial Velocity Planet Detection

Radial-velocity searches for planets around other stars began well before the 1995 discovery of 51 Peg b. Griffin & Griffin (1973) showed that the fundamental limit to the precision of classical radial velocity techniques was not instruments used, but rather was a result of the calibration processes. They pointed out that the optical paths followed by the stellar beam and the separate comparison source illuminated

the spectrograph optics differently. Tull (1969) demonstrated how zonal errors in spectrograph optics contribute directly to wavelength (and thus velocity) errors. In addition, thermal and mechanical motion of the spectrograph in the time interval between obtaining the stellar and calibration observations also contributed to the measured velocity errors. Griffin & Griffin (1973) proposed that these sources of errors could be defeated through the calibration of the spectrograph by an absorption line spectrum imposed on the stellar light *before* it entered the spectrograph. They suggested that the use of the very convenient absorptions by the Earth’s atmospheric O<sub>2</sub> band at 6300Å would permit stellar radial velocities to be measured to a precision perhaps as good as 0.01 km s<sup>-1</sup>. Campbell & Walker (1979) first used an externally applied absorption spectrum to provide a stable velocity metric for precise radial velocity measurement as applied to planet detection. Instead of the telluric absorption spectrum, they chose to use a stabilized HF gas absorption cell in front of the coude spectrograph of the Canada France Hawaii Telescope (CFHT). The HF 3-0 R branch lines near 8700Å gave radial velocity precision of 15 m s<sup>-1</sup> in their twelve-year survey of 21 bright solar-type stars (Campbell et al. 1988; Walker et al. 1995). Although Walker et al. (1995) did not claim any planet detections based on the CFHT data alone, two of their target objects ( $\epsilon$  Eridani and  $\gamma$  Cephei) were subsequently found to have planetary companions when the CFHT data were combined with McDonald Observatory data (Hatzes et al. 2000, 2003).

The CFHT survey marked the start of a large number of diverse efforts to conduct high-precision radial velocity surveys. At the University of Arizona, McMillan et al. (1985, 1990, 1994) developed a precise radial velocity spectrometer based on the use of a Fabry-Perot etalon in transmission in front of a cross-dispersed echelle spectrograph. This instrument was able to achieve velocity precision of 8 m s<sup>-1</sup> for bright sources (McMillan et al. 1994), and led to the discovery of the radial velocity variability of K-giants (Smith et al. 1987; Cochran 1988). The idea of using various types of interferometers to obtain precise stellar velocity measurements has been quite popular, with designs proposed by Cochran et al. (1982), Connes (1985), Angel & Woolf (1997), and Erskine & Ge (2000). Of these designs, only van Eyken et al. (2003) were successful in developing the design into an instrument that actually discovered an extrasolar planet (Ge et al. 2006).

The use of molecular iodine as a velocity reference system had its beginnings in the solar rotation measurements of Beckers (1976). Libbrecht (1988) then

extended the use of  $I_2$  as a velocity metric in searching for p-mode oscillations of  $\alpha$  CMi. Marcy & Butler (1992) then implemented the use of the  $I_2$  velocity metric for large-scale precise radial velocity surveys for extrasolar planets. The use of an  $I_2$  cell offers the major advantage that the  $I_2$  lines can be used to measure the spectrometer instrumental profile (Valenti et al. 1995) and thus measure very precise radial velocity variations (Butler et al. 1996). The observed stellar spectrum is the result of a convolution between the intrinsic stellar spectrum and the spectrograph’s instrumental profile (IP). The iodine-cell technique described by Valenti et al. (1995), in which a temperature-controlled cell filled with  $I_2$  gas is placed in the light path of the spectrograph, allows the IP to be determined very accurately. By superimposing a dense forest of narrow  $I_2$  absorption lines on the target spectrum, the spectrograph optics are illuminated in exactly the same way for the target and the IP calibration. This method results in very precise determination of the IP, and hence improved radial-velocity precision. An alternative is to use an optical-fiber fed cross dispersed echelle spectrograph with simultaneous wavelength calibration. This was first done with ELODIE (Baranne et al. 1996) and later with CORALIE (Queloz et al. 2000). To further improve precision with this technique, the HARPS instrument (Mayor et al. 2003) is placed in a temperature-stabilized vacuum chamber. Throughout this work, previously published data have been obtained from the Geneva Observatory planet search (ELODIE, CORALIE) and the California/Carnegie Planet Search (Lick, Keck). The ELODIE survey for planets orbiting northern-hemisphere stars has been in operation since 1993 at the 1.93-m telescope at Haute Provence, France (Baranne et al. 1996). CORALIE is a spectrograph on the 1.2-m Euler telescope in La Silla, Chile, which has been used for a southern hemisphere planet search since 1999 (Queloz et al. 2000). The California group started the Lick planet search in 1987 using the Hamilton spectrometer (Vogt 1987) and the 3-m Shane telescope and 0.6-m Coude Auxiliary Telescope (CAT). The 10-m Keck telescope and HIRES spectrograph have also been used by the California team since 1996 (Vogt et al. 2000).

## 1.2 The Architecture of Planetary Systems

Within the last 20 years, the detection of substellar objects orbiting stars has progressed at a remarkable pace. (Latham et al. 1989) discovered HD 114762b, the

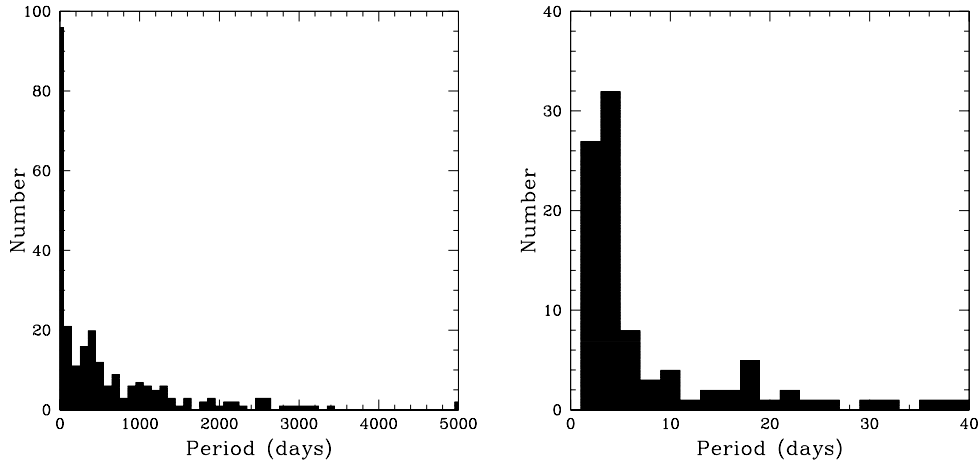


Figure 1.1 Distribution of the periods of 256 exoplanets, showing the pile-up at  $P \sim 4$  days. Left panel: Full range. Right panel: Same, but zoomed in on the range  $P < 40$  days. Planet data are from exoplanet.eu.

first companion with a minimum mass below  $13M_{\text{Jup}}$ , using radial-velocity measurements. This object has an orbital period of  $83.920 \pm 0.004$  days and a minimum mass  $M \sin i = 11.2 \pm 0.5 M_{\text{Jup}}$ . The  $\sin i$  ambiguity brought on by the unknown inclination of the system means that HD 114762b could have a substantially higher mass (Cochran et al. 1991). The planet/brown dwarf mass boundary is typically taken to be  $13 M_{\text{Jup}}$ , since this is the mass at which core deuterium burning occurs. For this reason, the planet orbiting 51 Peg (Mayor & Queloz 1995), with  $M \sin i \sim 0.5 M_{\text{Jup}}$ , is generally regarded as the first extrasolar planet discovered orbiting a solar-type star. 51 Peg b was an unexpected finding: a “hot Jupiter” with a 4.23-day orbital period. It was expected that extrasolar planetary systems would be similar to our Solar system, but the results of more than 12 years of discoveries paint a very different picture. Figure 1.1 shows the “pile-up” of short-period planets. This is most likely a selection effect since very short-period planets are easier to detect, since they induce proportionately larger radial-velocity variations which are more readily detectable.

One surprising result that has come out of the nearly 300 extrasolar planet discoveries to date is the wide range of eccentricities observed (Figure 1.2). Unlike our own Solar system, many of the extrasolar planets whose orbits have not been tidally circularized by their host stars have moderate eccentricities ( $e > 0.2$ ), and 19

planets have high eccentricities ( $e > 0.6$ ). These observations have spawned several theories as to the origin of highly eccentric extrasolar planets. One such method, planet-planet scattering, occurs when multiple jovian planets form several astronomical units (AU) from the host star and then interact, leaving one in an eccentric orbit and often ejecting the other (Rasio & Ford 1996). This method has been proposed to explain the architecture of the  $\nu$  And planetary system (Ford et al. 2005), which contains a hot Jupiter as well as two jovian planets in moderately eccentric orbits. Lin & Ida (1997) suggested a merger scenario in which inner protoplanets perturb each other and merge to form a single massive, eccentric planet with  $e \gtrsim 0.3$  and  $a \sim 0.5 - 1$  AU.

Interactions with stellar companions are another possible way to boost a planet's eccentricity. Of the 19 stars hosting a planet with  $e > 0.6$ , six are also known to possess stellar-mass companions in wide binary orbits: HD 3651 (Mugrauer et al. 2006; Luhman et al. 2007), HD 20782 (Desidera & Barbieri 2007), HD 80606, HD 89744 (Wilson et al. 2001; Mugrauer et al. 2004), 16 Cyg B, and HD 222582 (Raghavan et al. 2006). If the inclination angle between the planetary orbit and a stellar companion is large, the Kozai mechanism (Kozai 1962) can induce large-amplitude oscillations in the eccentricity of the planet (e.g. Malmberg et al. 2007). These oscillations can be damped by general relativistic effects and by interaction with other planets, and hence are most effective in systems with a single planet in an orbit  $a \gtrsim 1$  AU from the host star (Takeda & Rasio 2005). The Kozai mechanism has been suggested to explain the high eccentricity of 16 Cyg Bb (Holman et al. 1997; Mazeh et al. 1997) and HD 80606b (Wu & Murray 2003). Hauser & Marcy (1999) found the inclination of 16 Cyg B orbiting the system barycenter to lie between 100 and 160 degrees, where 90 degrees is an edge-on orientation. However, it is the difference in inclination between the orbital planes of the planetary and stellar companion that is critical in determining the importance of the Kozai mechanism, and the inclination of the planet's orbit is generally not known for non-transiting systems.

The extrasolar planet mass function is shown in Figure 1.3. A striking feature of the current sample is the abundance of low-mass planets. Such objects are more difficult to detect by the radial-velocity method, yet these planets appear to be much more prevalent.



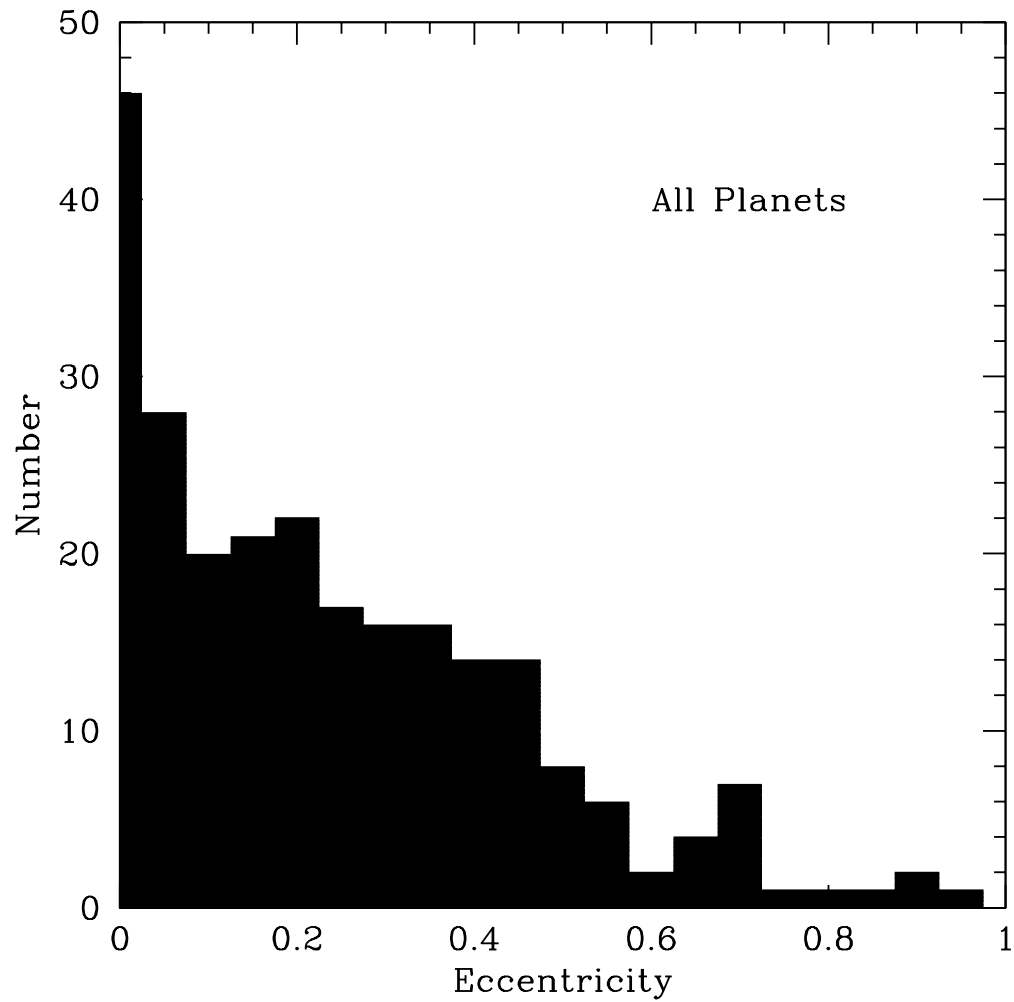


Figure 1.2 Distribution of extrasolar planet eccentricities. Unlike our own Solar system, a substantial number of planets have  $e > 0.2$ . Planet data are from exoplanet.eu.

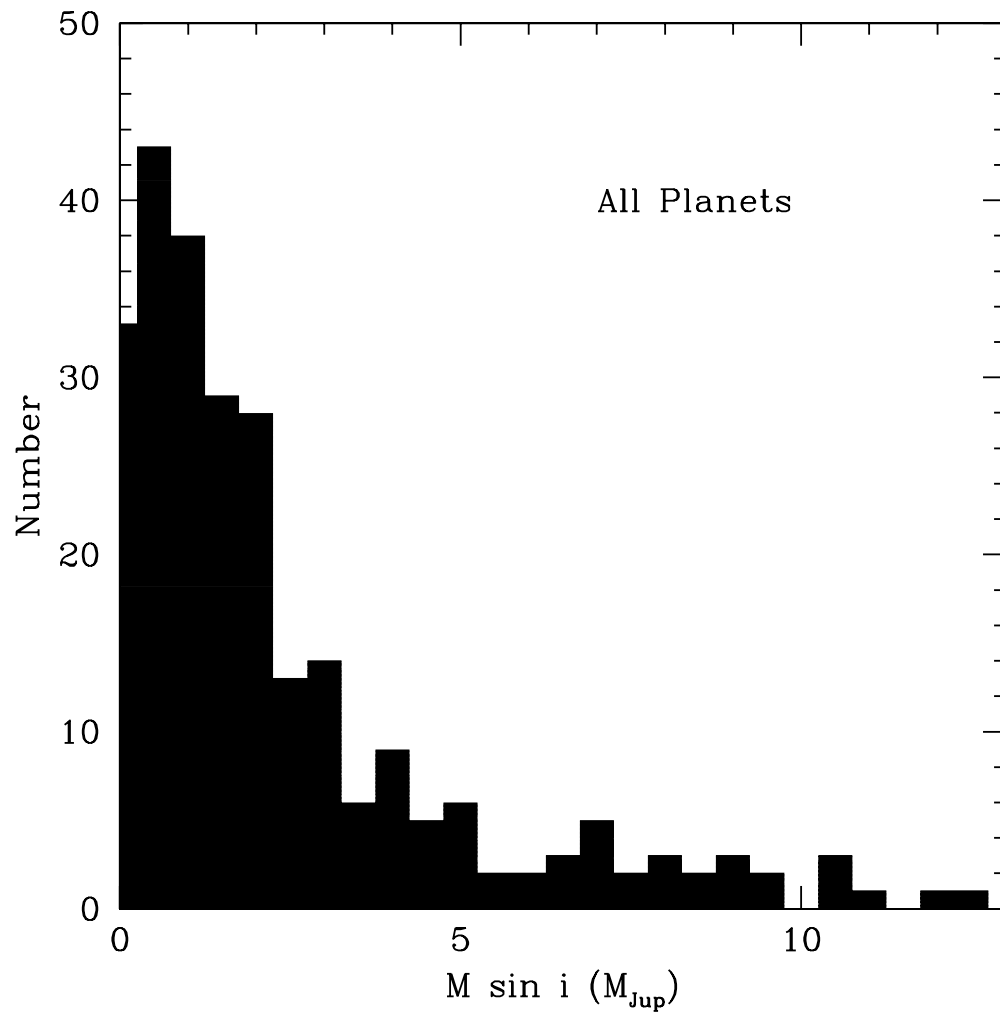


Figure 1.3 Distribution of projected exoplanet masses  $M \sin i$ . Low-mass planets are more prolific, despite being harder to detect. Planet data are from exoplanet.eu.

### 1.3 A Search for Multi-Planet Systems

The longest-running radial-velocity surveys are now approaching time baselines of 15-20 years (Butler et al. 1996; Cochran et al. 1997). These surveys now achieve internal measurement precisions and time baselines such that the signals from low-mass “hot Neptunes” and long-period giant planets ( $P \gtrsim 10\text{yr}$ ) are now entering the realm of detectability (Wittenmyer et al. 2006). For example, the High Resolution Spectrograph (HRS) on the Hobby-Eberly Telescope (HET) now has a velocity precision of 3-4  $\text{m s}^{-1}$  (Cochran et al. 2004), the Keck HIRES is achieving 1-2  $\text{m s}^{-1}$  since its 2004 CCD upgrade (Butler et al. 2006), and the HARPS instrument has demonstrated precision better than 1  $\text{m s}^{-1}$  (Lovis et al. 2006). Of particular interest are putative multi-planet systems, wherein the residuals of a known-planet’s orbit show Keplerian periodicity indicative of an additional companion in the system. Finding systems which contain long-period giant planets as well as planets in closer orbits could provide clues to address the question of how the processes of planet formation and migration can result in both “hot” and “cold” Jupiters in the same planetary system.

The preponderance of close-in giant planets (“hot Jupiters”) inferred by precision radial-velocity surveys has emphasized the importance of planetary migration. The core-accretion model of planetary formation (Lissauer 1995; Pollack et al. 1996) posits that rocky cores form in the outer regions of the protoplanetary disk and migrate inward, and that such cores at small semimajor axes experience runaway gas accretion once they reach a mass of  $\sim 10$  Earth masses, resulting in close-in giant planets (Bodenheimer et al. 2000). Alternatively, the disk-instability model suggests that such planets form by direct gravitational collapse of the protoplanetary disk (Boss 1995, 1998). Multi-planet systems can be formed by this method (Boss 2003), though subsequent evolution can easily eject planets, resulting in a wide variety of system end-states (Levison et al. 1998). The discovery of additional multi-planet systems will provide valuable added constraints to these two models of planet formation. Trilling et al. (1998) have proposed that gas giant planets migrating inward can overflow their Roche lobes and be stripped of their atmospheres. Under the core-accretion model of planet formation, a Neptune-mass rocky core would then remain in a close orbit, and the detection of such objects would lend support to that theory. Alternatively, the nondetection of close-in, low-mass planets would tend to favor the

disk-instability model, in which gas giant planets have no solid cores. Interestingly, a recent series of papers by Ida & Lin (2004a,b) predicts a paucity of planets (the “planet desert”) of 10-100 Earth masses within  $\sim 3$  AU. Their core-accretion simulations also predict an abundance of Jupiter-mass planets at intermediate orbital separations ( $a \sim 0.1 - 1$  AU), as well as close-in ( $a \lesssim 0.1$  AU) planets with masses below about  $10 M_{\oplus}$ . Lin and Ida further suggest that the distribution of planetary mass vs. semimajor axis will constrain the dominant formation processes of planets. Hence, an intensive effort to characterize the population of detectable planets around nearby stars will be extremely valuable for understanding the processes of planet formation and evolution.

Radial-velocity planet search campaigns have matured to the point where the discovery of individual jovian planets is virtually commonplace. With more than 15 years of high-precision data ( $\sigma \sim 3 \text{ m s}^{-1}$ ) now available, 25 multiple-planet systems have been discovered, comprising 10% of all known planetary systems<sup>1</sup>. Discoveries of additional objects in systems known to host at least one planet (Fischer et al. 2007; Udry et al. 2007; Wittenmyer et al. 2007a; Rivera et al. 2005; Vogt et al. 2005; McArthur et al. 2004; Santos et al. 2004b) suggest that multiple-planet systems may be common. Of particular interest are systems which host a jovian planet and a hot Neptune, e.g. 55 Cnc (=HD 75732), GJ 876,  $\mu$  Arae (=HD 160691), Gl 777A (=HD 190360). Recently, systems containing multiple low-mass planets have also been detected, e.g. GJ 581 (Udry et al. 2007) and HD 69830 (Lovis et al. 2006).

The final configuration of a planetary system is also dependent on the post-formation migration and dynamical interaction processes. Mandell et al. (2007) showed that the migration of a Jupiter-mass planet through a disk of planetesimals resulted in the formation of an interior terrestrial-mass planet. Simulations of known multi-planet systems by Barnes & Quinn (2004) and Barnes & Raymond (2004) suggest that planetary systems are “packed” – that is, they contain the maximum number of planets that is dynamically possible. In Barnes & Raymond (2004), the dynamically stable regions of the HD 74156 system were investigated in a manner similar to the HD 108874 system has been in the present work. Those authors used the results to predict that an additional planet, between planets b and c, could be present. The detection by Bean et al. (2008) of such an object lends support to the “packed planetary systems” hypothesis (Barnes et al. 2007), which would imply

---

<sup>1</sup>J. Schneider Extrasolar Planet Encyclopaedia, <http://exoplanet.eu>

that multiple-planet systems are common.

Motivated by the discoveries of hot Neptunes in known planetary systems, and the theory that planetary systems are “packed,” I have undertaken an intensive survey of selected planetary systems to search for additional low-mass companions. In Chapter 2, I describe the observing techniques and target selection, and discuss the radial-velocity error budget. Chapter 3 gives the results of the orbit fits and the search for new planets. The most intriguing targets are discussed further in Chapter 4, which describes the various tests a candidate planetary signal must undergo. The detection limits, which determine the sensitivity of this survey, are presented in Chapter 5. Dynamical simulations are presented in Chapter 6, in which the regions of stability are mapped for all of the target systems. Finally, Chapter 7 assesses the impact of these new data and analyses on the theories of planet formation and the population-level statistics of extrasolar planets. Hence, this work presents a three-fold approach to the question of planetary system architecture: 1) Are additional planets present in these known planetary systems? 2) Where could additional objects reside in stable orbits? 3) What limits can be placed on such objects?

## Chapter 2

# Observations and Stellar Characteristics

### 2.1 Target Selection

Twenty-two targets were chosen for this project from the list of  $\sim 150$  planet hosts known in 2004 September. The targets were selected according to the following criteria: 1) HET observability, with declination between  $-11^\circ$  and  $+72^\circ$ , and 2) Either a long-period ( $P \gtrsim 1$  yr) planet such that inner planets may be dynamically stable, or a very short-period ( $P \lesssim 10$  days) hot Jupiter which would allow for previously undetected outer planets, or 3) The orbital solution for the known planet in each system has RV residuals of 10-20  $\text{m s}^{-1}$ , so that an additional planet may be present but undetected. For example, the RV signal due to the Neptune-mass planet 55 Cancri e is  $\sim 6 \text{ m s}^{-1}$  (McArthur et al. 2004). The targets and their stellar parameters are listed in Table 2.1. Except where noted, masses are obtained from Takeda et al. (2007),  $[\text{Fe}/\text{H}]$ ,  $T_{\text{eff}}$ , and  $V \sin i$  from Valenti & Fischer (2005), and the chromospheric emission ratio  $\log R'_{HK}$  (Noyes et al. 1984) computed from measurements of the Ca II S-index obtained with the 2.7m telescope. The uncertainties on the stellar masses given in Takeda et al. (2007) are asymmetric about the central value; for the purposes of Table 2.1 and the determination of planetary parameters, the adopted stellar mass uncertainty was taken to be the larger of the two.

The 22 selected targets were observed with the HET in queue mode using a random observing interval of 2-10 days between visits. Each visit consisted of

Table 2.1. Stellar Parameters

Star	Spec. Type	Distance (pc)	Mass ( $M_{\odot}$ )	[Fe/H]	$T_{eff}$ (K)	V sin $i$ (km s $^{-1}$ )	$\log R'_{HK}$
HD 3651	K0V	11.1±0.1	0.882±0.026	0.24±0.03	5221±44	1.1	-4.99±0.05
HD 8574	F8	44.2±1.6	1.122±0.022	-0.03±0.03	6050±44	4.5	-4.88±0.04
HD 10697	G5IV	32.6±0.9	1.112±0.026	0.17±0.03	5680±44	2.5	-5.07±0.15
HD 19994	F8V	22.4±0.4	1.365±0.042	0.27±0.03	6188±44	8.6	-4.93±0.04
HD 20367	G0	27.1±0.8	1.04±0.06 <sup>a</sup>	-0.11±0.10 <sup>b</sup>	5929±75	3.0	-4.50±0.05
HD 23596	F8V	52.0±2.3	1.159±0.062	0.33±0.03	5904±44	4.2	-4.96±0.05
HD 28185	G5	39.6±1.7	0.98±0.05 <sup>c</sup>	0.15±0.10 <sup>b</sup>	5483±75	3.0	-5.37±0.40
HD 38529	G4IV	42.4±1.7	1.477±0.052	0.51±0.03	5697±44	3.9	-5.01±0.03
HD 40979	F8V	33.3±0.9	1.154±0.028	0.15±0.03	6089±44	7.4	-4.59±0.01
HD 72659	G0V	51.4±2.7	1.068±0.022	-0.02±0.03	5920±44	2.2	-5.02±0.09
HD 74156	G0	64.6±4.6	1.238±0.044	0.11±0.03	6068±44	4.3	...
HD 80606	G5	58±20	0.958±0.072	0.47±0.03	5573±44	1.8	...
HD 89744	F7V	39.0±1.1	1.558±0.048	0.26±0.03	6291±44	9.5	-5.03±0.04
47 UMa	G0V	14.1±0.1	1.063±0.029	0.04±0.03	5882±44	2.8	-5.03±0.07
HD 106252	G0	37.4±1.3	1.007±0.024	-0.07±0.03	5870±44	1.9	-4.91±0.14
HD 108874	G5	68.5±5.8	0.950±0.036	0.19±0.03	5551±44	2.2	...
HD 114783	K0	20.4±0.4	0.853±0.034	0.21±0.03	5135±44	0.9	...
HD 128311	K0	16.6±0.3	0.828±0.012	0.08±0.03	4965±44	3.6	...
HD 130322	K0V	29.8±1.3	0.836±0.018	-0.02±0.03	5308±44	1.6	-4.76±0.02
HD 136118	F9V	52.3±2.3	1.191±0.026	-0.11±0.03	6097±44	7.3	-4.91±0.04
HD 178911B	G5	47±11	1.014±0.057	0.34±0.03	5668±44	1.9	-4.83±0.02
HD 190228	G5IV	62.1±3.1	1.821±0.050	-0.24±0.03	5348±44	1.9	-4.98±0.02

<sup>a</sup>Mass obtained from Nordström et al. (2004).

<sup>b</sup>[Fe/H],  $T_{eff}$ , and V sin  $i$  obtained from Nordström et al. (2004).

<sup>c</sup>Mass obtained from Santos et al. (2004a).

Table 2.2. Summary of Published Radial-Velocity Data I.

Star	Reference	$N$	$\langle \sigma \rangle$ ( $\text{m s}^{-1}$ )	RMS about fit ( $\text{m s}^{-1}$ )
HD 3651	Butler et al. (2006)	163	3.4	6.6
HD 8574	Perrier et al. (2003)	41	10.3	13.1
HD 8574	Butler et al. (2006)	26	10.4	23.0
HD 10697	Butler et al. (2006)	59	2.7	6.8
HD 19994	Mayor et al. (2004)	48	6.7	8.1
HD 23596	Perrier et al. (2003)	39	9.1	9.2
HD 28185	Santos et al. (2001)	40	6.5	10.0
HD 38529	Butler et al. (2006)	162	5.3	13
HD 40979	Butler et al. (2006)	65	9.1	23
HD 72659	Butler et al. (2006)	32	3.2	4.2
HD 74156	Naef et al. (2004)	95	10.8	10.6
HD 80606	Naef et al. (2001b)	61	13.7	17.7
HD 80606	Butler et al. (2006)	46	5.1	5.4
HD 89744	Butler et al. (2006)	50	11.2	16.0
47 UMa	Fischer et al. (2002a)	91	5.7	7.4
47 UMa	Naef et al. (2004)	44	7.3	7.4
HD 106252	Perrier et al. (2003)	40	10.7	10.5
HD 106252	Butler et al. (2006)	15	11.4	9.1
HD 108874	Vogt et al. (2005)	49	3.4	3.7
HD 114783	Butler et al. (2006)	54	2.7	4.7
HD 128311	Vogt et al. (2005)	76	3.3	18.0
HD 130322	Udry et al. (2000)	118	12.4	16.1
HD 130322	Butler et al. (2006)	12	2.7	11.0
HD 136118	Butler et al. (2006)	37	16.1	22.0
HD 178911B	Zucker et al. (2002)	51	10.4	11.0
HD 178911B	Butler et al. (2006)	14	2.7	7.7
HD 190228	Perrier et al. (2003)	51	8.7	8.0

one spectrum, except for the brightest targets (HD 3651, HD 19994, HD 38529, HD 74156, 47 UMa) for which 3 consecutive spectra were obtained in each visit. Additional data were obtained for HD 128311 and HD 136118 in cooperative agreement with the program of F. Benedict. Data obtained from the Benedict program also consisted of triple exposures. These targets were observed with the HET for nine trimesters, from 2004 December through 2007 November. During the three years of this study, supplemental observations were also made using the 2.7m telescope.

All available published radial-velocity data were also gathered from the literature for the purpose of fitting orbits to the known planets. These data are summarized in Tables 2.2–2.3. For HD 20367, the velocity measurements are not publicly tabulated, and the only mention of this planet appears in the conference proceedings announcing it (Udry et al. 2003).



Table 2.3. Summary of Published Radial-Velocity Data II.

Planet	Period (days)	$T_0$ (JD-2400000)	$e$	$\omega$ (degrees)	K (m s <sup>-1</sup> )	M sin $i$ (M <sub>Jup</sub> )	$a$ (AU)	rms m s <sup>-1</sup>	Reference <sup>a</sup>
HD 3651 b	62.23±0.03	52501.7±1.2	0.63±0.04	235.7±6.6	15.9±1.7	0.20	0.284	6.27	F03b
HD 8574 b	227.55±0.77	51467.5±6.6	0.288±0.053	3.6±10.9	66±5	2.11	0.77	13.1	P03
HD 10697 b	1072.3±9.6	51482±39	0.12±0.02	113±14	119±3	6.35	2.12	7.75	V00
HD 19994 b	535.7±3.1	50944±12	0.30±0.04	41±8	36.2±1.9	1.68	1.42	8.1	M04
HD 20367 b	469.5±9.3	51860±18	0.32±0.09	135±16	29±3	1.17	1.25	10.1	U03
HD 23596 b	1565±21	51604±15	0.292±0.023	274.1±3.9	124±3	8.10 2.88	9.2	P03	
HD 28185 b	383±2	51863±26	0.07±0.04	351±25	161±11	5.7	1.03	10	S01
HD 38529 b	14.309±0.05	50005.8±1.5	0.29±0.02	87.7±4.0	54.2±1.2	0.78	0.129	10.99	F03a
HD 38529 c	2174.3±30.0	50073.8±35.0	0.36±0.05	14.7±10.0	170.5±9.0	12.70	3.68	10.99	F03a
HD 40979 b	263.1±3.0	52327.2±17.0	0.25±0.05	310.7±8.0	101.2±5.6	3.28	0.83	18.7	F03a
HD 72659 b	2185±3000	52140±500	0.18±0.2	350±100	42±20	2.55	3.24	6.98	B03
HD 74156 b	51.643±0.011	51981.321±0.091	0.636±0.009	181.5±1.4	112.0±1.9	1.86	0.294	10.6	N04
HD 74156 c	2025±11	50901±10	0.583±0.039	242.4±4.0	104.0±5.5	6.17	3.40	10.6	N04
HD 80606 b	111.81±0.23	51973.72±0.29	0.927±0.012	291.0±6.7	411±31	3.90	0.469	17.7	N01
HD 89744 b	256.0±0.7	50994±2	0.70±0.02	195±3	257±14	7.2	0.88	20.5	K00
47 UMa b	1089.0±2.9	50356.0±33.6	0.061±0.014	171.8±15.2	49.3±1.2	2.54	2.09	7.4	F02a
47 UMa c	2594±90	51363.5±495.3	0.005±0.115	127.0±11.1	1.1±0.76	3.73	7.4	F02a	
HD 106252 b	1600±18	51871±17	0.471±0.028	292.2±3.2	147±4	7.56	2.70	10.5	P03
HD 108874 b <sup>b</sup>	397.5±4	51310.6±5	0.17±0.06	256±30	48±4	1.71	1.06	7.82	B03
HD 108874 c	1605.8±88	49584.8±180	0.25±0.07	17.3±23	18.4±1.6	1.018	2.68	3.72	V05
HD 114783 b	501±14	51840±59	0.10±0.08	97±40	27±2	1.0	1.2	4.08	V02
HD 128311 b <sup>b</sup>	422±10	50028±30	0.31±0.1	228±40	85±7	2.57	1.02	29.5	B03
HD 128311 c	928.3±18	50012.2±401	0.17±0.09	195.5±150	76.2±4.6	3.21	1.76	16.6	V05
HD 130322 b	10.720±0.007	51287.38±0.68	0.044±0.018	203.6±23.1	115±2	1.02	0.088	15.4	U00
HD 136118 b	1209.6±24.0	51800.6±36.6	0.366±0.025	315.0±4.5	212.9±6.0	11.9	2.335	22.1	F02b
HD 178911B b	71.487±0.018	50305.70±0.62	0.124±0.008	169.8±3.6	339.3±3.1	6.29	0.32	11.0	Z02
HD 190228 b	1146±16	51236±25	0.499±0.047	100.7±3.2	91±5	3.58	2.02	8.0	P03

Table 2.3 (cont'd)

Planet	Period (days)	$T_0$ (JD-2400000)	$e$	$\omega$ (degrees)	$K$ (m s <sup>-1</sup> )	$M \sin i$ (M <sub>Jup</sub> )	$a$ (AU)	rms m s <sup>-1</sup>	Reference <sup>a</sup>
--------	------------------	-----------------------	-----	-----------------------	-----------------------------	-----------------------------------	-------------	--------------------------	------------------------

<sup>a</sup>Key to references—F03b: Fischer et al. (2003b), P03: Perrier et al. (2003), V00: Vogt et al. (2000), M04: Mayor et al. (2004), U03: Udry et al. (2003), S01: Santos et al. (2001), F03a: Fischer et al. (2003a), B03: Butler et al. (2003), N04: Naef et al. (2004), N01: Naef et al. (2001b), K00: Korzennik et al. (2000), F02a: Fischer et al. (2002a), V05: Vogt et al. (2005), V02: Vogt et al. (2002), U00: Udry et al. (2000), F02b: Fischer et al. (2002b), Z02: Zucker et al. (2002).

<sup>b</sup>Only the inner planet was known at the start of this survey in 2004 October. Parameters for the outer planet are from Vogt et al. (2005).

## 2.2 Observational Techniques

### 2.2.1 Hobby-Eberly Telescope

The majority of the observational data used in this work made use of the 9.2m Hobby-Eberly Telescope (HET) and its High-Resolution Spectrograph (HRS). As a queue-scheduled telescope, time on the HET is given in hours rather than nights, and the PI can assign a given observation a range of priority, from 1 (highest) to 4 (lowest). In this manner, observations can be timed for maximum efficacy, e.g. the discovery of HD 37605b (Cochran et al. 2004), and the determination of the true orbit for the highly eccentric planet HD 45350b (Endl et al. 2006).

The HRS (Tull 1998) is a white-pupil spectrograph which resides in an insulated room beneath the telescope. Starlight is fed to the HRS via a 34m fiber with a diameter of  $2''$  on the sky. All of the HET observations for this program were performed at a resolution of 60,000, with the 316 gr/mm cross-disperser and a central wavelength of  $5936\text{\AA}$ . An iodine cell temperature-controlled at 70C was used as the velocity metric (Marcy & Butler 1992). This setup, referred to as “316g5936,” places the iodine region ( $\sim 5000\text{-}6000\text{\AA}$ ) almost entirely onto the blue CCD, which is cosmetically superior to the red CCD. For each target, an iodine-free template spectrum was obtained near the beginning of the first season in which it was observable. All subsequent observations included the iodine cell. Table 2.4 lists the  $V$  magnitudes and exposure times for each target. The exposure times were determined according to the following:

$$\text{Exposure time} = 10^{0.4(V-6)} \times 100 \text{ seconds.} \quad (2.1)$$

A maximum exposure time of 900 s was set in order to limit velocity errors induced by uncertainties in the barycentric correction, which become especially important in poor conditions when the flux-weighted mid-exposure time is different from the midpoint of the exposure. The times listed in Table 2.4 were increased by up to a factor of 3 in conditions of poor seeing or sky transparency. Spectra were reduced and extracted using standard IRAF<sup>1</sup> routines for echelle spectra. The RADIAL code developed by W.D. Cochran models the instrumental profile of the spectrograph

---

<sup>1</sup>Image Reduction and Analysis Facility is distributed by the National Optical Astronomy Observatories.

based on the method of Valenti et al. (1995) (cf. 4), and computes a velocity for each spectrum. Each echelle order in the  $I_2$  region is divided into 20 chunks, for a total of 480 chunks. A barycentric radial velocity is determined for each chunk, then a chunk-merging algorithm removes the velocity offsets between the chunks. This is accomplished in the following way: The offset between chunks 1 and 2 of each spectrum are averaged, outlying chunks are rejected according to a sigma-clipping routine, and the process is repeated for every chunk. Once the offset between each chunk is determined, the chunks in each spectrum are merged into a single velocity. The uncertainty on that velocity is then the standard error of the mean of the chunks in the spectrum. The AUSTRAL code of M. Endl (Endl et al. 2000) is also based on the IP modeling techniques described in Valenti et al. (1995) and Butler et al. (1996), but differs from RADIAL in a few aspects. The most important difference is in the chunk-merging process. In AUSTRAL, the chunks in a given spectrum are not offset with respect to each other, but are tied to a zero-point defined by the  $I_2$  spectrum. The velocity of each spectrum is then based only on the chunk distribution of that spectrum. All HET radial-velocity data obtained for this study are tabulated in Appendix A.

### 2.2.2 HET/HRS Error Budget

The uncertainty of an individual HET measurement as determined by RADIAL is typically 1-2  $\text{m s}^{-1}$ . However, the rms scatter of the HET velocities can be substantially larger, since the stated error bar represents the internal error only. For the high signal-to-noise (S/N) of these observations (S/N $\sim$ 150), the internal error is dominated by photon noise. External errors can arise from fluctuations in the spectrograph temperature, focus, or intrinsic stellar variability. In order to weight the HET/HRS data properly in the orbit fits, the amount of excess scatter (“jitter”) was empirically determined from the complete archive of HET observations. The radial-velocity data from 298 stars in the HET program were examined, and 82 targets were chosen with  $N > 5$  which were constant in velocity or showed linear trends. For each of these stars, the rms about a linear fit and the mean error bar ( $\bar{\sigma}$ ) were computed (Table 2.5). The distributions of these quantities are shown in Figure 2.1. The excess scatter was then defined as:

$$\text{Excess scatter} = \sqrt{(rms)^2 - (\bar{\sigma})^2}. \quad (2.2)$$

Table 2.4. HET/HRS Exposure Times

Star	<i>V</i> magnitude	Exp. Time (s)
HD 3651	5.8	90
HD 8574	7.8	530
HD 10697	6.29	130
HD 19994	5.07	45
HD 20367	6.41	150
HD 23596	7.24	320
HD 28185	7.81	530
HD 38529	5.94	60
HD 40979	6.75	200
HD 72659	7.48	400
HD 74156	7.62	150
HD 80606	8.93	900
HD 89744	5.74	80
47 UMa	5.1	45
HD 106252	7.36	350
HD 108874	8.76	900
HD 114783	7.57	440
HD 128311	7.51	180
HD 130322	8.05	660
HD 136118	6.9	120
HD 178911B	7.98	620
HD 190228	7.3	330

For one star, HD 88446, this quantity is undefined (mean error is greater than the rms), and a value of zero was adopted. A histogram of these jitter values is shown in Figure 2.2. The distribution is essentially normal, with a tail toward higher jitter values. The small secondary peak at  $12 \text{ m s}^{-1}$  is due to the earlier-type (mid-F) stars in the sample, and the remainder of the tail might be attributable to undetected planets. Figure 2.3 shows the relation between the excess scatter and the mean S/N of the available spectra for the 82 stars considered; no significant dependence is evident. Here we are assuming that the excess scatter is dominated by factors intrinsic to the star. Of course, stars are complex, and this is a multidimensional problem dependent on the star’s temperature, evolutionary stage, rotation speed, surface gravity, etc. Wright (2005) produced a detailed jitter model for stars from the California and Carnegie planet search program, as a function of color, chromospheric Ca II emission, and height above the main sequence. In this work, I choose to focus on the star’s  $(B - V)$  color since precise measurements of  $(B - V)$  are more readily available in the literature. A simple linear regression was performed to derive the dependence of the velocity jitter on each star’s  $(B - V)$  obtained from *Hipparcos* (Perryman et al. 1997). For this linear fit, an uncertainty of  $3 \text{ m s}^{-1}$  was assigned to each jitter value, as this is the approximate FWHM of the Gaussian portion of the histogram in Fig. 2.2. The empirical jitter model for the HET/HRS system is then

$$\text{Jitter} = 14.211 - 10.420(B - V) \text{ m s}^{-1}. \quad (2.3)$$

This relation is plotted as a solid line in Figure 2.4. The fit has an rms scatter of  $3.33 \text{ m s}^{-1}$  and  $\chi^2_{\nu} = 1.25$ . Applying this model to the planet hosts targeted in this study yields the jitter values shown in Table 2.6. These estimates of stellar jitter were added in quadrature to the internal errors of all HET radial velocities.

Table 2.5. Determination of HET/HRS Jitter

Star	S/N	RMS ( $\text{m s}^{-1}$ ) $\text{m s}^{-1}$	$\bar{\sigma}$ ( $\text{m s}^{-1}$ ) $\text{m s}^{-1}$	Scatter ( $\text{m s}^{-1}$ ) $\text{m s}^{-1}$	(B-V)
BD+00 523	125	15.17	6.19	13.85	0.7
BD+65 737	123	11.81	8.11	8.59	0.67
HD 6512	160	6.61	1.51	6.43	0.656
HD 6715	166	3.78	1.82	3.32	0.71
HD 10013	152	3.91	1.78	3.48	0.773
HD 13783	172	6.38	2.39	5.92	0.674
HD 16397	155	5.97	2.51	5.41	0.583
HD 17674	147	2.36	1.94	1.35	0.584
HD 21543	154	5.96	3.205	5.03	0.619
HD 22879	160	9.64	2.50	9.31	0.554
HD 24702	167	5.28	2.17	4.82	0.688
HD 28099	135	15.30	2.51	15.09	0.664
HD 28192	165	20.04	1.94	19.94	0.629
HD 29587	139	7.72	4.77	6.06	0.633
HD 31609	148	13.33	2.96	13.00	0.737
HD 32259	125	9.44	2.21	9.18	0.615
HD 38277	162	3.39	1.94	2.78	0.637
HD 41708	133	8.78	1.77	8.60	0.626
HD 44420	145	8.10	1.45	7.97	0.686
HD 51046	132	9.43	2.14	9.18	0.679
HD 55647	154	18.54	17.60	5.83	0.744
HD 66348	138	12.69	2.19	12.50	0.571
HD 66550	144	4.68	1.53	4.42	0.806
HD 68017	135	7.79	1.86	7.57	0.679
HD 69056	186	9.58	1.77	9.42	0.731
HD 69960	151	6.14	1.25	6.01	0.756
HD 73226	147	8.30	1.68	8.12	0.632
HD 75488	139	7.59	2.03	7.32	0.557
HD 77278	165	4.75	2.38	4.11	0.81
HD 86560	137	6.68	2.74	6.09	0.55
HD 87127	153	13.24	4.41	12.48	0.533
HD 87836	144	3.99	1.00	3.87	0.708
HD 88446	159	5.04	5.40	...	0.552
HD 91148	153	9.46	2.08	9.23	0.711
HD 93215	178	5.86	1.58	5.64	0.67
HD 96937	137	2.99	1.58	2.53	0.777
HD 99491	155	6.45	1.56	6.26	0.778
HD 100446	146	8.05	4.34	6.78	0.549
HD 102618	170	8.60	2.01	8.36	0.573

Table 2.5 (cont'd)

Star	S/N	RMS ( $\text{m s}^{-1}$ ) $\text{m s}^{-1}$	$\bar{\sigma}$ ( $\text{m s}^{-1}$ ) $\text{m s}^{-1}$	Scatter ( $\text{m s}^{-1}$ ) $\text{m s}^{-1}$	(B-V)
HD 105618	131	4.29	1.74	3.92	0.71
HD 107148	133	4.17	1.28	3.97	0.707
HD 108024	152	7.43	2.46	7.01	0.578
HD 110313	154	3.28	1.20	3.05	0.61
HD 110537	152	5.49	1.63	5.25	0.675
HD 111066	163	8.68	2.40	8.35	0.54
HD 114174	131	12.02	1.56	11.92	0.667
HD 120162	145	11.39	2.28	11.16	0.552
HD 124694	162	20.06	6.64	18.92	0.53
HD 126511	116	4.28	1.94	3.82	0.757
HD 128428	157	7.65	2.34	7.29	0.755
HD 131042	158	6.45	1.75	6.21	0.643
HD 139324	141	7.46	1.44	7.32	0.633
HD 142267	162	10.97	3.30	10.46	0.598
HD 147231	145	6.61	1.63	6.41	0.722
HD 148816	137	12.13	2.18	11.94	0.545
HD 149028	160	4.57	1.40	4.35	0.76
HD 149222	127	6.25	1.63	6.04	0.585
HD 150433	165	10.55	1.56	10.43	0.631
HD 153344	162	6.53	1.31	6.40	0.676
HD 155968	118	4.59	1.22	4.43	0.687
HD 158226	121	8.40	2.29	8.08	0.626
HD 163489	141	9.05	1.19	8.97	1.11
HD 165504	146	7.23	2.63	6.74	0.639
HD 165672	146	10.79	1.14	10.73	0.663
HD 175425	139	8.16	1.52	8.02	0.669
HD 176841	132	7.34	1.19	7.25	0.676
HD 186104	116	5.34	1.84	5.01	0.664
HD 190594	186	3.77	1.38	3.51	0.776
HD 191649	140	7.39	1.75	7.18	0.568
HD 196361	156	7.58	1.56	7.42	0.656
HD 200078	161	4.93	1.71	4.62	0.707
HD 205353	159	8.10	1.57	7.95	0.602
HD 208906	128	11.98	2.61	11.70	0.501
HD 215274	165	6.60	4.29	5.01	0.703
HD 216123	164	8.10	6.61	4.68	0.747
HD 216840	154	7.00	1.79	6.76	0.684
HD 218355	150	7.91	1.78	7.70	0.625
HD 218473	155	6.65	1.46	6.49	0.643



Table 2.5 (cont'd)

Star	S/N	RMS ( $\text{m s}^{-1}$ ) $\text{m s}^{-1}$	$\bar{\sigma}$ ( $\text{m s}^{-1}$ ) $\text{m s}^{-1}$	Scatter ( $\text{m s}^{-1}$ ) $\text{m s}^{-1}$	(B-V)
HD 220255	167	8.41	1.50	8.27	0.619
HD 222794	147	7.28	2.76	6.73	0.645
HD 224531	151	6.32	2.28	5.89	0.734
HIP 109931	183	7.28	2.24	6.93	0.66

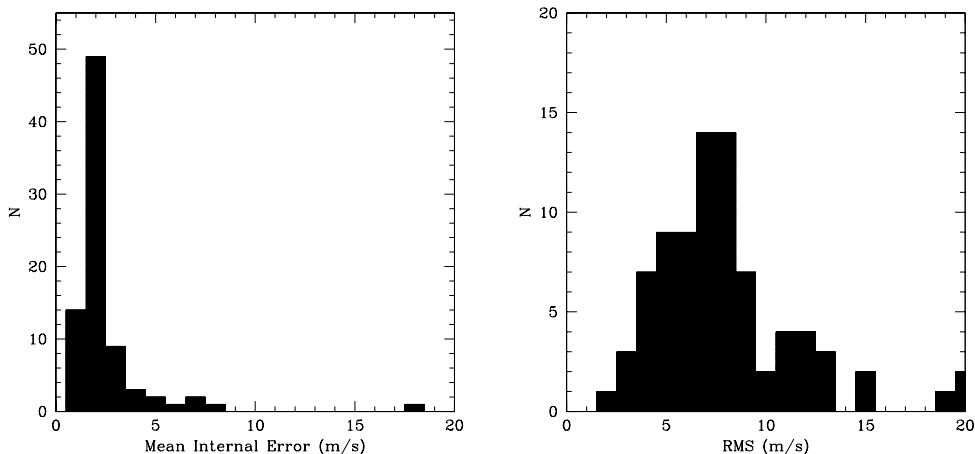


Figure 2.1 Histograms of the mean internal error (left panel) and total velocity RMS (right panel) for 82 stars in the HET program.

### 2.2.3 Harlan J. Smith Telescope

The McDonald Observatory Planetary Search program comprises a large, multi-faceted investigation to detect and characterize planetary companions to other stars in our galaxy. It began in 1988 as a high-precision radial velocity survey of bright nearby stars using the McDonald Observatory 2.7m Harlan J. Smith Telescope and coudé spectrograph, but has expanded substantially in size and scope since then. Phase I of the radial velocity planet search program used the telluric  $\text{O}_2$  lines near  $6300\text{\AA}$  as the velocity metric, a technique suggested by Griffin & Griffin (1973). A single order of the McDonald 2.7m telescope coudé echelle spectrograph (cs12) was isolated onto a Texas Instruments  $800 \times 800$  CCD at  $R = 210,000$ . This system gave about  $20 \text{ m s}^{-1}$  precision on stars down to  $V = 6$ , but suffered from systematic velocity errors, possibly due to prevailing atmospheric winds. Diurnal and seasonal

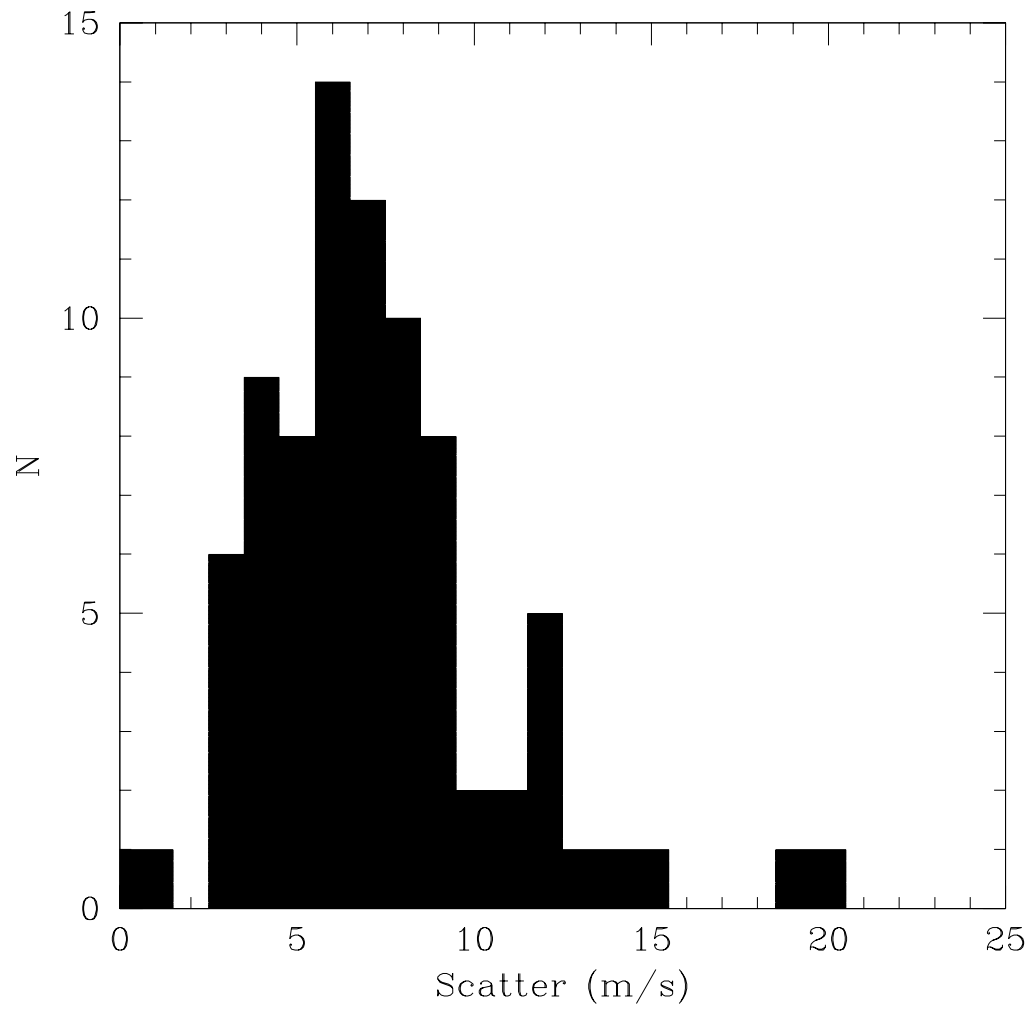


Figure 2.2 Histogram of excess velocity scatter (“jitter”) for 82 stars in the HET program. The distribution peaks at  $6 \text{ m s}^{-1}$  and has a FWHM of approximately  $3 \text{ m s}^{-1}$ .

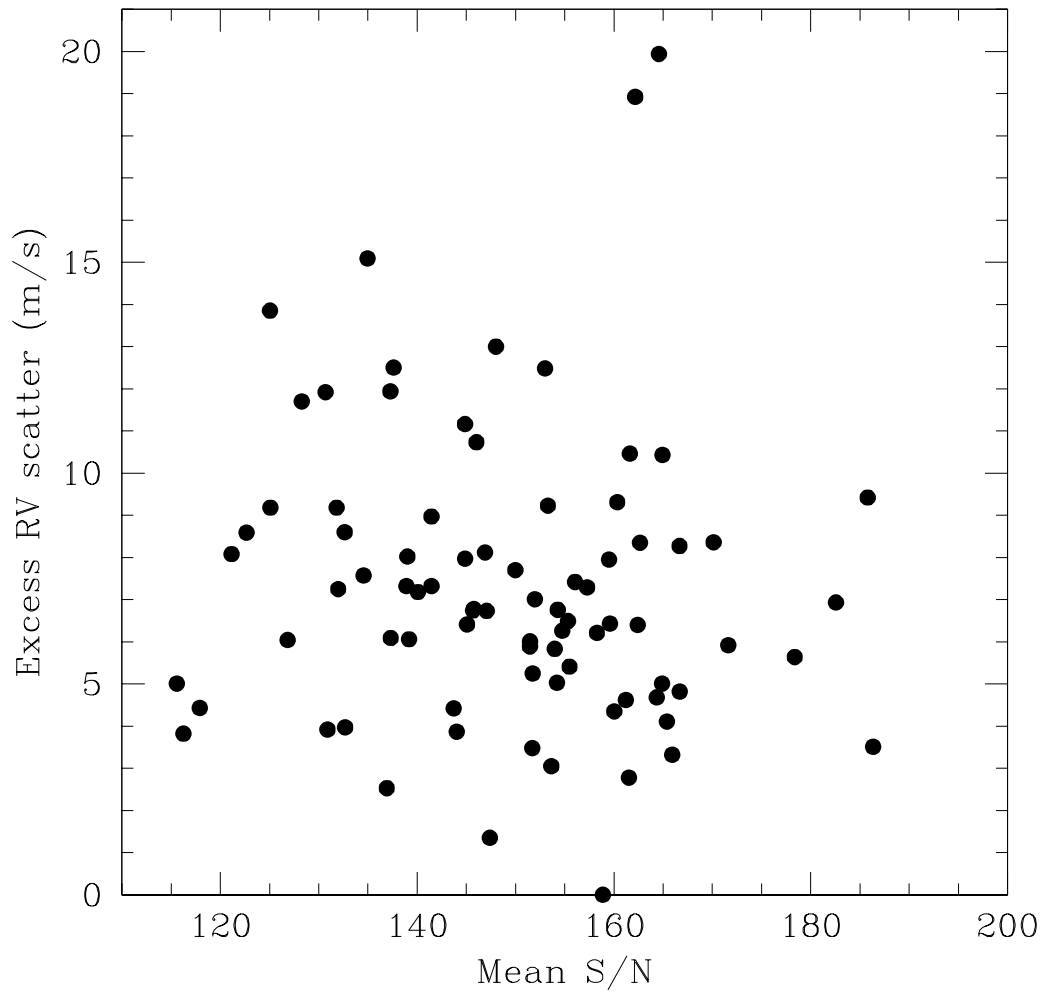


Figure 2.3 Relation of excess velocity scatter to the mean S/N for 82 stars in the HET program. A linear fit shows no significant dependence.

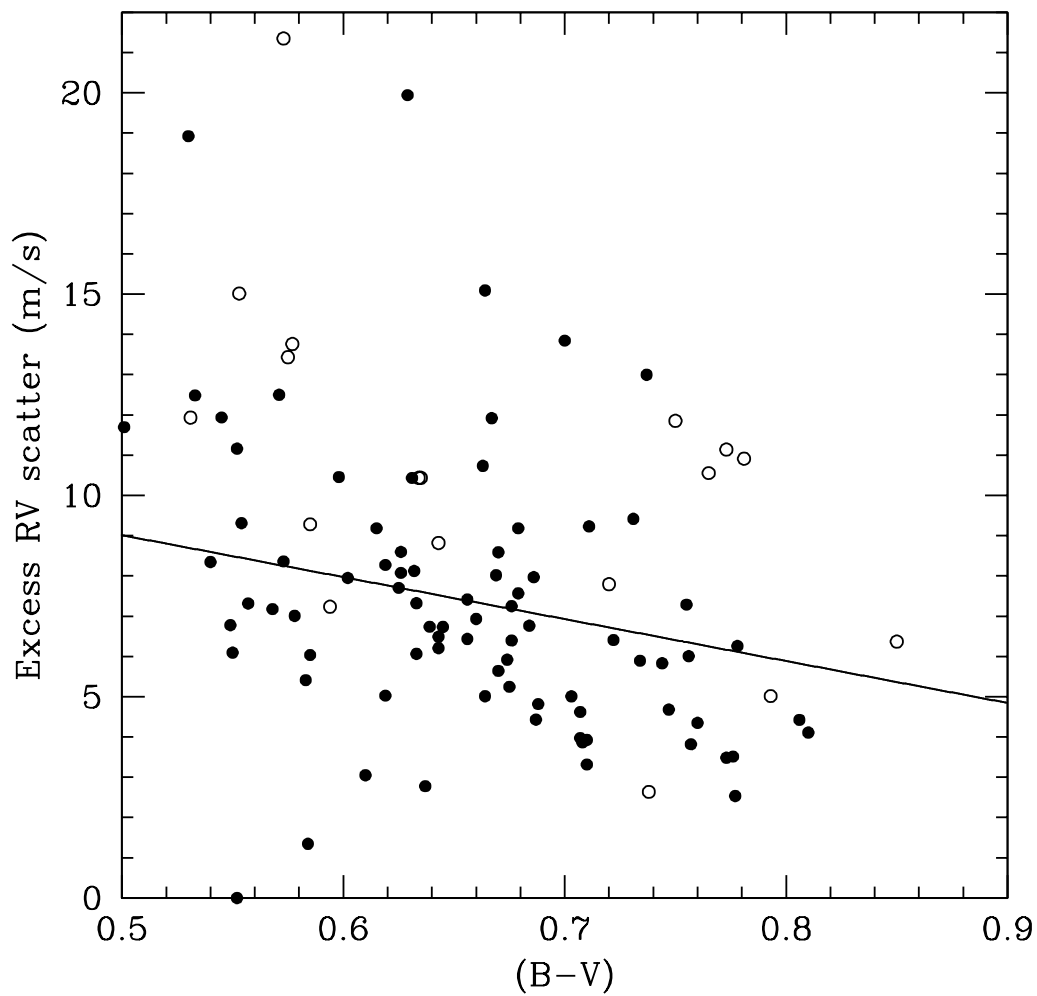


Figure 2.4 Excess velocity scatter (“jitter”) versus (B-V) for 82 stars in the HET program. The solid line is a linear fit to the plotted points. This result is consistent with the expectation that stellar jitter decreases in later-type stars. The planet hosts considered in this work are shown as open circles and were not used in the fit.

Table 2.6. HET/HRS Jitter for Planet Hosts

Star	(B-V)	Jitter ( $\text{m s}^{-1}$ )
HD 3651	0.850	5.35
HD 8574	0.577	8.20
HD 10697	0.720	6.71
HD 19994	0.575	8.22
HD 20367	0.574	8.23
HD 23596	0.634	7.60
HD 28185	0.750	6.40
HD 38529	0.773	6.16
HD 40979	0.573	8.24
HD 72659	0.612	7.70
HD 74156	0.585	8.12
HD 80606	0.765	6.24
HD 89744	0.531	8.68
47 UMa	0.594	8.02
HD 106252	0.635	7.59
HD 108874	0.738	6.52
HD 114783	0.930	4.52
HD 128311	0.973	4.07
HD 130322	0.781	6.07
HD 136118	0.553	8.45
HD 178911B	0.643	7.51
HD 190228	0.793	5.95

variability in the winds introduced spurious periodic signals in the data. The program therefore switched to a temperature stabilized I<sub>2</sub> cell as the velocity metric in 1992. This eliminated the systematic errors, and gave a routine radial velocity precision of  $\sim 15 \text{ m s}^{-1}$ . This precision was limited by the 9.6 Å bandpass of the single order of the echelle grating, and by the poor charge-transfer and readout properties of the TI 800x800 CCD.

To solve these problems, and to achieve substantially improved precision, the program began Phase III of the radial velocity program in July 1998, using the same I<sub>2</sub> cell with the newly installed 2dcoudé cross-dispersed echelle spectrograph (Tull et al. 1994) with its 2048x2048 Tektronix CCD. The spectrograph now includes echelle orders from 3594Å to 10762Å, which covers the Ca II H and K lines used to measure stellar activity. Wavelength coverage is complete from the blue end to 5691Å, and there are increasingly large inter-order gaps from there to the red end (Tull et al. 1995). Using the full 1200 Å bandpass of the I<sub>2</sub> absorption band at the  $R = 60,000$  focus of the 2dcoudé allows routine internal precision of 6–9  $\text{m s}^{-1}$  to be achieved. All data on the planet hosts targeted in this work are from Phase III. Velocities are derived from 2.7m data using the AUSTRAL code of M. Endl (Endl et al. 2000), and are given in Appendix B.

## Chapter 3

# The Search for New Planets

To search for additional planets in the selected systems, we must first characterize the orbit of the known planet and remove it from the radial-velocity data. The inclusion of all available velocity data allows the orbit of the known planet to be determined with high accuracy. The aim of this project is that removing the strong signal of the known planet may reveal weaker signals from as-yet undetected planets. This chapter describes the orbit-fitting process, and the initial examination of the velocity residuals. Chapter 4 will go into further detail on those targets which proved to be interesting. In this chapter, we use the terms “2.7m” to refer to data taken with the McDonald Observatory 2.7-m Harlan J. Smith (2.7m) Telescope, and “HET” to refer to data taken with the 9.2-m Hobby-Eberly Telescope. The results of periodogram analysis of the residuals to these fits are discussed in the paragraph pertaining to each target. In Section 3.2, I discuss a “wide-field” genetic algorithm search for additional Keplerian signals in the data.

### 3.1 Orbit Fitting and Period Search

Normally, HET data consist of a single exposure per visit, but for some bright ( $V < 6$ ) stars, it is advantageous to take 2-3 exposures in each visit. There are two main reasons: 1) Exposure times for such bright stars are typically much shorter than the “overhead” (setup) time used to acquire the target, so taking multiple exposures makes better use of limited time; 2) By obtaining several velocity measurements in a short time, one can reduce the effect of short-term stellar variability. HET data

consisting of multiple exposures per visit were binned using the weighted mean value of the velocities in each visit. We adopted the quadrature sum of the rms about the mean and the mean internal error as the error bar of each binned point. This procedure was done for HD 3651, HD 19994, HD 38529, HD 74156, HD 128311, and HD 136118. For these objects, the velocity jitter estimated in § 2.2 was added in quadrature to each individual data point before binning.

Available published data were combined with velocities from the HET and 2.7m to fit Keplerian orbits using GaussFit (Jefferys et al. 1987), which is a generalized least-squares program used here to solve a Keplerian radial-velocity orbit model. The GaussFit model has the ability to allow the offsets between data sets to be a free parameter. This is important because the radial velocities cited in published works, and those computed from HET and 2.7m data, are not absolute radial velocities, but rather are measured relative to the iodine-free stellar template. Each data set thus has an arbitrary zero-point offset which must be accounted for in the orbit-fitting procedure. For each of the targets, GaussFit was used first to solve a plain least-squares Keplerian orbit model, then the final system solution was obtained using a robust estimation model (“fair”). This robust estimation iteratively re-weights the data to reduce the effect of outliers. If more than one template spectrum was available, the one which produced the lowest velocity rms about the fit was adopted for all further analysis.

Results of the fits for 47 UMa are given in Table 3.1, and the fitted parameters for all targets are given in Table 3.2, and a summary of the fit results for each individual data set is given in Table 3.3. In computing the planetary minimum mass  $M \sin i$  and semimajor axis  $a$ , the stellar masses listed in Table 2.1 were used. The addition of a large amount of new data and the use of multiple independent data sets in fitting Keplerian orbits have generally improved the precision of the derived planetary parameters by a factor of 2-4 over the best published results. At present, the Catalog of Nearby Exoplanets (Butler et al. 2006) is the most comprehensive source of planetary system parameters. In particular, the precision of the orbital periods have been improved by the addition of new data, due to the increased number of orbits now observed. In this section, we briefly describe the results of our combined fits. Our parameters generally agree within  $2\sigma$  of previously published estimates; any noteworthy disagreements are discussed further in the following paragraphs on each system.



For each object, we searched for periodic signals in the residuals to the known planet’s orbit using the periodogram method (Lomb 1976; Scargle 1982). To assess the statistical significance of those periods, the false alarm probabilities (FAP) were calculated using the bootstrap randomization method detailed by Kürster et al. (1997) and Endl et al. (2002). The bootstrap method randomly shuffles the velocity observations while keeping the times of observation fixed. The periodogram of this shuffled data set is then computed and its highest peak recorded. In this way, we can assess the probability that a periodogram peak of a given power level will arise by chance, without making any assumptions about the error distribution of the data. All bootstrap FAP estimates result from 10000 such realizations. Those results are shown in Table 3.4.

The Saturn-mass ( $M \sin i = 0.2M_{\text{Jup}}$ ) planet HD 3651b was discovered by Fischer et al. (2003b) using observations from Lick and Keck. I fit these data, which were updated in Butler et al. (2006), in combination with observations from the 2.7m and HET at McDonald Observatory (Figure 3.1). The fitted orbital parameters for HD 3651b are of comparable precision to those reported in Butler et al. (2006), and agree within  $2\sigma$ . The recent discovery of a T dwarf companion to HD 3651 (Mugrauer et al. 2006; Luhman et al. 2007) prompts an interesting exercise: Can the radial-velocity trend due to the T dwarf companion be detected in the residuals after removing the planet? We detect a slope of  $-0.30 \pm 0.06 \text{ m s}^{-1} \text{ yr}^{-1}$ , indicating that we are indeed able to discern a trend which is possibly due to the binary companion. However, the reduced  $\chi^2$  of the orbital solution is not significantly improved by the inclusion of a linear trend ( $\Delta\chi^2_{\nu}=0.11$ ). This is probably due to the short time coverage of each data set relative to the orbital period of the distant brown dwarf. The Gaussfit model adjusts the offsets between data sets to compensate for the slope, resulting in a small change in  $\chi^2$  despite the  $5\sigma$  detection of the slope. The parameters given in Table 3.2 were obtained from the fit which did not include a trend.

Four data sets were used in the fit for HD 8574b (Figure 3.2): ELODIE (Perrier et al. 2003), HET, 2.7m, and Lick & Keck (Butler et al. 2006). The Lick and Keck velocities were already combined in Butler et al. (2006), and are considered a single data set here. The fitted planetary parameters agree with those of Butler et al. (2006) within about  $2\sigma$ , and the precision is improved by a factor of 2-5, particularly in the orbital period, due to the inclusion of many cycles. For HD 10697

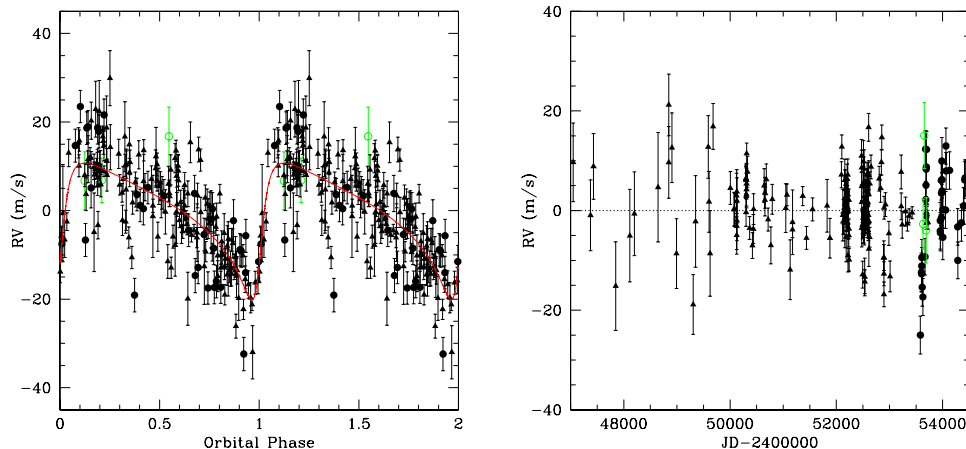


Figure 3.1 Left panel: Phased Keplerian fit to all data for HD 3651b. Filled circles—HET, open circles—2.7m, triangles—Butler et al. (2006). Right panel: Residuals of fit.

(=109 Psc) we fit three data sets: Keck (Butler et al. 2006), 2.7m, and HET. The planetary parameters remain within  $1\sigma$  of those given in Butler et al. (2006), with a marginal improvement in precision. The fit and residuals are shown in Figure 3.4.

HD 19994 (=94 Cet) presents an intriguing challenge. The known planet, from CORALIE data (Mayor et al. 2004), has a published period of 535 days, but with the addition of 56 independent HET visits, fits with those parameters grew steadily worse, reaching an rms of more than  $18 \text{ m s}^{-1}$ . Fitting the HET and 2.7m data only, a period of about 412 days is preferred; starting GaussFit at this value and fitting all of the data results in the one-planet solution given in Table 3.2, with the planet at  $P = 466$  days (Fig. 3.5). However, the rms scatter of the residuals is still rather large ( $15.8 \text{ m s}^{-1}$ ). A strong periodicity is present in the residuals at 326.8 days (bootstrap FAP=0.4%). Further investigations of this system are discussed in Chapter 4.

Another mystery is found in HD 20367, an ELODIE planet which was first announced in a conference proceedings (Udry et al. 2003), but has not yet appeared in a refereed journal. The Geneva planet search group website<sup>1</sup> lists the planet’s period as 469.5 days, with an eccentricity of 0.32 and  $M \sin i = 1.17 M_{\text{Jup}}$ . Eighty-two observations of HD 20367 were obtained at HET over three observing seasons, but

<sup>1</sup><http://obswww.unige.ch/~udry/planet/hd20367.html>

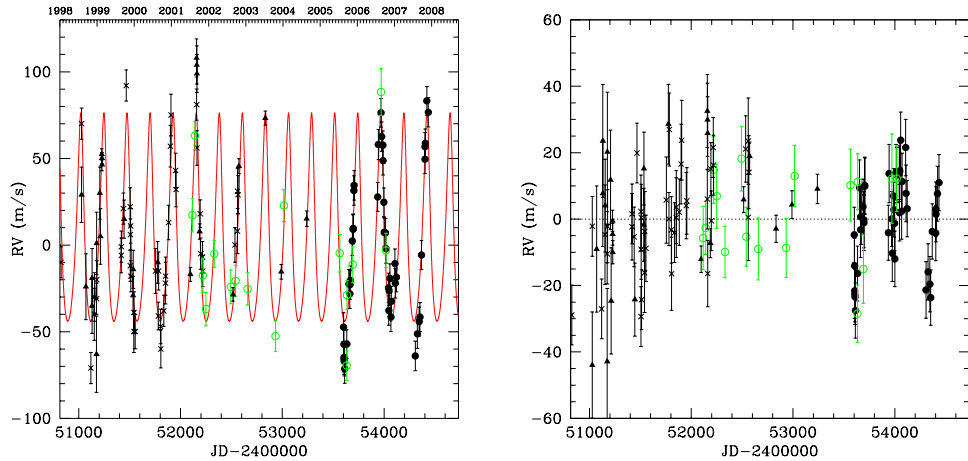


Figure 3.2 Left panel: Keplerian fit to all data for HD 8574b. Filled circles—HET, open circles—2.7m, triangles—Butler et al. (2006), crosses—Perrier et al. (2003). Right panel: Residuals of fit.

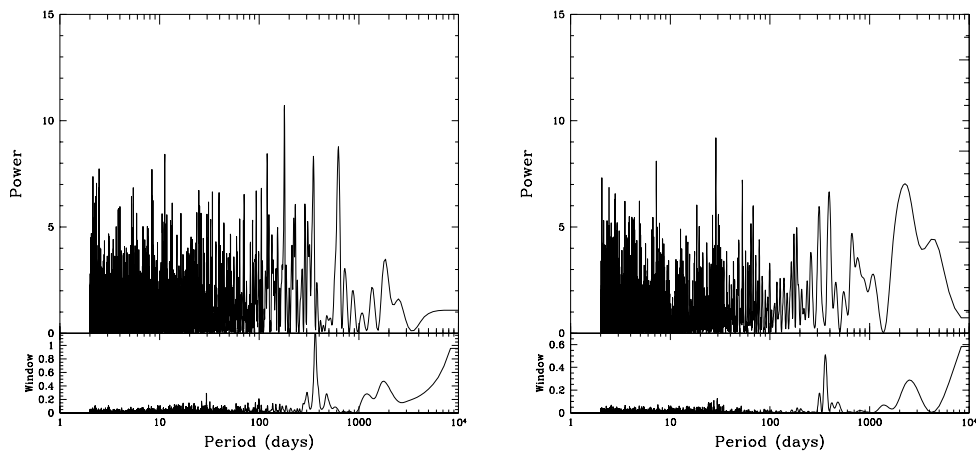


Figure 3.3 Left panel: Lomb-Scargle periodogram of the residuals to the Keplerian fit for HD 3651. The window function is shown in the lower panel. Right panel: Same, but for the HD 8574 system.

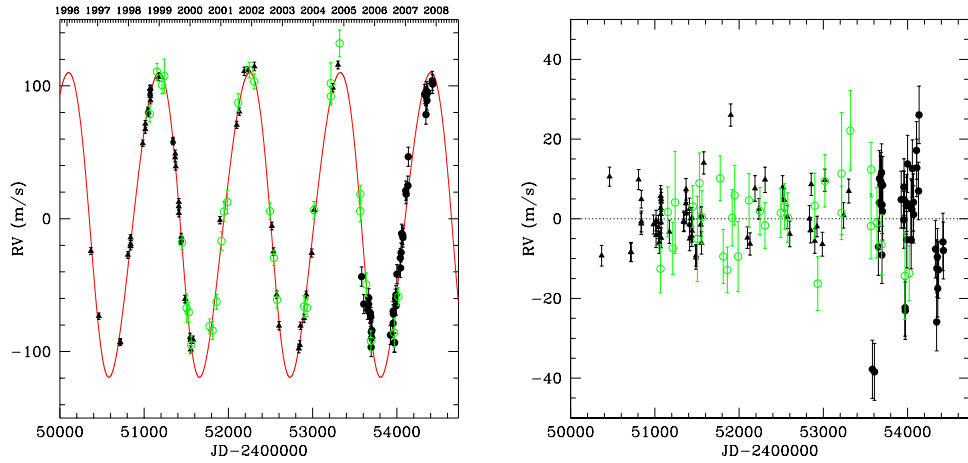


Figure 3.4 Left panel: Keplerian fit to all data for HD 10697b. Filled circles–HET, open circles–2.7m, triangles–Butler et al. (2006). Right panel: Residuals of fit.

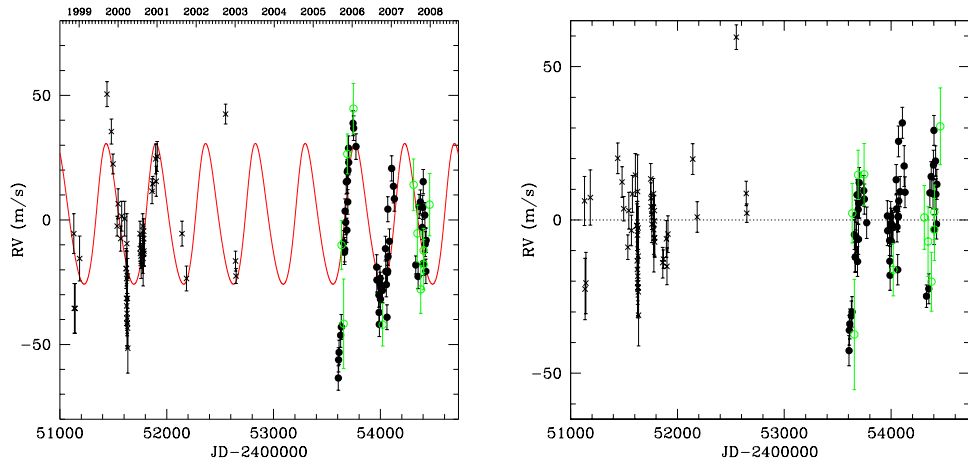


Figure 3.5 Left panel: Keplerian fit to all data for HD 19994b. Filled circles–HET, open circles–2.7m, crosses–Mayor et al. (2004). Right panel: Residuals of fit.

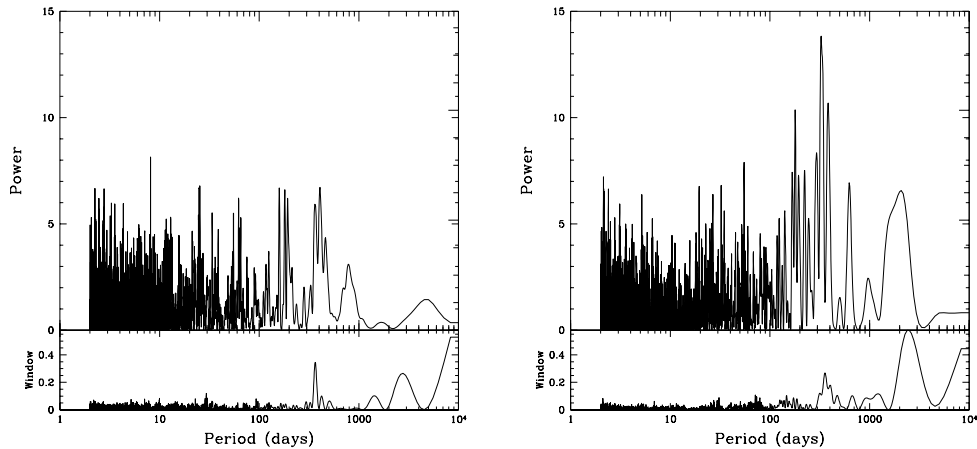


Figure 3.6 Same as Fig. 3.3, but for the HD 10697 (left) and HD 19994 (right) systems.

period searches of these data gave no indication of such a signal. Figure 3.7 shows the periodograms of the velocities from two templates (RADIAL results) and Fig. 3.8 shows the AUSTRAL results. The periods found in these four realizations of the HET data are as follows: Template 1–RADIAL:  $P=781.3$  days,  $FAP<0.01\%$ ; Template 2–RADIAL:  $P=357.1$  days,  $FAP<0.01\%$ ; Template 1–AUSTRAL:  $P=5.6$  days,  $FAP=0.5\%$ ; Template 2–AUSTRAL:  $P=95.8$  days,  $FAP=14.0\%$ . As the periodogram peaks are cleaner and do not show enhanced power at the 1-year window, we adopt the Template 1 results for further orbit fitting. At present, the HET data processed by RADIAL can be fit with a 774-day planet with  $e = 0.67$  and an rms of  $9.19 \text{ m s}^{-1}$ . (Figure 3.9); however, the AUSTRAL version of the same data shows no significant periodicity. The HET RADIAL data can also be fit nearly as well with a 252-day planet ( $\text{rms}=9.55 \text{ m s}^{-1}$ ). We have sufficient time coverage (846 days) to be able to detect both of these candidate periods, but for both, there remain substantial and worrisome phase gaps. At this time, there is not an unambiguous solution for HD 20367b; indeed, the disagreement between RADIAL and AUSTRAL results casts doubt on the presence of a planet at all. Hence, for this work we conclude that there is not convincing evidence for the existence of a planet HD 20367b.

I fit three data sets for the long-period planet HD 23596b: ELODIE (Perrier et al. 2003), HET, and 2.7m (Fig. 3.12. The removal of one outlier from the HET

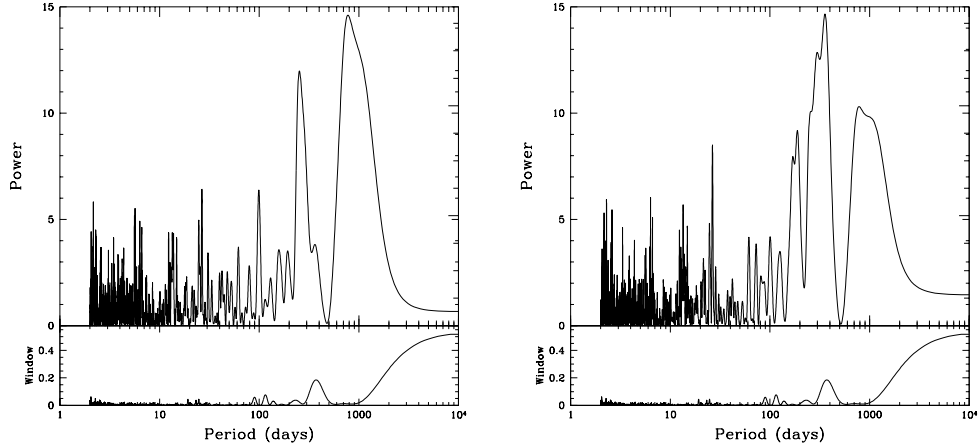


Figure 3.7 Left panel: Periodogram of HET (RADIAL) data for HD 20367. The two highest peaks are at 781 and 252 days. Right panel: Same, but using velocities derived from a different template. The two main peaks are at 357 and 781 days.

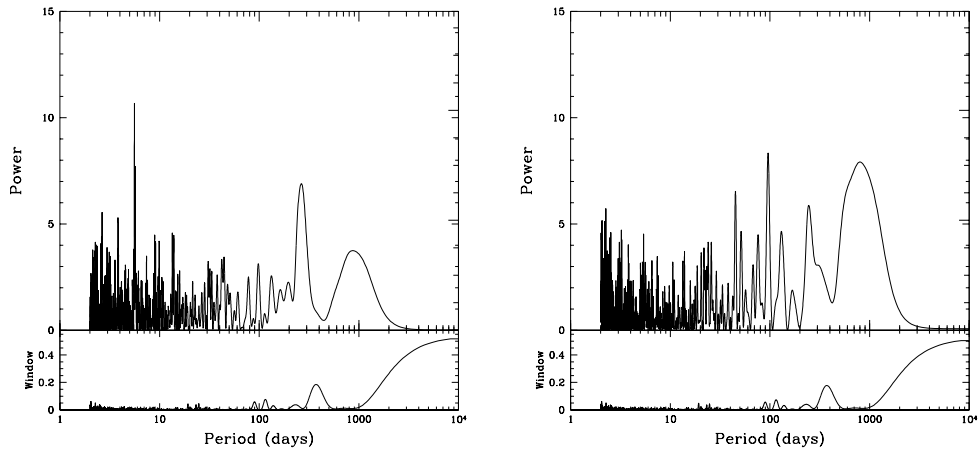


Figure 3.8 Left panel: Periodogram of HET (AUSTRAL) data for HD 20367. The main peak is at 5.6 days. Right panel: Same, but using velocities derived from a different template. The main peak is at 95.8 days.

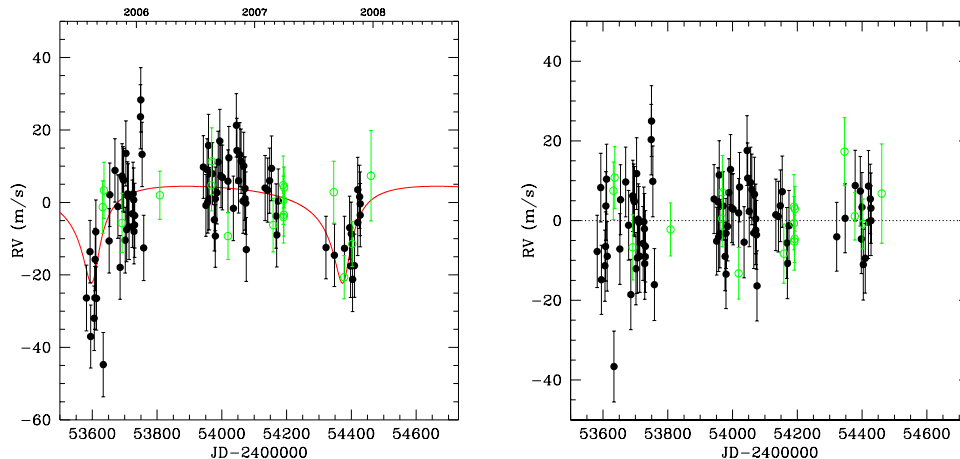


Figure 3.9 Left panel: Keplerian fit to all data for HD 20367b. Filled circles–HET, open circles–2.7m. Right panel: Residuals of fit. The high eccentricity and large phase gaps cast doubt on the planet hypothesis for HD 20367.

data, at JD 2453581, dropped the  $\chi^2_\nu$  from 2.06 to 1.63. The fitted parameters are consistent with those of Perrier et al. (2003), and of comparable precision. A periodogram of the residuals shows a substantial peak at about 188 days (Figure 3.14), which will be discussed further in Chapter 4.

For HD 28185, the 2.7m and HET data are fit together with CORALIE observations from Santos et al. (2001), as shown in Figure 3.13. Several parameters differ from the published values by  $2\text{--}3\sigma$ , but the current values are more precise by a factor of 3–10, reflecting a doubling of the quantity of data. The residuals show a significant peak at 2.1 days (Fig. 3.14), which is discussed in § 4.2.4. The HD 38529 system contains 2 widely separated planets with periods of 14 and 2153 days (Fischer et al. 2003a). I fit the Lick & Keck data of Butler et al. (2006) along with observations from HET and 2.7m. The fitted orbit of HD 38529b after removing the outer planet is shown in the left panel of Figure 3.15, and the fitted orbit for HD 38529c after removing the inner planet is shown in the right panel. A strong residual period of 32 days is evident (Fig. 3.19) and will be discussed further in Chapter 4.

HD 40979, with its 264-day planet and a published rms of more than  $20 \text{ m s}^{-1}$  (Fischer et al. 2003a; Butler et al. 2006), presented an attractive target for the possibility of additional planets hiding in the residual velocity scatter. Though

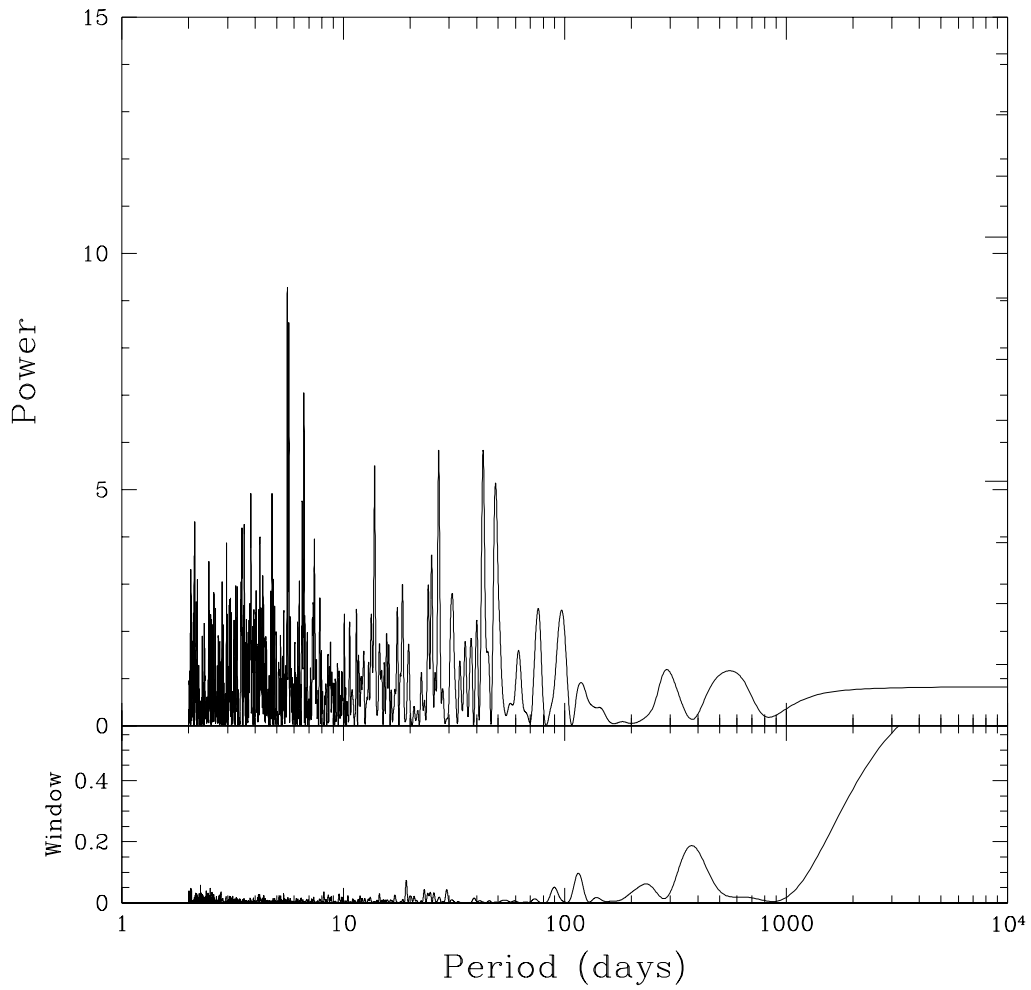


Figure 3.10 Same as Fig. 3.3, but for the HD 20367 system. The highest peak is at 5.6 days.



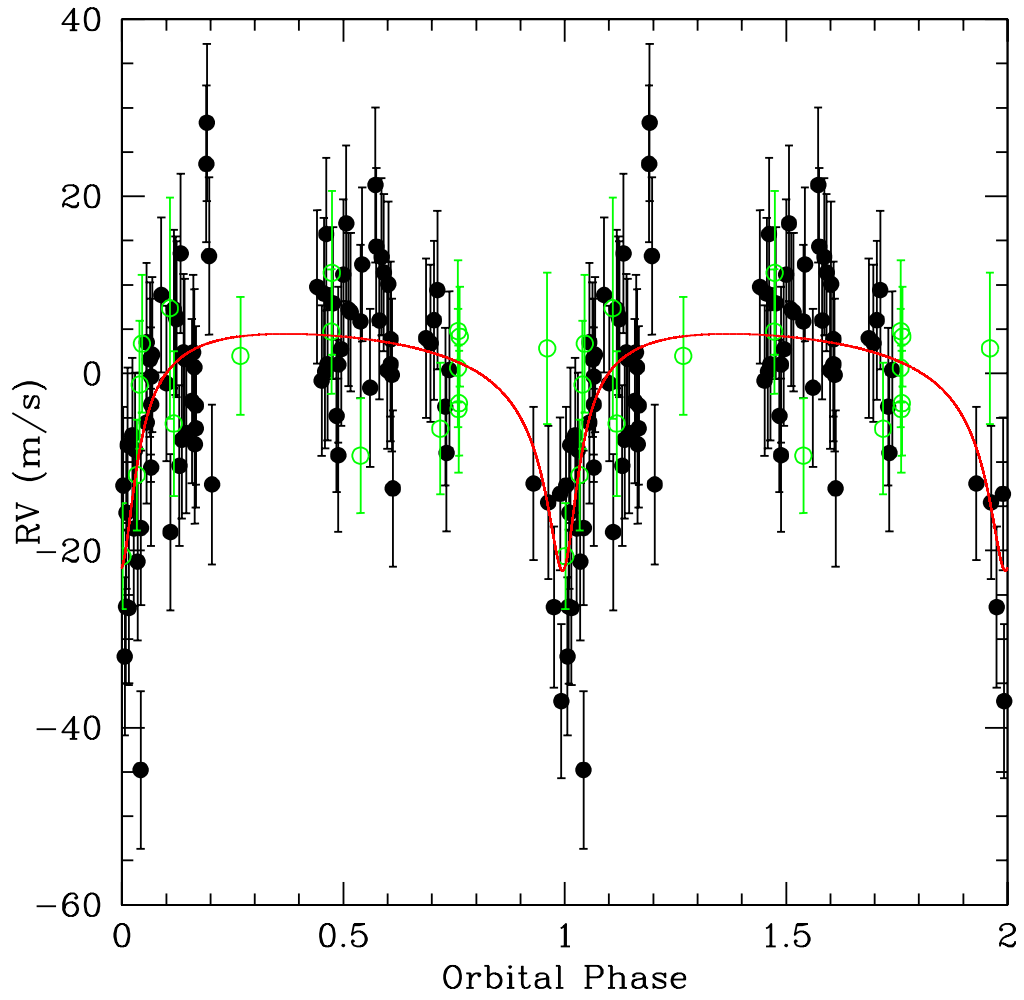


Figure 3.11 HET (filled circles) and 2.7m (open circles) data for HD 20367, phased to the best-fit period of 774 days.

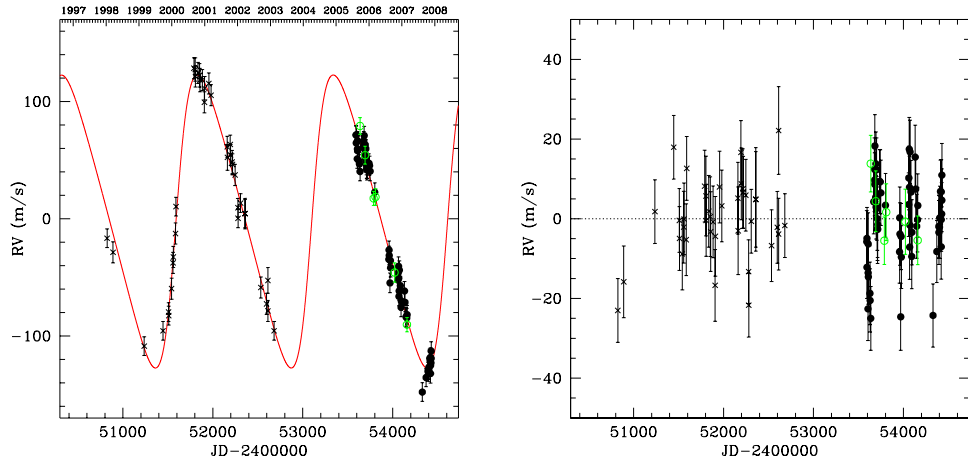


Figure 3.12 Left panel: Keplerian fit to all data for HD 23596b. Filled circles–HET, open circles–2.7m, crosses–Perrier et al. (2003). Right panel: Residuals of fit.

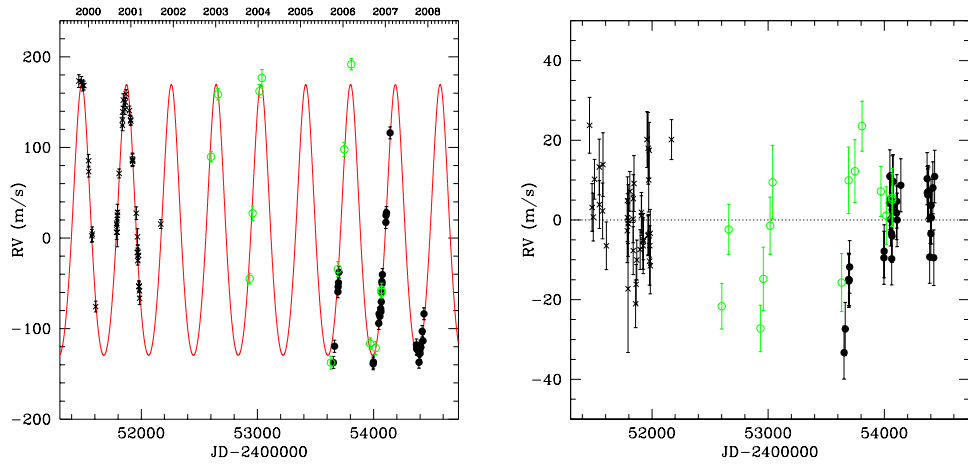


Figure 3.13 Left panel: Keplerian fit to all data for HD 28185b. Filled circles–HET, open circles–2.7m, crosses–Santos et al. (2001). Right panel: Residuals of fit.

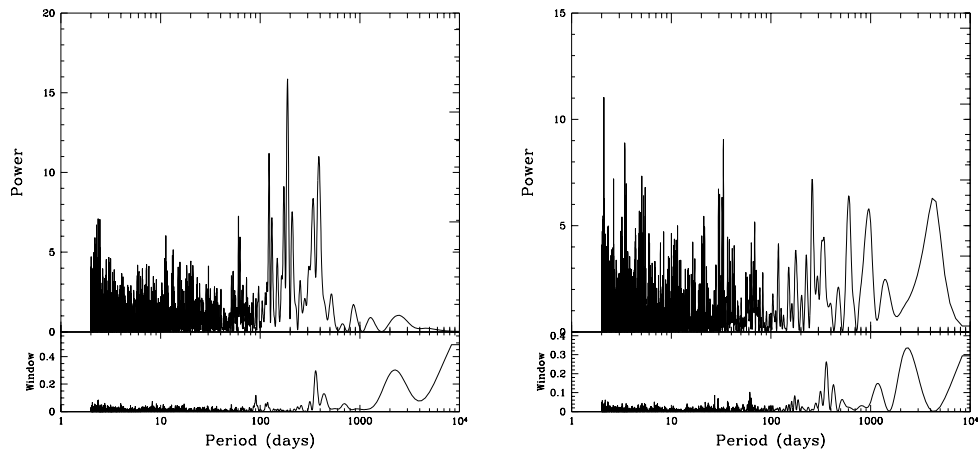


Figure 3.14 Same as Fig. 3.3, but for the HD 23596 (left) and HD 28185 (right) systems.

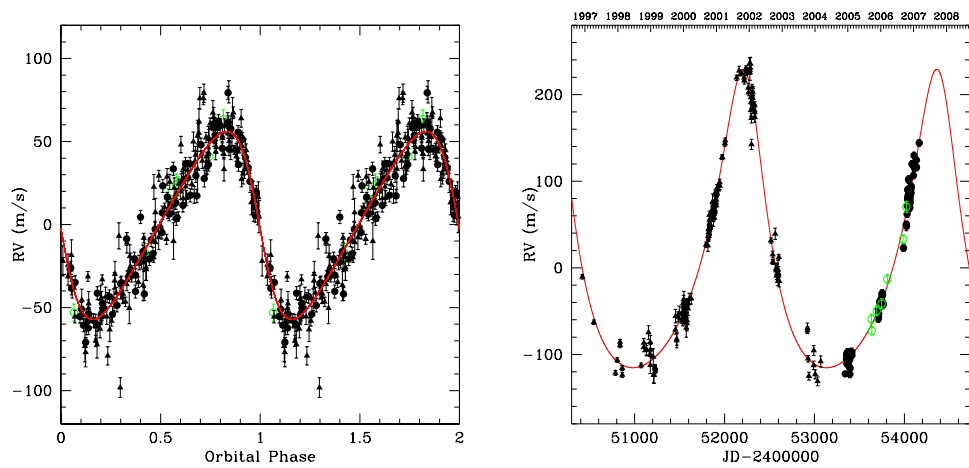


Figure 3.15 Left panel: Phased Keplerian fit to all data for HD 38529b. Filled circles—HET, open circles—2.7m, triangles—Butler et al. (2006). Right panel: Fit to all data for HD 38529c.

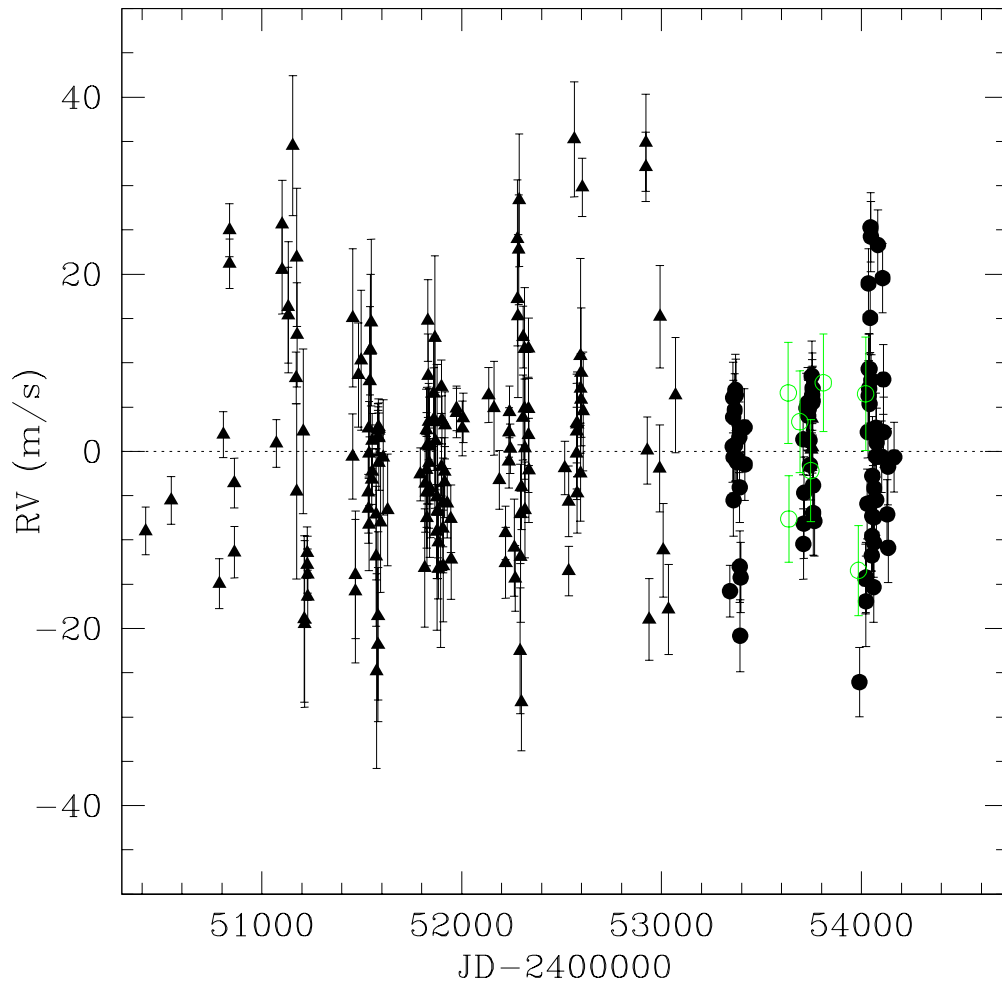


Figure 3.16 Residuals of Keplerian fit to all data for HD 38529. Filled circles–HET, open circles–2.7m, triangles–Butler et al. (2006).

the addition of 92 HET data points has improved the precision of the planetary parameters by a factor of  $\sim 3$ , the rms about the fit (Table 3.3) remains large. This star is a relatively rapid rotator, with  $V \sin i = 7.4 \text{ km s}^{-1}$  (Valenti & Fischer 2005). The chromospheric activity index  $\log R'_{HK}$  is a measure of the ratio of emission in the Ca II H and K lines to the total bolometric emission of the star (Noyes et al. 1984). The mean value of  $\log R'_{HK}$  for the targets in this work is  $-4.93 \pm 0.19$ ; this level is usually considered “inactive.” For HD 40979,  $\log R'_{HK} = -4.59 \pm 0.01$ ; of the targets, only HD 20367 has a higher emission level ( $\log R'_{HK} = -4.50 \pm 0.05$ ). With a spectral type of F8, HD 40979 presents a host of obstacles for precision radial velocity work. The effective temperature is higher than that of the G-type stars most frequently observed in planet search programs. This has the effect of reducing the strength and number of spectral lines suitable for velocity measurement. Rotation broadens the remaining lines, further reducing the level of precision that can be achieved. For this star, we also encountered a new problem: the HET velocities produced by RADIAL showed a large seasonal systematic trend upward by nearly  $80 \text{ m s}^{-1}$  each season (Figure 3.17). The RADIAL results from several HET planet search targets have shown similar trends; at this writing, the problem appears to be a floating zero-point in the  $I_2$  reference spectrum which occasionally causes imperfect removal of the barycentric velocity. Performing the fit using the AUSTRAL velocities from HET gives no indication of such a systematic, and those data were used for the adopted solution and all subsequent analysis.

HD 72659b is a very long-period ( $P \sim 10 \text{ yr}$ ) planet first reported by Butler et al. (2003) well before an orbit had been completed. This object has since achieved phase closure, and the current best fit is consistent with that reported by Butler et al. (2006), but with increased precision. The fit and its residuals are shown in Figure 3.20. For HD 74156, I fit the two planets at 51 and 2440 days using ELODIE and CORALIE data from Naef et al. (2004), and 85 independent HET visits. The left panel of Figure 3.21 shows the orbit of HD 74156b after removing the outer planet, and the right panel shows HD 74156c after removing the inner planet. The HET data for HD 74156 presented here are derived from the same spectra as the velocities given in Bean et al. (2008), but these were obtained using RADIAL. Further investigation of the residual 126-day signal and the third planet reported by Bean et al. (2008) is discussed in § 4.2.6.

The planet orbiting HD 80606, first announced by Naef et al. (2001a), is the

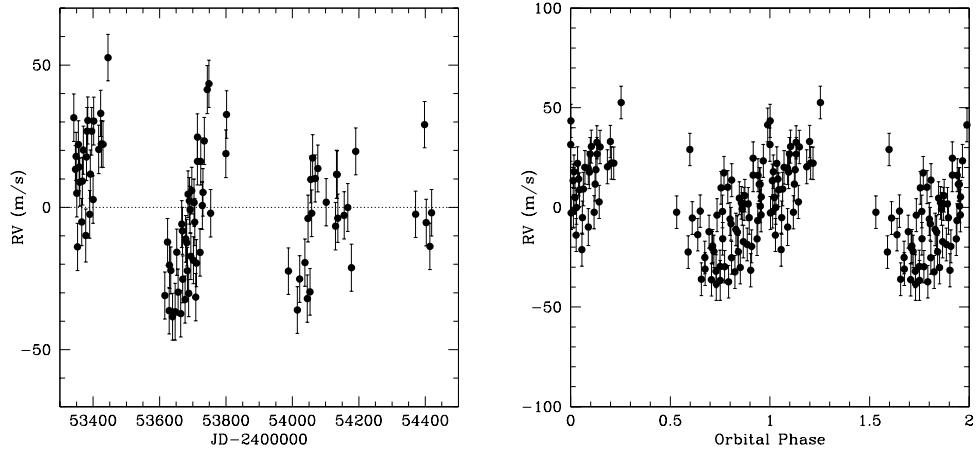


Figure 3.17 Left panel: Residuals of HET data (RADIAL results) to a Keplerian fit for HD 40979b. Right panel: The same HET residuals phased to a period of 406 days.

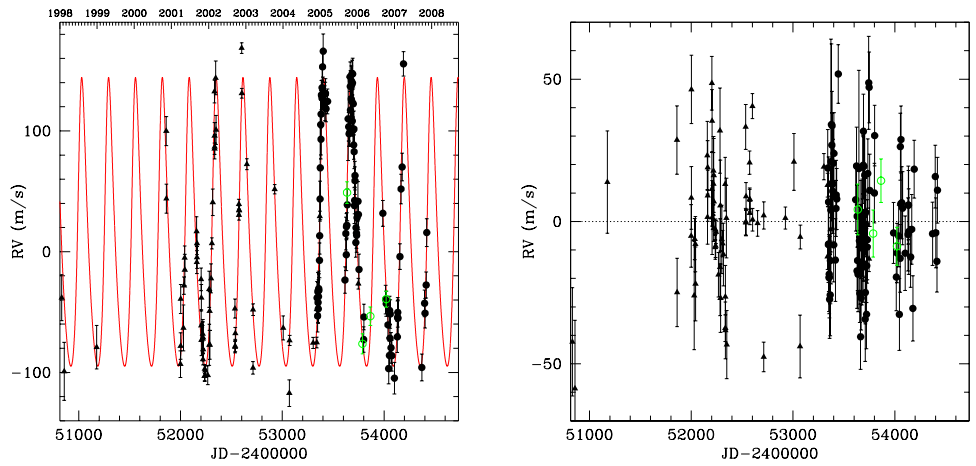


Figure 3.18 Left panel: Keplerian fit to all data for HD 40979b. Filled circles–HET (AUSTRAL results), open circles–2.7m, triangles–Butler et al. (2006). Right panel: Residuals of fit.

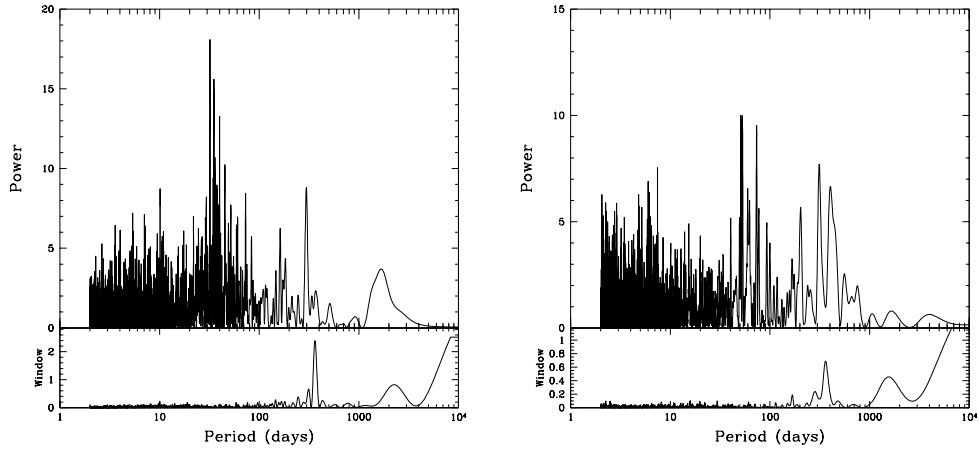


Figure 3.19 Same as Fig. 3.3, but for the HD 38529 (left) and HD 40979 (right) systems. AUSTRAL results were used for HD 40979.

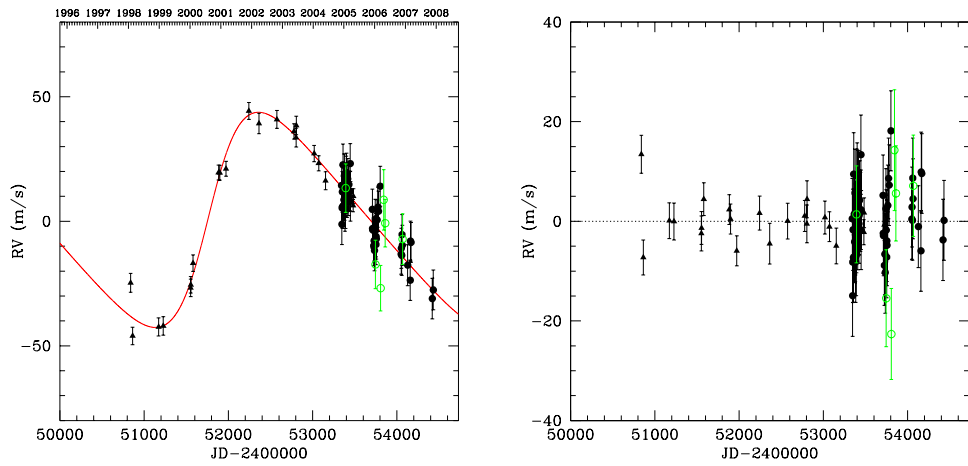


Figure 3.20 Left panel: Keplerian fit to all data for HD 72659b. Filled circles–HET, open circles–2.7m, triangles–Butler et al. (2006). Right panel: Residuals of fit.

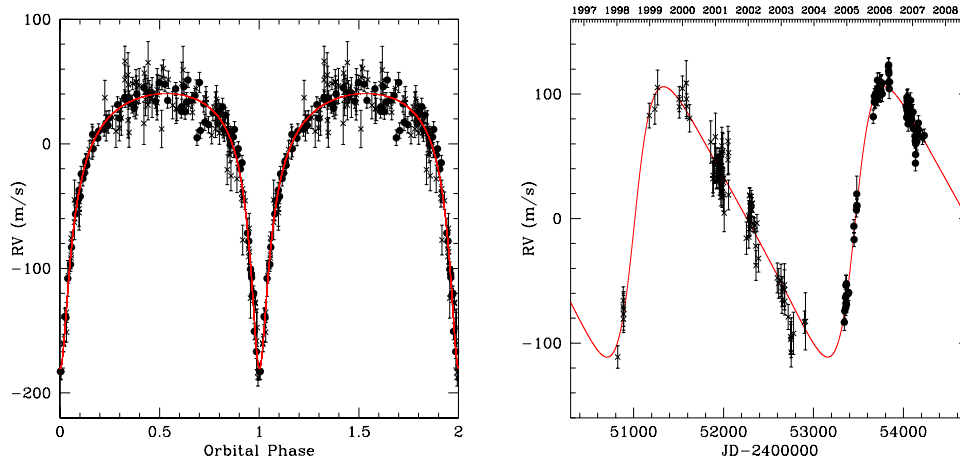


Figure 3.21 Left panel: Phased Keplerian fit to all data for HD 74156b. Filled circles–HET, crosses–Naef et al. (2004). Right panel: Fit to all data for HD 74156c.

most eccentric extrasolar planet known, with  $e = 0.933 \pm 0.001$  (Table 3.2). I have fit the CORALIE data in combination with the Keck data given in Butler et al. (2006) and 23 observations from HET. The fit and its residuals are shown in Figure 3.24.

For HD 89744b, we combine data from the HET with 6 measurements from the 2.7m telescope and Lick data from Butler et al. (2006). Our derived parameters agree with those of Butler et al. (2006) within  $2\sigma$ . The scatter about our fit remains large (Fig. 3.25), most likely because of the star’s early spectral type (F7V), which hinders precise radial-velocity measurements due to the smaller number of spectral lines. For example, the F7V star HD 221287 was recently found to host a planet (Naef et al. 2007); despite the superb instrumental precision of the HARPS spectrograph, that orbital solution has a residual rms of  $8.5 \text{ m s}^{-1}$ .

Butler et al. (1996) first reported the 1090-day companion to 47 UMa (=HD 95128) using data from Lick Observatory. With additional velocity measurements over 13 years, Fischer et al. (2002a) announced a long-period second planet, 47 UMa c, with a period of  $2594 \pm 90$  days and a mass of  $0.76 M_{\text{Jup}}$ . Naef et al. (2004) presented ELODIE observations of 47 UMa, and noted that the second planet was not evident in their data, which were fit well with a single Keplerian model.

We now fit four data sets for 47 UMa: Lick (Fischer et al 2002), ELODIE (Naef et al. 2004), 2.7m telescope, and the HET. The one-planet fit (Model 1)



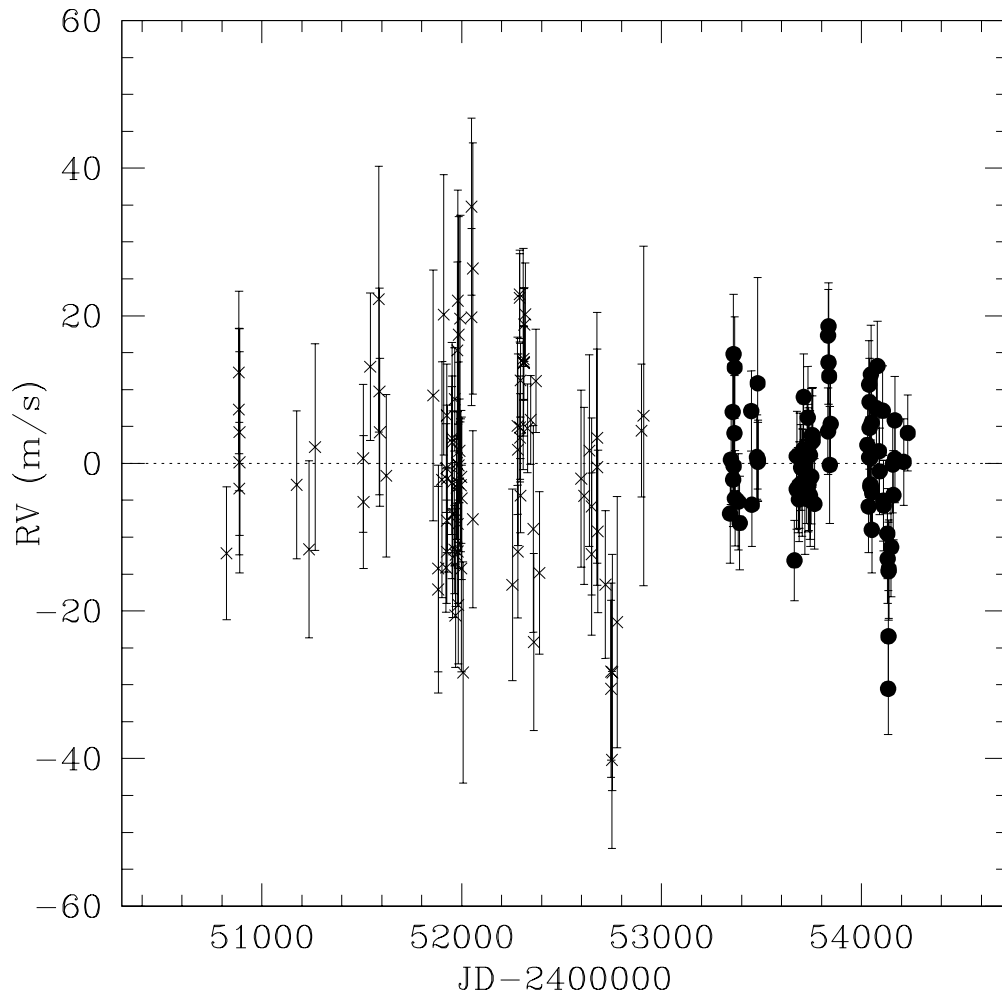


Figure 3.22 Residuals of Keplerian fit to all data for HD 74156. Filled circles—HET, cross—Naef et al. (2004).

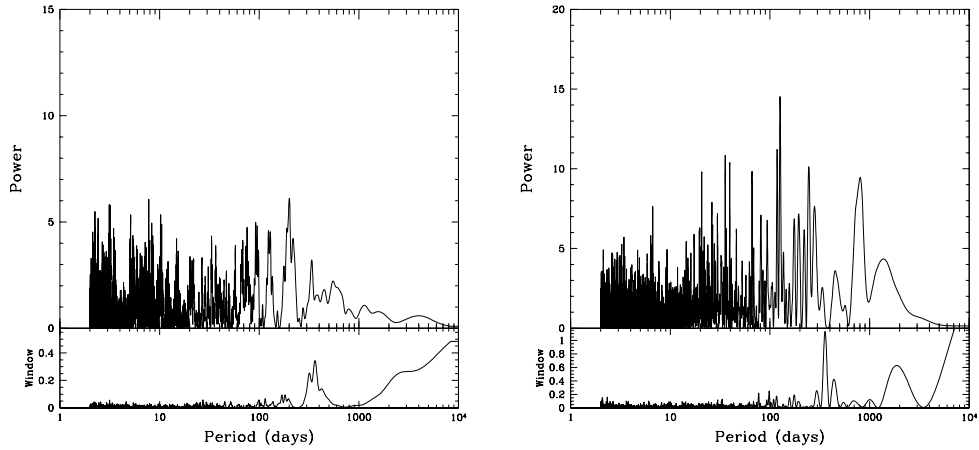


Figure 3.23 Same as Fig. 3.3, but for the HD 72659 (left) and HD 74156 (right) systems. The recently-announced planet HD 74156d, between planets b and c, was not included.

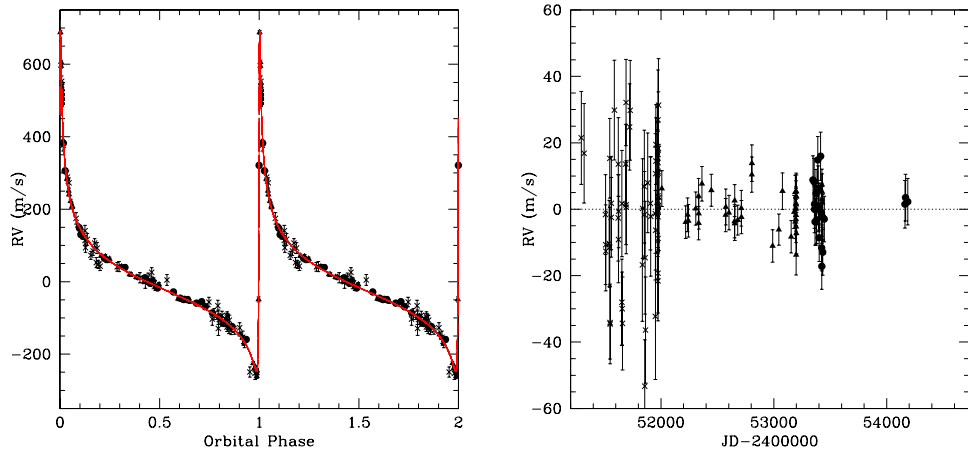


Figure 3.24 Left panel: Phased Keplerian fit to all data for HD 80606b. Filled circles—HET, crosses—Naef et al. (2004), triangles—Butler et al. (2006). Right panel: Residuals of fit.

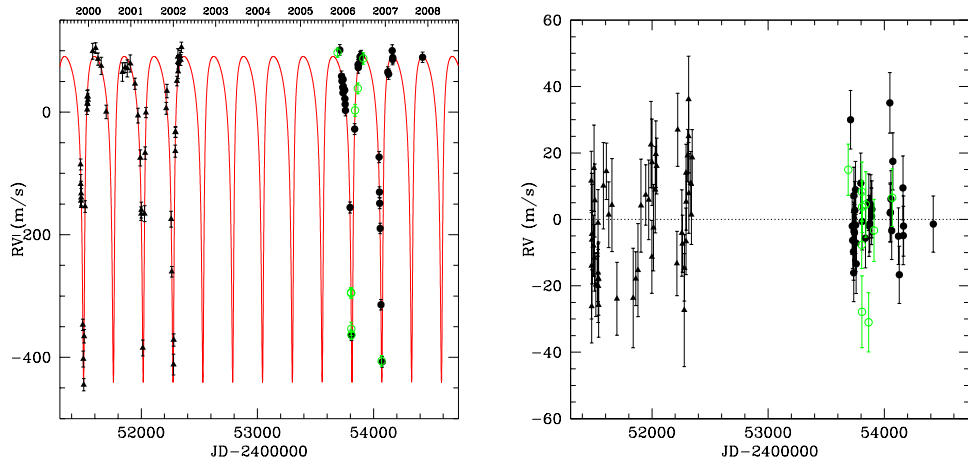


Figure 3.25 Left panel: Keplerian fit to all data for HD 89744b. Filled circles–HET, open circles–2.7m, triangles–Butler et al. (2006). Right panel: Residuals of fit.

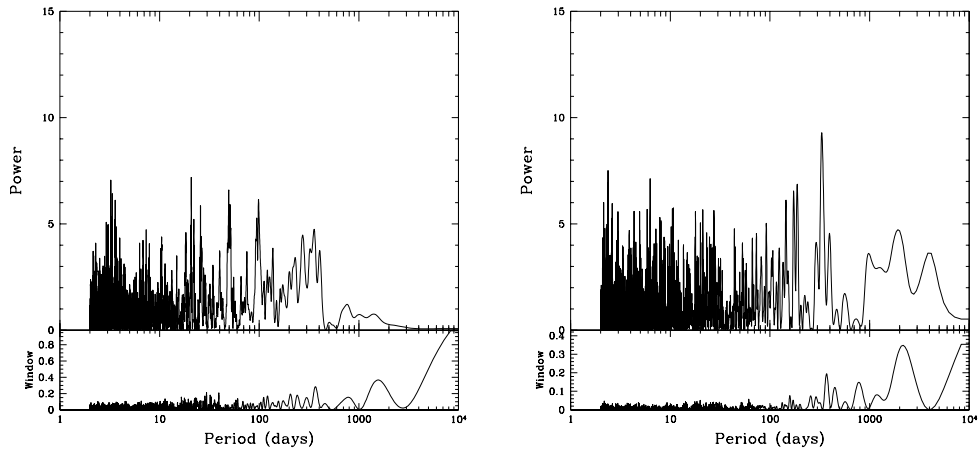


Figure 3.26 Same as Fig. 3.3, but for the HD 80606 (left) and HD 89744 (right) systems.

and the residuals to that fit are shown in Figure 3.29. We emphasize that this fit includes all available published data, over a time span of more than 20 years, and includes 200 high-precision measurements obtained with the HET High-Resolution Spectrograph at 78 independent epochs. The total rms about the combined one-planet fit is  $10.1 \text{ m s}^{-1}$ . The rms scatter about the one-planet fit for each of the four datasets is: Lick– $10.9 \text{ m s}^{-1}$ , ELODIE– $12.1 \text{ m s}^{-1}$ , 2.7m– $11.1 \text{ m s}^{-1}$ , HET– $7.1 \text{ m s}^{-1}$ . A periodogram of the residuals of all of the data to the 1-planet fit is shown in Figure 3.27. No clear peak rises above the noise level at any period between 2 and 10000 days; the total duration of the available data is now 7472 days (20.5 years). While a peak is present at about 2193 days, close to the period reported for 47 UMa c by Fischer et al. (2002a), its bootstrap false-alarm probability (FAP) is 4.0%.

To further explore the possible presence of 47 UMa c, we fit all of the datasets with a two-planet model fixed at the parameters of Fischer et al. (2002a) (Model 2), and then repeated the fit allowing all parameters to be free except for  $e$  and  $\omega$  of the second planet (Model 3), which were fixed at  $0.005$  and  $127^\circ$ , respectively, after Fischer et al. (2002a). No models achieved convergence with those two parameters free. These tests are summarized in Table 3.1. Model 2 had a reduced chi-square ( $\chi_\nu^2$ ) of 4.51 and an rms of  $11.5 \text{ m s}^{-1}$  about the fit, whereas Model 3 had a  $\chi_\nu^2$  of 2.18 and an rms of  $8.5 \text{ m s}^{-1}$ . For comparison, the one-planet fit (Model 1) had a  $\chi_\nu^2$  of 3.23 and an rms of  $10.1 \text{ m s}^{-1}$ . Noting that the poor fit of Model 2 was largely due to errors in the period of the inner planet, we re-did the fits allowing the parameters for the inner planet to be free while fixing those of the outer planet at the values reported by Fischer et al. (2002a) (Model 4). The  $\chi_\nu^2$  of this fit was 3.39, with an rms of  $11.0 \text{ m s}^{-1}$ . Model 4 results in a worse fit than the single-planet model, and the residuals periodogram shows a strong peak at the period of the outer planet. This is an indication that a non-existent signal has been fitted and removed. Figure 3.28 shows the results of Model 3; note that the residuals of the two-planet fit show distinct curvature, casting further doubt on the 2-planet model.

The free two-planet (Model 3) fit was the best of the four, in terms of both the goodness-of-fit criterion ( $\chi_\nu^2$ ) and the total rms scatter about the fits. The rms about the individual datasets for this fit is the following: Lick– $8.0 \text{ m s}^{-1}$ , ELODIE– $11.1 \text{ m s}^{-1}$ , 2.7m– $10.1 \text{ m s}^{-1}$ , HET– $5.3 \text{ m s}^{-1}$ . The parameters for the 47 UMa planetary system given in Table 3.2 are those obtained by Model 3. Although

the best-fit set of parameters obtained a period of 9157 days for the outer planet, there is no corresponding peak in the periodogram of the residuals from the single-planet fit (Fig. 3.29). However, the periodogram method is not as reliable when the periodic signal approaches or exceeds the total duration of observations, as is the case here, where the total time baseline is 7472 days. We note that we have been able to reproduce the result of Fischer et al. (2002a) by this method: a periodogram analysis of the Lick data alone after removing 47 UMa b revealed a strong peak at 2083 days, with a bootstrap FAP of 0.15%. We are also able to recover the Fischer et al. (2002a) parameters of 47 UMa c from the Lick data alone. Since the total time coverage of the Lick data presented in Fischer et al. (2002a) is 5114 days (14 yr), an analysis of those data alone is not adequate to fully constrain the 9157-day period obtained by our best-fit model which adds six years to the total duration of observations. It is possible that the shorter period for 47 UMa c reported by Fischer et al. (2002a) is an alias of the true period; at present, our fits indicate that period to be about 3-4 times longer, but with substantial uncertainty. An earlier version of this same analysis reported in Wittenmyer et al. (2007a) indicated a period of 7586 days for the outer planet, with an identical  $\chi^2_\nu$  and a similar rms about the fit. Due to the high level of uncertainty concerning the two-planet model, we adopt the 1-planet solution in this work.

For HD 106252, we fit four data sets: ELODIE (Perrier et al. 2003), Lick (Butler et al. 2006), HET, and 2.7m. The fitted parameters agree within  $1\sigma$  of Butler et al. (2006), except for  $K$ , which decreased from  $152 \text{ m s}^{-1}$  to  $137 \text{ m s}^{-1}$ . The current uncertainties are a factor of 4-10 smaller, due to the inclusion of several orbital cycles from the combination of data sets. The fit and residuals are shown in Figure 3.30; no significant signals are present in the residuals.

The 394-day planet orbiting HD 108874 was discovered in Keck observations by Butler et al. (2003), and a second planet at 1599 days was announced in Vogt et al. (2005) after HET observations had begun. The total rms about our combined fit is  $3.8 \text{ m s}^{-1}$ , which is the best of all the fits described here (Fig. 3.31). Such a small residual scatter leaves little room for undetected planets, and the periodogram shows only noise (Fig. 3.32).

Vogt et al. (2002) reported the planet orbiting HD 114783, and recently, Wright et al. (2007) proposed an outer companion with a period of at least 8 yr. We combine the Keck data given in Butler et al. (2006) with HET observations, and

Table 3.1. 47 UMa Orbital Solutions

Parameter	Model 1	Model 2 <sup>a</sup>	Model 3 <sup>b</sup>	Model 4 <sup>c</sup>
$P_b$ (days)	1077.2	1089.0	1080.2	1072.5
$T_b$ (JD-2400000)	52450	50356	52283	51995
$e_b$	0.027	0.061	0.019	0.047
$\omega_b$ (degrees)	147	171.8	93	1
$K_b$ ( $\text{m s}^{-1}$ )	46.2	49.3	48.4	52.0
$P_c$ (days)	...	2594	9157	2594
$T_c$ (JD-2400000)	...	51363.5	52554	51363.5
$e_c$	...	0.005	0.005	0.005
$\omega_c$ (degrees)	...	127	127	127
$K_c$ ( $\text{m s}^{-1}$ )	...	11.1	16.1	11.1
rms ( $\text{m s}^{-1}$ )	10.1	11.5	8.5	11.0
$\chi^2_\nu$	3.23	4.51	2.18	3.39

<sup>a</sup>All parameters fixed at those of Fischer et al. (2002a)

<sup>b</sup>All parameters free except for  $e_c$  and  $\omega_c$

<sup>c</sup>Only parameters for planet c fixed at those of Fischer et al. (2002a)

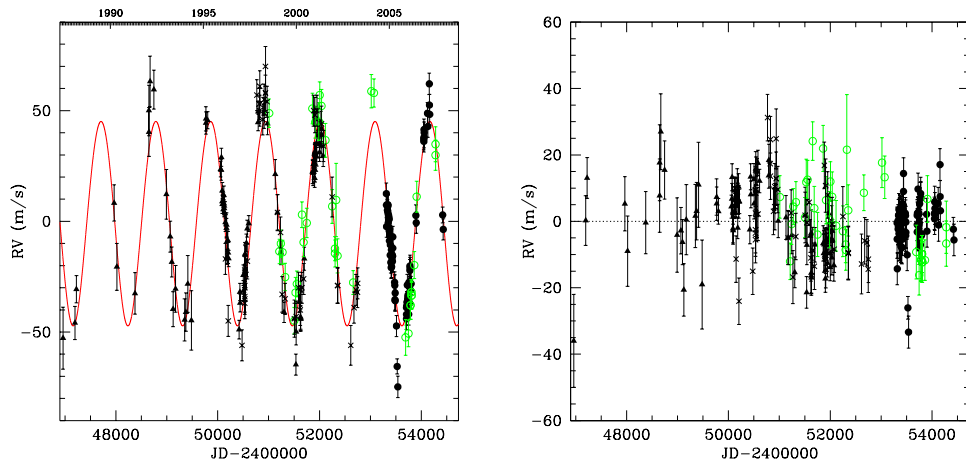


Figure 3.27 Left panel: Keplerian fit to all data for 47 UMa b (1-planet fit). Filled circles–HET, open circles–2.7m, triangles–Fischer et al. (2002a), crosses–Naef et al. (2004). Right panel: Residuals of fit.

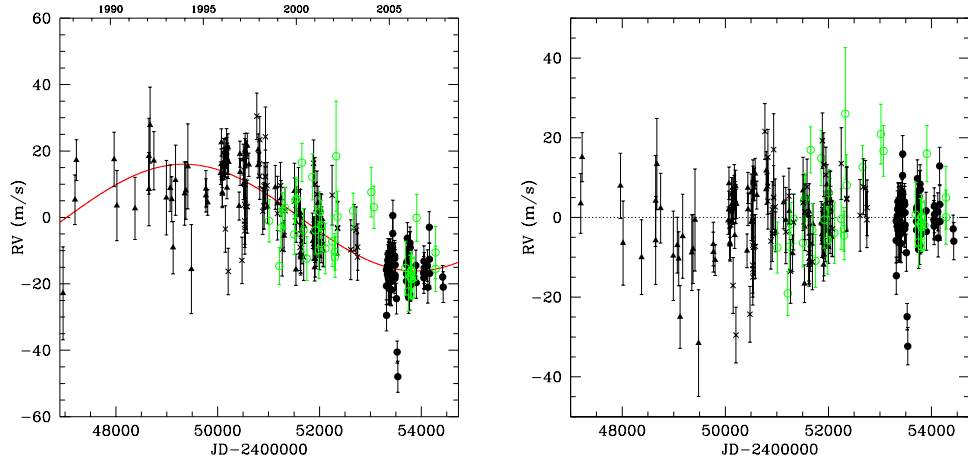


Figure 3.28 Left panel: Keplerian fit to all data for 47 UMa c after the inner planet has been removed. This fit is referenced in the text as Model 3. Filled circles—HET, open circles—2.7m, triangles—Fischer et al. (2002a), crosses—Naef et al. (2004). Right panel: Residuals of fit.

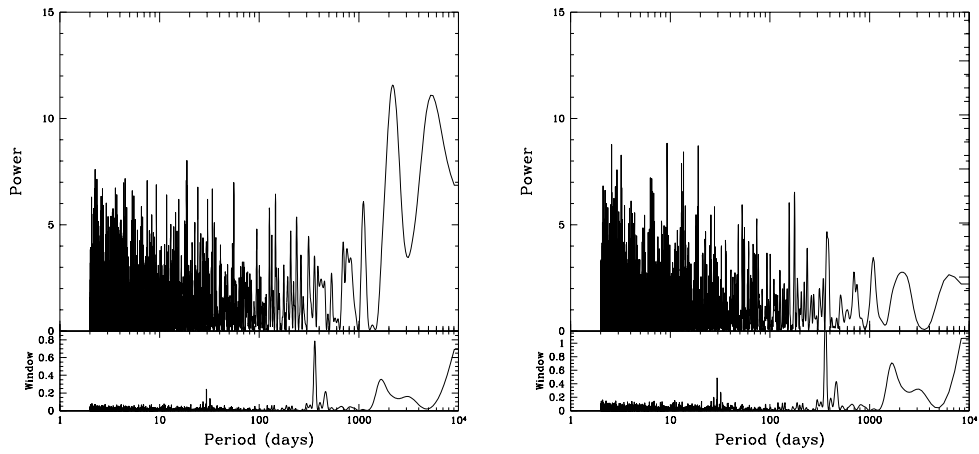


Figure 3.29 Same as Fig. 3.3, but for the 47 UMa system. Left panel: periodogram of residuals to a 1-planet fit. Right panel: periodogram of residuals to a 2-planet fit.

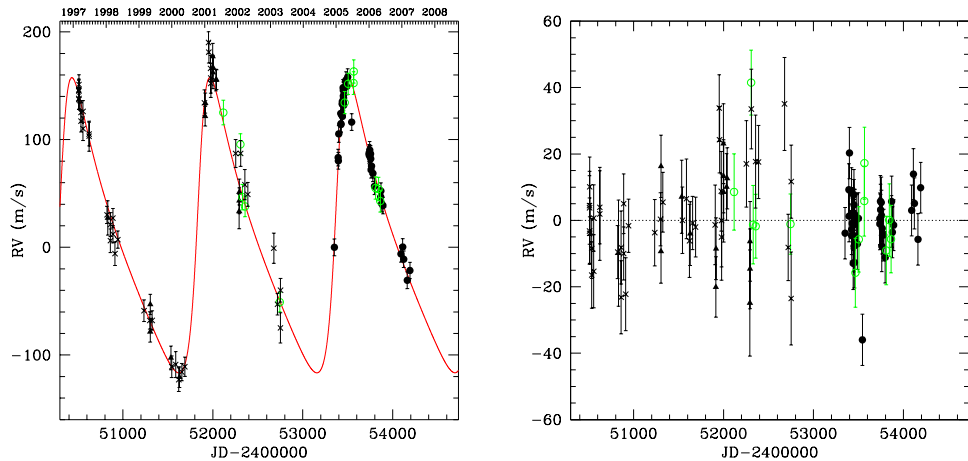


Figure 3.30 Left panel: Keplerian fit to all data for HD 106252b. Filled circles–HET, open circles–2.7m, triangles–Butler et al. (2006), crosses–Perrier et al. (2003). Right panel: Residuals of fit.

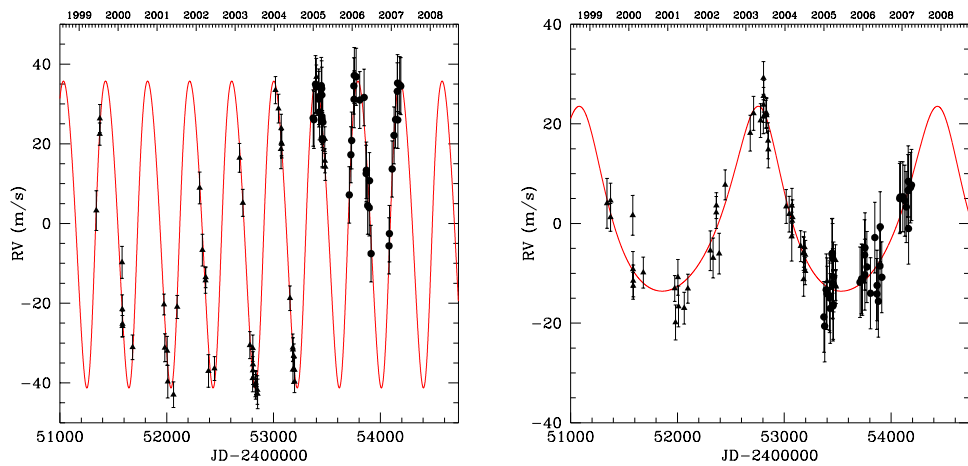


Figure 3.31 Left panel: Keplerian fit to all data for HD 108874b. Filled circles–HET, triangles–Vogt et al. (2005), crosses–Perrier et al. (2003). Right panel: Same, for HD 108874c.



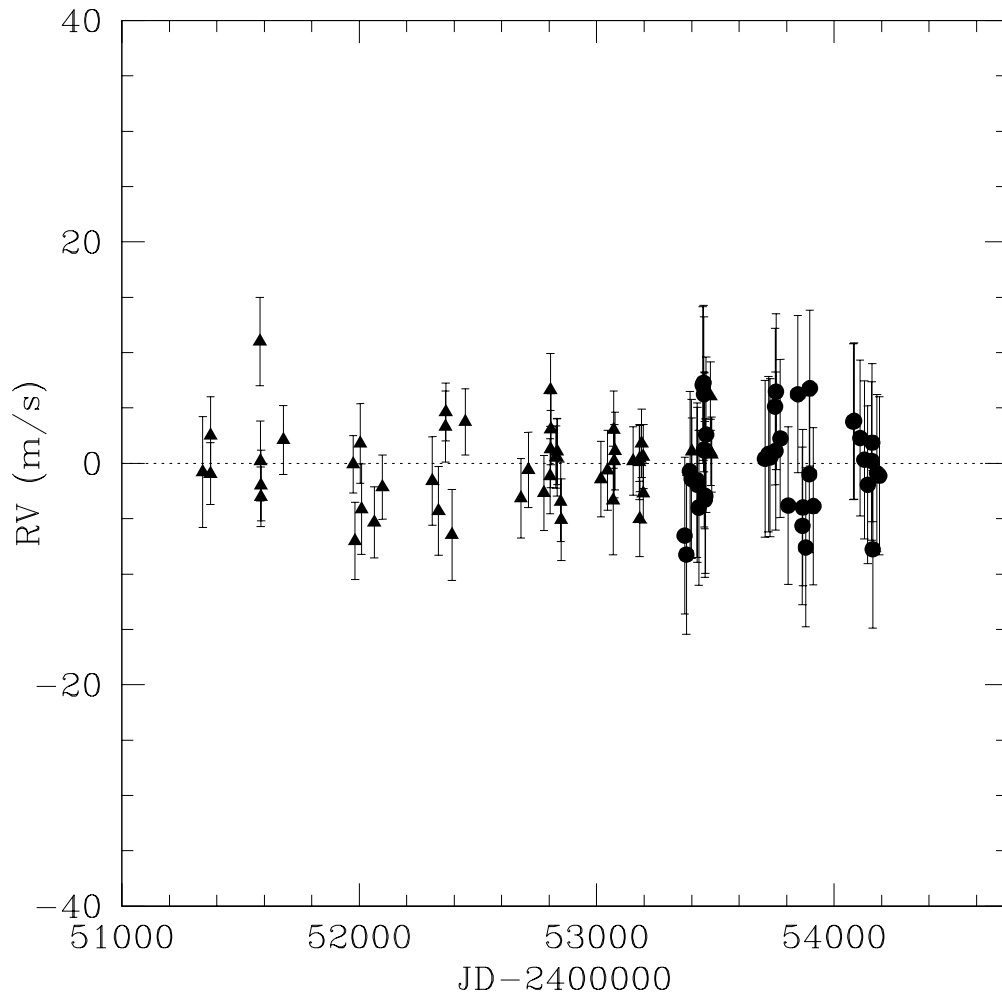


Figure 3.32 Residuals of Keplerian fit to all data for HD 108874. Filled circles—HET, triangles—Vogt et al. (2005).

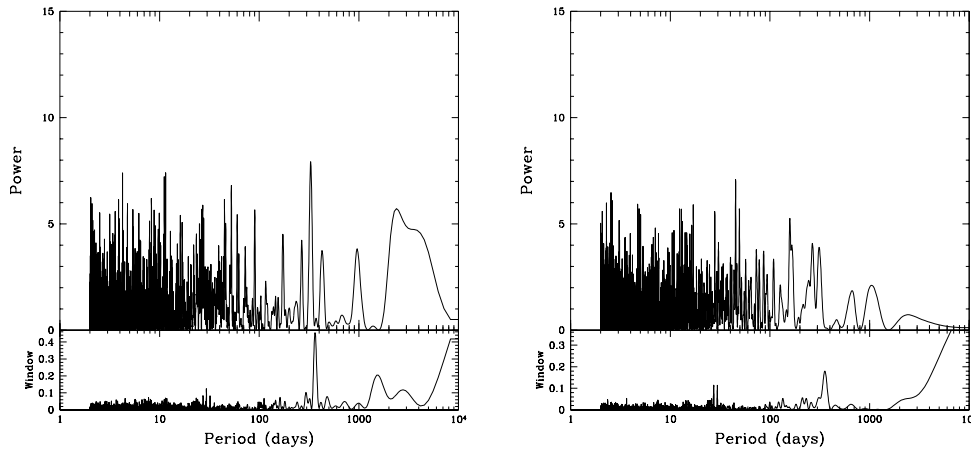


Figure 3.33 Same as Fig. 3.3, but for the HD 106252 (left) and HD 108874 (right) systems.

these results support the claim of an outer planet. A single-planet fit has a total rms of  $6.8 \text{ m s}^{-1}$  and  $\chi^2_\nu=5.05$ , whereas a two-planet fit reduces the rms to  $4.9 \text{ m s}^{-1}$  and the  $\chi^2_\nu$  to 2.00. A periodogram of the residuals to the 1-planet fit (Fig. 3.35) shows a large, broad peak near 3300 days, indicative of an additional long-period signal. The data considered in Wright et al. (2007) were of insufficient duration to establish a solution for the outer planet, but the combination of data allows for a Keplerian fit to converge, although substantial uncertainty remains in the period. The parameters given in Table 3.2 are those from the 2-planet fit.

The inner planet ( $P \sim 450$  days) in the HD 128311 system was first discovered by Butler et al. (2003), who noted a linear trend in the residuals to the fit, as well as the extremely high activity level. Those authors estimated the stellar jitter at  $30 \text{ m s}^{-1}$ , and expressed concern that the planetary signal may have its origin in the stellar velocity jitter. Additional data proved that the inner planet was indeed real, and Vogt et al. (2005) reported a second planet at the 2:1 mean-motion resonance (MMR), and published a solution consisting of two superposed Keplerian orbits, noting that preliminary dynamical tests showed the system to be unstable, and that the system was likely in a protected 2:1 resonance. Goździewski & Konacki (2006), in their dynamical analysis of available radial-velocity data, suggested that the observed signal could be attributed to a 1:1 resonance, i.e. a pair of Trojan

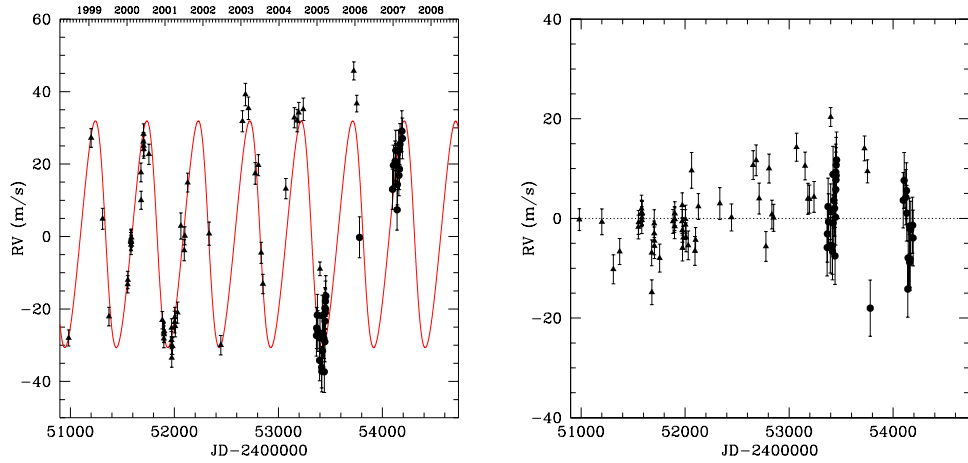


Figure 3.34 Left panel: 1-planet Keplerian fit to all data for HD 114783b. Filled circles—HET, triangles—Butler et al. (2006). Right panel: Residuals of fit.

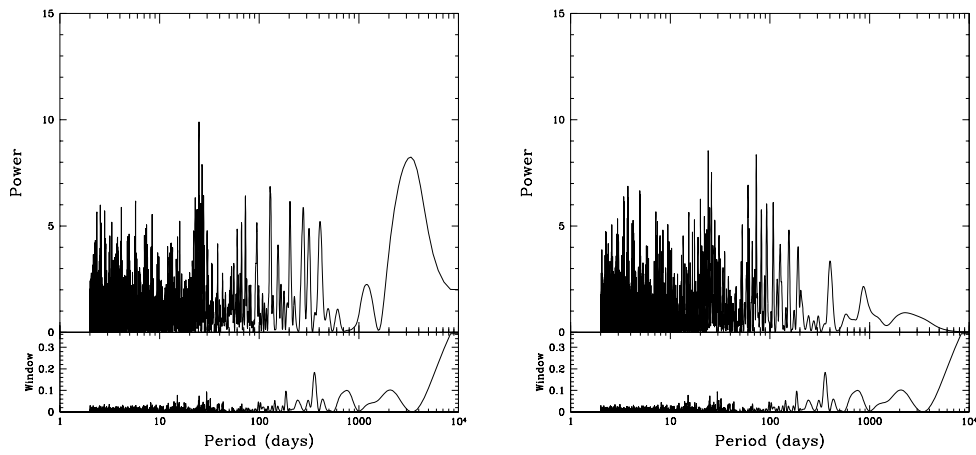


Figure 3.35 Same as Fig. 3.3, but for the HD 114783 system. Left panel: periodogram of residuals to a 1-planet fit. Right panel: periodogram of residuals to a 2-planet fit.

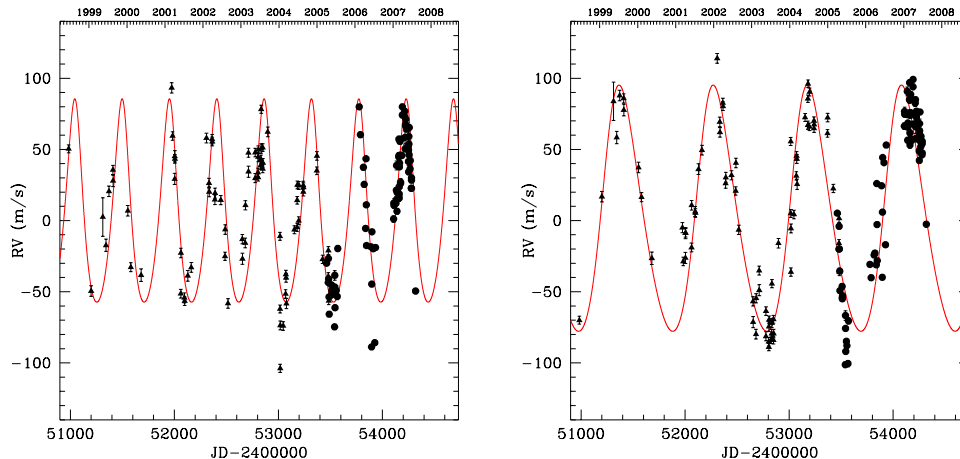


Figure 3.36 Left panel: Fit to all data for HD 128311b, after removing the outer planet. Filled circles–HET, triangles–Vogt et al. (2005). Right panel: Same, for HD 128311c after removing the inner planet.

planets. In this work, we first attempt a 2-Keplerian fit of the combined Keck and HET data. Convergence is achieved, with a total rms of  $17.5 \text{ m s}^{-1}$  about both data sets (Keck– $17.1 \text{ m s}^{-1}$ , HET– $18.0 \text{ m s}^{-1}$ ). AUSTRAL results for the HET data give a similar fit. Both of the Keplerian trials leave a residual periodicities near 11.5 days. A simulation using the Mercury N-body integrator (Chambers 1999) using the fitted planetary parameters results in the planets colliding within 1000 yr. A self-consistent dynamical fit (Laughlin et al. 2005; Rivera et al. 2005; Laughlin & Chambers 2001) was performed by Eugenio Rivera at UC Santa Cruz. For systems in which the planets interact on observable timescales, a dynamical fit is preferred to a superposition of Keplerian orbits. The orbital elements are then treated as “osculating,” or instantaneous elements. The initial epoch of those elements is varied, and a 3-body integration (star and 2 planets) is performed to derive the reflex motion of the star. That motion is then compared to the observed stellar radial velocity, and the  $\chi^2$  is minimized by a Levenberg-Marquardt algorithm (Press et al. 1992). The parameters from the dynamical fit to HD 128311 are given in Table 3.2, and the residuals from that fit were used for all subsequent analysis described here and in Chapter 4. A sharp peak is found in the residuals at 11.5 days (Figure 3.39), with a bootstrap FAP of 0.01%.

HD 130322 is host to a hot Jupiter in a 10.7-day period, discovered with the

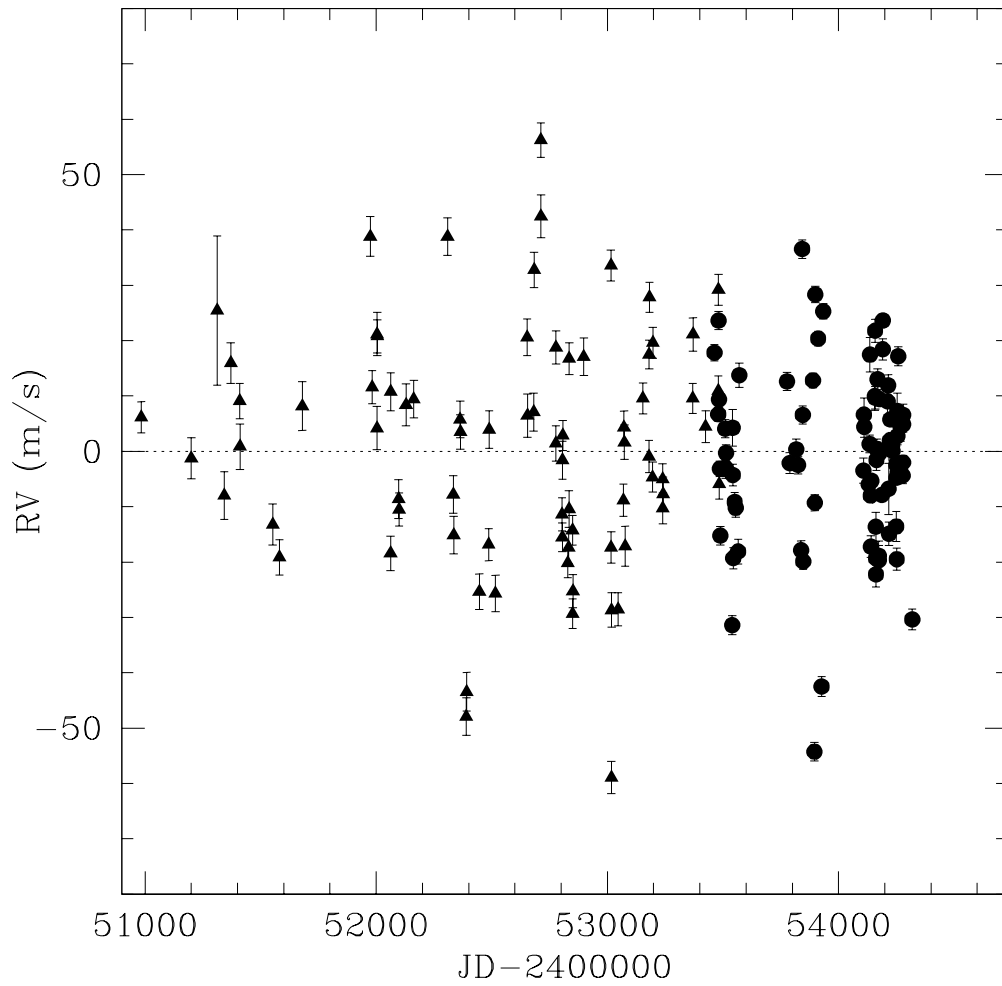


Figure 3.37 Residuals of fit to HD 128311. Filled circles–HET, triangles–Vogt et al. (2005)

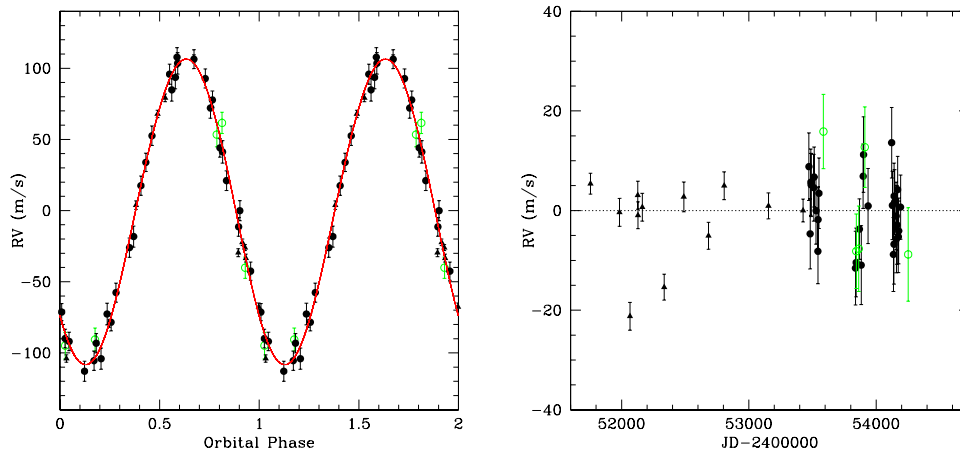


Figure 3.38 Left panel: Phased Keplerian fit to all data for HD 130322b. Filled circles–HET (AUSTRAL results), open circles–2.7m, triangles–Butler et al. (2006). Right panel: Residuals of fit.

CORALIE observations of Udry et al. (2000). Four data sets are available for this object: CORALIE (Udry et al. 2000), Keck (Butler et al. 2006), HET, and 2.7m. Fitting all four sets together results in a total rms of  $15.5 \text{ m s}^{-1}$ , but removing the CORALIE data drops the rms to  $11.3 \text{ m s}^{-1}$ . The precision of the derived orbital parameters is not significantly affected by this removal, since the Geneva data span only 167 days. Using the AUSTRAL version of the HET data further drops the rms to  $7.6 \text{ m s}^{-1}$ , and these data were used in the adopted solutions. This fit and its residuals are shown in Figure 3.38.

The long-period, massive planet orbiting HD 136118 was announced by Fischer et al. (2002b), and new Lick data were presented in Butler et al. (2006). We now fit these Lick data with observations from the HET and 2.7m (Fig. 3.40). The derived parameters are within  $2\sigma$  of those in Butler et al. (2006), and are more precise by a factor of 2-3. The current minimum mass estimate  $M \sin i = 11.4 M_{\text{Jup}}$  puts HD 136118b quite close to the brown-dwarf threshold ( $13 M_{\text{Jup}}$ ). For inclinations smaller than  $62.2^\circ$ , the true mass is greater than  $13 M_{\text{Jup}}$ . The probability of an inclination  $i < 62.2^\circ$  (assuming randomly distributed orientations) is  $1 - \cos i$ , or 53.4%. Indeed, Martioli et al. (2007) have recently combined *Hubble Space Telescope* astrometry with radial velocities to deduce that the inclination is  $i = 26^\circ \pm 12^\circ$ , resulting in a true mass of  $M_p = 28_{-9}^{+24} M_{\text{Jup}}$ , well outside of the planetary regime.

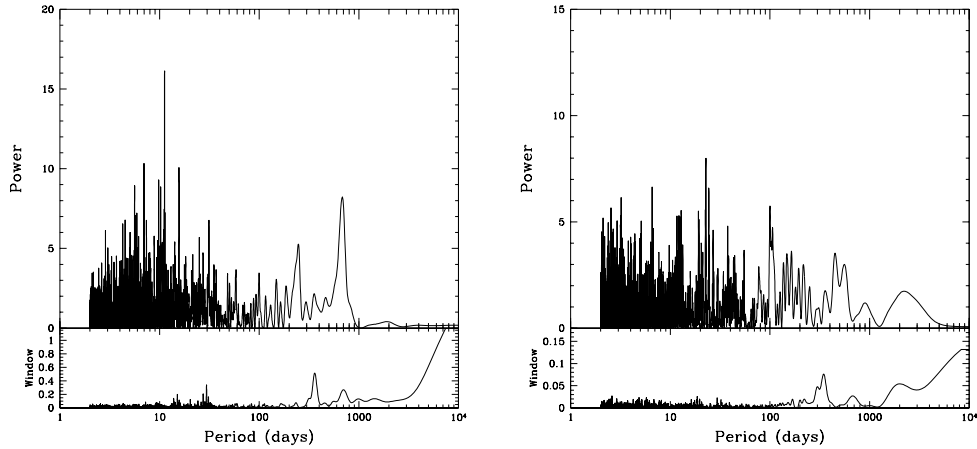


Figure 3.39 Same as Fig. 3.3, but for the HD 128311 (left) and HD 130322 (right) systems.

Examination of the residuals shows no significant periodicities.

The stellar triple system HD 178911 was found to host a 71-day planet by Zucker et al. (2002). HD 178911A and B are a visual binary pair, and HD 178911A is a spectroscopic binary as well (Tokovinin et al. 2000). The projected separation of HD 178911A and B is about 640 AU (Zucker et al. 2002), so the radial-velocity signal imposed on B by the stellar companion is negligible over the 9.3 yr span of observations. Four data sets are available for HD 178911B: ELODIE & Keck (Zucker et al. 2002), Keck (Butler et al. 2006), HET, and 2.7m. The fit and residuals are shown in Figure 3.41. A periodogram of the residuals of the fit (Fig. 3.42) shows a peak at 307 days with prominent sidelobes and a bootstrap FAP of 0.8% (Table 3.4). For HD 190228, we fit three data sets: ELODIE (Perrier et al. 2003), HET, and 2.7m. The fit and its residuals are shown in Figure 3.43. The fitted parameters are in agreement with those of Butler et al. (2006), and no significant periodicities are evident (Fig. 3.44).

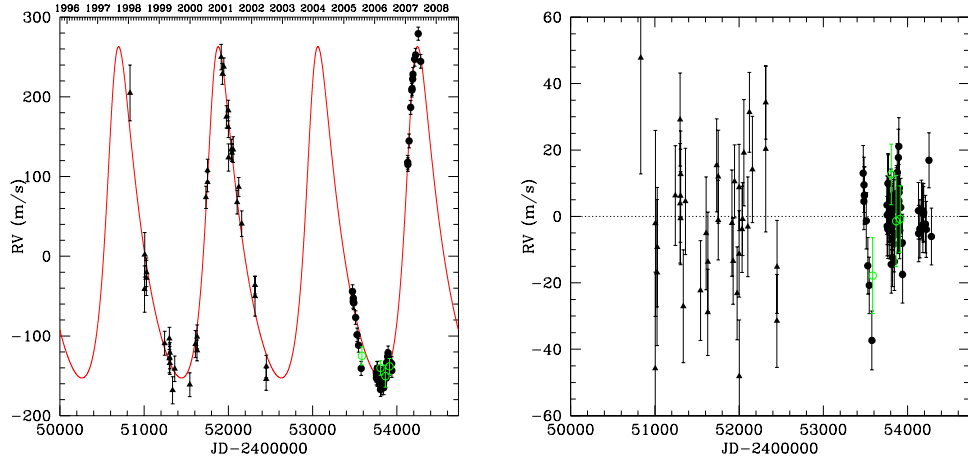


Figure 3.40 Left panel: Keplerian fit to all data for HD 136118b. Filled circles–HET, open circles–2.7m, triangles–Butler et al. (2006). Right panel: Residuals of fit.

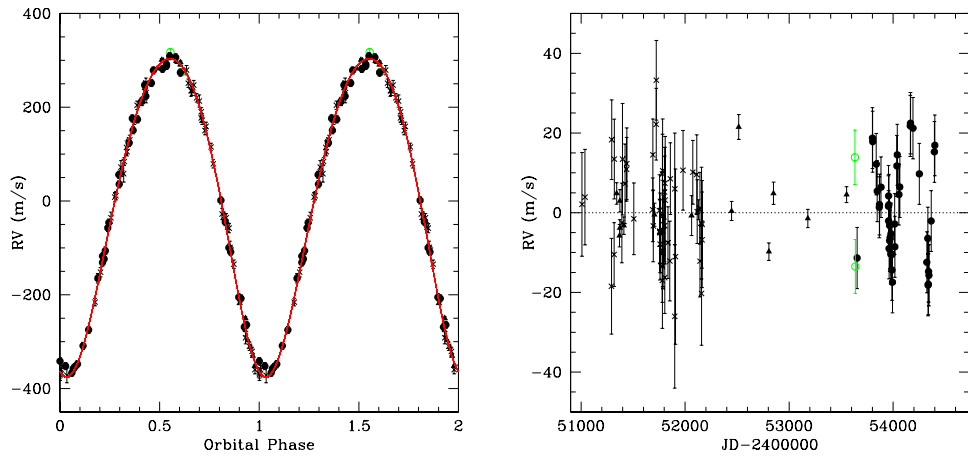


Figure 3.41 Left panel: Keplerian fit to all data for HD 178911Bb. Filled circles–HET, open circles–2.7m, triangles–Butler et al. (2006), crosses–Zucker et al. (2002). Right panel: Residuals of fit.



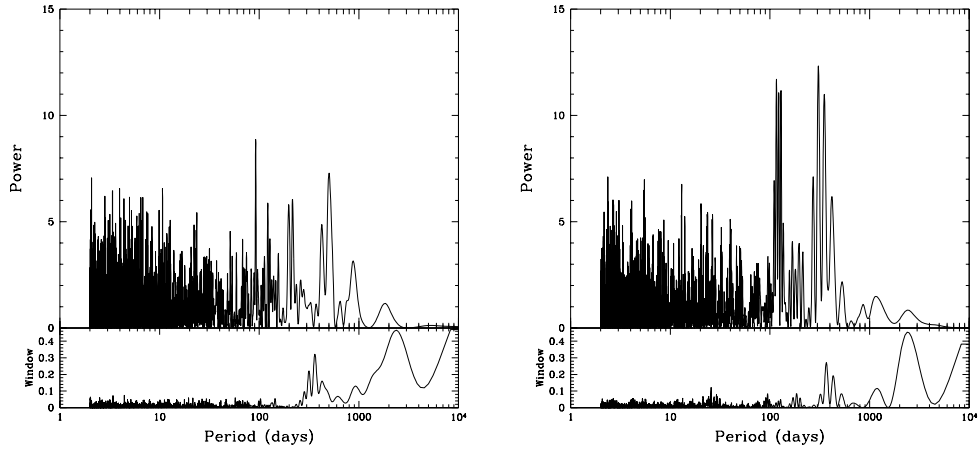


Figure 3.42 Same as Fig. 3.3, but for the HD 136118 (left) and HD 178911B (right) systems.

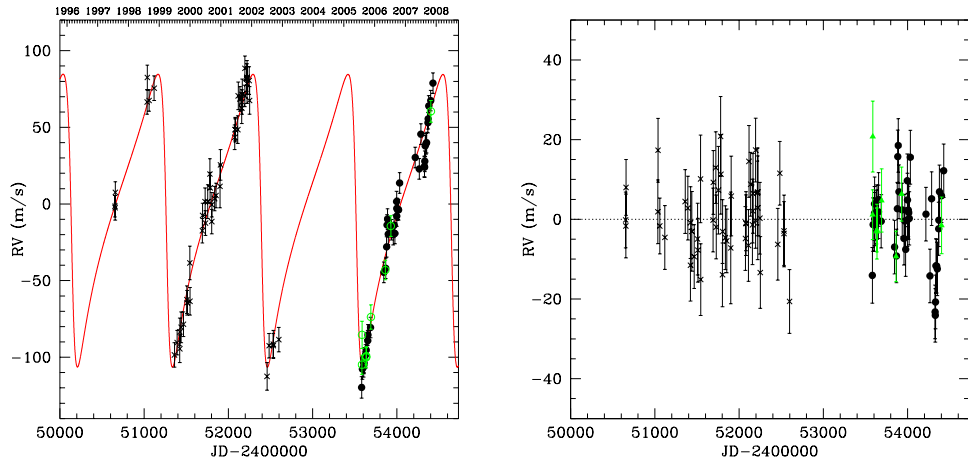


Figure 3.43 Left panel: Keplerian fit to all data for HD 190228b. Filled circles—HET, open circles—2.7m, crosses—Perrier et al. (2003). Right panel: Residuals of fit.

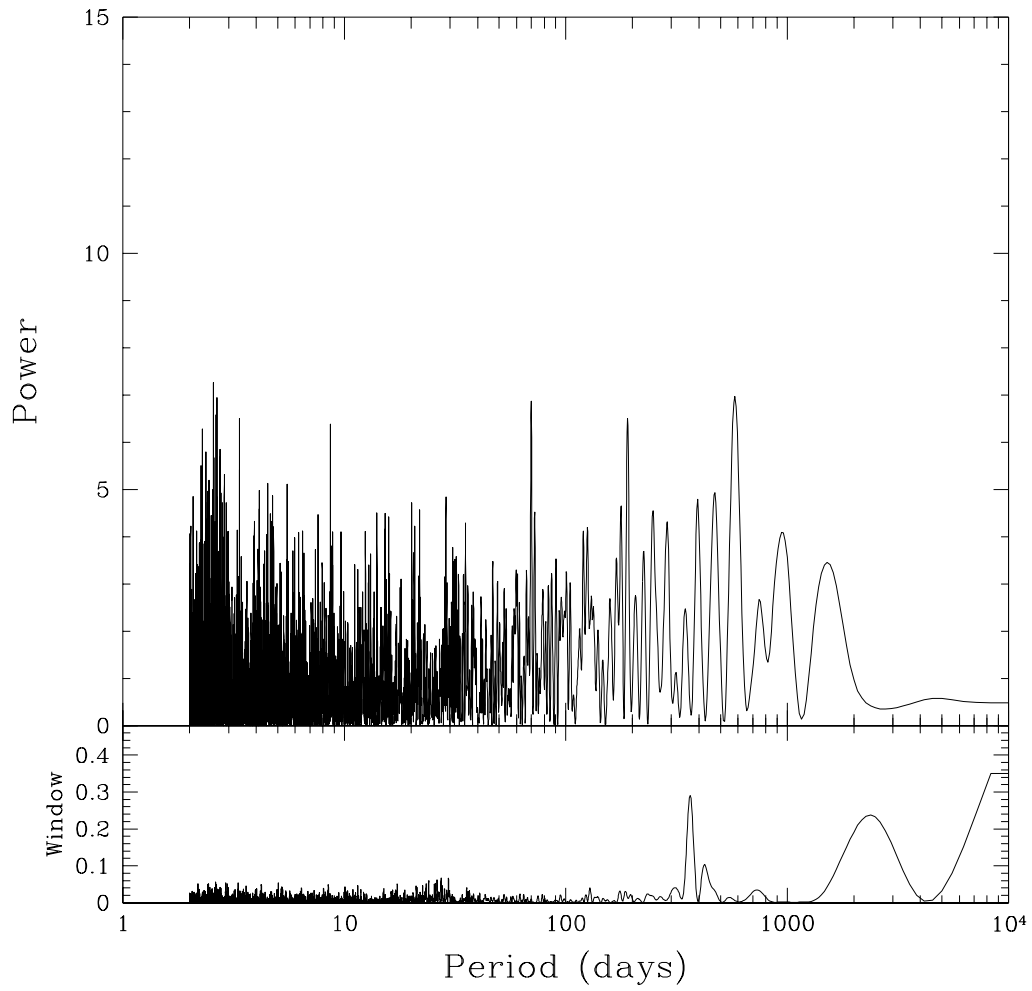


Figure 3.44 Same as Fig. 3.3, but for the HD 190228 system.

Table 3.2. Keplerian Orbital Solutions

Planet	Period (days)	$T_0$ (JD-2400000)	$e$	$\omega$ (degrees)	K (m s <sup>-1</sup> )	M sin $i$ (M <sub>Jup</sub> )	$a$ (AU)	$\chi^2_\nu$	rms m s <sup>-1</sup>
HD 3651 b	62.200±0.014	53931.8±0.5	0.619±0.044	240.4±5.5	15.4±1.0	0.217±0.009	0.295±0.003	4.68	7.1
HD 8574 b	226.8±0.2	53976.1±3.7	0.288±0.028	20.5±6.3	60.1±2.1	1.86±0.07	0.757±0.005	2.73	15.2
HD 10697 b	1075.4±1.6	53642±20	0.096±0.008	115.1±7.1	114.7±1.1	6.17±0.16	2.132±0.019	4.24	9.9
HD 19994 b	466.1±2.2	53714±40	0.127±0.082	313±31	28.3±2.4	1.31±0.12	1.305±0.016	9.02	15.8
HD 23596 b	1510.2±11	53093±24	0.305±0.021	266.3±4.1	125.0±2.8	7.39±0.40	2.709±0.060	1.63	10.1
HD 28185 b	385.9±0.6	53805.8±7.2	0.134±0.018	3.9±6.1	149.5±2.8	5.23±0.27	1.032±0.019	3.21	11.2
HD 38529 b	14.3099±0.0005	54012.63±0.15	0.276±0.015	91.9±3.7	56.6±0.9	0.843±0.030	0.131±0.002	6.90	11.9
HD 38529 c	2153.4±5.5	52255.7±6.6	0.347±0.006	17.5±1.2	172.3±1.2	13.31±0.39	3.727±0.048	6.90	11.9
HD 40979 b	264.21±0.24	53919.4±2.7	0.257±0.014	323.6±4.2	119.6±2.3	4.01±0.13	0.846±0.007	1.55	20.6
HD 72659 b	3926±225	51770±59	0.301±0.030	273±9	43.2±1.3	3.34±0.18	4.982±0.212	1.09	6.5
HD 74156 b <sup>a</sup>	51.642±0.003	53788.47±0.07	0.636±0.007	176.2±1.0	110.4±1.7	1.80±0.06	0.292±0.004	2.03	11.6
HD 74156 c	2454±13	53454±13	0.395±0.013	266.4±2.7	108.6±2.6	7.63±0.33	3.830±0.055	2.03	11.6
HD 80606 b	111.429±0.002	53421.929±0.004	0.9325±0.0008	300.4±0.3	469.9±2.0	3.90±0.19	0.447±0.011	1.55	13.5
HD 89744 b	256.82±0.05	54073.3±0.4	0.679±0.007	194.0±0.9	265.8±4.2	8.20±0.23	0.918±0.010	2.19	14.3
47 UMa b <sup>a</sup>	1077.2±2.1	53527±145	0.027±0.023	147±49	46.2±1.1	2.42±0.10	2.100±0.022	3.23	10.1
HD 106252 b	1535.5±5.2	53386.8±5.1	0.467±0.011	288.6±1.9	137.1±2.1	6.91±0.18	2.616±0.027	1.61	12.4
HD 108874 b	394.04±0.53	54055.6±10.5	0.114±0.020	231.0±9.0	38.5±0.8	1.33±0.06	1.034±0.014	0.79	3.8
HD 108874 c	1677.4±26.6	52787±40	0.273±0.030	12±9	18.6±0.8	1.01±0.06	2.717±0.065	0.79	3.8
HD 114783 b <sup>b</sup>	492.8±1.6	53809±26	0.069±0.026	97±19	28.6±0.7	1.00±0.05	1.158±0.018	2.00	4.9
HD 114783 c	3937±718	53766±275	0.301±0.073	10±39	11.7±1.2	0.78±0.13	4.628±0.721	2.00	4.9
HD 128311 b	454.8±10.2	51083±27	0.247±0.073	57±16	56.5±15.5	1.79±0.29	1.075±0.016	27.83	18.3
HD 128311 c	906.8±11.8	50786±109	0.140±0.095	118±37	84.0±4.5	3.43±0.15	1.706±0.015	27.83	18.3
HD 130322 b <sup>c</sup>	10.7083±0.0003	53994.6±1.7	0.013±0.016	133±56	107.3±1.6	1.03±0.03	0.0896±0.0006	3.47	7.6
HD 136118 b	1183.5±2.0	53001.9±4.1	0.329±0.010	322.2±1.6	207.9±1.9	11.42±0.23	2.328±0.019	2.04	14.4
HD 178911B b	71.488±0.004	53807.5±0.5	0.109±0.005	164.8±2.5	339.3±1.5	6.95±0.29	0.339±0.006	2.58	11.4
HD 190228 b	1127.7±10.9	53524.4±15.9	0.590±0.045	101.1±3.1	95.6±5.3	5.89±0.21	2.592±0.033	1.57	9.2

<sup>a</sup>Results from one-planet fit.<sup>b</sup>Results from two-planet fit.<sup>c</sup>Results for HD 130322 exclude data from Udry et al. (2000).

Table 3.3. Summary of Radial-Velocity Data

Star	$N$	RMS about fit ( $\text{m s}^{-1}$ )	$\Delta T$ (days)	Source
HD 3651	163	6.5		Butler et al. (2006)
HD 3651	3	11.2		2.7m <sup>a</sup>
HD 3651	36	9.3		HET <sup>b</sup>
HD 3651 (total)	202	7.1	7376	
HD 8574	41	14.5		Perrier et al. (2003)
HD 8574	45	13.0		HET
HD 8574	16	13.3		2.7m
HD 8574	26	20.7		Butler et al. (2006)
HD 8574 (total)	128	15.2	3609	
HD 10697	59	6.6		Butler et al. (2006)
HD 10697	32	8.9		2.7m
HD 10697	40	14.2		HET
HD 10697 (total)	131	9.9	4057	
HD 19994	48	15.3		Mayor et al. (2004)
HD 19994	56	15.8		HET
HD 19994	11	18.7		2.7m
HD 19994 (total)	115	15.8	3331	
HD 20367	82	9.4		HET
HD 20367	17	8.3		2.7m
HD 20367 (total)	97	9.2	846	
HD 23596	39	9.8		Perrier et al. (2003)
HD 23596	62	10.6		HET
HD 23596	6	7.4		2.7m
HD 23596 (total)	107	10.1	3603	
HD 28185	40	10.7		Santos et al. (2001)
HD 28185	14	14.4		2.7m
HD 28185	36	10.8		HET
HD 28185 (total)	90	11.2	2971	
HD 38529	162	12.8		Butler et al. (2006)
HD 38529	76	10.1		HET
HD 38529	7	8.2		2.7m
HD 38529 (total)	245	11.9	3745	
HD 40979	65	22.8		Butler et al. (2006)
HD 40979	91	19.4		HET-AUSTRAL
HD 40979	4	10.3		2.7m
HD 40979 (total)	160	20.6	3588	
HD 72659	32	4.1		Butler et al. (2006)
HD 72659	53	6.5		HET
HD 72659	6	14.4		2.7m
HD 72659 (total)	91	6.5	3593	

Table 3.3 (cont'd)

Star	$N$	RMS about fit ( $\text{m s}^{-1}$ )	$\Delta T$ (days)	Source
HD 74156	95	14.1		Naef et al. (2004)
HD 74156	85	8.2		HET
HD 74156 (total)	180	11.6	3408	
HD 80606	61	18.7		Naef et al. (2001b)
HD 80606	23	8.1		HET
HD 80606	46	5.4		Butler et al. (2006)
HD 80606 (total)	130	13.5	2893	
HD 89744	50	16.1		Butler et al. (2006)
HD 89744	34	10.9		HET
HD 89744	9	16.5		2.7m
HD 89744 (total)	93	14.3	2943	
47 UMa	91	10.9		Fischer et al. (2002a)
47 UMa	44	12.1		Naef et al. (2004)
47 UMa	37	11.1		2.7m
47 UMa	78	7.1		HET
47 UMa (total)	250	10.1	7472	
HD 106252	40	14.4		Perrier et al. (2003)
HD 106252	43	8.7		HET
HD 106252	15	14.4		Butler et al. (2006)
HD 106252	12	15.2		2.7m
HD 106252 (total)	110	12.4	3682	
HD 108874	49	3.5		Vogt et al. (2005)
HD 108874	40	4.3		HET
HD 108874 (total)	89	3.8	2850	
HD 114783	54	4.3		Butler et al. (2006)
HD 114783	34	5.9		HET
HD 114783 (total)	88	4.9	3208	
HD 128311	76	21.1		Vogt et al. (2005)
HD 128311	82	15.5		HET
HD 128311 (total)	158	18.3	3335	
HD 130322	12	8.5		Butler et al. (2006)
HD 130322	30	6.7		HET-AUSTRAL
HD 130322	5	12.4		2.7m
HD 130322 (total)	47	7.6	2496	
HD 136118	37	21.2		Butler et al. (2006)
HD 136118	67	9.2		HET
HD 136118	4	12.9		2.7m
HD 136118 (total)	108	14.4	3450	
HD 178911B	51	11.6		Zucker et al. (2002)
HD 178911B	40	12.2		HET

Table 3.3 (cont'd)

Star	$N$	RMS about fit ( $\text{m s}^{-1}$ )	$\Delta T$ (days)	Source
HD 178911B	2	19.4		2.7m
HD 178911B	14	7.3		Butler et al. (2006)
HD 178911B (total)	107	11.4	3392	
HD 190228	51	8.8		Perrier et al. (2003)
HD 190228	42	9.8		HET
HD 190228	8	9.3		2.7m
HD 190228 (total)	101	9.2	3776	

<sup>a</sup>McDonald Observatory 2.7 m Harlan J. Smith Telescope.

<sup>b</sup>McDonald Observatory 9.2 m Hobby-Eberly Telescope.

## 3.2 Genetic Algorithm

The periodogram method of searching for additional planetary signals in radial-velocity data is quite efficient at detecting weak signals in noisy data. However, this method is less effective as the periodic signals depart from a sinusoidal shape. A more rigorous approach is to search for Keplerian orbits rather than simple sine curves in the residuals. In this section I describe the results of a broad (“wide-field”) search for Keplerian signals which may be present in the residuals of the fits given in § 3.1. The main purpose of this endeavour is to see if any signals were missed by the periodogram searches. A genetic algorithm was developed by M. Endl for this purpose, and was applied in Cochran et al. (2007) to determine the nature of the outer planet in the HD 155358 system. The genetic algorithm generates a random population, whose members are described by the set of parameters to be solved for. The user defines an allowed range for each parameter, and the “genotype” of each population member is chosen randomly from within that range. Then the  $\chi^2$  merit function is computed for each member (set of planetary parameters), and that  $\chi^2$  corresponds to its “fitness” in the population: models resulting in lower  $\chi^2$  are more fit. As in evolution, recombination and mutations occur, and the fittest population members have a higher probability of reproducing for the next generation. In this manner, the genetic algorithm slowly converges to a global  $\chi^2$  minimum by sampling all allowable parameter space. The genetic algorithm runs described here consisted of a population of 1000 models, allowed to evolve until the change in total  $\chi^2$  was less than  $10^{-3}$  between successive generations. A total of  $10^4$  such iterations was

Table 3.4. Results of Periodogram Analysis

Star	Period (days)	FAP
HD 3651	179.211	0.078
HD 8574	28.653	0.257
HD 10697	8.116	0.534
HD 19994	324.675	0.0009
HD 20367	5.577	0.039
HD 23596	187.970	< 0.0001
HD 28185	2.106	0.034
HD 38529	32.010	< 0.0001
HD 40979 <sup>a</sup>	51.177	0.095
HD 72659	200.803	0.968
HD 74156	126.906	0.0004
HD 80606	20.781	0.624
HD 89744	331.123	0.171
47 UMa <sup>b</sup>	2192.982	0.040
47 UMa <sup>c</sup>	19.062	0.422
HD 106252	328.947	0.513
HD 108874	45.249	0.833
HD 114783 <sup>c</sup>	24.015	0.304
HD 128311	11.208	0.0001
HD 130322	22.748	0.213
HD 136118	92.081	0.195
HD 178911B	306.748	0.008
HD 190228	2.565	0.867

<sup>a</sup>HET AUSTRAL results used.

<sup>b</sup>Residuals from one-planet fit.

<sup>c</sup>Residuals from two-planet fit.

performed, each one resulting in a set of parameters and a  $\chi^2$  for a model including the added planet.

For each system, the genetic algorithm was made to fit the known planet(s) and an additional planet. The parameters of the known planets were restricted to  $\sim 5\sigma$  of their best-fit values. For the added planet, the period was allowed in the range of 2-2000 days, and the eccentricity was limited to  $e \leq 0.6$ . No restrictions were placed on the other parameters  $\omega$ ,  $K$ , and  $T_0$ . Table 3.5 summarizes the parameters of the additional planets found by the algorithm, as well as the  $\chi^2_\nu$  of the system and the degree of improvement over the best fits from Table 3.2. The genetic algorithm will always find *some* solution, even a non-physical one, as it simply “evolves” the systems toward lower  $\chi^2$  values. In several cases, the 1-year alias was favored, and for HD 128311, the 11.2-day stellar rotation period was the best fit.

In those systems where the genetic search resulted in a lower  $\chi^2$  than the best-fit from Table 3.2, a multi-planet least-squares fit was attempted. Often, this resulted in either a failure to converge, or an unrealistic set of parameters for the second planet. Convergence failures or crashes occurred when gaps in the data allowed the eccentricity of the added planet to be unconstrained. For HD 10697, the best 2-planet fit converged on an eccentricity  $e_2 = 0.93$ , with an rms of  $9.6 \text{ m s}^{-1}$ . The 2-planet fit for HD 19994 lowers the total rms from  $15.8$  to  $11.2 \text{ m s}^{-1}$ , but a dynamical test results in a collision after only 88 yr. For HD 23596, a second planet at 189 days lowers the rms from  $10.1$  to  $7.9 \text{ m s}^{-1}$ , but as will be discussed in Chapter 4, this signal is likely an alias of the 1-year window. For HD 28185, the second period found by the genetic algorithm is very close to the 385-day period of the known planet, and so it is an unphysical result. In the HD 106252 system, where the second period found is 1932 days, the known planet’s orbit would cross and so it is also deemed an unusable result. For HD 130322, a second planet can be fit using the parameters in Table 3.5 as initial values. This results in a reduced  $\chi^2$  of 1.13, an improvement of 2.34 over the single-planet fit. The resulting eccentricity of the second orbit is  $e = 0.38 \pm 0.13$ , causing it to cross that of the known planet. Dynamical simulations starting the 22-day planet ( $M \sin i = 0.12 M_{\text{Jup}}$ ) at  $e = 0$  show that such an object remains stable for at least  $10^5$  yr. Trials with initial eccentricities for the outer planet  $e_2 = 0.1$  and  $e_2 = 0.2$  also remained stable for  $10^5$  yr. In the HD 178911B system, the genetic algorithm identified a 347-day signal (Table 3.5,



Table 3.5. Planet Parameters Found by Genetic Algorithm

Star	$P$ (days)	$K$ $\text{m s}^{-1}$	$e$	$\omega$ (degrees)	$T_0$ JD-2400000	$\chi^2_\nu$	$\Delta\chi^2_\nu$
HD 3651	357.38	4.09	0.45	60.3	54618.2	4.12	+0.16
HD 8574	767.78	12.96	0.45	192.12	54352.5	2.03	-0.79
HD 10697	159.50	5.77	0.27	359.04	53975.1	3.59	-0.63
HD 19994	384.58	29.03	0.10	359.45	53337.3	3.79	-5.23
HD 23596	188.77	9.17	0.33	306.07	54235.4	1.52	-0.11
HD 28185	328.51	17.66	0.13	51.99	53493.7	1.82	-1.40
HD 38529	1084.20	6.12	0.14	228.81	53451.0	7.40	+0.50
HD 40979	422.46	16.97	0.52	44.58	54738.4	3.61	+2.06
HD 72659	1996.67	20.46	0.02	148.2	53089.7	1.29	+0.20
HD 74156	1228.63	67.64	0.16	273.0	54719.4	2.00	-0.02
HD 80606	365.22	4.75	0.20	89.94	53636.6	1.66	+0.11
HD 89744	346.87	11.96	0.60	312.52	55073.5	1.70	-0.49
47 UMa	408.14	10.20	0.43	126.05	54322.8	2.38	-0.84
HD 106252	1931.99	16.16	0.43	112.01	54408.6	1.35	-0.22
HD 108874	469.59	3.77	0.59	340.78	53745.6	0.77	-0.02
HD 114783	3743.4	10.31	0.14	27.08	53920.6	2.14	-2.91
HD 128311	11.21	13.16	0.38	91.11	53307.7	21.63	-6.20
HD 130322	22.79	11.05	0.25	226.04	53821.7	2.08	-1.39
HD 136118	1041.15	25.03	0.59	162.43	54605.1	1.41	-0.63
HD 178911B	347.40	14.18	0.60	150.73	55020.0	2.12	-0.46
HD 190228	569.45	10.88	0.59	197.16	54900.5	1.03	-0.54

which can be fit well with a 2-planet model ( $\text{rms}=8.9\text{m s}^{-1}$ ); however, attempts to perform the same fit on the AUSTRAL velocities were unsuccessful. This 347-day signal is close enough to the 1-year period to raise suspicions, especially given the appearance of spurious signals near 1 year in the RADIAL results from other objects. For HD 190228, a 569-day planet (half the period of HD 190228b) can be fit, but the best-fit system results in crossing orbits.

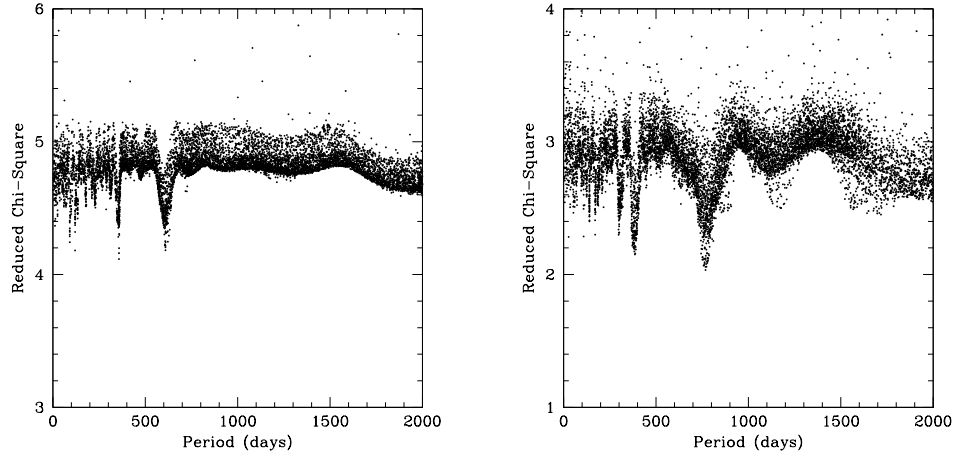


Figure 3.45 Left panel: “Wide-field” genetic algorithm search for additional planets in the HD 3651 system, fitting for the known planet and a second body. Right panel: Same, but for the HD 8574 system.

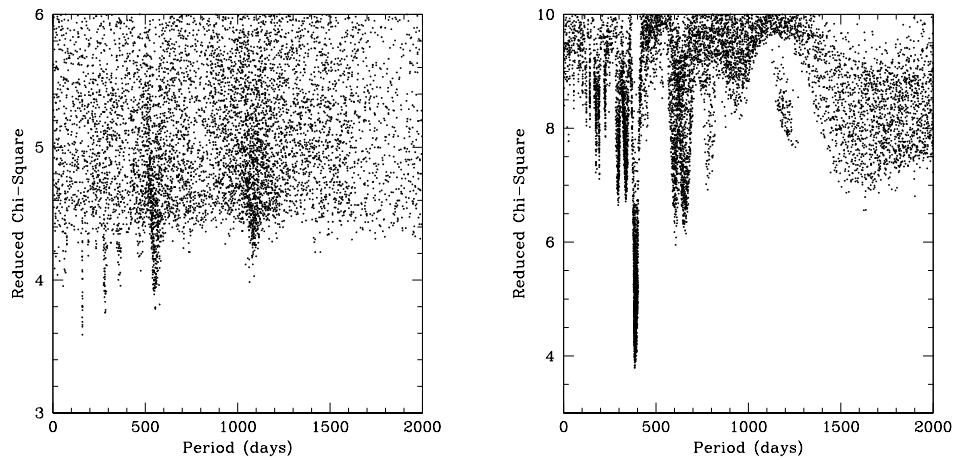


Figure 3.46 Left panel: “Wide-field” genetic algorithm search for additional planets in the HD 10697 system, fitting for the known planet and a second body. Right panel: Same, but for the HD 19994 system.

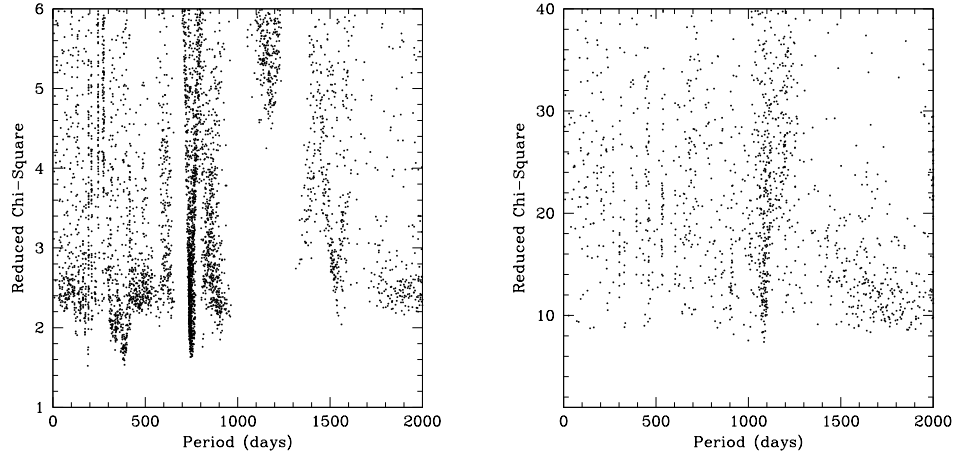


Figure 3.47 Left panel: “Wide-field” genetic algorithm search for additional planets in the HD 23596 system, fitting for the known planet and a second body. Right panel: Same, but fitting for a third body in the HD 38529 system.

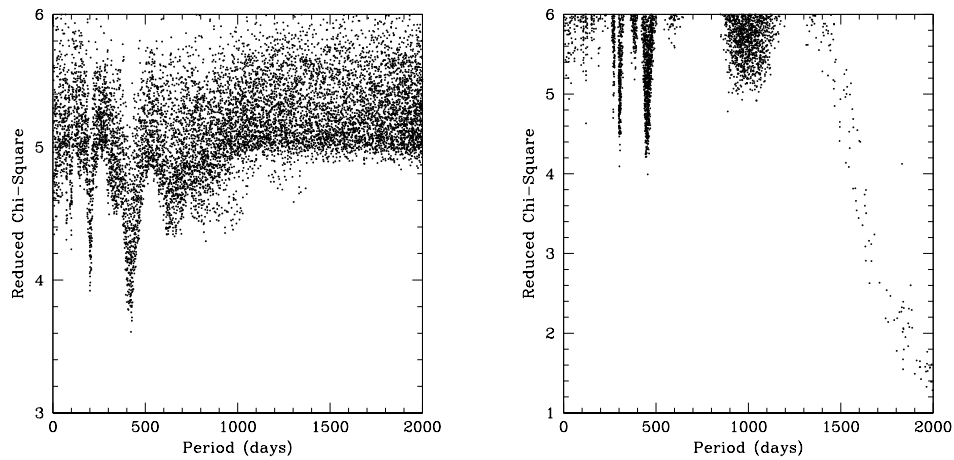


Figure 3.48 Left panel: “Wide-field” genetic algorithm search for additional planets in the HD 40979 system, fitting for the known planet and a second body. Right panel: Same, but for the HD 72659 system.

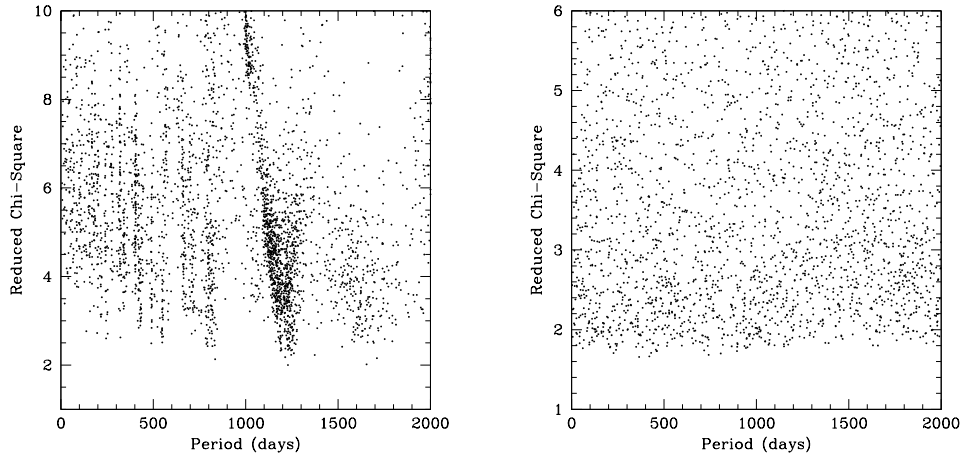


Figure 3.49 Left panel: “Wide-field” genetic algorithm search for additional planets in the HD 74156 system, fitting for the known planet and a third body. Right panel: Same, but fitting for a second body in the HD 80606 system.

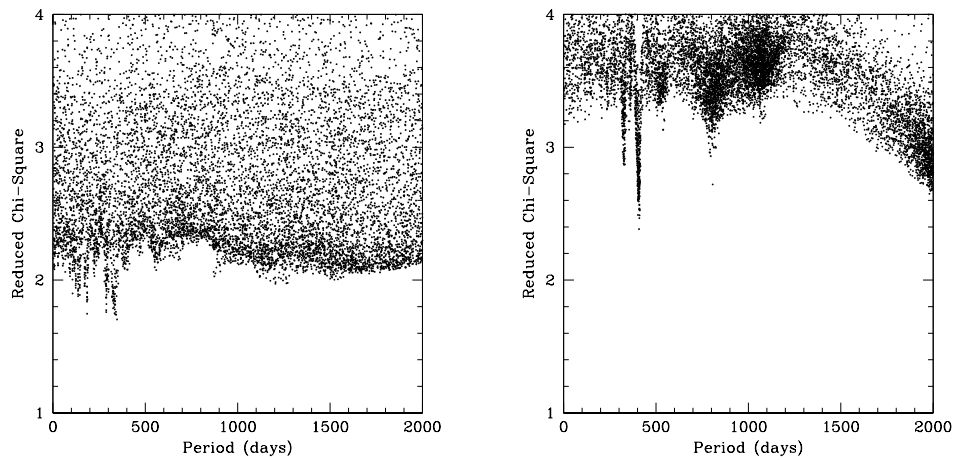


Figure 3.50 Left panel: “Wide-field” genetic algorithm search for additional planets in the HD 89744 system, fitting for the known planet and a second body. Right panel: Same, but for the 47 UMa system.

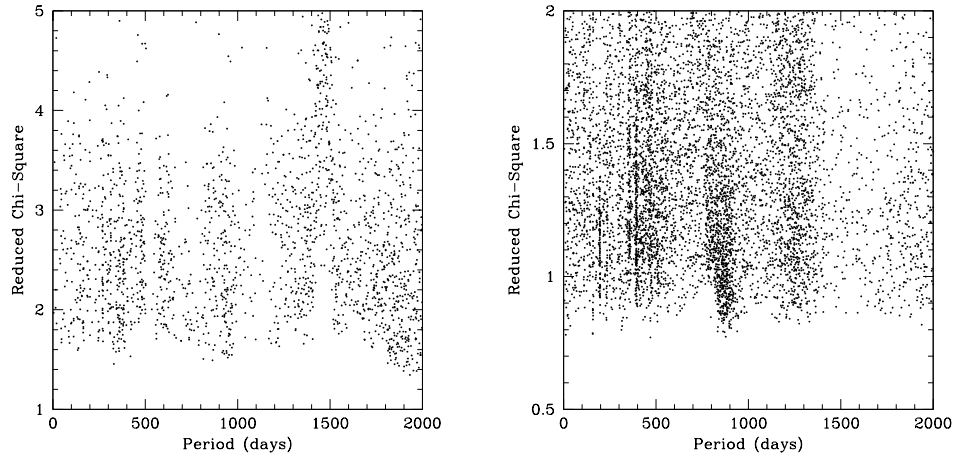


Figure 3.51 Left panel: “Wide-field” genetic algorithm search for additional planets in the HD 106252 system, fitting for the known planet and a second body. Right panel: Same, but fitting for a third body in the HD 108874 system.

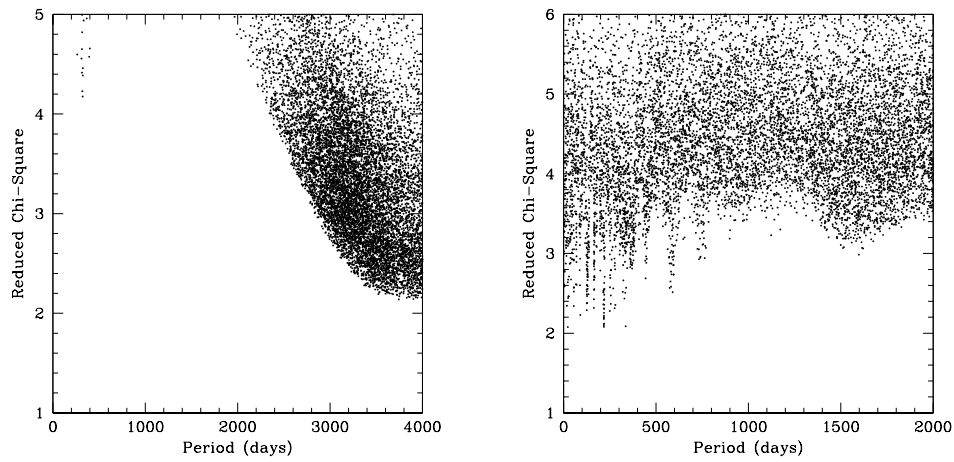


Figure 3.52 Left panel: “Wide-field” genetic algorithm search for additional planets in the HD 114783 system, fitting for the known planet and a second body. Right panel: Same, but for the HD 130322 system.

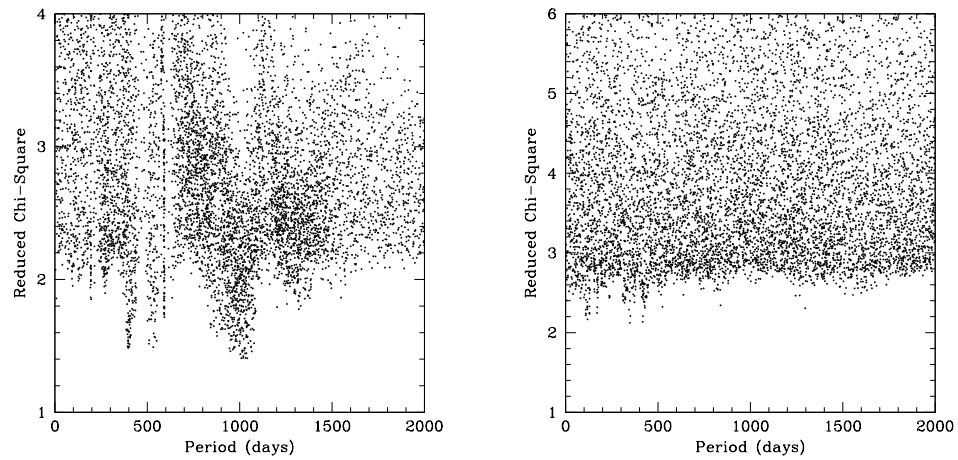


Figure 3.53 Left panel: “Wide-field” genetic algorithm search for additional planets in the HD 136118 system, fitting for the known planet and a second body. Right panel: Same, but for the HD 178911B system.

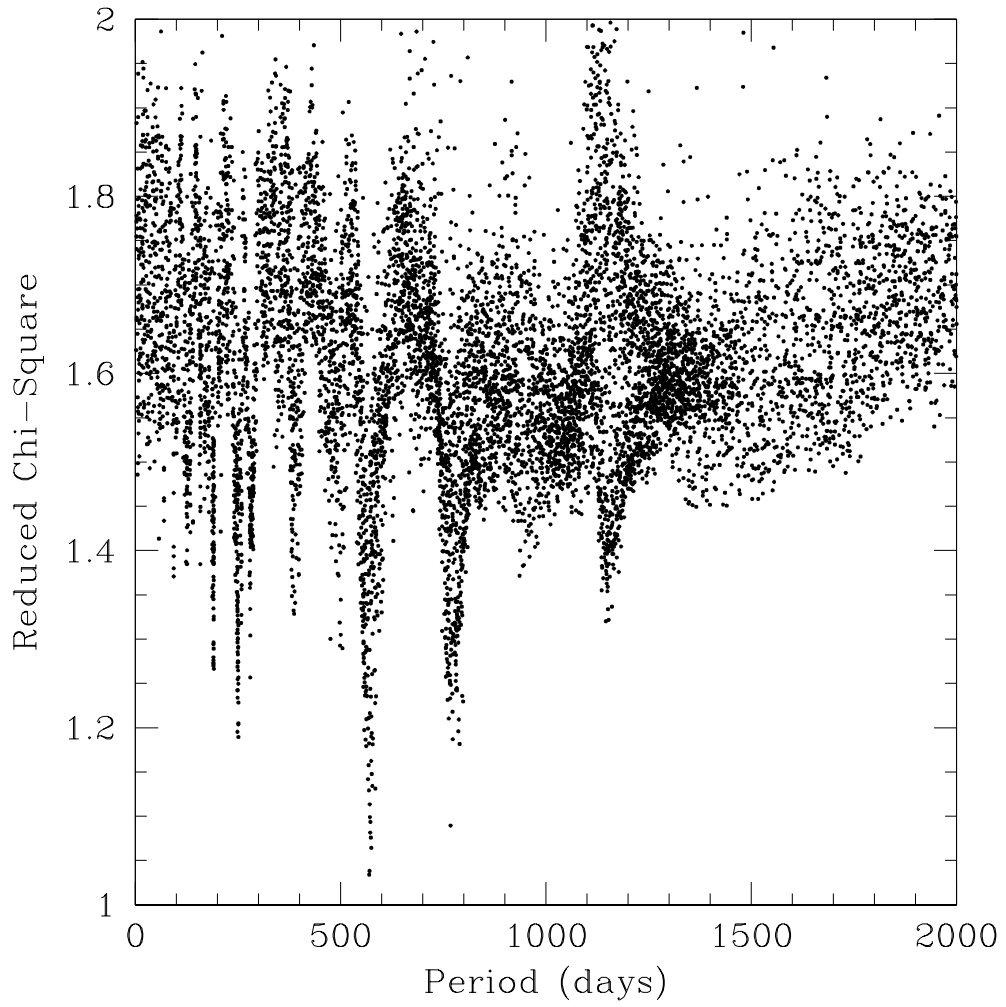


Figure 3.54 “Wide-field” genetic algorithm search for additional planets in the HD 190228 system, fitting for the known planet and a second body.

## Chapter 4

# Candidates: Further Tests

After fitting for and removing the known planet(s), we search for additional signals. While it is desired that these signals are caused by planets, there is a wide range of confounding factors which can lead to false detections. These include stellar rotation, instrumental systematics, the 30-day and 1-year observing windows, outlier data points, and other sources of random noise. In this chapter, I describe the tests applied to each target which showed variations in the radial-velocity residuals that could be additional planetary signals. Following the outline of the various tests, I detail the results of these tests for each target which warranted them. The criterion for further discussion is that the bootstrap FAP of the highest peak in the residuals periodogram was less than 5%. The choice of 5% is somewhat arbitrary; this is the level at which a signal typically becomes “interesting” enough to merit increased attention.

### 4.1 Methods

#### 4.1.1 Phasing the Residuals

One weakness of the periodogram method is that, in its effort to find suitable sinusoids fitting the residuals, the program can be easily driven by outlier data points. By phase-folding the residual data on the period with the highest peak, one can quickly determine that this is the case by noting the shape of the phased dataset. If the phase plot gives the appearance of random scatter, and/or has large gaps, then one should proceed with caution, as the detected period may be an artifact.



However, if the phased data present a well-sampled curve resembling a Keplerian orbit, then further investigation is required.

#### 4.1.2 Examining Each Data Set Separately

The individual data sets from each telescope/spectrograph configuration included in the combined orbital fits have time coverage of several years. Signals of short-period planets, if present, would be included for many orbital cycles in each data set. Hence, performing the periodogram search on each data set separately is a simple method of distinguishing real signals from chance periodicities or instrument-specific systematics. It should be noted that this comparison is most useful when the data sets are of similar quality and sampling density. For example, the HARPS instrument has detected 3 planets orbiting GJ 581 (Udry et al. 2007), but HET observations do not yet show evidence of the two “super-Earth” planets GJ 581c ( $M \sin i = 5M_{\oplus}$ ) and GJ 581d ( $M \sin i = 8M_{\oplus}$ ). This is because the radial-velocity signals due to planets c and d are of order  $3 \text{ m s}^{-1}$ , and the precision of HARPS is typically  $1 \text{ m s}^{-1}$ , but it is  $3 \text{ m s}^{-1}$  for the HET. False-alarm probabilities reported in this chapter for subsets of the residuals were estimated using the formula from Horne & Baliunas (1986) rather than the bootstrap method. The analytic FAP of Horne & Baliunas (1986) assumes that the errors in the data are independent and normally distributed, which is not always true for radial-velocity data. For this reason, that method tends to give lower FAP estimates (i.e. higher significance levels) than the bootstrap method, but is useful for a quick look to differentiate between data sets.

#### 4.1.3 Comparing Velocity Computation Codes

As described in Chapter 2, velocities are determined from the HET spectra using the RADIAL code of W. Cochran (Cochran et al. 2004). This is considered the “default” mode of operation, since RADIAL has been optimized for HET data over a period of seven years. Recently, M. Endl has modified his independent velocity code, AUSTRAL, for HET data as well. These efforts have resulted in a valuable new tool for the verification of planet candidates. The differences between RADIAL and AUSTRAL are discussed in § 2.2.1 (18). A real planetary signal should appear in the results from both codes, although at different significance levels. AUSTRAL

has been used most profitably in the detection of the planets  $\gamma$  Cep b (Hatzes et al. 2003),  $\epsilon$  Eri b (Hatzes et al. 2000),  $\beta$  Gem b (Hatzes et al. 2006), and HD 197037b (Wittenmyer et al. 2008), and the brown dwarfs HD 91669b (Wittenmyer et al. 2008) and HD 137510b (Endl et al. 2004).

#### 4.1.4 Fitting a Multi-Keplerian Model

For planet candidates which pass the previous tests, we attempt to fit a multi-planet model to determine whether 1) such a solution can be obtained at all, 2) the addition of a planet substantially improves the  $\chi^2$  and rms of the orbit fit, and 3) the resulting system is physically meaningful. The last criterion is particularly important, as the GaussFit model will converge on non-physical solutions with crossing orbits. If the putative planet has phase gaps in the data, the model will often choose a very high eccentricity, low-amplitude orbit as there are insufficient observational constraints. Outliers in the data can also drive the least-squares solution to a high eccentricity. Unlike the orbit-fitting routine, we know that a planet with a period shorter than about 5 days should have a relatively small eccentricity ( $e \lesssim 0.2$ ). This is because the tidal circularization timescale (Bodenheimer et al. 2001; Goldreich & Soter 1966) of such a planet is shorter than the typical age of planet-host stars (a few Gyr). Owing to the observation that about 90% of extrasolar planets have eccentricities  $e < 0.6$ , we can also be generally suspicious of solutions which converge on significantly larger values of  $e$ .

#### 4.1.5 Dynamical Simulations

If a physically meaningful multi-planet fit can be obtained (i.e. non-crossing orbits, “reasonable” eccentricities), then the next step is to conduct an N-body dynamical simulation to assess the stability of the proposed system. Gravitational interactions between planets can result in instabilities, which usually manifest themselves as chaotically oscillating eccentricities that eventually result in collisions or ejections. These simulations are performed with the MERCURY6 code (Chambers 1999) using the conservative Bulirsch-Stoer integrator (“BS2”), which is able to integrate close encounters with minimal energy error ( $dE/E \sim 10^{-8}$ ). The test systems are run for up to  $10^7$  yr; in the vast majority of unstable cases, instabilities result in system destruction within  $10^5$  yr.

### 4.1.6 Photometric Monitoring

Spots on a rotating star produce low-amplitude radial-velocity variations which can mimic those expected for a planetary companion. For periodicities which are suspected to be induced by the rotational modulation of starspots, one can sometimes determine the star's rotation period photometrically. This method is especially useful for investigating periods  $P \lesssim 50$  days, as the rotation periods for the solar-type stars considered herein generally fall within this range. Non-radial stellar oscillations (Gray & Hatzes 1997), or a non-spherical star may also cause photometric variability. The orbital motion of the planet about the star does not produce a photometric variability detectable in visible wavelengths. The phase-dependent reflected light from the hot Jupiter HD 189733b has been measured at 8 microns using the Spitzer Space Telescope (Knutson et al. 2007). The detection of a photometric periodicity from ground-based photometry, however, would argue against a planetary origin for a radial-velocity signal with the same period. Through a collaboration with Greg Henry, candidates can be added to the target list for the Automatic Photometric Telescopes (APT) located at Fairborn Observatory in the Patagonia Mountains of southern Arizona (Henry 1999; Eaton, Henry & Fekel 2003). Precision photometers use dichroic mirrors to split the incoming light into two beams and two EMI 9124QB bi-alkali photomultiplier tubes to measure Strömrgren  $b$  and  $y$  simultaneously. Differential magnitudes from the two passbands were combined into a single  $(b + y)/2$  band for greater precision, which is typically 0.0012 mag for a single measurement.

## 4.2 Applications

### 4.2.1 HD 19994

New data from the 2.7m and HET indicate a period for the known planet of 467 rather than 535 days. The residuals to the combined 467-day fit also show a signal at 338 days (Figure 4.1). As this is suspiciously close to 1 year, we tried testing each data set separately. The residuals show the following: CORALIE –  $P=44.7$  days,  $FAP=8.9\%$ ,  $rms=15.4 \text{ m s}^{-1}$ ; HET –  $P=337.8$  days,  $FAP=0.03\%$ ,  $rms=15.8 \text{ m s}^{-1}$ . The periodograms are given in Figure 4.2; for the HET results, the window function shows a peak near a period of 338 days. A real 338-day signal would have been evident in the data of Mayor et al. (2004) since those data span more than 1500

days. As discussed in the following sections, spurious periodicities near 1 year are not uncommon in the RADIAL version of HET data. The 1-planet fit was re-done using the AUSTRAL velocities, and the residuals periodogram is shown in Fig. 4.3. The total rms of this fit is  $17.7 \text{ m s}^{-1}$ . No significant signals are present, further supporting the interpretation of the 338-day period as an artifact.

#### 4.2.2 HD 20367

As described in Chapter 3, there is not a consensus on the orbital parameters, or even the presence, of a planet around HD 20367. Early in the observations, a well-defined period of 5.6 days turned up in velocity data obtained from both HET templates for HD 20367. This period could be well-fit with a Keplerian orbit and, suspecting a hot Neptune candidate, I contacted Greg Henry for photometry to search for transits and to rule out stellar rotation. The results indicate a stellar rotation period of  $5.50 \pm 0.02$  days, with a photometric amplitude of  $0.0055 \pm 0.0003$  mag (Figure 4.4). From these observations, we concluded that the 5.6-day radial-velocity period was caused by starspots rotating into and out of view. This is consistent with the estimate of  $P_{rot} = 6$  days reported by Wright et al. (2004), and the high level of chromospheric activity for this star ( $\log R'_{HK} = -4.50$ ; see page 43). The literature contains conflicting age estimates for HD 20367: Nordström et al. (2004) estimate an age of  $6.4^{+2.5}_{-2.2}$  Gyr, whereas Wright et al. (2004) report an age of 0.9 Gyr. Based on the rapid rotation rate, and the high level of chromospheric emission, the younger age estimate is favored.

#### 4.2.3 HD 23596

A periodogram search of the residuals to this fit shows a highly significant period at 187.97 days with a bootstrap FAP less than 0.01% (Table 3.4). Figure 4.5 shows the residuals phased to this period; no obvious phase gaps are present, and there are no high-leverage points which would drive a periodogram. Performing the periodogram search on the datasets separately yields the following: ELODIE –  $P=2.15$  days, FAP=19.8%; HET –  $P=364.96$  days, FAP=0.1%. The 2.7m data were too few ( $N=6$ ) to obtain a meaningful result by this method. Using the AUSTRAL results in the fit yields a residual period of 7.49 days with FAP=7.1%. Since the 188-day periodicity appeared only in the RADIAL version of the HET data, we conclude

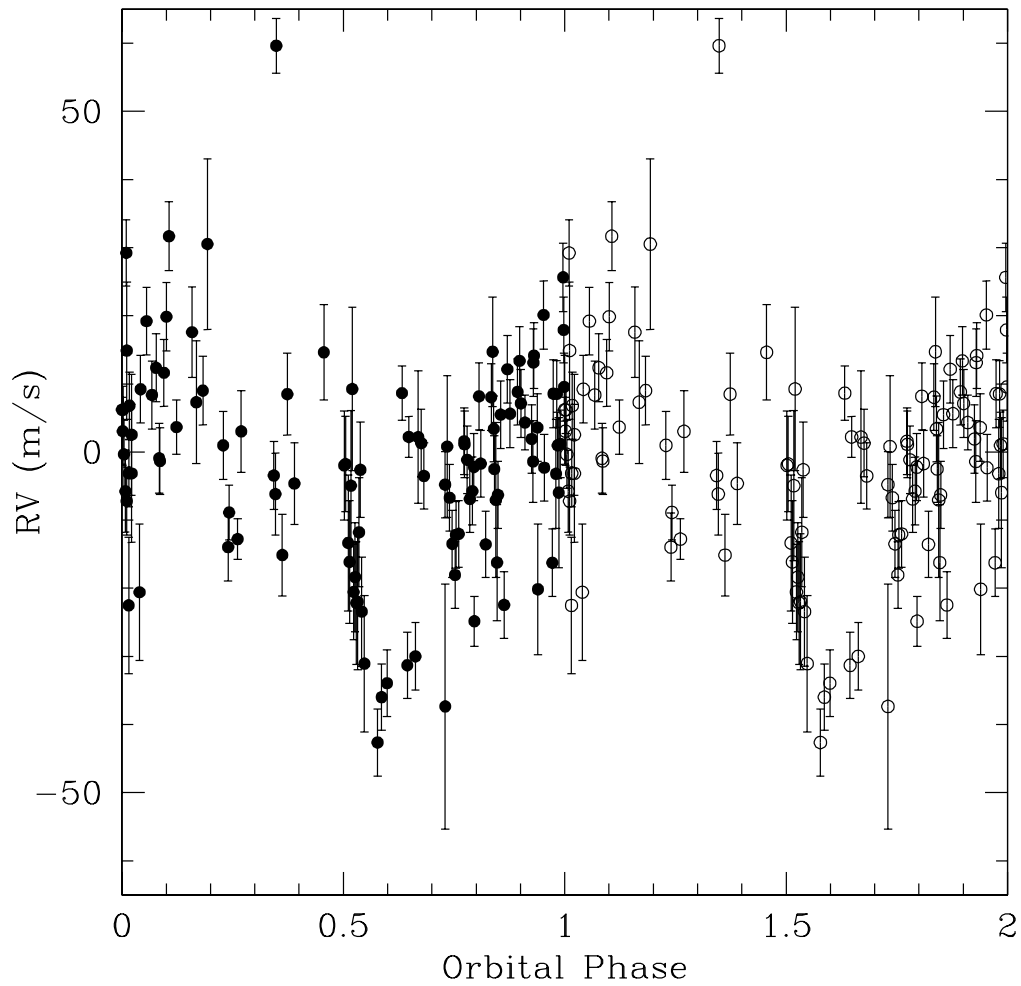


Figure 4.1 Residuals of a 1-planet fit for HD 19994, phased to a period of 338.8 days. Data from HET, CORALIE, and the 2.7m are shown.

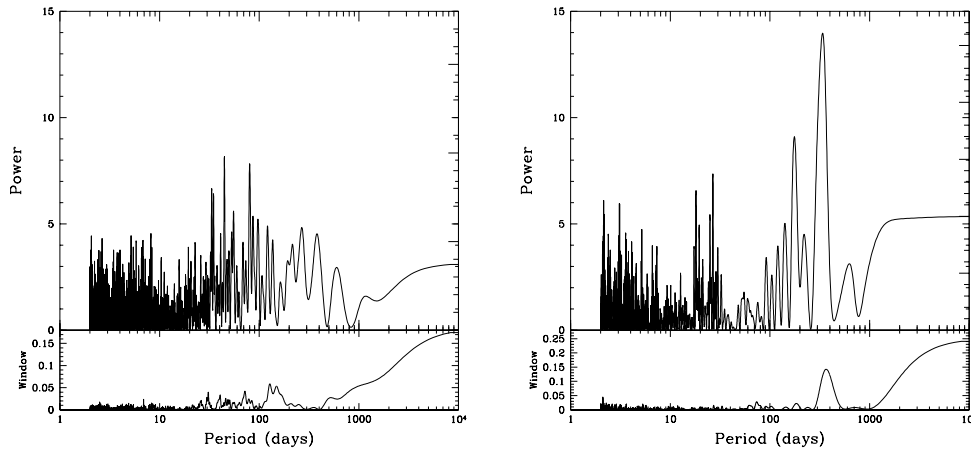


Figure 4.2 Periodograms on the residuals to a 1-planet fit for HD 19994. Left panel: CORALIE residuals only. The peak is at 44.7 days. Right panel: HET residuals only, with the main peak at 337.8 days.

that it is an alias of the strong 1-year window which appears in the HET data, and not a planet.

#### 4.2.4 HD 28185

The residuals periodogram for HD 28185 shows a 2.1-day signal with a bootstrap FAP of 3.4%. Phasing the residuals to this period (Fig. 4.6) shows no significant gaps or outliers. Considering each data set separately, we find: ELODIE – P=2.1 days, FAP=40.1%, rms=10.7 m s<sup>-1</sup>; HET – P=961.5 days, FAP=3.0%, rms=10.8 m s<sup>-1</sup>. The residuals of the AUSTRAL results have the highest peak at 42.7 days, and the FAP is 7.2%. The RADIAL and AUSTRAL data have a similar rms scatter about a 1-planet fit on all data: using RADIAL, the total rms is 11.3 m s<sup>-1</sup>, compared to 11.5 m s<sup>-1</sup> using AUSTRAL. Since the two methods give similar fits, but different distributions of residual power, we can dismiss these peaks as noise rather than real planetary signals.

#### 4.2.5 HD 38529

After removing the two planets in the HD 38529 system from all data sets, a strong peak remains at 32.0 days, with a bootstrap FAP less than 0.01%. A phase plot of

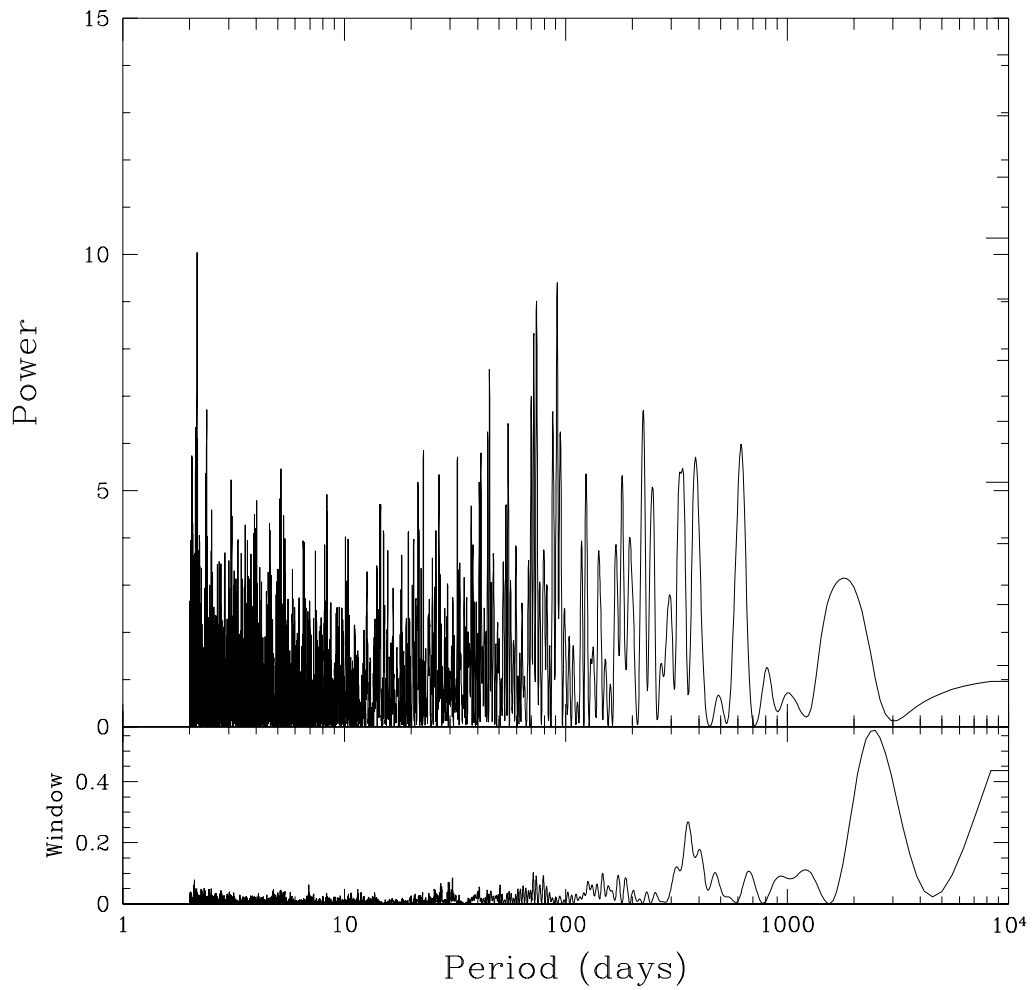


Figure 4.3 Periodogram of residuals of a 1-planet fit for HD 19994, using all three datasets and HET AUSTRAL velocities. The bootstrap FAP of the highest peak is 8.9%.

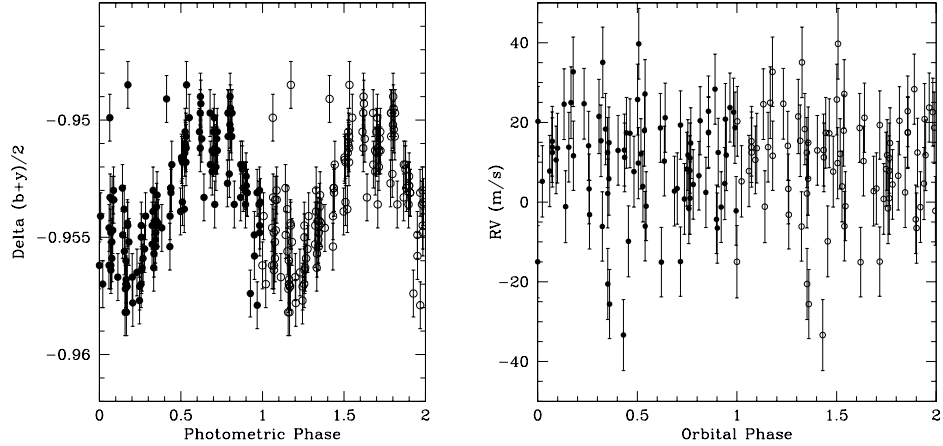


Figure 4.4 Left panel: Photometric observations of HD 20367 phased to the stellar rotation period of 5.50 days. Data courtesy G. Henry. Right panel: HET radial velocities for HD 20367, phased to a period of 5.50 days.

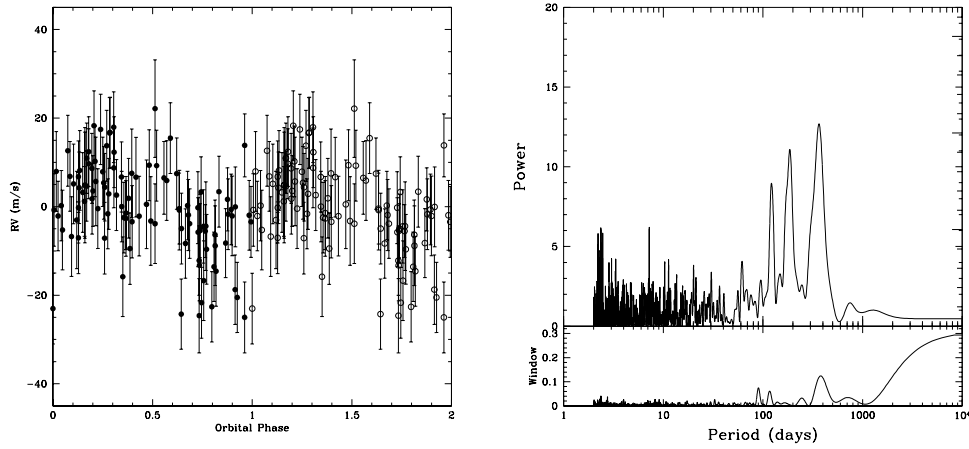


Figure 4.5 Left panel: Residuals of a 1-planet fit for HD 23596b, phased to a period of 187.97 days. Right panel: Periodogram of the HET (RADIAL) residuals only. Note the strong peaks at 365, 186, and 122 days.



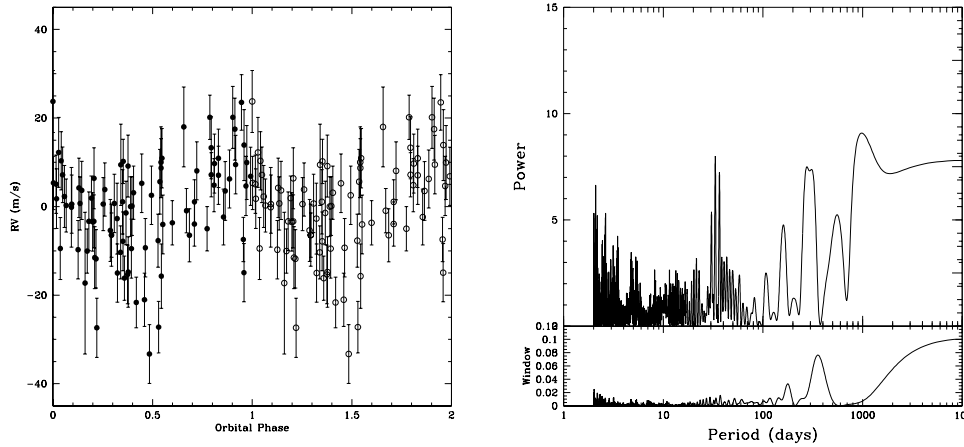


Figure 4.6 Left panel: Residuals of a 1-planet fit for HD 28185b, phased to a period of 2.1 days. Right panel: Periodogram of the HET (RADIAL) residuals only.

these residuals is shown in Fig. 4.7. Coverage is complete, and the removal of one  $10\sigma$  outlier from the fit does not alter the residuals periodogram. Considering the data sets separately, we obtain the following: Butler et al. (2006) – 32.0 days, FAP=0.5%, rms=12.9 m s<sup>-1</sup>; HET – 35.4 days, FAP=0.1%, rms=10.0 m s<sup>-1</sup> (Figure 4.8). Since the periodicity is strong in both data sets, we now turn to the AUSTRAL version of the HET velocities. Fitting the system using the AUSTRAL data also results in a residual periodicity:  $P = 32.0$  days, FAP=0.06% (Figure 4.9). The individual sets of residuals give the following: Butler et al. (2006) – 32.0 days, FAP=0.7%, rms=13.1 m s<sup>-1</sup>; HET – 71.5 days, FAP=0.3%, rms=10.2 m s<sup>-1</sup>. For a real signal of this strength, one would not expect such disagreement between the RADIAL and AUSTRAL fits, nor the inconsistencies when the data sets are considered separately. Candidate periods in the 20-40 day range inspire trepidation, as this is the range of rotation periods for typical solar-type planet-search stars. Wright et al. (2004) report a rotation period for HD 38529 of 37 days; the fact that the periodogram peaks are not especially “clean” (i.e. sharp and isolated, clearly rising above the noise level) further supports the interpretation of this signal as a stellar rotation period.

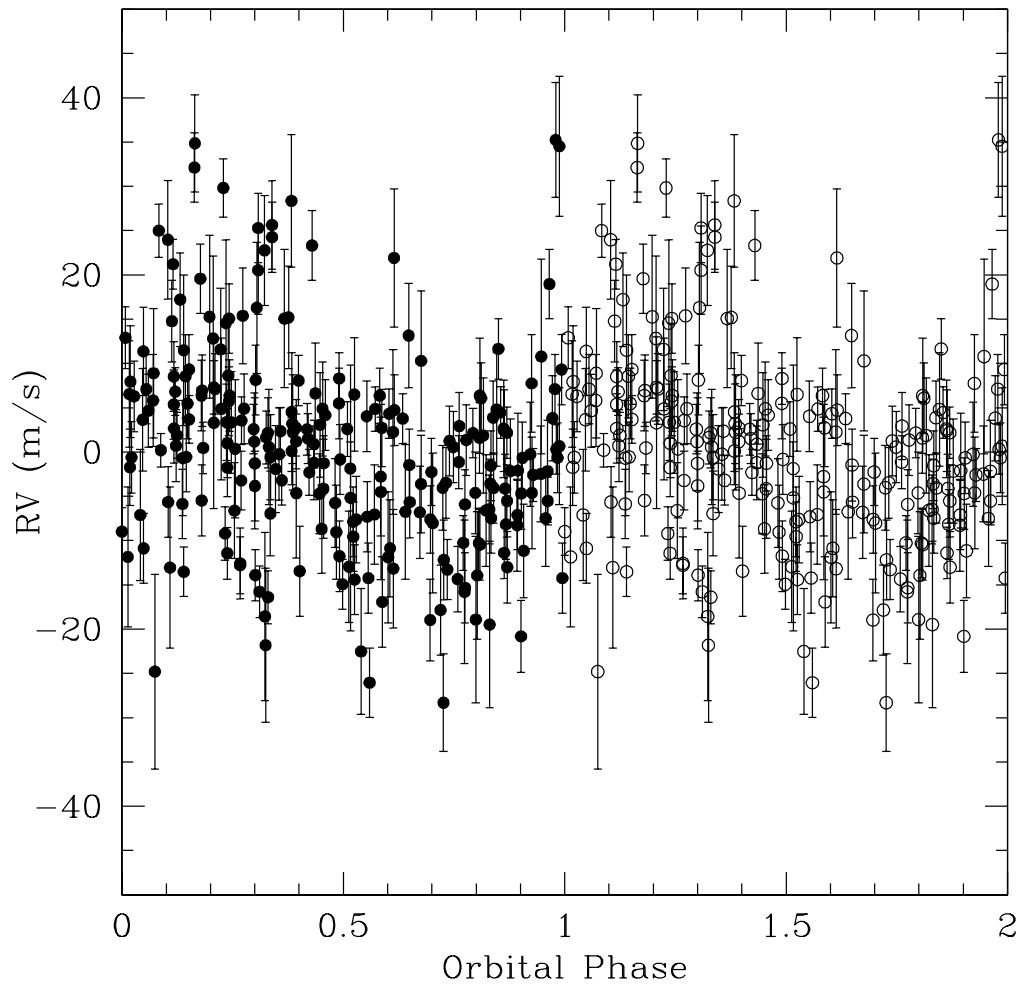


Figure 4.7 Residuals of a 2-planet fit to all data for HD 38529, phased to a period of 32.0 days. The HET data are RADIAL results.

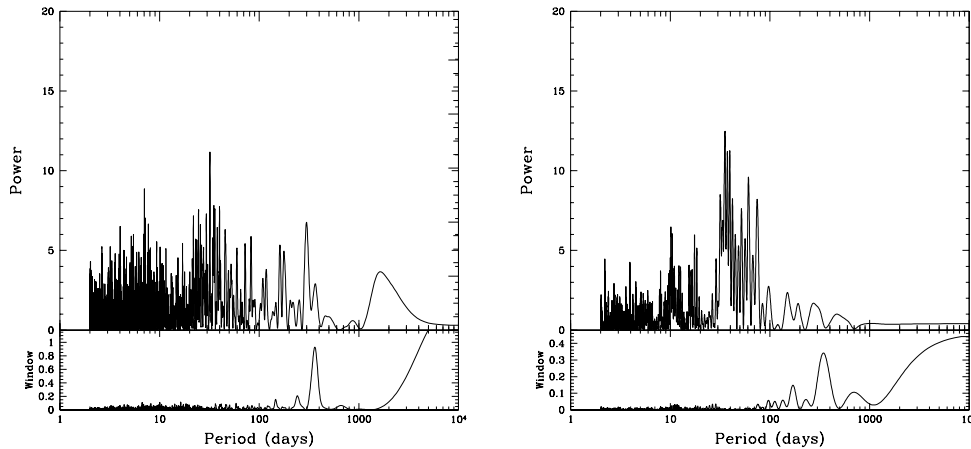


Figure 4.8 Left panel: Periodogram of the Lick & Keck residuals only for HD 38529. The peak is at 32.0 days. Right panel: Periodogram of the HET (RADIAL) residuals only, with the main peak at 35.4 days.

#### 4.2.6 HD 74156

Fits to the 2-planet system HD 74156 have consistently indicated a residual 126-day period, with a bootstrap FAP of 0.04%. This system also warrants further scrutiny in light of the recent report by Bean et al. (2008) of a third planet, with a period of 346 days and a radial-velocity semi-amplitude  $K = 13.5 \text{ m s}^{-1}$ . That result was obtained using the same HET spectra as considered in this work, but velocities were derived using an independent method devised by J. Bean (Bean et al. 2008). In this subsection, we further investigate the possibility of an additional planet in the HD 74156 system. Applying the orbit-fitting methods as described in Chapter 3 to the velocities for HD 74156 given in Bean et al. (2008), a periodogram peak is evident near 346 days, and we obtain a three-planet Keplerian orbit fit which is consistent with that of Bean et al. (2008). In that work, the iodine-free template spectrum was obtained at a resolving power of 120,000, rather than the  $R=60,000$  which is standard for targets in this study. We obtained an  $R=120,000$  template spectrum on 2007 Nov 12, but velocities obtained using this template resulted in a 2-planet fit with a slightly higher rms ( $12.2 \text{ m s}^{-1}$ ) than the original  $R=60,000$  template ( $11.9 \text{ m s}^{-1}$ ). All subsequent analysis for HD 74156 refers to velocities obtained using the  $R=60,000$  template from 2005 Dec 9.

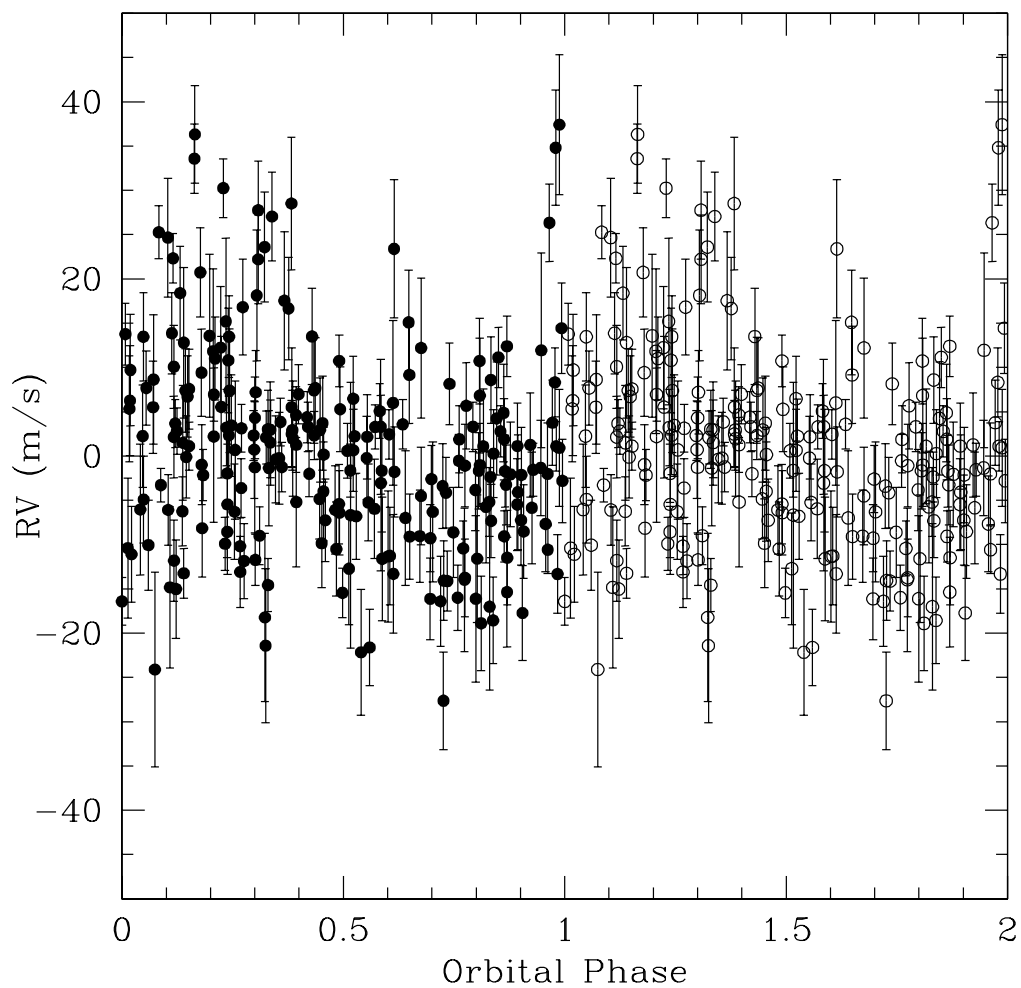


Figure 4.9 Residuals of a 2-planet fit to all data for HD 38529, phased to a period of 32.0 days. The HET data are AUSTRAL results.

The residuals of the 2-planet fit, phased to a period of 126.6 days, are shown in Figure 4.10; there is ample phase coverage and no obvious outliers appear to be driving the 126-day periodicity. However, removing 8  $3\sigma$  outliers from the residuals eliminated the 126-day peak (Fig. 4.10). Periodograms on the individual data sets are shown in Figure 4.11. Separate periodogram analysis yields residual periods as follows: Naef et al. (2004) – 126.6 days, FAP=7.1%; HET – P=119.3 days, FAP=0.2%. Using the AUSTRAL version of the HET data for the fits also shows a peak at  $P = 125.3$  days with FAP=0.2% (Figure 4.12).

Fitting a three-planet Keplerian model to the data ( $P_3 = 126$  d) reduces the total rms from 11.6 to 10.5  $\text{m s}^{-1}$ . The eccentricity of the 126-day planet had to be held at zero, as the GaussFit model failed to converge with eccentricity as a free parameter. At this stage, one can save effort by determining whether the planet one intends to fit is in a stable orbit. As will be shown in Chapter 6, massless test particles in the HD 74156 system are removed from all regions save a narrow strip near 1 AU. Furthermore, test runs which placed massive planets in 126-day orbits for  $e=0.0, 0.1, 0.2,$  and  $0.3$  all resulted in system destruction within 140 yr. For these reasons, we discount the possibility of a 126-day planet in the HD 74156 system.

To investigate the possibility of the 346-day planet proposed by Bean et al. (2008), we conducted the same tests as used above to exclude the 126-day periodicity. The residuals of the 2-planet fit are phased to the 346.6 day period in Figure 4.13. The phase gaps are expected since the phased period is close to 1 year, and no clear Keplerian signal is evident despite the large number of data points ( $N=180$ ). As shown in Figure 4.11, neither of the individual data sets show a 346-day periodicity in the residuals. The velocities used by Bean et al. (2008) to infer the third planet were derived using a method independent of RADIAL or AUSTRAL, described in Bean et al. (2007). Fitting those velocities with a 2-planet model as done elsewhere in this work, the 346-day residual period is present, indicating that the fitting method used here is not responsible for our non-detection of HD 74156d. A direct comparison of the different radial-velocity data sets is shown in Figure 4.14. Performing a periodogram search on the difference between the RADIAL data and those of Bean et al. (2008), a 390-day periodicity is evident, with a bootstrap FAP < 0.001%. The same test on AUSTRAL velocities shows no significant periodicities.

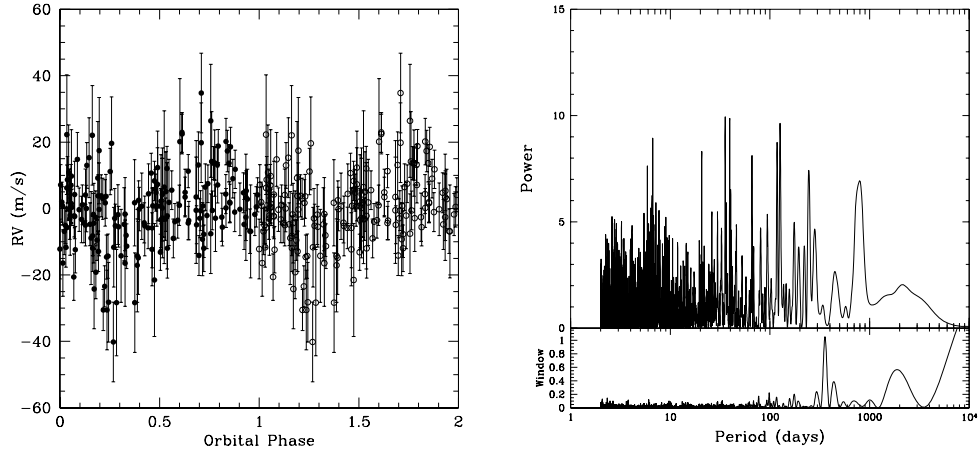


Figure 4.10 Left panel: Residuals of a 2-planet fit for HD 74156, phased to a period of 126.6 days. HET (RADIAL) and CORALIE data are shown. A second cycle is plotted with open circles. Right panel: Periodogram of the residuals to a 2-planet fit for HD 74156. The  $3\sigma$  outliers were removed from the residuals before computing the periodogram.

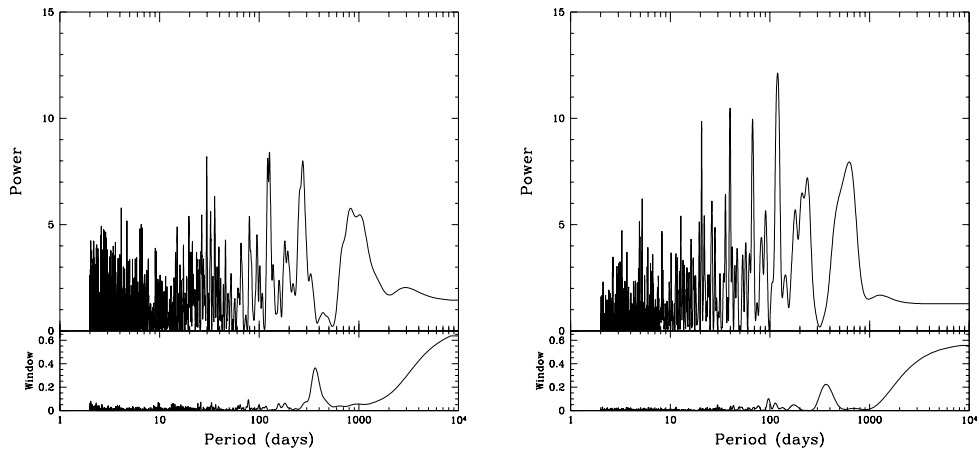


Figure 4.11 Left panel: Periodogram of the Naef et al. (2004) residuals only for HD 74156. Peaks are at 126.6, 121.7, and 29.7 days. Right panel: Periodogram of the HET (RADIAL) residuals only, with the main peak at 119.3 days.

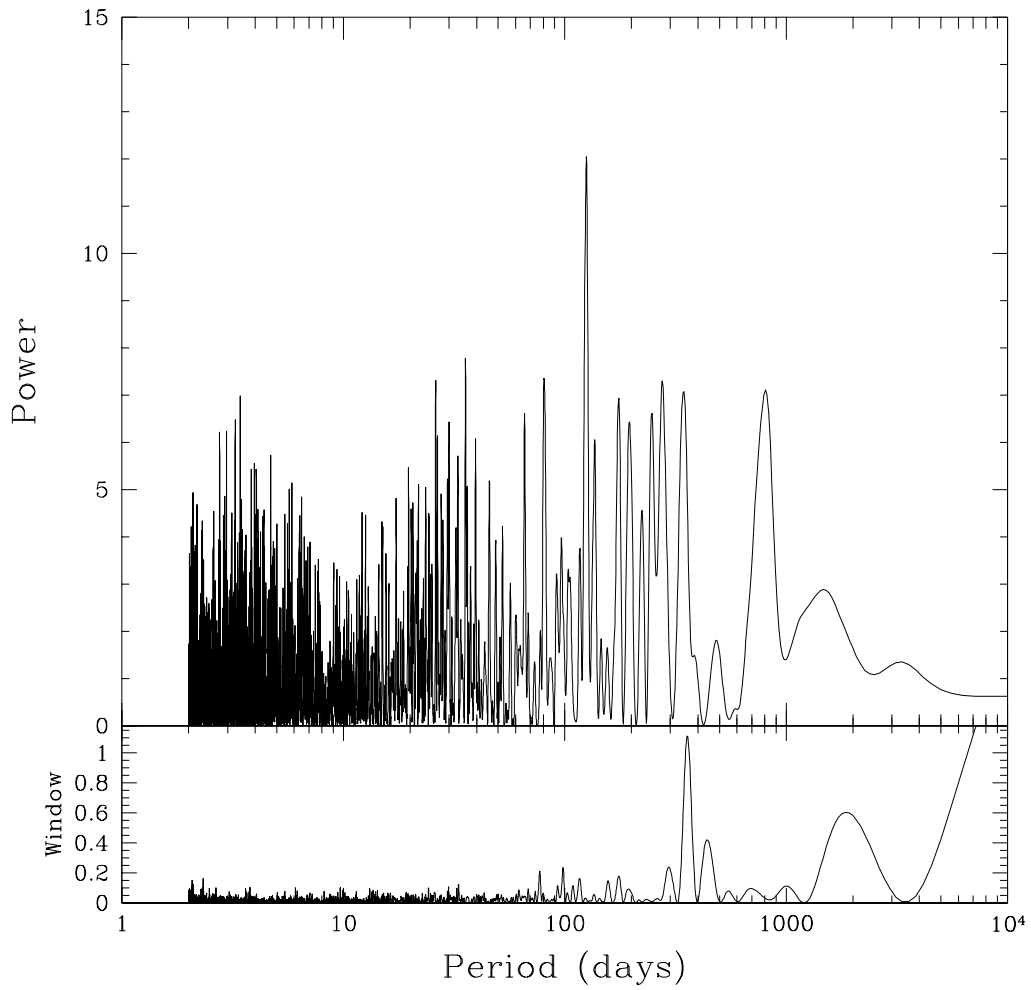


Figure 4.12 Periodogram of the residuals to a 2-planet fit for HD 74156, with velocities derived using AUSTRAL. There is no evidence of a 346-day signal.

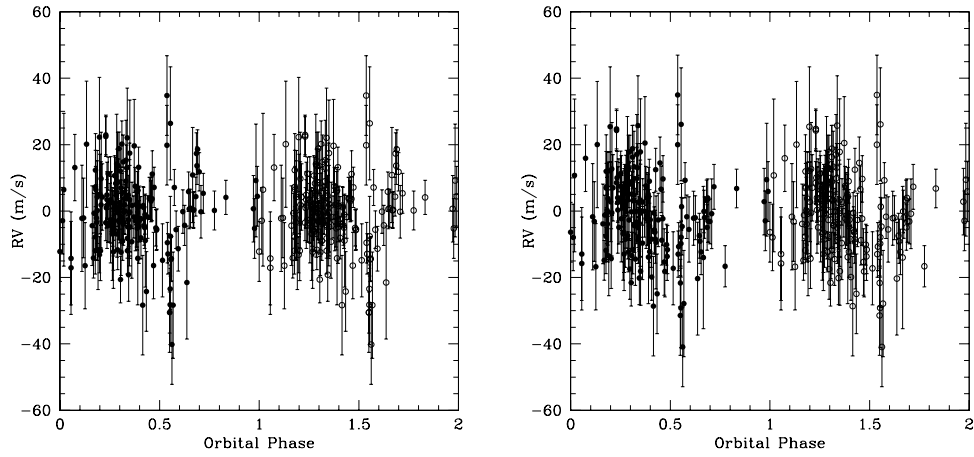


Figure 4.13 Residuals of a 2-planet fit for HD 74156, phased to a period of 346.6 days. Left panel: RADIAL results. Right panel: AUSTRAL results.

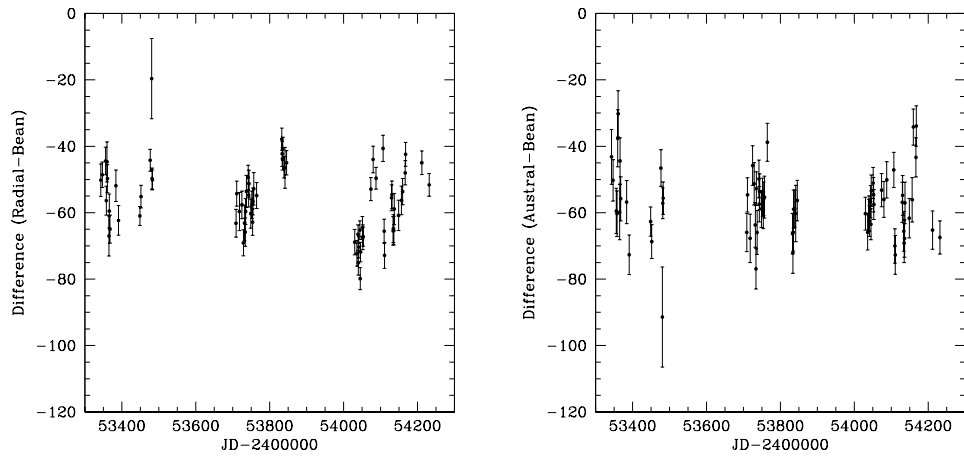


Figure 4.14 Left panel: Difference between the HET velocities (RADIAL results) and the velocities of Bean et al. (2008) obtained from the same spectra. Right panel: Same, but for AUSTRAL results.



Table 4.1. Periodogram Analysis for HD 74156

Template	Velocity Code	Period (days) Highest Peak	FAP Highest Peak	FAP P=346 d
60k, 20041203	Radial	126.906	0.0004	1.000
60k, 20041203	Austral	11.961	0.013	0.903
60k, 20041207	Radial	126.582	< 0.0001	1.000
60k, 20051209	Radial	126.263	0.0005	1.000
120k	Radial	126.263	0.006	1.000
120k	Austral	126.263	0.001	1.000

#### 4.2.7 47 UMa

As discussed in Chapter 3, a single-planet fit for the 47 UMa system gives a residual periodicity of 2193 days at the 4% FAP level. This is close enough to the period for an outer planet claimed by (Fischer et al. 2002a) that it merits further investigation. The phased residuals of the combined fit on four data sets are shown in Figure 4.15; the amplitude is small and there is substantial scatter. Considering the data sets separately, we obtain: Fischer et al. (2002a) – P=2272.7 days, FAP<0.0001%; Naef et al. (2004) – P=1162.8 days, FAP=0.4%; 2.7m – P=4.4 days, FAP=3.8%; HET – P=19.0 days, FAP=82.7%. All of these periodograms for 47 UMa are plotted on the same scale for ease of comparison. The AUSTRAL velocities also show two broad peaks, at 5000 (FAP=2.0%) and 2174 days, but they do not rise significantly above the noise level (Figure 4.18). Attempts to fit a second planet in the 47 UMa system, as described in § 3.1, resulted in convergence on a very long period, despite starting the least-squares fitting at  $P_2 = 2173$  days. The residual power may be spectral leakage from an outer planet with a period longer than the span of the observations (Wittenmyer et al. 2007a).

To further test the methods by which we conclude that the parameters of 47 UMa c reported by Fischer et al. (2002a) may be ambiguous, we performed some Monte Carlo simulations. From each of the four data sets considered in the fits described above, we generated 1000 simulated sets of velocities consisting of a Keplerian signal for each of the two planets, plus Gaussian noise equivalent to the quadrature sum of the mean uncertainty of each data set and  $8 \text{ m s}^{-1}$  stellar jitter (cf. Table 2.6). The parameters for the inner planet were those listed in Table 3.2,

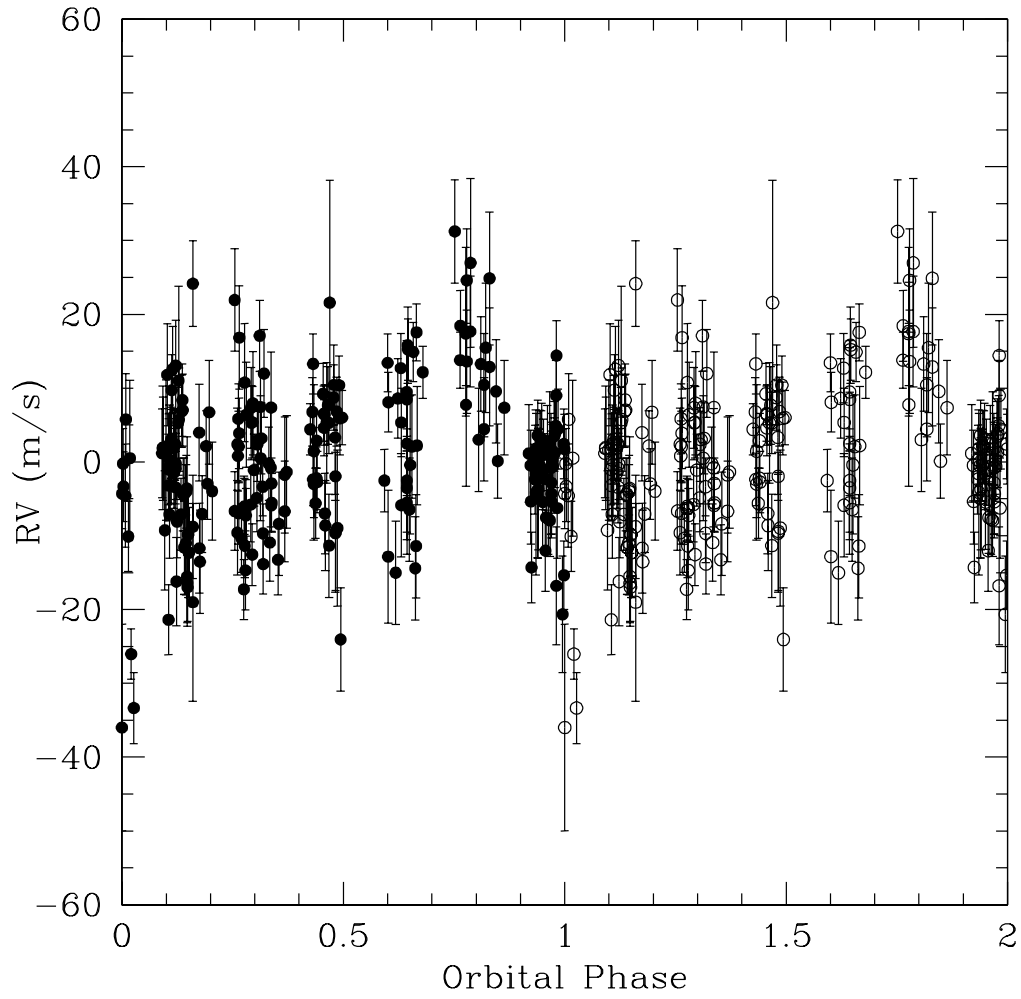


Figure 4.15 Residuals of a 1-planet fit for 47 UMa, phased to a period of 2173.9 days.

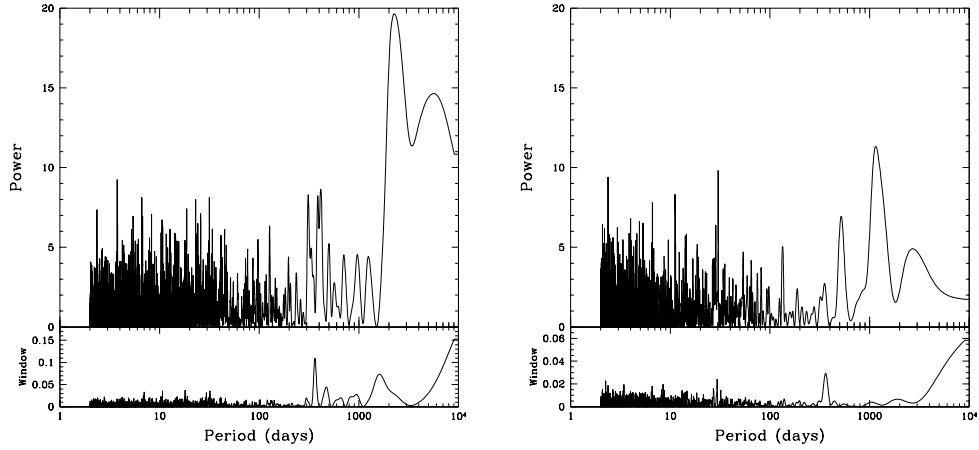


Figure 4.16 Left panel: Periodogram of the Fischer et al. (2002a) residuals only for 47 UMa (1-planet fit), with a large peak at 2272.7 days. Right panel: Periodogram of the Naef et al. (2004) residuals only, with the main peak at 1162.8 days.

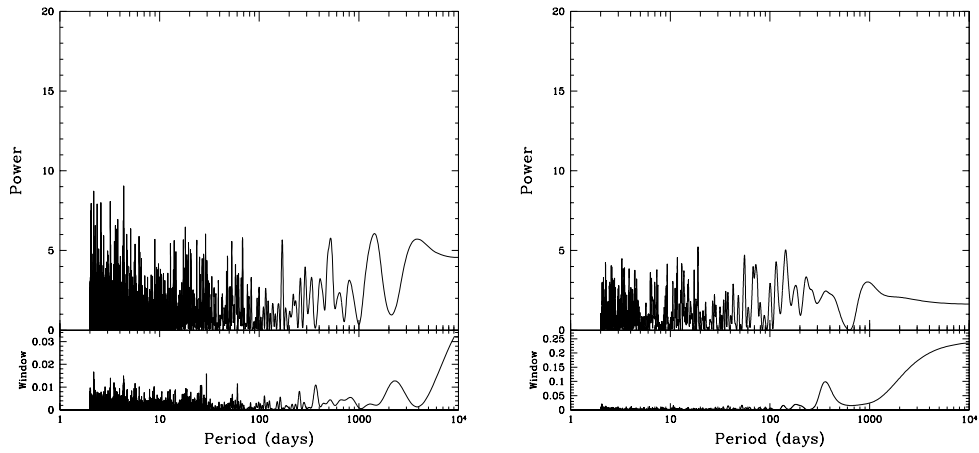


Figure 4.17 Left panel: Periodogram of the 2.7m residuals only for 47 UMa (1-planet fit), with a the highest peak at 4.4 days. Right panel: Periodogram of the HET RADIAL residuals only, with the highest peak at 19.0 days.

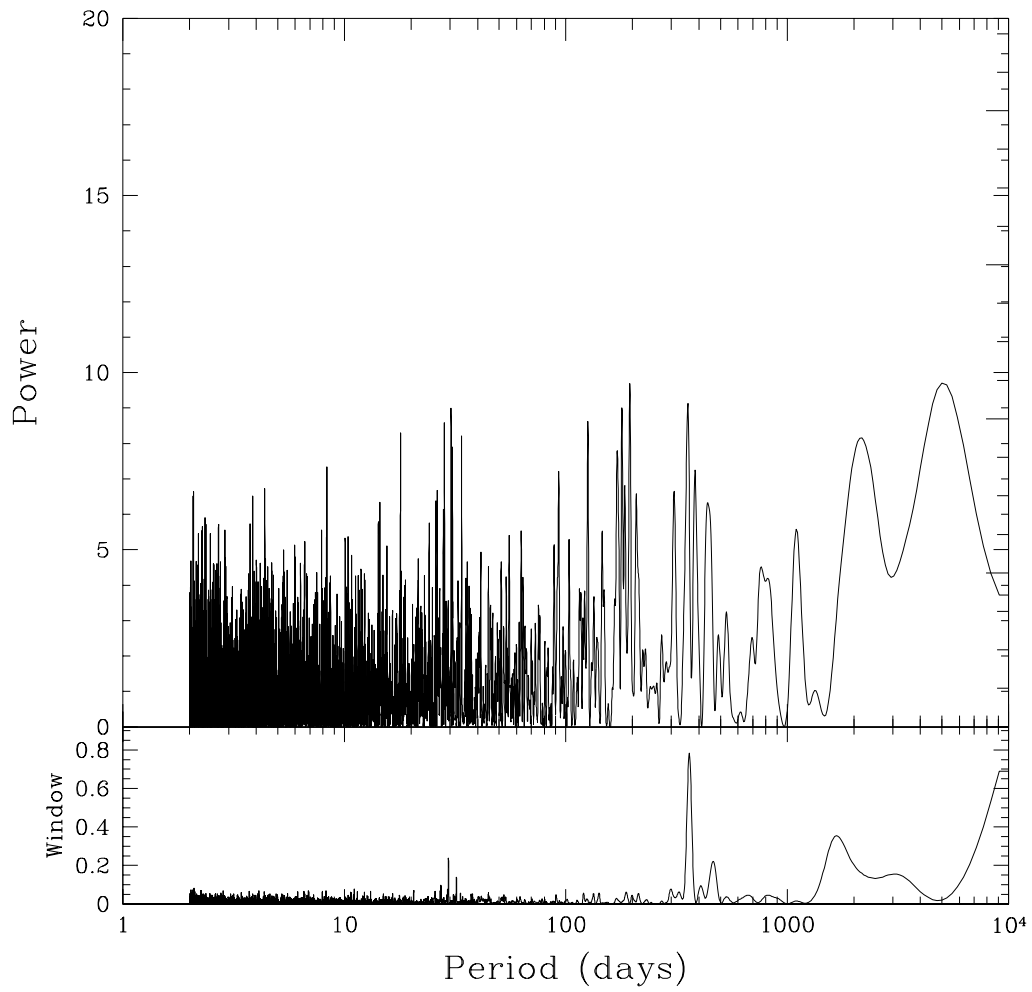


Figure 4.18 Periodogram of residuals of a 1-planet fit for 47 UMa, using all four datasets and HET AUSTRAL velocities.

and those of the outer planet were those of Fischer et al. (2002a). These simulated datasets retained the times of observation and the error bars of the originals. The simulated data were then fit with a one-planet model exactly as described in Chapter 3, then the residuals of the one-planet fit were examined by the periodogram method, to determine whether the signal of the second planet was recovered. The criteria for recovery were that the period of the second planet had to be detected correctly and with a FAP of less than 0.1%. This FAP was computed using the analytic FAP formula of Horne & Baliunas (1986). Of the 1000 trials, only 2 did not result in a successful recovery of the signal of the second planet. The correct period was recovered 1000 times, and the FAP exceeded 0.1% only 2 times; the worst FAP was 0.65%. For comparison, the analytic FAP of the 2174-day peak in the residuals of the 1-planet fit is 0.31%. These results indicate that our method should have been able to detect the signal of 47 UMa c, had it been present with the parameters given by Fischer et al. (2002a) and Butler et al. (2006). We conclude that while an additional long-period object may be present, the data currently available do not provide sufficient evidence for an orbital solution.

#### 4.2.8 HD 128311

The residuals of 2-Keplerian and dynamical fits for the HD 128311 system have strong periodicities near 11.5 days, with bootstrap FAP less than 0.01%. Photometry of HD 128311 by G. Henry in Vogt et al. (2005) indicates a rotation period of 11.53 days with a photometric amplitude of 0.03 mag. One can fit a fictitious planet to estimate the amplitude of the radial-velocity variations induced by stellar rotation. A three-planet fit performed for this purpose by E. Rivera gives a velocity semi-amplitude  $K = 12.4 \pm 2.0 \text{ m s}^{-1}$ . Hence, it is quite clear that the residual signal is caused by stellar rotation in this highly active star.

#### 4.2.9 HD 178911B

The residuals to our combined fit for HD 178911Bb show a period of 306.7 days with a bootstrap FAP of 0.8%. A phase plot is shown in Figure 4.19. In separate analysis of the data sets, we find: Zucker et al. (2002) – P=5.5 days, FAP=56.7%, rms=11.6 m s<sup>-1</sup>; HET – P=116.8 days, FAP=0.07%, rms=12.2 m s<sup>-1</sup>. The data sets from the 2.7m and from Butler et al. (2006) contained too few points for a

reliable periodogram analysis. Visual examination of the HET residuals shows a clear periodicity of  $\sim 350$  days (Fig. 4.21). By re-doing the Keplerian fit on only the data of Zucker et al. (2002) and Butler et al. (2006), there is no trace of a residual signal (Fig. 4.21), and hence we interpret the 306-day peak as an artifact, likely a seasonal systematic effect. A fit using all data, with the AUSTRAL velocities rather than the RADIAL ones, shows no evidence of this signal (Fig. 4.22). Those residuals have only a peak at  $P=7.9$  days with a bootstrap FAP of 7.4%.

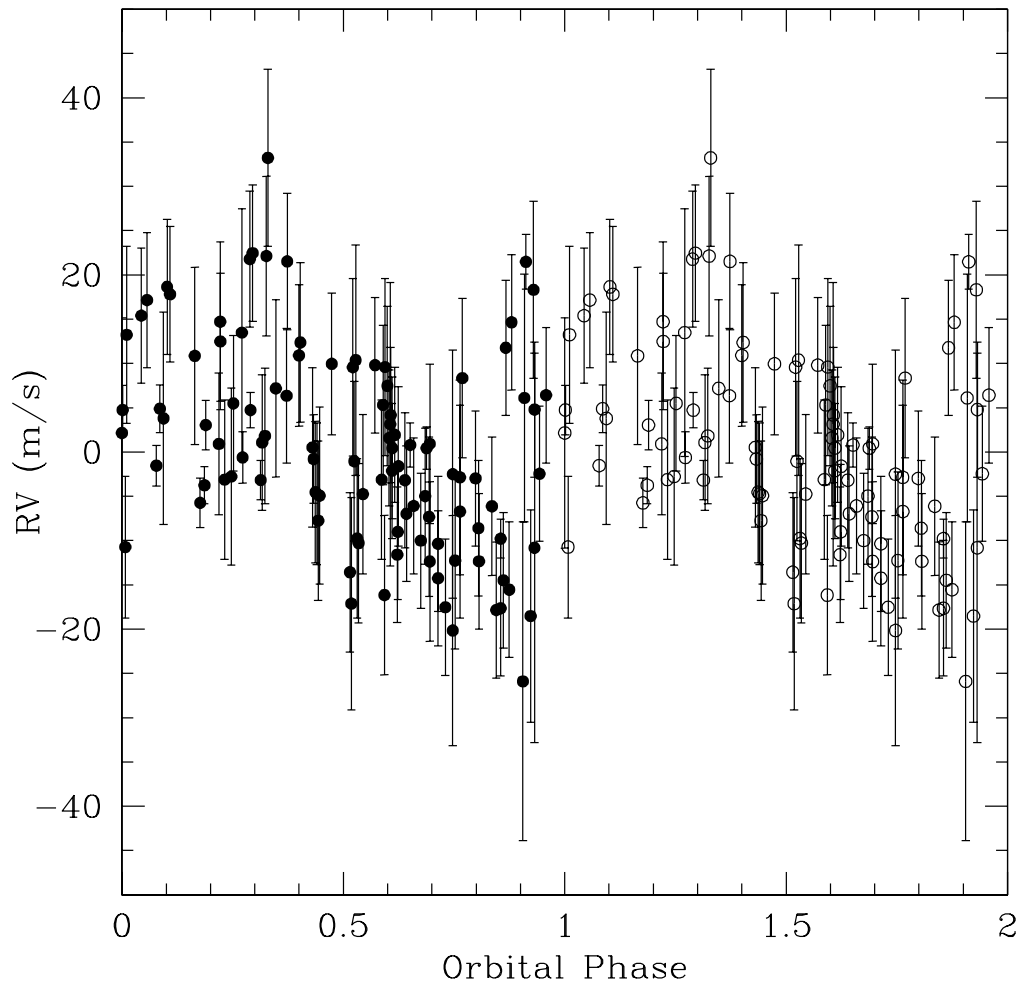


Figure 4.19 Residuals of a 1-planet fit for HD 178911Bb, phased to a period of 306.7 days.

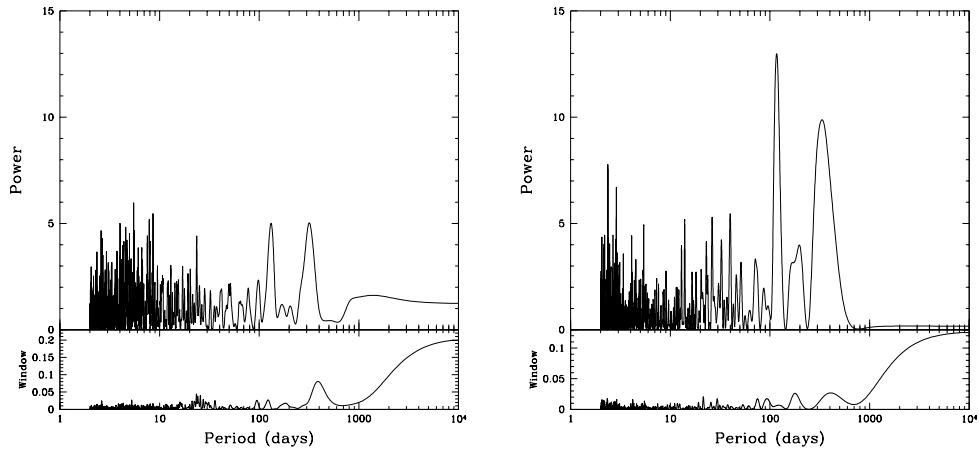


Figure 4.20 Left panel: Periodogram of the Zucker et al. (2002) residuals only for HD 178911Bb, with peaks at 5.5 and 300 days. Right panel: Periodogram of the HET (RADIAL) residuals only, with the main peak at 116.8 days.

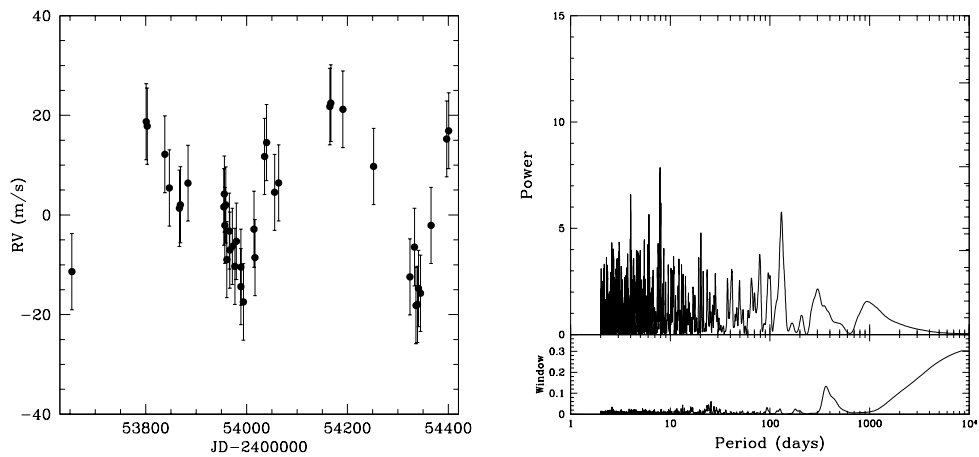


Figure 4.21 Left panel: HET (RADIAL) residuals after fitting and removing HD 178911Bb. Note the clear periodicity of about 350 days. Right panel: Periodogram of the residuals of a fit excluding HET data. The highest peak has a FAP of 11.9%.



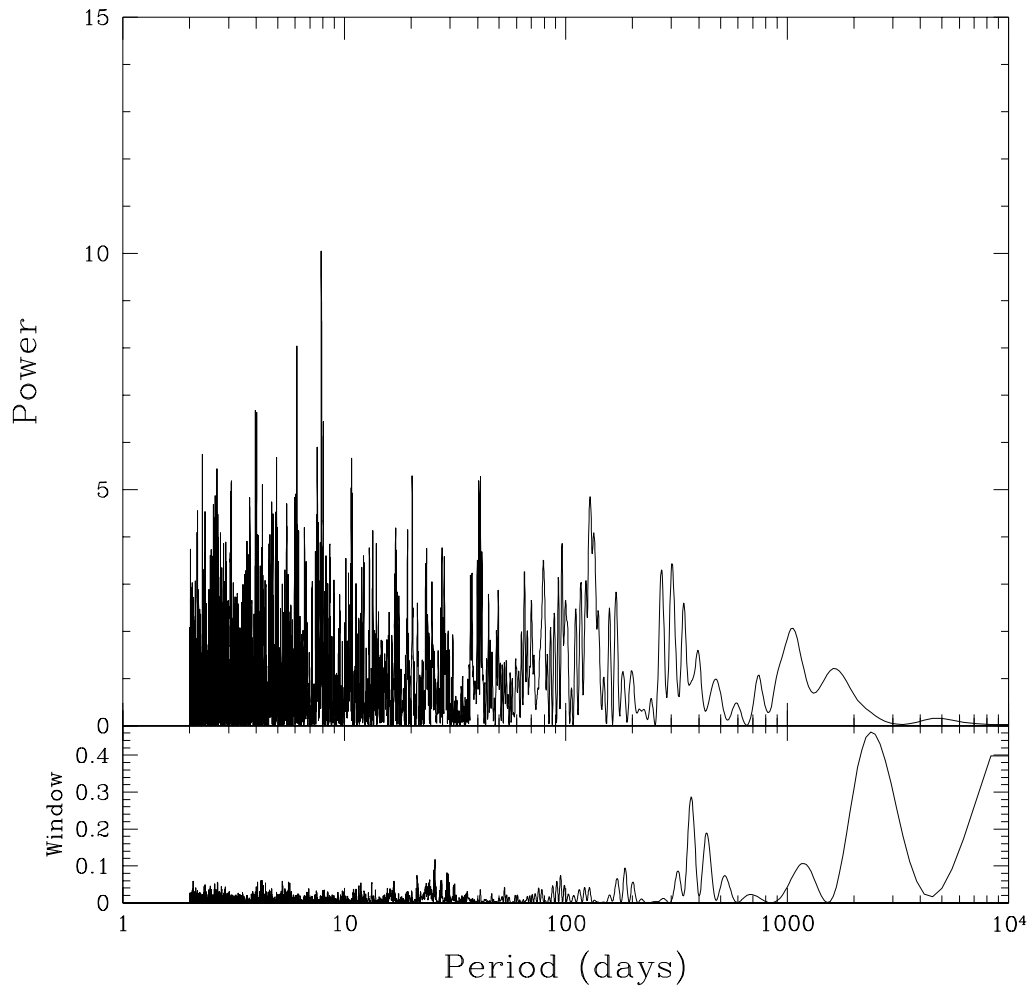


Figure 4.22 Periodogram of the residuals of all data after removing HD 178911Bb, using the AUSTRAL results for HET.

## Chapter 5

# Detection Limits

An important component of this research is the interpretation of a null result; with three years of high-precision data, one can place tight limits on planets which would have been detected. This work builds on previous efforts to place upper limits on substellar and planetary companions from radial-velocity surveys. Murdoch et al. (1993) determined detection limits for the Mt. John radial-velocity program by adding the program's mean velocity error ( $65 \text{ m s}^{-1}$ ) to the signals of planets in circular orbits. The planetary signals were then recovered by the periodogram and F-test methods, and those planets for which 95% of phases were recovered with  $\text{FAP} < 1\%$  were considered detectable. Similarly, Cumming et al. (1999) computed detection limits from the Lick planet search data by 1) noting the highest peak  $z_{max}$  in the periodogram for each target, and 2) generating simulated data sets with sinusoidal (circular-orbit) signals and finding the velocity amplitude  $K$  for which 99% of signals had power exceeding  $z_{max}$ . The 12-year CFHT survey of Walker et al. (1995), with a velocity precision of  $15 \text{ m s}^{-1}$ , achieved detection limits approaching a Jupiter mass for planets in circular orbits and periods shorter than  $\sim 10$  yr. Nelson & Angel (1998) derived an analytic expression for the probability that a particular velocity amplitude  $K$  would appear by chance, and re-examined the data of Walker et al. (1995) to set 99% confidence limits on substellar companions in those data to orbital separations of about 10 AU.

This chapter describes the method by which detection limits were computed for two classes of targets: those which showed no evidence of radial-velocity variation (“constant stars”), and the known planet hosts listed in Chapter 2. The first

sample, of constant stars, can be considered the “easy” case for which the tools were developed before progressing to the more difficult case of the planet hosts. Since the null hypotheses are different for these two cases, they will be treated in separate sections. For the first case, the constant stars, the null hypothesis is that no planets are present, and so the detection-limit algorithm can be applied straightaway to the velocity data. In the case of the known planet hosts, this is not true, and it would not do to “pre-whiten” that data by removing the known planet’s orbit as if its parameters were known perfectly. Modifications to the technique are described in § 5.2.

## 5.1 Constant Stars from the the McDonald Observatory Planet Search

### 5.1.1 Observational Data Presented Here

Current Doppler surveys now routinely achieve precisions of 2-3 m s<sup>-1</sup> (e.g. Cochran et al. 2004), facilitating the detection of ever-lower-mass companions, such as the “hot Neptunes” (Bonfils et al. 2005; McArthur et al. 2004; Santos et al. 2004b; Butler et al. 2004) and even “super-Earths” (Udry et al. 2007; Rivera et al. 2005). However, there exists a relatively long record of radial velocity data at somewhat lower precision ( $\sim 15\text{-}20$  m s<sup>-1</sup>) which ought not to be ignored. Such data now cover nearly a quarter-century (Campbell & Walker 1979; Campbell et al. 1988; Walker et al. 1995), and as such are extremely useful in probing nearby stars for long-period giant planets akin to our own Jupiter (orbital period 11.9 years). These data sets are valuable tools in the search for extrasolar analogs to our Solar System. We are now beginning to obtain meaningful answers to some of the following questions: What is the frequency of long-period giant planets in the solar neighborhood? What implications would the lack of such planets have on theories of planet formation? How many planetary systems resemble our own Solar system?

The majority of the data used in this section were obtained by the McDonald Observatory program using the 2.7m Harlan J. Smith telescope. The characteristics of Phases I, II, and III are described in § 2.2.2. A list of the target stars is given in Table 5.1. For 17 of the 31 stars in this study, additional data were available from the CFHT precision radial-velocity work of Walker et al. (1995). Table 5.2 gives a

summary of all four data sets, including the total time span, rms of each data set, and the chromospheric emission ratio  $\log R'_{HK}$  (Noyes et al. 1984) computed from the McDonald Phase III measurements of the Ca II S-index. The rms values listed in Table 5.2 include the internal uncertainties of  $6\text{--}9\text{ m s}^{-1}$  and the velocity jitter inherent to each star.

### 5.1.2 Merging the Data

Since each of the four data sets consists of velocities measured relative to an independent and arbitrary zero-point, it was necessary to implement a consistent and robust method of combining them. Before merging, an iterative outlier-rejection routine was applied to each data set separately. Data points which were more than  $3.3\times\text{RMS}$  from the mean were rejected. This criterion corresponds to a 99.9% confidence level for a Gaussian distribution, assuming that no planetary signals are present. The mean and RMS were then re-computed and the outlier rejection was repeated until no more points were rejected. As the targets are well-studied constant-velocity stars, we are confident that we have a well-defined distribution about the mean. For the visual binary 70 Oph A, several velocities were systematically too low due to spectral contamination caused by the chance alignment of both components on the slit (separation  $4.6''$ ), and these points were also removed. The fainter component ( $\Delta m = 1.8$  mag) adds a Doppler-shifted second spectrum, which results in a distorted composite line shape. Since our velocity computation method assumes a single set of lines, the resultant velocity is skewed by this contamination.

The merging of these data sets was accomplished in the following manner: McDonald Phases II and III are joined with a trial offset, and a least-squares linear fit of a trend of velocity with time is performed on the combination. The offset between the Phase II and III data sets which minimizes the RMS about that linear fit is the one which is applied in order to merge two phases together. This process was then repeated sequentially to join the Phase I and then the CFHT data to the growing data string. The least-squares fitting allows for a linear trend to be present; the merging process was re-done for all non-binaries, this time forcing the slope to be zero (i.e. minimizing the RMS about the mean of the combined data for a grid of trial offsets). The RMS about the mean of data merged in this manner was compared to the RMS about a linear fit to data merged allowing a trend. Since

our null hypothesis is that the stars are radial-velocity constants, the method which allowed a slope was only chosen for the 10 stars which showed an improvement in the RMS of the merged data set when a slope was allowed. Those stars were:  $\eta$  Cep,  $\eta$  Cas,  $\alpha$  For,  $\theta$  UMa,  $\xi$  Boo A,  $\mu$  Her, 16 Cyg A, 70 Oph A, and 61 Cyg A & B. All of these stars are well-known long-period binaries, so the use of a slope was justified.

The orbital periods of these 10 known binaries were sufficiently long that a simple linear approximation was sufficient, except for  $\mu$  Her,  $\xi$  Boo A (quadratic trend) and 70 Oph A (Keplerian solution). Fits to these trends were subtracted from the data sets and the residuals were used as input for the detection-limit algorithm. The three data sets on the visual binary  $\mu$  Her were merged in a similar manner. The binary period (43.2 years; Worley & Heintz 1995) is such that a linear trend is a suboptimal approximation for the purposes of merging the 16.9 years of data, so a quadratic fit was used to approximate the shape of the orbit. This procedure was also used for  $\xi$  Boo A; the data and fits are shown in Fig. 5.1. For 70 Oph A, the quadratic approximation was still insufficient, as the 16.1 years of available data represents a significant portion of the 88.3 year published orbital period (Heintz 1988; Pourbaix 2000). An orbital solution for the binary system had to be obtained using a Keplerian orbit model in the non-linear least-squares solver GaussFit (Jefferys et al. 1987). The solution to the combined data set (McDonald Phases I-III plus much lower-precision data from Batten et al. (1984) is given in Table 5.3, and plotted in Fig. 5.2. The large uncertainties in the fitted parameters are due to the fact that the available data do not encompass a complete orbit, and hence the model is poorly constrained. The eccentricity was held fixed at  $e = 0.499$  (Pourbaix 2000). Only the McDonald data were used in the computation of companion limits for 70 Oph A.

### 5.1.3 Periodogram Analysis

After the data sets were merged together, and trends due to binary orbits were subtracted, we searched for periodicities using a Lomb-Scargle periodogram (Lomb 1976; Scargle 1982). False alarm probabilities (FAP) were established using a bootstrap randomization method as described in Kürster et al. (1997) and Endl et al. (2002). This bootstrap method does not assume that the errors are independent and normally distributed, unlike the nominal analytic FAP formula of Horne & Baliunas

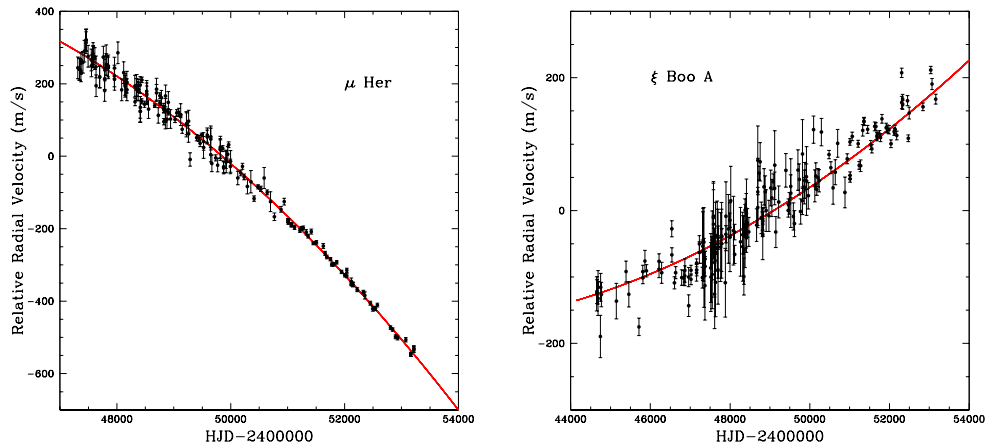


Figure 5.1 Quadratic fits to  $\mu$  Her data (left panel) and  $\xi$  Boo A (right panel).

(1986). The periodogram search interval was from 2 days up to the full extent of observations for each object. We used 10,000 bootstrap randomizations to determine the FAP of the highest peak in the periodogram for each star; the results are given in Table 5.4. Four stars had periodicities with significance greater than 99%:  $\tau$  Cet,  $\iota$  Per,  $\kappa^1$  Cet, and  $\pi^3$  Ori. However, none of these stars exhibited a peak in the periodogram of the more precise McDonald Phase III data alone, supporting our conclusion that the indicated periodicities are spurious noise spikes.

### 5.1.4 Determination of Companion Limits

Companion limits were determined via an algorithm which injected test signals into the data, and then attempted to recover that signal using a periodogram search. This method builds on earlier detection-limit techniques described in Endl et al. (2001), Cumming et al. (1999), and Walker et al. (1995). Test signals were generated using the method of Lehmann-Filhés (Lehmann-Filhés 1894) as described in Binnendijk (1960):

$$V_r = \gamma + K[e \cos \omega + \cos(\nu + \omega)], \quad (5.1)$$

where  $V_r$  is the radial velocity,  $\gamma$  is the systemic velocity,  $K$  is the velocity semi-amplitude,  $e$  the orbital eccentricity,  $\omega$  the argument of periastron, and  $\nu$  the true

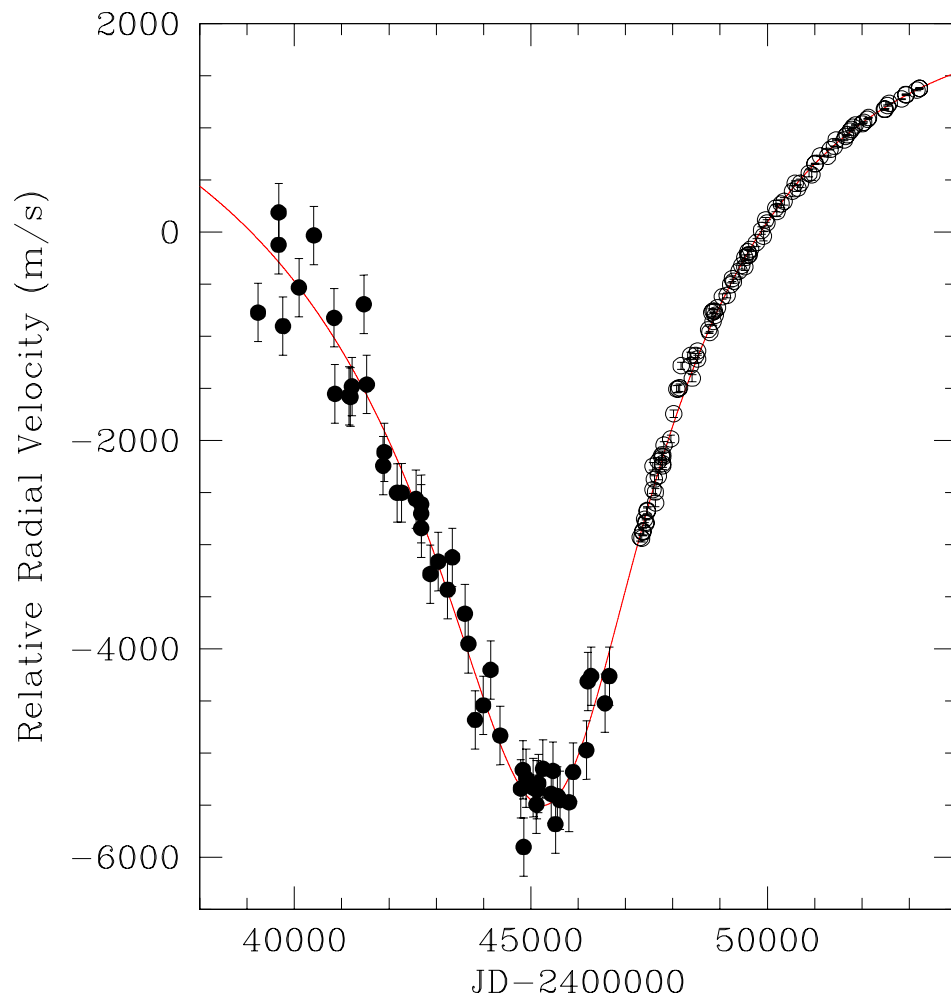


Figure 5.2 Orbital solution for the visual binary 70 Oph A using radial-velocity data from Batten et al. (1984) (filled circles) and McDonald Observatory phase I-III (open circles).

anomaly. In the above equation,  $\nu$  can be expressed in terms of observables via the following relations:

$$\tan \frac{\nu}{2} = \left[ \frac{(1+e)}{(1-e)} \right]^{1/2} \tan \frac{E}{2} \quad (5.2)$$

and

$$M = \frac{2\pi}{P}(t - T_0) = E - e \sin E, \quad (5.3)$$

for a signal with period  $P$ , periastron passage time  $T_0$ , observation time  $t$ , mean anomaly  $M$ , and eccentric anomaly  $E$ . For each data set, the algorithm stepped through 300 trial periods at even steps in the logarithm between 2 days and the total duration of observations. At each trial period, the program sampled 30 phase steps of the periastron time  $T_0$ , and for nonzero eccentricities, sampled 36 values of the argument of periastron  $\omega$ , at intervals of 10 degrees. The velocity semi-amplitude  $K$  of the test signal was allowed to vary from 5 to 100 m s<sup>-1</sup>. The systemic velocity  $\gamma$  of each combined data set was forced to be equal to zero. For each set of Keplerian orbital parameters, synthetic radial velocities were generated using the observation times from the input data. This simulated signal was then added to the data, and a Lomb-Scargle periodogram was used to attempt to recover that signal. For a signal to count as having been recovered, the periodogram's highest peak had to occur within 5% of the correct period with a FAP of less than 0.1%. The FAP was estimated using the formula from Horne & Baliunas (1986). For each  $K$  velocity, 99% of the 1080 test signals<sup>1</sup> had to be recovered in this manner in order for that velocity semiamplitude (corresponding to a planet of a given mass at a given semimajor axis) to be considered "ruled out" by the data. If more than 1% of the orbital configurations tested at a given  $K$  value were *not* ruled out in this manner, the algorithm increased  $K$  by 1 m s<sup>-1</sup> and repeated the process until it was able to recover 99% of the parameter configurations ( $e, \omega, T_0$ ) that were tested. Once this occurred, the planetary mass ruled out was computed by the following:

$$M_2 \sin i = (1 - e^2)^{1/2} \left[ (1.036 \times 10^{-7}) M_1^2 P K^3 \right]^{1/3} M_\odot, \quad (5.4)$$

where  $M_1$  is the stellar mass in solar masses,  $P$  is the orbital period in days,  $K$  is the

---

<sup>1</sup>For signals with  $e = 0$ , *all* 30 variations in  $T_0$  had to be recovered, as  $\omega$  had no meaning.



radial-velocity semiamplitude in  $\text{km s}^{-1}$ , and  $M_2 \sin i$  is the projected planetary mass in solar masses. The algorithm then moved to the next trial period and repeated the entire process.

Unlike most previous companion limit determinations (Murdoch et al. 1993; Walker et al. 1995; Nelson & Angel 1998; Cumming et al. 1999; Endl et al. 2002), this procedure allows for nonzero eccentricities in the trial orbits (but see Desidera et al. 2003). For the eccentric case, a value of  $e = 0.6$  was chosen; of the known extrasolar planets, 90% have  $e < 0.6$  Marcy et al. (2005). Allowing higher eccentricities substantially reduced the ability to rule out the test signals, as the sporadic sampling of the data would likely miss the points near periastron where the velocity is changing rapidly. Fig. 5.3 shows the effect of allowing various ranges of eccentricity. Note that although the limits derived by this study are rendered somewhat less stringent by the inclusion of nonzero eccentricities, the effect is relatively minor for our adopted value of  $e = 0.6$ . Allowing a larger range of eccentricities (up to  $e = 0.9$ ), however, substantially reduces the sensitivity of the companion-limit determination, as demonstrated in Fig. 5.3. We emphasize that the upper limits derived by the method described above are much more stringent, and hence will result in higher companion-mass limits than those reported by previous studies.

### 5.1.5 Results and Discussion

Limits to planetary companions derived using these data are shown in Figures 5.4-5.11. In each panel, the lower set of points (solid line) represents the companion limits for the zero-eccentricity case, and the dotted line is for the case of  $e = 0.6$ . Notably, despite the abundance and quality of data available in this study, we are as yet unable to rule out *any* planets with  $M \sin i \lesssim 1 M_{\text{Jup}}$  in 5.2 AU orbits with eccentricities as large as  $e = 0.6$ . When only circular orbits are considered, such objects can be ruled out for  $\tau$  Ceti,  $\sigma$  Dra, 61 Cyg A, and 61 Cyg B. Of course, the mass limits of planets that can be ruled out by these observations are dependent on the masses of the host stars (Eq. 5.4). Table 5.5 lists the minimum planet masses that can be excluded by these data at selected semimajor axes, for the  $e = 0$  and  $e = 0.6$  cases. The results given in Table 5.5 are shown in histogram format in Fig. 5.12, which indicates that for most stars in this survey, Saturn-mass planets in close orbits ( $a \sim 0.1$  AU) can be ruled out.

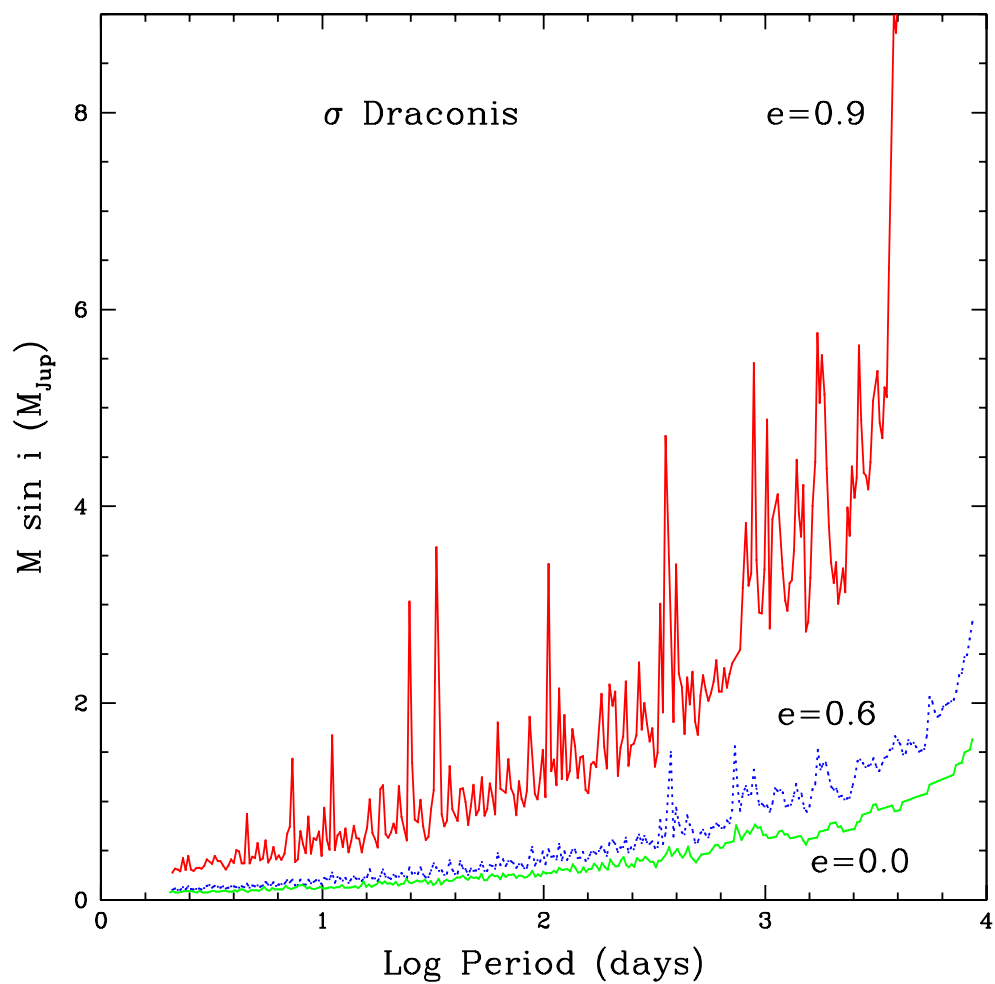


Figure 5.3 The effect of eccentricity on limit determinations. Allowing higher eccentricities reduces the sensitivity somewhat, due to the increased probability of unfortunately-phased observations.

It is also useful to consider the effect of giant planets in intermediate orbits ( $a \sim 2 - 3$  AU) which may perturb lower-mass planets within the habitable zone of the star. If such objects can be excluded with confidence, their host stars become attractive candidates for the *Terrestrial Planet Finder* (TPF) and Darwin missions, which aim to detect Earth-like planets in the habitable zone. Menou & Tabachnik (2003) defined a planet’s zone of influence to extend from  $R_{in} = (1 - e)a - 3R_{Hill}$  to  $R_{out} = (1 + e)a + 3R_{Hill}$ , where the Hill radius is

$$R_{Hill} = a \left( \frac{M_p}{3M_*} \right)^{1/3}, \quad (5.5)$$

and  $e$  is the planet’s eccentricity,  $a$  is its semimajor axis,  $M_p$  is its mass, and  $M_*$  is the mass of the star. Simulations by Menou & Tabachnik (2003) demonstrated that terrestrial planets were nearly always ejected or consumed in systems where an eccentric giant planet’s zone of influence overlapped the habitable zone. We can then ask whether the companion limits derived in this work can be used to exclude such perturbing bodies. Such a pursuit is limited by the fact that even distant giant planets can disrupt the habitable zone if their orbits are sufficiently eccentric, and as shown in Fig. 5.3, the nature of the radial-velocity data is such that we are least sensitive to the most eccentric planets. Nevertheless, for small eccentricities ( $e \lesssim 0.2$ ), it is possible to combine these dynamical calculations with our companion-limit determinations to define a “safe zone”: a region of parameter space in which we can exclude perturbing giant planets exterior to the habitable zone. For such regions, the possibility of terrestrial planets in the habitable zone remains open for programs such as TPF and Darwin. In Figures 5.4-5.1.5, the region to the left of the dot-dashed line and above the dotted ( $e = 0.6$ ) or solid ( $e = 0.0$ ) line defines the “safe zone” for perturbing outer giant planets with  $e < 0.2$ . These were only plotted for main-sequence stars, using the definition of the “continuously habitable zone” given in Kasting et al. (1993). The region left of the dot-dashed line and *below* our limits represents a set of potentially dangerous objects which would disrupt the habitable zone, yet be undetectable with the current data. Higher eccentricities would push the dot-dashed line to the right and reduce its slope, such that for perturbers with  $e \gtrsim 0.5$ , our limits computations can say nothing about such objects (i.e. the curves would not intersect). The companion limits we have derived thus place some constraints on potentially disruptive objects in these systems, which will

assist in target selection for the TPF (Beichman et al. 1999) and Darwin (Léger et al. 1996) missions.

Noting that the Phase III data are of substantially higher quality than the previous data sets, we asked what velocity rms would be required to rule out a Jupiter analog orbiting a solar-type star. We generated simulated observations consisting of Gaussian noise at the actual observation times (spanning 16 years) for 16 Cyg A, the star in this study which is closest in spectral type (G1.5 V) to our Sun. Fig. 5.13 shows the results of the companion-limit algorithm on four of these simulated data sets with four levels of rms scatter. In order to rule out a planet with  $M \sin i$  of  $1 M_{\text{Jup}}$  in a 5.2 AU orbit ( $e = 0.1$ ), the data need to have an rms less than about  $10 \text{ m s}^{-1}$ . The rms of Phase III observations of 16 Cyg A is  $5.8 \text{ m s}^{-1}$  over a period of 7.9 years, whereas the complete 17.9 years has an overall rms of  $26.6 \text{ m s}^{-1}$ . Hence, a Jupiter analog could be ruled out for 16 Cyg A with about 5 more years of data of the same quality as McDonald Phase III. The weighted mean rms of all McDonald Phase III observations in this survey is  $12.6 \text{ m s}^{-1}$ . Eleven stars (see Table 5.2) currently achieve a Phase III rms better than  $10 \text{ m s}^{-1}$ ; this represents one-third of the stars discussed in this work. These simulations show that the average precision of Phase III needs to be improved by about 2-3  $\text{m s}^{-1}$  in order to achieve the sensitivity required to detect or exclude Jupiter analogs for all of these stars.

## 5.2 Planet Hosts

For the known planet hosts, the method described above is not strictly applicable. In principle, one could fit the known planet(s) “once for all,” generate a single residuals file, and perform the detection-limits analysis on those data. However, the presence of additional Keplerian signals will act to modify the fitted parameters of the known planet. If two or more planets are present, and only one has been fitted, then part of the signal from the additional planets can be absorbed into the orbital elements of the 1-planet fit. To approach this task with the maximum rigor, these effects must be accounted for. Hence, the detection-limit algorithm was modified in the following way: the test Keplerian signal was added to each of the *original data sets*, then these modified data sets were fitted for the known planet(s) using GaussFit. A residuals file was generated and then subjected to the periodogram search as

Table 5.1. Target List and Stellar Parameters

Star	HR	Spec. Type	$V$ magnitude	Mass ( $M_{\odot}$ )	Reference for Mass Estimate
$\eta$ Cas	219	G0V	3.44	0.991	Takeda et al. (2007)
$\tau$ Cet	509	G8V	3.50	0.799	Takeda et al. (2007)
$\theta$ Per	799	F8V	4.12	1.238	Takeda et al. (2007)
$\iota$ Per	937	G0V	4.04	1.183	Takeda et al. (2007)
$\alpha$ For	963	F8V	3.87	1.30	Allende Prieto & Lambert (1999)
$\kappa^1$ Cet	996	G5V	4.82	1.034	Takeda et al. (2007)
$\delta$ Eri	1136	K0IV	3.54	1.193	Takeda et al. (2007)
$\sigma^2$ Eri	1325	K1V	4.43	0.808	Takeda et al. (2007)
$\pi^3$ Ori	1543	F6V	3.19	1.236	Takeda et al. (2007)
$\lambda$ Aur	1729	G1.5IV-V	4.71	1.081	Takeda et al. (2007)
$\theta$ UMa	3775	F6IV	3.17	1.53	Allende Prieto & Lambert (1999)
36 UMa	4112	F8V	4.82	1.121	Takeda et al. (2007)
$\beta$ Vir	4540	F8V	3.61	1.353	Takeda et al. (2007)
$\beta$ Com	4983	G0V	4.28	1.147	Takeda et al. (2007)
61 Vir	5019	G6V	4.75	0.942	Takeda et al. (2007)
$\xi$ Boo A	5544	G8V	4.55	0.931	Takeda et al. (2007)
$\lambda$ Ser	5868	G0V	4.43	1.105	Takeda et al. (2007)
$\gamma$ Ser	5933	F6V	3.85	1.214	Takeda et al. (2007)
36 Oph A	6402	K1V	5.29	0.78	Walker et al. (1995)
$\mu$ Her	6623	G5IV	3.42	1.091	Takeda et al. (2007)
70 Oph A	6752	K0V	4.03	0.97	Allende Prieto & Lambert (1999)
$\sigma$ Dra	7462	K0V	4.68	0.803	Takeda et al. (2007)
16 Cyg A	7503	G1.5V	5.96	1.022	Takeda et al. (2007)
31 Aql	7373	G8IV	5.16	1.147	Takeda et al. (2007)
$\beta$ Aql	7602	G8IV	3.71	1.472	Takeda et al. (2007)
$\gamma^2$ Del	7948	K1IV	4.27	1.90	do Nascimento et al. (2003)
$\eta$ Cep	7957	K0IV	3.43	1.39	Allende Prieto & Lambert (1999)
61 Cyg A	8085	K5V	5.21	0.660	Takeda et al. (2007)
61 Cyg B	8086	K7V	6.03	0.561	Takeda et al. (2007)
HR 8832	8832	K3V	5.56	0.794	Takeda et al. (2007)
$\iota$ Psc	8969	F7V	4.13	1.272	Takeda et al. (2007)

Table 5.2. Summary of Observations

Star	$N$	$T$ (years)	CFHT rms ( $\text{m s}^{-1}$ )	Phase I rms ( $\text{m s}^{-1}$ )	Phase II rms ( $\text{m s}^{-1}$ )	Phase III rms ( $\text{m s}^{-1}$ )	$\log R'_{HK}$
$\eta$ Cas	134	18.6	...	28.1	28.9	6.8	-4.926
$\tau$ Cet	192	26.1	14.2	22.3	28.7	11.2	-4.979
$\theta$ Per	102	13.5	...	...	59.6	15.8	-4.919
$\iota$ Per	175	25.9	18.2	30.0	18.6	9.7	-5.041
$\alpha$ For	72	18.2	...	28.9	41.3	24.0	-5.023
$\kappa^1$ Cet	155	24.9	23.7	34.4	29.7	22.4	-4.441
$\delta$ Eri	116	18.2	...	17.8	22.5	10.2	-5.228
$o^2$ Eri	168	26.3	18.6	30.4	18.0	13.6	-4.951
$\pi^3$ Ori	167	18.0	...	169.9	113.3	25.1	-4.716
$\lambda$ Aur	74	13.3	...	...	20.6	10.4	-5.051
$\theta$ UMa	275	21.0	18.8	43.1	43.7	14.4	-5.608
36 UMa	197	25.3	21.0	19.4	22.4	9.5	-4.811
$\beta$ Vir	215	26.3	28.4	30.5	32.6	7.5	-4.942
$\beta$ Com	201	26.0	18.4	31.7	42.0	10.1	-4.749
61 Vir	149	23.0	18.4	25.8	31.0	9.4	-5.030
$\xi$ Boo A	193	25.4	23.6	34.5	31.9	23.0	-4.420
$\lambda$ Ser	72	13.0	...	...	7.9	8.9	-4.936
$\gamma$ Ser	170	18.2	...	84.7	41.6	23.4	-4.934
36 Oph A	91	21.9	20.1	21.5	33.1	15.4	-4.614
$\mu$ Her	185	19.2	...	28.4	24.4	8.8	-5.092
70 Oph A	98	16.2	...	111.4	43.3	17.4	-4.736
$\sigma$ Dra	184	25.3	14.5	21.5	23.1	10.0	-4.865
16 Cyg A	109	17.9	...	34.4	29.0	5.8	-5.018
31 Aql	48	10.2	...	...	22.5	11.9	-5.123
$\beta$ Aql	198	25.5	14.6	28.0	20.1	11.3	-5.171
$\gamma^2$ Del	117	18.5	...	23.7	21.7	15.8	-5.354
$\eta$ Cep	191	26.3	19.2	29.5	16.4	8.8	-5.223
61 Cyg A	182	26.4	20.7	22.3	13.5	6.1	-4.862
61 Cyg B	162	25.4	16.9	23.5	16.2	4.5	-4.962
HR 8832	136	25.7	14.9	22.8	13.8	10.0	-5.013
$\iota$ Psc	65	13.4	...	...	26.4	13.1	-4.915

Table 5.3. Radial-Velocity Orbital Solution for 70 Oph A

Parameter	Estimate	Uncertainty
Period (years)	85.6	1.8
$T_0$ (JD)	2445513.8	84.5
$e$	0.499	(fixed)
$\omega$ (degrees)	190.4	1.4
$K_A$ ( $\text{m s}^{-1}$ )	3693	105

Table 5.4. Results of Periodogram Analysis

Star	Period (days)	FAP
$\eta$ Cas	2.964	0.145
$\tau$ Cet	8.388	0.009
$\theta$ Per	359.712	0.206
$\iota$ Per	11.999	0.005
$\alpha$ For	8.262	0.030
$\kappa^1$ Cet	2.377	0.005
$\delta$ Eri	5.246	0.883
$\rho^2$ Eri	3.153	0.615
$\pi^3$ Ori	73.314	0.003
$\lambda$ Aur	2.847	0.149
$\theta$ UMa	3.902	0.230
36 UMa	4132.231	0.722
$\beta$ Vir	3.308	0.207
$\beta$ Com	9.946	0.132
61 Vir	9.779	0.061
$\xi$ Boo A	6.299	0.158
$\lambda$ Ser	3.278	0.776
$\gamma$ Ser	8.962	0.114
36 Oph A	5.792	0.345
$\mu$ Her	7.624	0.044
70 Oph A	6.138	0.989
$\sigma$ Dra	30.562	0.106
16 Cyg A	3.206	0.523
31 Aql	3.230	0.071
$\beta$ Aql	2.800	0.014
$\gamma^2$ Del	5.393	0.559
$\eta$ Cep	5.940	0.040
61 Cyg A	25.265	0.192
61 Cyg B	6.868	0.673
HR 8832	25.227	0.088
$\iota$ Psc	7.455	0.358

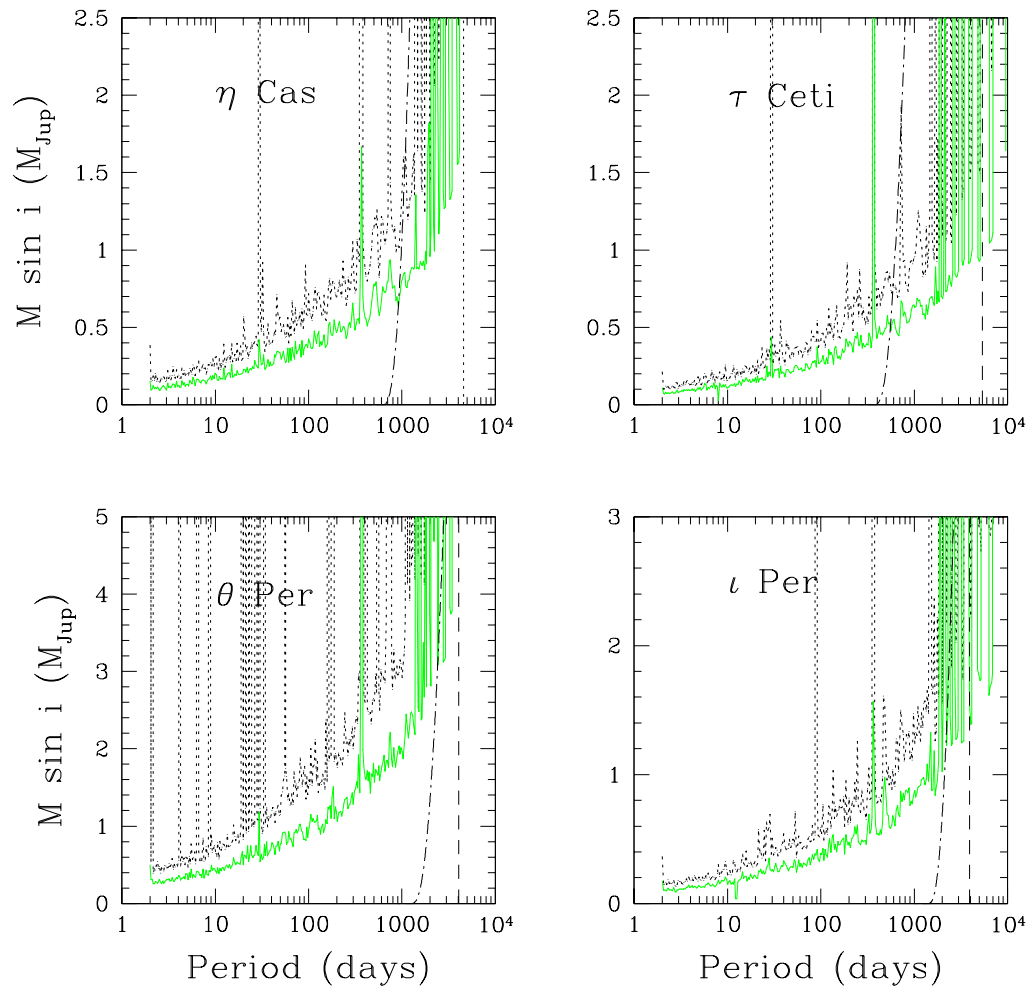


Figure 5.4 Planetary companion limits for  $\eta$  Cas,  $\tau$  Ceti,  $\theta$  Per, and  $\iota$  Per. The vertical dashed line indicates the 11.87 yr orbital period of Jupiter. Planets in the parameter space above the plotted points are excluded at the 99% confidence level. The solid line represents the companion limits for the zero-eccentricity case, and the dotted line is for the case of  $e = 0.6$ . The region left of the dot-dashed line represents the set of perturbers at  $e = 0.2$  which would disrupt the habitable zone.



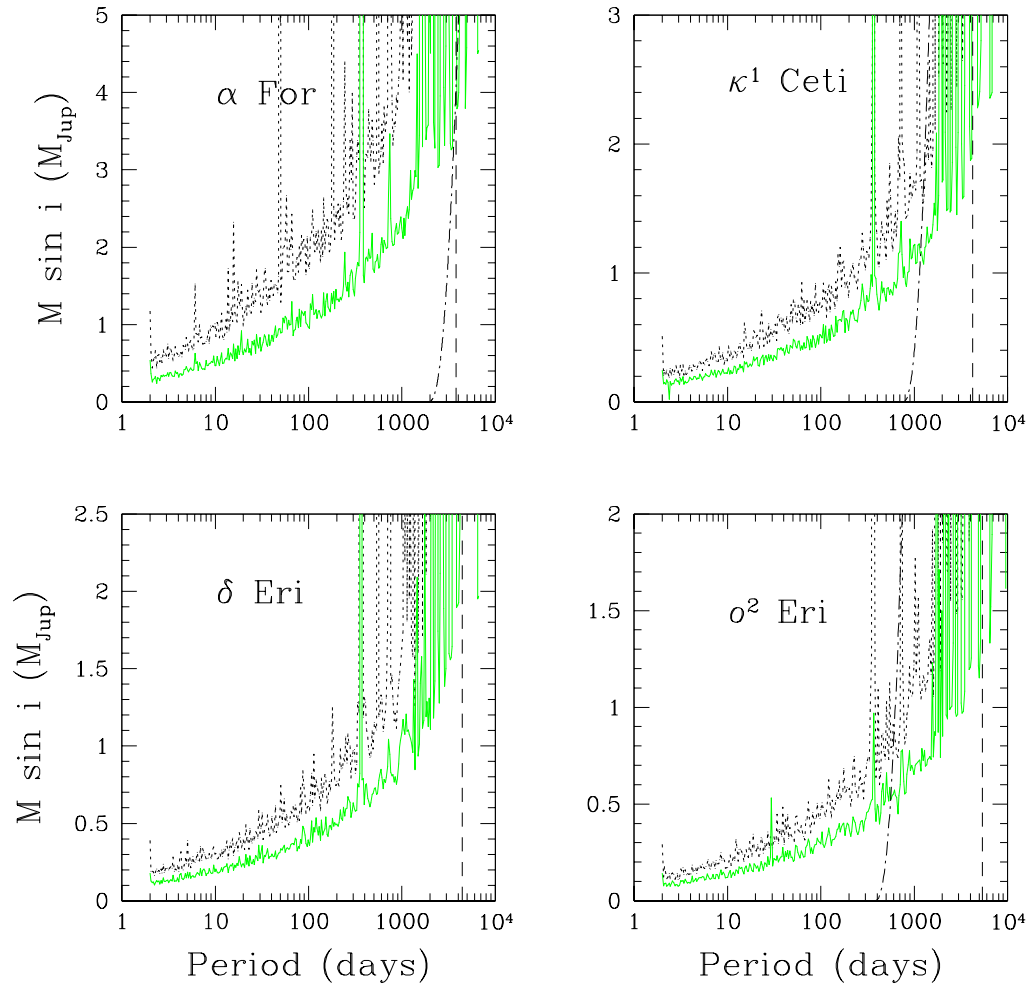


Figure 5.5 Same as Fig. 5.4, but for  $\alpha$  For,  $\kappa^1$  Cet,  $\delta$  Eri, and  $o^2$  Eri.

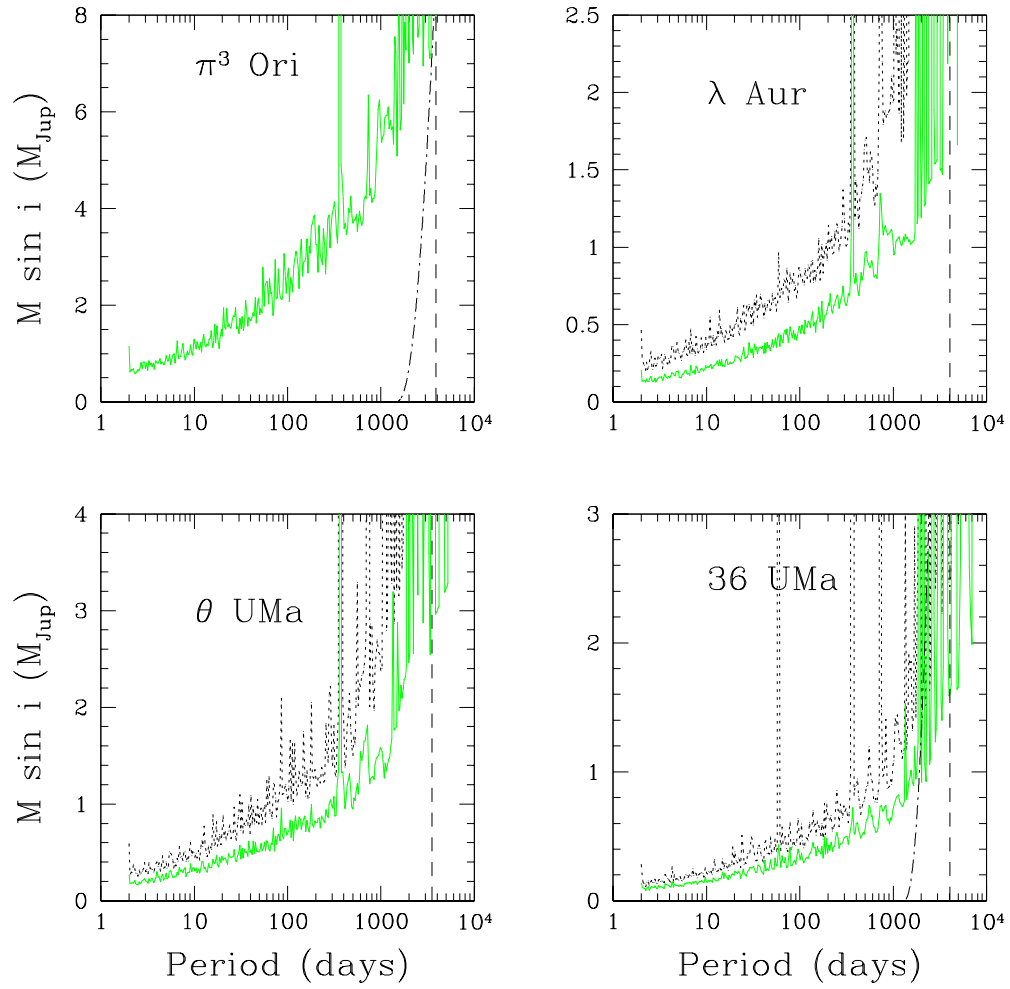


Figure 5.6 Same as Fig. 5.4, for  $\pi^3$  Ori,  $\lambda$  Aur,  $\theta$  UMa, and 36 UMa.

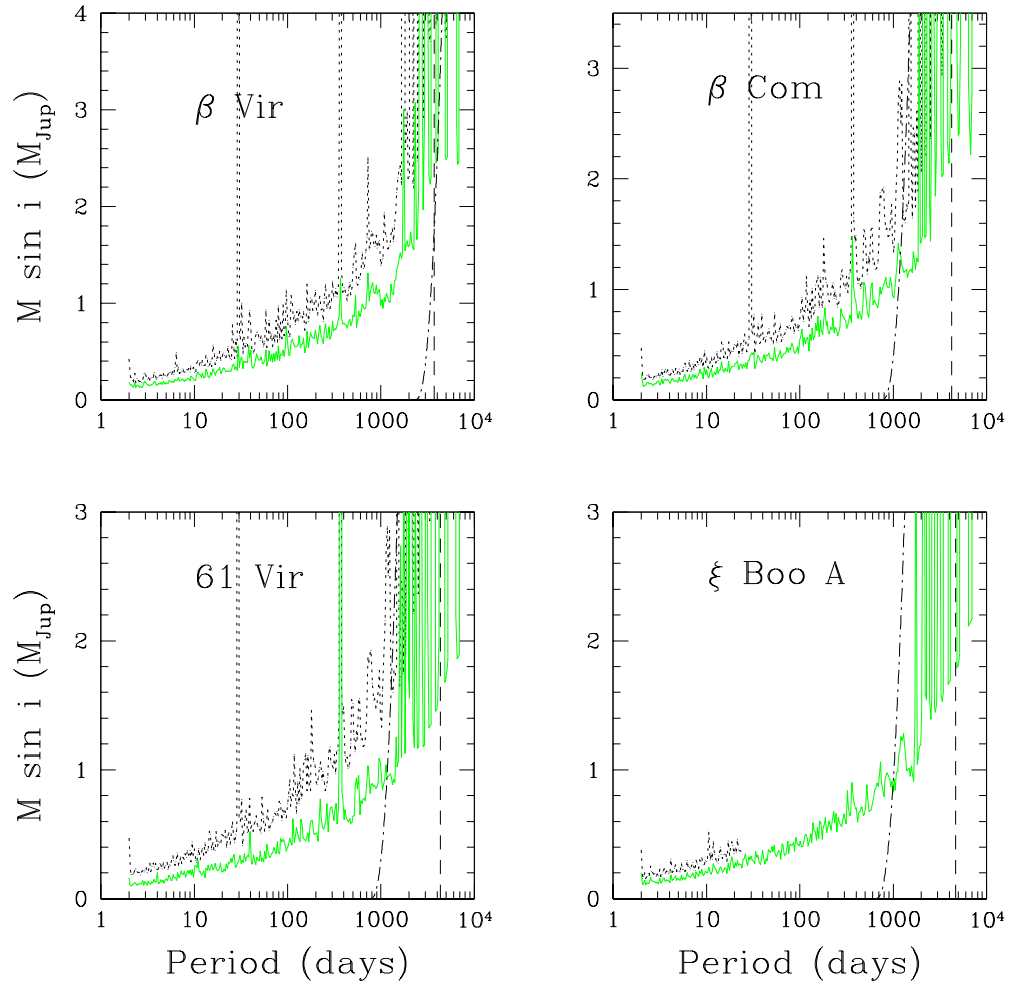


Figure 5.7 Same as Fig. 5.4, for  $\beta$  Vir,  $\beta$  Com, 61 Vir, and  $\xi$  Boo A.

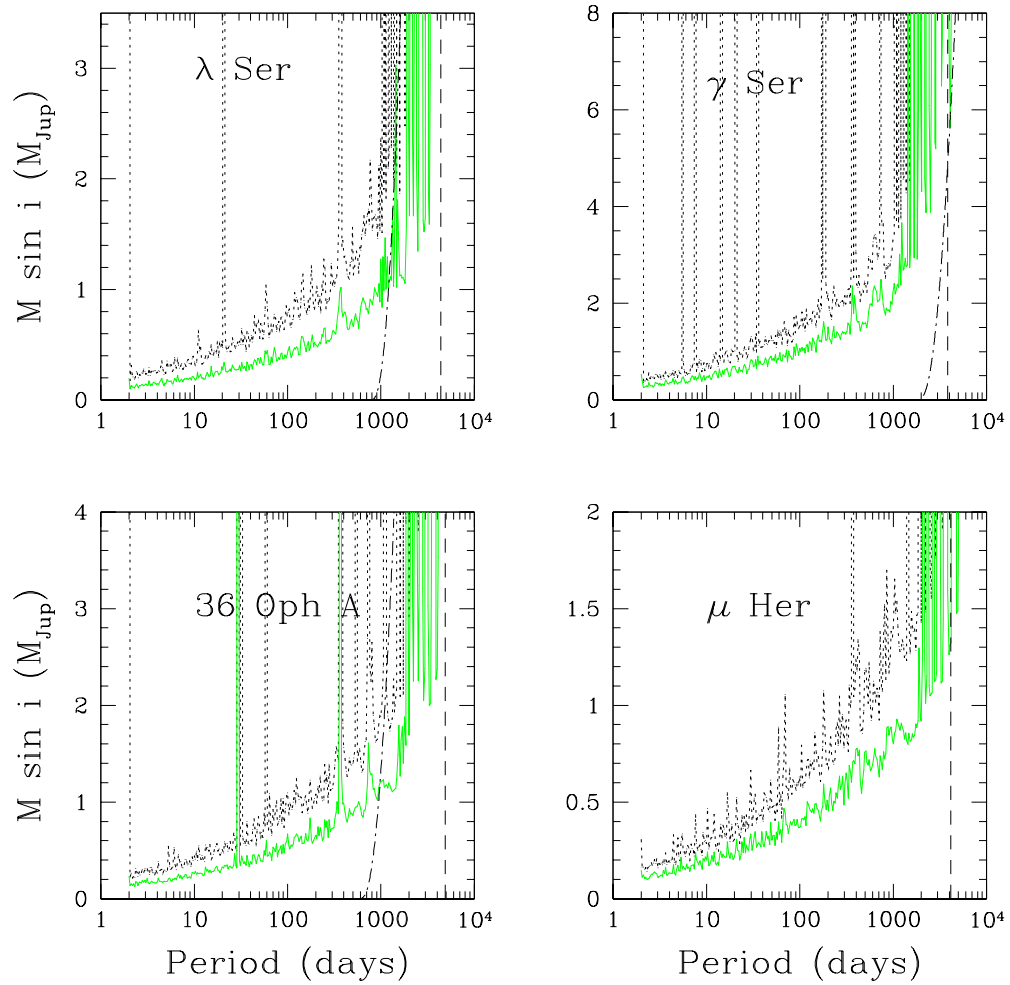


Figure 5.8 Same as Fig. 5.4, for  $\lambda$  Ser,  $\gamma$  Ser, 36 Oph A, and  $\mu$  Her.

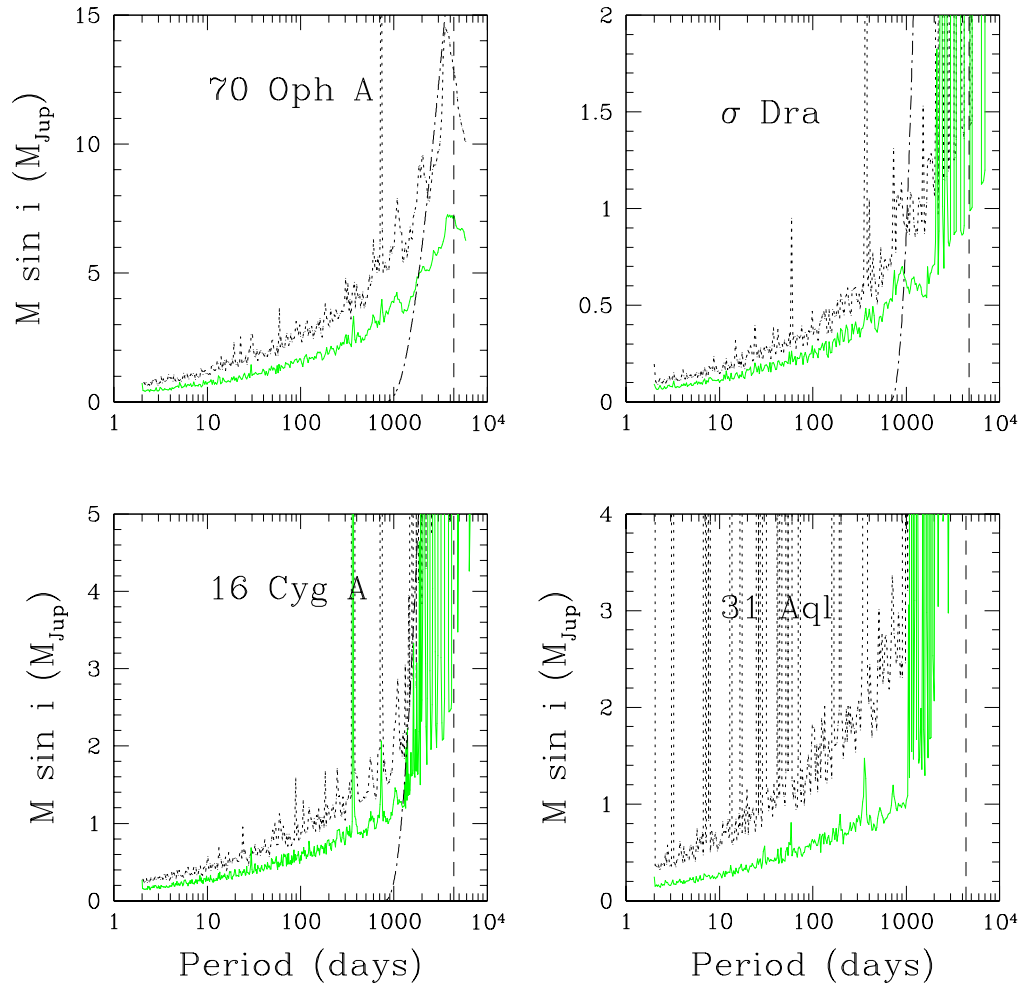


Figure 5.9 Same as Fig. 5.4, for 70 Oph A,  $\sigma$  Dra, 16 Cyg A, and  $\beta$  Aql.

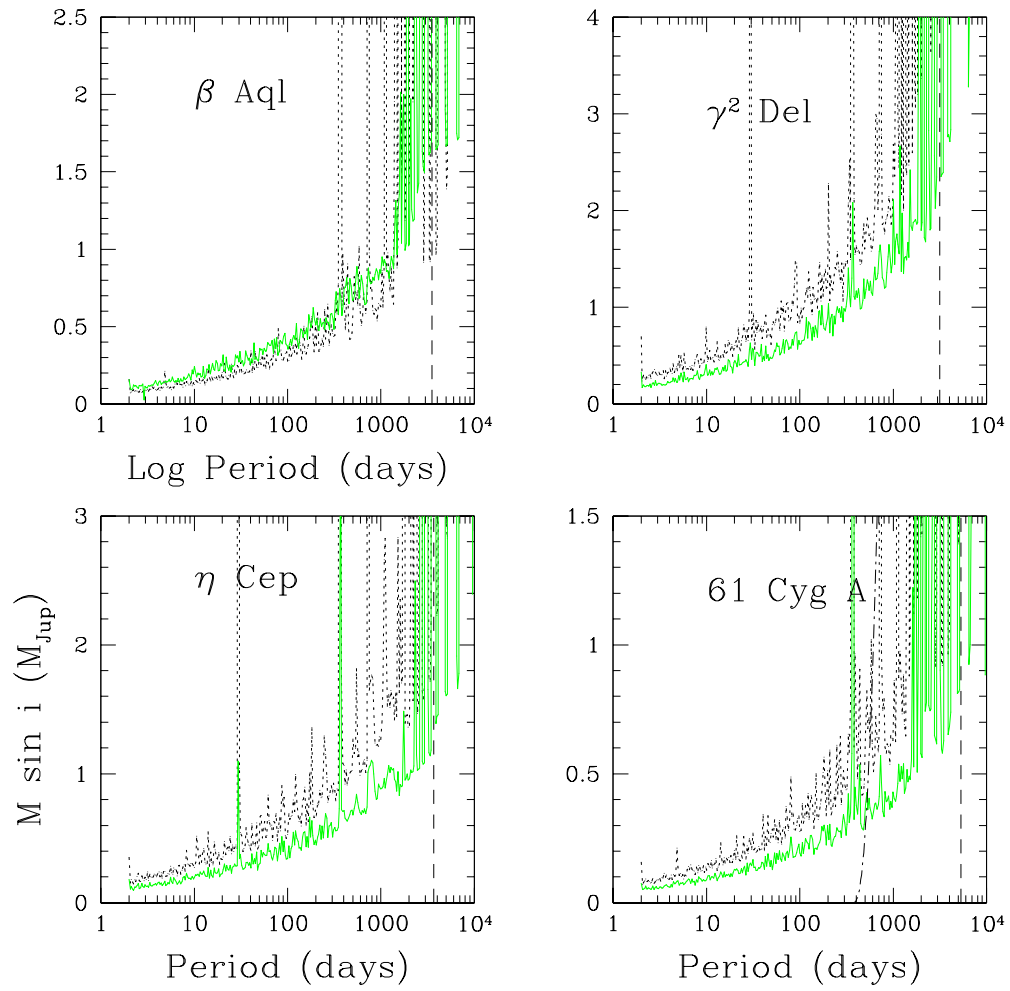


Figure 5.10 Same as Fig. 5.4, for 31 Aql,  $\gamma^2$  Del,  $\eta$  Cep, and 61 Cyg A.

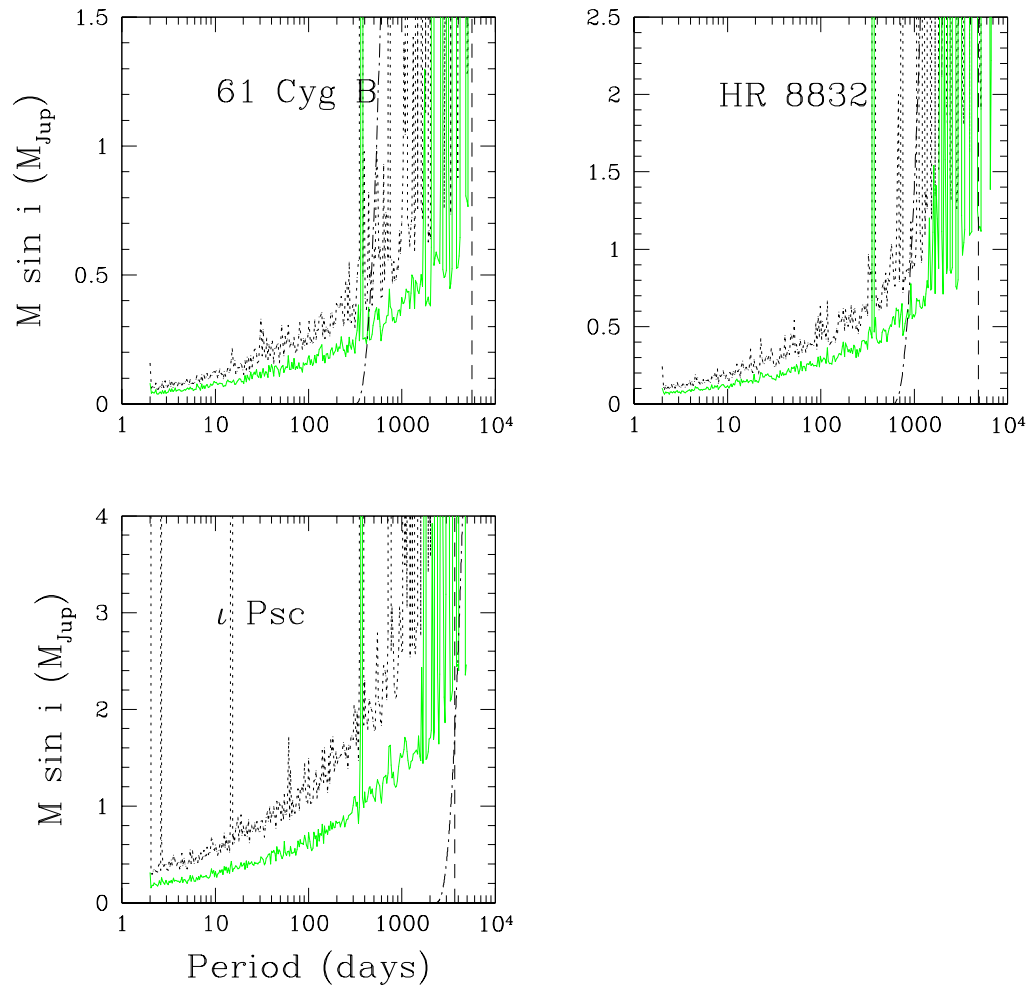


Figure 5.11 Same as Fig. 5.4, for 61 Cyg B, HR 8832, and  $\iota$  Psc.

Table 5.5. Minimum-Mass Companion Limits

Star	M sin i (M <sub>JUP</sub> ) 0.05 AU <i>e</i> = 0.0	M sin i (M <sub>JUP</sub> ) 0.1 AU <i>e</i> = 0.0	M sin i (M <sub>JUP</sub> ) 3 AU <i>e</i> = 0.6	M sin i (M <sub>JUP</sub> ) 3 AU <i>e</i> = 0.0	M sin i (M <sub>JUP</sub> ) 5.2 AU <i>e</i> = 0.6	M sin i (M <sub>JUP</sub> ) 5.2 AU <i>e</i> = 0.0
<i>η</i> Cas	0.13	0.17	1.30	0.87	2.31	1.37
<i>τ</i> Cet	0.09	0.16	1.14	0.67	1.34	0.90
<i>θ</i> Per	0.48	0.62	5.71	3.46	...	...
<i>ι</i> Per	0.12	0.16	1.46	0.95	2.70	1.69
<i>α</i> For	0.32	0.57	6.12	3.05	8.46	4.37
<i>κ</i> <sup>1</sup> Cet	0.18	0.27	2.34	1.44	3.81	2.05
<i>δ</i> Eri	0.13	0.19	2.10	1.07	12.74	1.88
<i>ο</i> <sup>2</sup> Eri	0.12	0.16	1.33	0.88	1.66	1.16
<i>π</i> <sup>3</sup> Ori	0.84	1.51	9.79	6.01	46.70	8.54
<i>λ</i> Aur	0.18	0.24	2.19	1.25	...	...
<i>θ</i> UMa	0.24	0.36	3.09	1.96	4.60	2.57
36 UMa	0.13	0.17	1.46	0.91	2.54	1.71
<i>β</i> Vir	0.16	0.23	2.49	1.57	4.19	2.61
<i>β</i> Com	0.16	0.26	1.95	1.24	3.29	2.22
61 Vir	0.14	0.20	1.62	1.16	2.58	1.69
<i>ξ</i> Boo A	0.16	0.19	2.00	1.24	2.61	1.78
<i>λ</i> Ser	0.16	0.21	2.01	1.14	...	...
<i>γ</i> Ser	0.44	0.49	4.15	2.97	10.89	5.80
36 Oph A	0.19	0.23	2.24	1.39	5.83	2.33
<i>μ</i> Her	0.14	0.21	1.53	0.96	2.55	1.52
70 Oph A	0.46	0.84	8.71	5.04	12.78	7.19
<i>σ</i> Dra	0.11	0.12	1.12	0.79	1.60	1.03
16 Cyg A	0.18	0.32	2.21	1.38	5.44	2.45
31 Aql	0.22	0.38	... <sup>a</sup>	1.90	...	...
<i>β</i> Aql	0.12	0.18	1.61	1.04	2.67	1.77
<i>γ</i> <sup>2</sup> Del	0.22	0.32	2.55	1.60	4.70	2.32
<i>η</i> Cep	0.13	0.17	2.02	0.86	2.41	1.52
61 Cyg A	0.09	0.14	1.60	0.85	2.10	0.98
61 Cyg B	0.07	0.10	1.12	0.66	1.48	0.80
HR 8832	0.11	0.14	1.65	0.81	2.56	1.14
<i>ι</i> Psc	0.26	0.38	4.35	1.85	4.91	2.64

<sup>a</sup>Too few data points for a reliable periodogram search, due to undersampling of eccentric test signals.



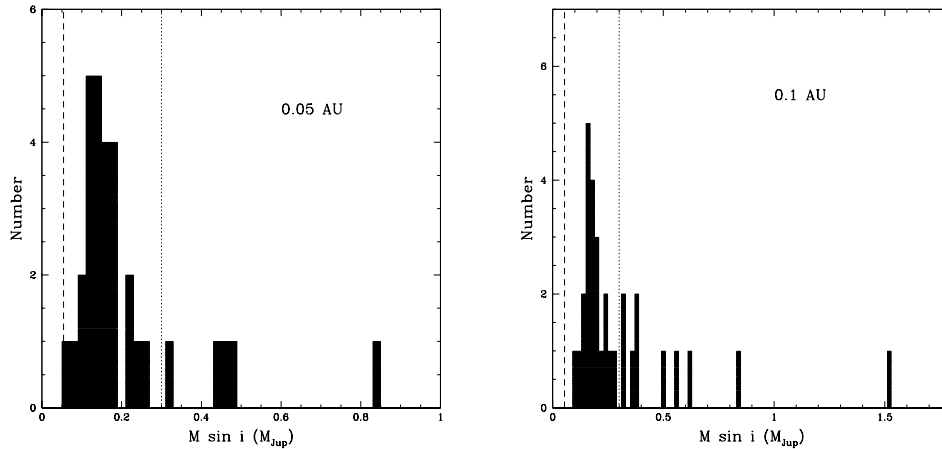


Figure 5.12 Histogram showing the  $M \sin i$  of planets ruled out at semimajor axes of 0.05 AU (left panel) and 0.1 AU (right panel). The dotted vertical line indicates the mass of Saturn, and the dashed line indicates the mass of Neptune.

described above. This process of fitting and removing the known planet occurred for *every* injected test signal. This method has the advantage of being essentially identical to the planet-search method described in Chapter 3. All data used in the fits for each planet host were subjected to the limits-determination routine, over a range of trial periods from 2 days to the full duration of the observations. The results are plotted in Figures 5.14-5.24; planets with masses above the solid line can be ruled out by the data with 99% confidence. The eccentricity of the injected test signals was chosen to be the mean eccentricity of the surviving test particles from the simulations to be described in Chapter 6. This approach was chosen because the dynamical simulations demonstrated that objects placed in circular orbits do not stay that way; the eccentricity of an undetected low-mass planet is expected to be influenced to nonzero values by the known giant planet. These limits determinations were also performed using test signals with  $e = 0$ , and the results are nearly identical. Results from the circular case are shown as a dotted line in Fig. 5.14 for HD 3651 only, for reasons of clarity.

Though the limits determinations tested a large range of periods, it happened for all targets that periods longer than about 400 days were undetectable by this method, despite the  $\sim 10$  yr duration of high-quality data now available. It is important to note that the limits presented here represent the companions that can

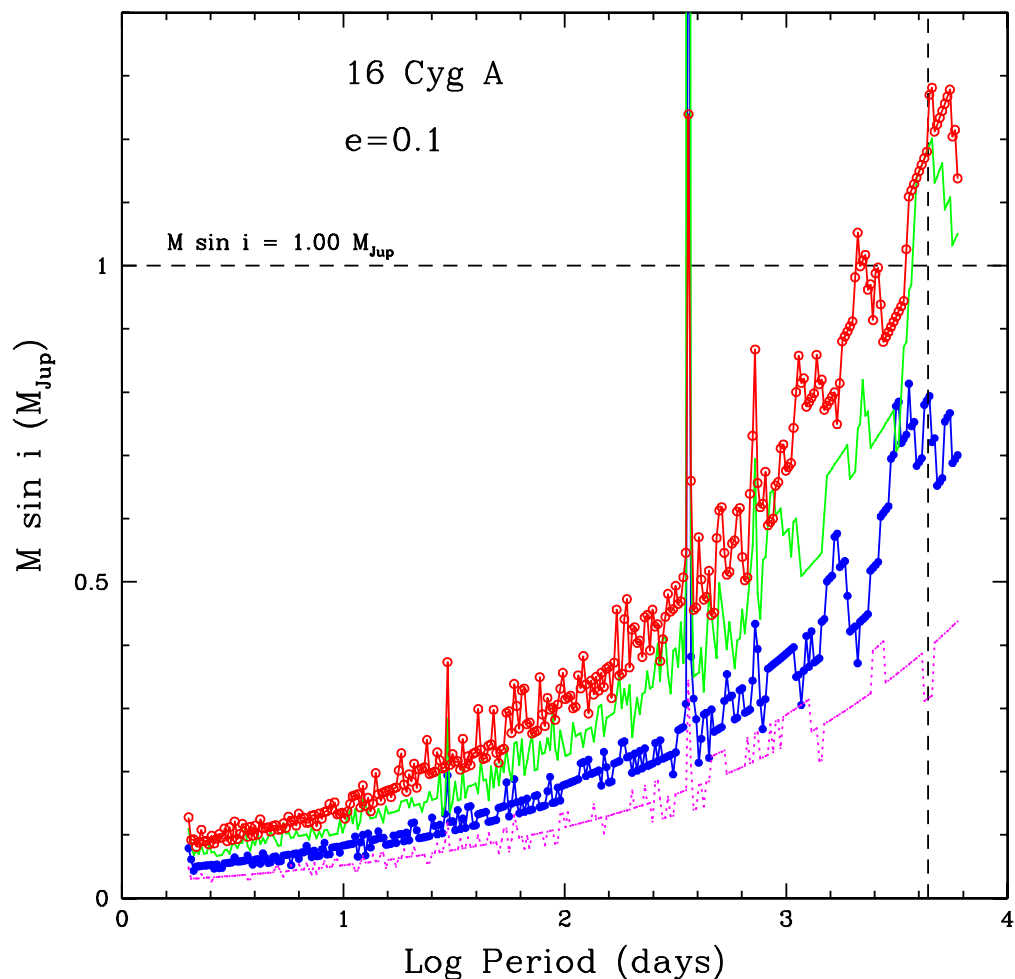


Figure 5.13 Planetary companion limits for 16 Cyg A, using simulated data matching our observation times, but with an rms of  $14 \text{ m s}^{-1}$  (red, open circles),  $11 \text{ m s}^{-1}$  (green, solid line),  $8 \text{ m s}^{-1}$  (blue, filled circles) and  $5 \text{ m s}^{-1}$  (magenta, dotted line). The vertical dashed line indicates the 11.87 yr orbital period of Jupiter. Planets in the parameter space above the plotted points are excluded at the 99.9% confidence level. This shows that a Jupiter analog could be ruled out at the 99.9% level with a sufficiently long baseline of data similar in quality to the McDonald Observatory Phase III.

be ruled out by the data with 99% confidence. Lower-mass planets could have been detected in this survey, but not necessarily at all (or 99% of all) possible configurations. Throughout this section, “detectable” thus refers to those planets which would have been detected with  $\text{FAP} < 0.1\%$  in 99% of trials. One weakness of this limits-determination method is that the injected signal can have undue influence on the parameters of the established planet(s). At this time, unfortunately, the Gauss-Fit model does not have the ability to restrict the range of a free parameter. This effect proved most problematic for longer periods and larger-amplitude test signals. For this reason, the results given in this chapter are best applied in the short-period regime ( $P \lesssim 100$  days).

These computations show that 99% of Neptune-mass planets in periods less than about 10 days could have been detected in the HD 3651 and HD 108874 systems. For all of the systems, the limits shown in Figures 5.14-5.24 exhibit some “blind spots” evident where the periodogram method failed to recover the injected signals with  $\text{FAP} < 0.1\%$ . Typically this occurs at certain trial periods for which the phase coverage of the observational data is poor, and often at the 1-month and 1-year windows. The window function for HD 3651 is shown in Figure 5.14 as an example of the correlation between the observing window and detection limits. Using this method of fitting the known planet for each trial planet, such regions of ignorance are also present at periods close to that of the existing planet. For HD 8574 (Fig. 5.15), only the region  $P < 225$  days is shown, since the period of HD 8574b is 226 days, and longer-period objects were completely undetectable by this method. In the HD 10697 system, planets down to about 2 Neptune masses were detectable with  $P \lesssim 10$  days (Figure 5.15). For HD 19994 (Figure 5.16, the scatter about the 1-planet fit was too large to permit tight limits determination, despite the large number of independent epochs observed by the HET ( $N=56$ ). While all targets in this study had about 3 yr of high-precision HET data, the quality of the detection limits achieved is highly variable. Table 5.6 and Table 5.7 summarize the results of the detection limits computations, and the characteristics of the data used for these targets. An investigation of the factors which influence the limits determinations is given in § 5.3.

In the HD 23596 (Fig. 5.16), HD 28185 and HD 38529 (Fig. 5.17) systems, the detection limits reach 2-3 Neptune masses for periods shorter than  $P \lesssim 10$  days. In the same region of the HD 40979 system, Saturn-mass planets ( $0.3 M_{\text{Jup}}$ ) could

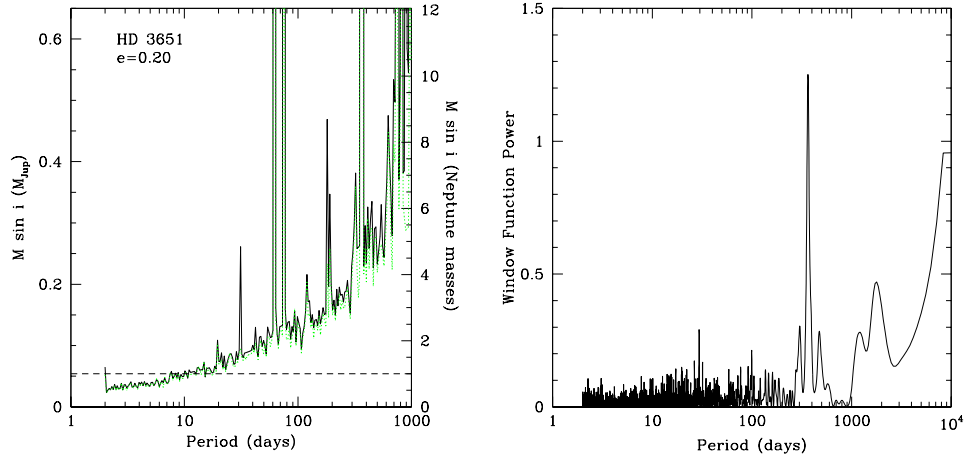


Figure 5.14 Left panel: Detection limits for additional planets in orbits with  $e = 0.20$  in the HD 3651 system. Planets in the parameter space above the plotted points are excluded at the 99% confidence level. The horizontal dashed line indicates the mass of Neptune. Right panel: Window function for the HD 3651 observations. Note the peaks near periods of 1 month and 1 year.

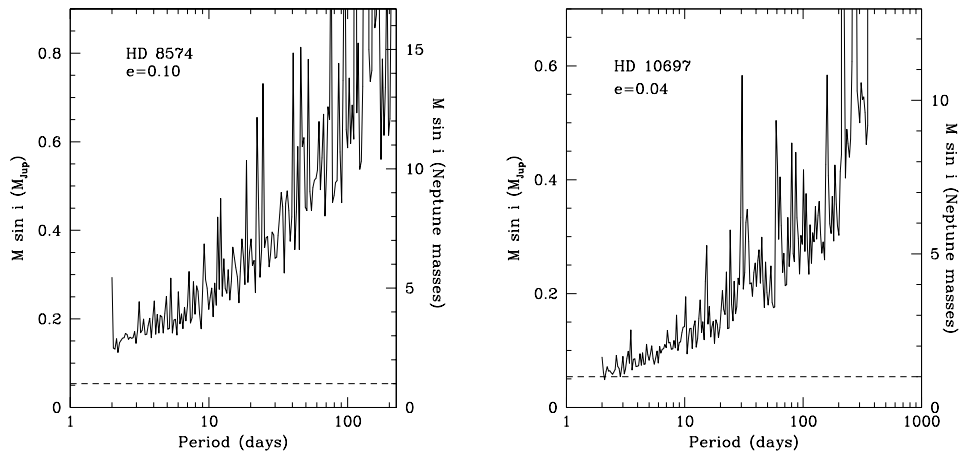


Figure 5.15 Left panel: Detection limits for additional planets in orbits with  $e = 0.10$  in the HD 8574 system. Planets in the parameter space above the plotted points are excluded at the 99% confidence level. The horizontal dashed line indicates the mass of Neptune. Right panel: Same, but for planets with  $e = 0.04$  in the HD 10697 system.

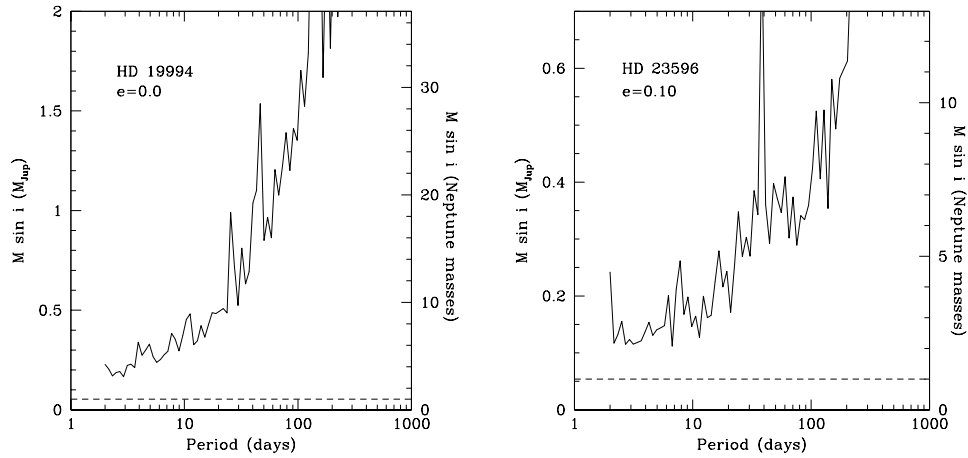


Figure 5.16 Left panel: Detection limits for additional planets in orbits with  $e = 0.0$  in the HD 19994 system. Planets in the parameter space above the plotted points are excluded at the 99% confidence level. The horizontal dashed line indicates the mass of Neptune. Right panel: Same, but for planets with  $e = 0.10$  in the HD 23596 system.

have been detected. Despite a very large amount of high-quality data, the results for HD 38529 fell short of expectations. This may be because the outer planet, with a period of 2153 days, was not sufficiently constrained by the data (which cover  $\sim 1.5$  cycles), and so the addition of test signals may have prevented convergence of the 2-planet model. The results for HD 74156 are similar, and the architecture of this system is much like that of HD 38529.

The limits-detection algorithm performed abominably for the HD 72659 system (Fig. 5.18), despite the relatively small rms ( $6.5 \text{ m s}^{-1}$ ) about the 1-planet fit. This outcome is probably due to the fact that the period of HD 72659b is very nearly the total duration of observations, and so perturbations to that signal (by the test planet) were enough to cause convergence failures in the GaussFit model. The highly eccentric systems HD 80606 and HD 89744 are shown in Fig. 5.19 and Fig. 5.20. For HD 89744, only the range  $P < 100$  days is shown, as more distant objects are dynamically excluded (Wittenmyer et al. 2007b).

Figures 5.20-5.21 show the results for the 47 UMa and HD 106252 systems. There are numerous “jagged” regions—periods at which the test signals were completely undetectable—distributed across the range of periods explored. This is a

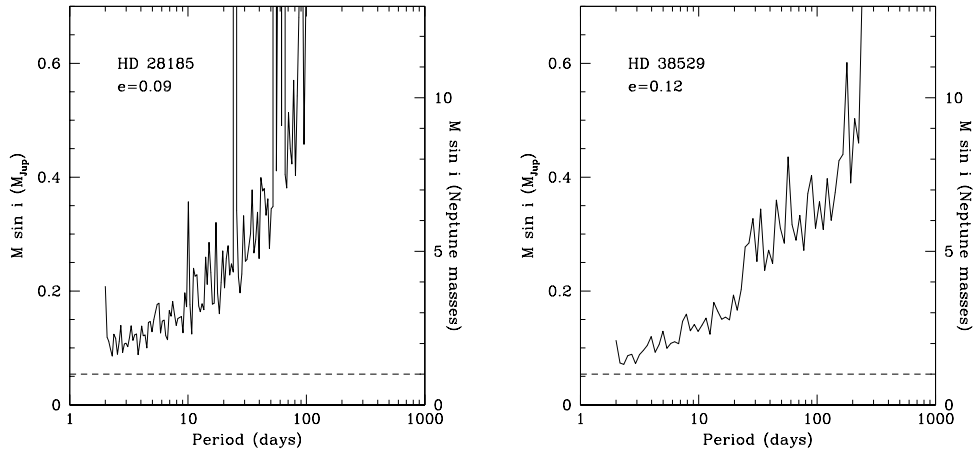


Figure 5.17 Left panel: Detection limits for additional planets in orbits with  $e = 0.09$  in the HD 28185 system. Planets in the parameter space above the plotted points are excluded at the 99% confidence level. The horizontal dashed line indicates the mass of Neptune. Right panel: Same, but for planets with  $e = 0.12$  in the HD 38529 system.

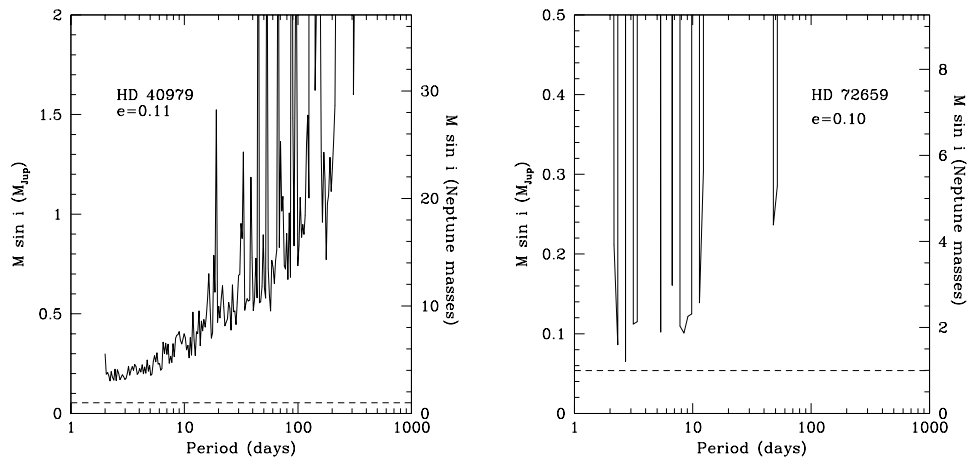


Figure 5.18 Left panel: Detection limits for additional planets in orbits with  $e = 0.11$  in the HD 40979 system. Planets in the parameter space above the plotted points are excluded at the 99% confidence level. The horizontal dashed line indicates the mass of Neptune. Right panel: Same, but for planets with  $e = 0.10$  in the HD 72659 system.

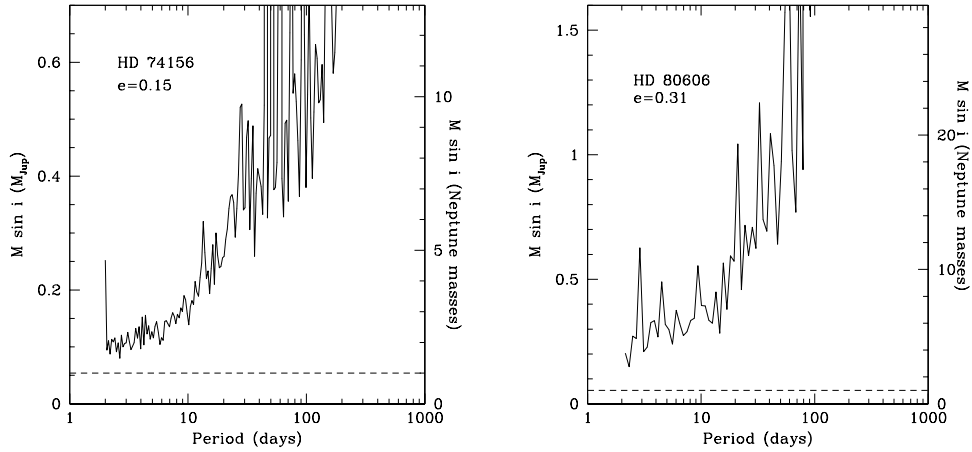


Figure 5.19 Left panel: Detection limits for additional planets in orbits with  $e = 0.15$  in the HD 74156 system. Planets in the parameter space above the plotted points are excluded at the 99% confidence level. The horizontal dashed line indicates the mass of Neptune. Right panel: Same, but for planets with  $e = 0.31$  in the HD 80606 system.

mystery, as there is no physical reason why a planet with, e.g.  $P = 6.29$  days should be detectable while one with  $P = 6.54$  days should not. HD 190228 (Fig. 5.24) also exhibits this behavior. One possible explanation for these results is that the sampling of the observations was poorly distributed in phase for many of the injected test signals, making significant recovery by the periodogram method difficult. Attempts to address problematic results such as these are discussed further in § 5.3.

Keplerian fits proved inadequate for the HD 128311 system, as discussed in § 3.1, so the limit-determination method described in this section would be inappropriate. At a practical level, the Keplerian limits-determination method would have extreme difficulty fitting the two known planets in the presence of any additional signals, and the results would be less than illuminating. Figure 5.22 shows the results from the non-Keplerian limits determination described in § 5.1, for  $e = 0.0$  and  $e = 0.6$ . A test particle simulation was not run for HD 128311 due to the uncertainties in constraining the system parameters, and the amount of time required. However, given the relatively low eccentricities of test particles in the remaining systems, the choice of  $e = 0.6$  is a conservative one. For the HD 130322 system, the Keplerian limits-determination method failed to recover the injected signals at all

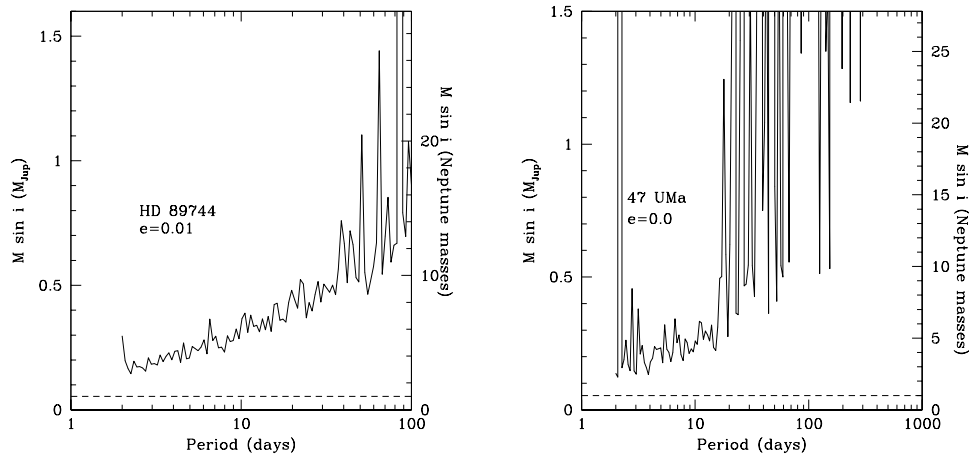


Figure 5.20 Left panel: Detection limits for additional planets in orbits with  $e = 0.01$  in the HD 89744 system. Planets in the parameter space above the plotted points are excluded at the 99% confidence level. The horizontal dashed line indicates the mass of Neptune. Right panel: Same, but for planets with  $e = 0.0$  in the 47 UMa system. Remaining test particles had a mean eccentricity of  $e = 0.02$ , but the limits calculations could not finish by the time of writing.

periods, even when the tolerance was relaxed to accept recovery of periods within 10% of the injected period. Holding the offsets between data sets fixed at the best-fit values also had the same result. The results shown for HD 130322 in Fig. 5.23 are also from the non-Keplerian method described in § 5.1.

### 5.3 Lessons Learned

The main question to arise from the limits determinations presented here is: How can we do better? More directly, why can the current data rule out 99% of hot Neptunes for only a few targets (Figure 5.25), and how can future surveys of this nature be designed to improve upon the detectability statistics given here? Table 5.7 summarizes the relevant data from the detection-limit computations. The median velocity semi-amplitude  $K$  ( $= \tilde{K}$ ) ruled out by the limits-detection algorithm was used as the metric for determining the “quality” of the derived limits; a smaller  $K$  implies tighter limits on undetected planets. This median value was determined by ignoring all periods for which a limit was not successfully obtained (i.e. when the



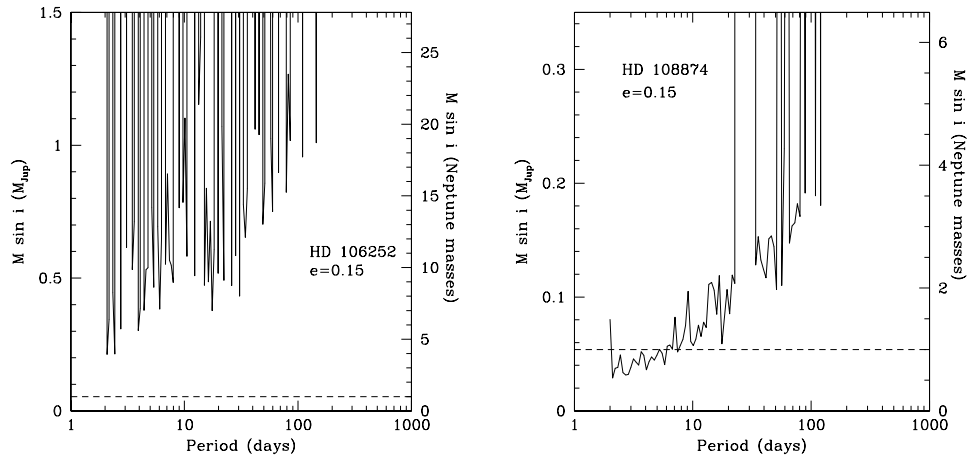


Figure 5.21 Left panel: Detection limits for additional planets in orbits with  $e = 0.15$  in the HD 106252 system. Planets in the parameter space above the plotted points are excluded at the 99% confidence level. The horizontal dashed line indicates the mass of Neptune. Right panel: Same, but for planets with  $e = 0.15$  in the HD 108874 system.

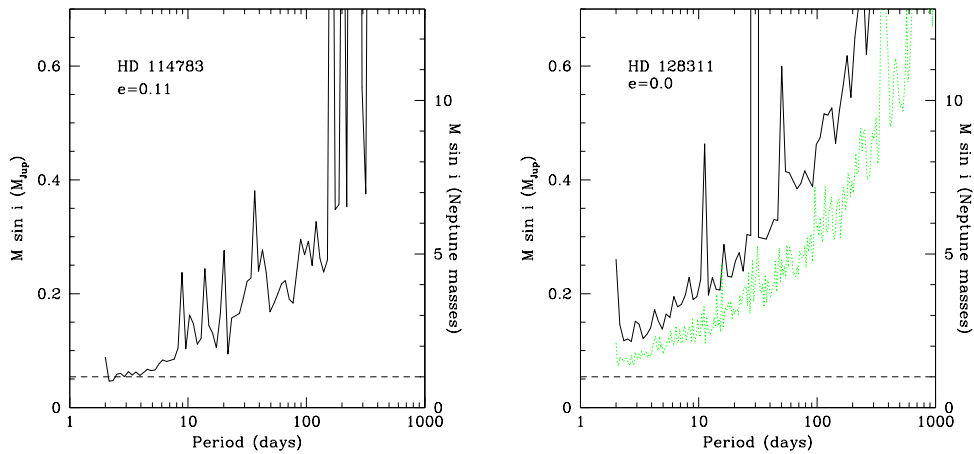


Figure 5.22 Left panel: Detection limits for additional planets in orbits with  $e = 0.11$  in the HD 114783 system. Planets in the parameter space above the plotted points are excluded at the 99% confidence level. The horizontal dashed line indicates the mass of Neptune. Right panel: Same, but for planets with  $e = 0.0$  in the HD 128311 system. For HD 128311, the method described in § 5.1 was used, wherein the test signals are added to a fixed residuals file.

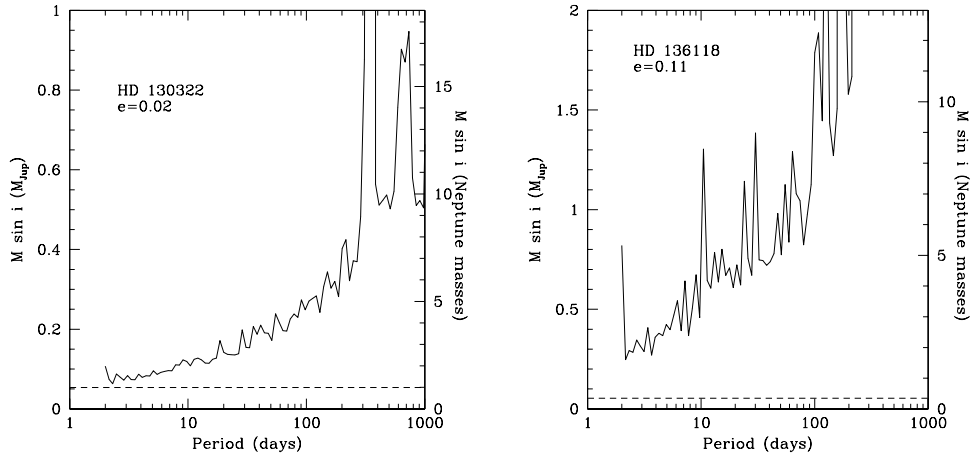


Figure 5.23 Left panel: Detection limits for additional planets in orbits with  $e = 0.02$  in the HD 130322 system. The horizontal dashed line indicates the mass of Neptune. Planets in the parameter space above the plotted points are excluded at the 99% confidence level. For HD 130322, the method described in § 5.1 was used, wherein the test signals are added to a fixed residuals file. Right panel: Same, but for planets with  $e = 0.11$  in the HD 136118 system.

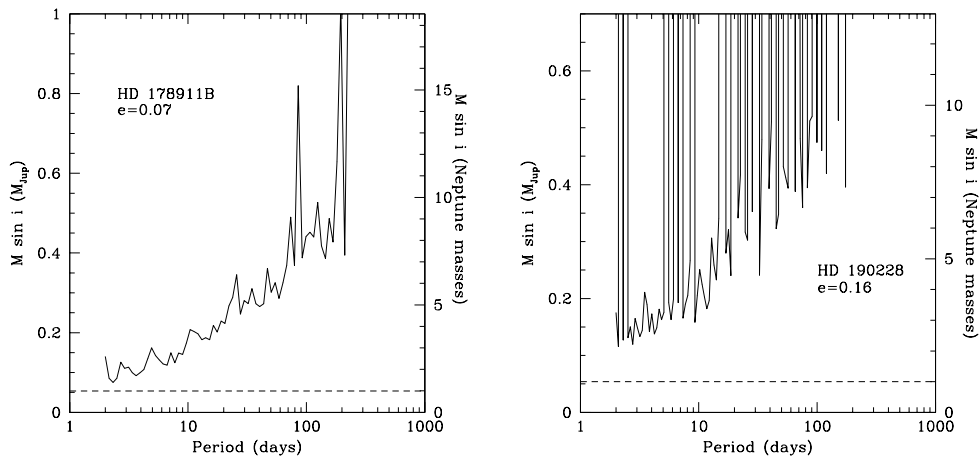


Figure 5.24 Left panel: Detection limits for additional planets in orbits with  $e = 0.07$  in the HD 178911B system. Planets in the parameter space above the plotted points are excluded at the 99% confidence level. The horizontal dashed line indicates the mass of Neptune. Right panel: Same, but for planets with  $e = 0.16$  in the HD 190228 system.

Table 5.6. Minimum-Mass Companion Limits

Star	Eccentricity	M sin i ( $M_{\text{Jup}}$ ) 0.05 AU	M sin i ( $M_{\text{Jup}}$ ) 0.1 AU
HD 3651	0.20	0.035	0.053
HD 8574	0.10	0.157	0.281
HD 10697	0.04	0.072	0.138
HD 19994	0.00	0.229	0.373
HD 23596	0.10	0.121	0.165
HD 28185	0.09	0.121	0.226
HD 38529	0.12	0.096	0.141
HD 40979	0.11	0.197	0.342
HD 72659	0.10	0.115	0.139
HD 74156	0.15	0.132	0.178
HD 80606	0.31	0.269	0.334
HD 89744	0.01	0.180	0.324
47 UMa	0.02	0.188	0.312
HD 106252	0.15	0.387	0.509
HD 108874	0.15	0.043	0.071
HD 114783	0.11	0.067	0.121
HD 128311	0.00	0.100	0.128
HD 130322	0.02	0.083	0.123
HD 136118	0.11	0.270	1.304
HD 178911B	0.07	0.099	0.203
HD 190228	0.16	0.148	0.266

maximum allowed  $K$  was reached). The median was chosen since the maximum  $K$  attempted in these calculations was not uniform across all targets, ranging from 100-200  $\text{m s}^{-1}$ . Choosing the median avoids biases created when for example, a limit is successfully determined at a very large  $K$  just shy of the maximum. It would be most useful to derive a relationship between the characteristics of a data set and the quality of the detection limits which can be obtained from it. Figure 5.26 shows the  $\tilde{K}$  values plotted against various combinations of the number of data points  $N$ , mean uncertainty  $\bar{\sigma}$ , and the RMS about the orbital solution. Error bars are the standard error of the median, which is approximately  $\sqrt{(\pi/2)}\sigma_{\bar{x}}$  for  $N \gtrsim 30$ . It is reasonable to expect that the detection limits will improve (smaller median  $K$ ) as the RMS and  $\bar{\sigma}$  get smaller, and as  $N$  gets larger. However, as we see in Figure 5.26, the quality of limits has little if any relation to  $N$ . The expected relationships are evident for  $\bar{\sigma}$  and RMS: higher values of each of these quantities generally result in worse limits. Somewhat tighter relationships occur in the right-hand panels of Figure 5.26. Based on this result, one can parameterize the quality of limits by a relation of the form

$$\tilde{K} \propto \bar{\sigma}^\alpha \text{RMS}^\beta \quad (5.6)$$

For these relations, as plotted in Figure 5.26, there are five distinct outliers: 47 UMa, HD 40979, HD 80606, HD 106252, and HD 136118. However, the error of the median  $K$  for each of these is large, and so they receive little weight when these data are fit. A linear fit to the data shown in Fig. 5.26 gives the following relation:

$$\tilde{K} = 4.27 + 0.15(\text{RMS} \times \bar{\sigma}) \quad (5.7)$$

The rms scatter about this fit is  $9.6 \text{ m s}^{-1}$ , and the mean uncertainty of  $\tilde{K}$  is  $13.5 \text{ m s}^{-1}$ . The fit and data are shown in Figure 5.27.

It would also be profitable if the quality of detection limits could be estimated *a priori*, before obtaining a large number of radial-velocity measurements. Figures 5.28-5.29 plot  $\tilde{K}$  against the stellar parameters given in Table 2.1. There does not appear to be a simple relationship between any one stellar characteristic and the radial-velocity detection sensitivity obtained by our method.

One possible reason for the disappointing performance of the limit-determination method was mentioned earlier in this chapter: the addition of a test Keplerian signal can change the shape of the known planet's radial-velocity orbit in unexpected ways.

Table 5.7. Statistics of Detection Limits

Star	mean $K$ ruled out	median $K$ ruled out	$N$	$\bar{\sigma}$ m s <sup>-1</sup>	RMS m s <sup>-1</sup>
HD 3651	7.9	6.1	202	3.95	7.1
HD 8574	29.4	23.9	128	9.54	15.2
HD 10697	12.8	11.1	131	5.28	9.9
HD 19994	42.0 <sup>a</sup>	32.1	115	6.19	15.8
HD 23596	17.8	16.8	107	8.34	10.1
HD 28185	19.3	18.0	89	6.63	11.2
HD 38529	12.1	11.3	245	4.88	11.9
HD 40979	41.3	31.6	160	11.40	20.6
HD 72659	14.7	12.0	91	6.50	6.5
HD 74156	18.8	17.0	180	7.60	11.8
HD 80606	50.3	44.0	130	9.48	13.5
HD 89744	23.3	22.2	93	10.05	14.3
47 UMa	32.2 <sup>a</sup>	23.3	250	5.87	10.1
HD 106252	56.1	46.6	110	9.57	12.4
HD 108874	20.1	7.8	89	5.04	3.8
HD 114783	18.3	12.5	88	3.81	4.9
HD 128311	16.6 <sup>b</sup>	15.3	158	2.55	18.3
HD 130322	14.8 <sup>c</sup>	12.7	47	5.96	7.6
HD 136118	50.8	45.2	108	9.89	14.4
HD 178911B	18.0	16.5	107	8.34	11.4
HD 190228	14.5	14.1	101	7.76	9.2

<sup>a</sup> $e = 0.00$ .

<sup>b</sup>Non-Keplerian limits,  $e = 0.00$ .

<sup>c</sup>Non-Keplerian limits,  $e = 0.02$ .

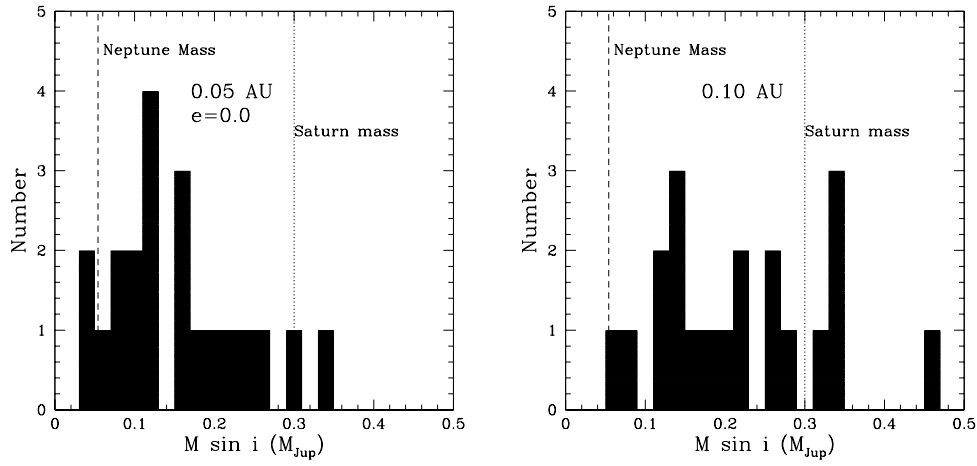


Figure 5.25 Histogram showing the  $M \sin i$  of planets ruled out at semimajor axes of 0.05 AU (left panel) and 0.1 AU (right panel). The dotted vertical line indicates the mass of Saturn, and the dashed line indicates the mass of Neptune. The results for 0.05 AU are for circular orbits only, consistent with observational evidence that close-in planets have small eccentricities.

Attempts to fit the original planet would then either converge on wildly inaccurate solutions or crash outright. While the Gaussfit model cannot restrict the range of a free parameter, one can hold the offsets (“gammas”) between data sets fixed, which may prevent the added signals from being “absorbed” in the gammas, and thus may improve the quality of the derived limits.

Figure 5.30 shows the effect of this change for 47 UMa, a target which has a large amount of data ( $N=250$ ), and uncertainties and an RMS which are not particularly egregious ( $\bar{\sigma} = 5.9 \text{ m s}^{-1}$ ,  $\text{RMS}=10.1 \text{ m s}^{-1}$ ). Holding the gammas fixed at the best-fit values, the median  $K$  which can be ruled out drops from  $27.6 \text{ m s}^{-1}$  to  $23.3 \text{ m s}^{-1}$ . Figure 5.30 also shows the results from the non-Keplerian limits-determination method as described in § 5.1; this method is equivalent to holding all parameters for the known planet fixed. For all three cases, the test signals had  $e = 0.0$  for two reasons: 1) a factor 10 increase in computation speed, and 2) test particles remaining after 10 Myr in the 47 UMa system had a very small mean eccentricity  $\langle e \rangle = 0.02$ . There is a marginal improvement by holding the gamma offsets fixed, but not enough to bring 47 UMa in line with the majority of points in the relations plotted in Fig. 5.26. The topmost (solid) line in Fig. 5.30 represents the most

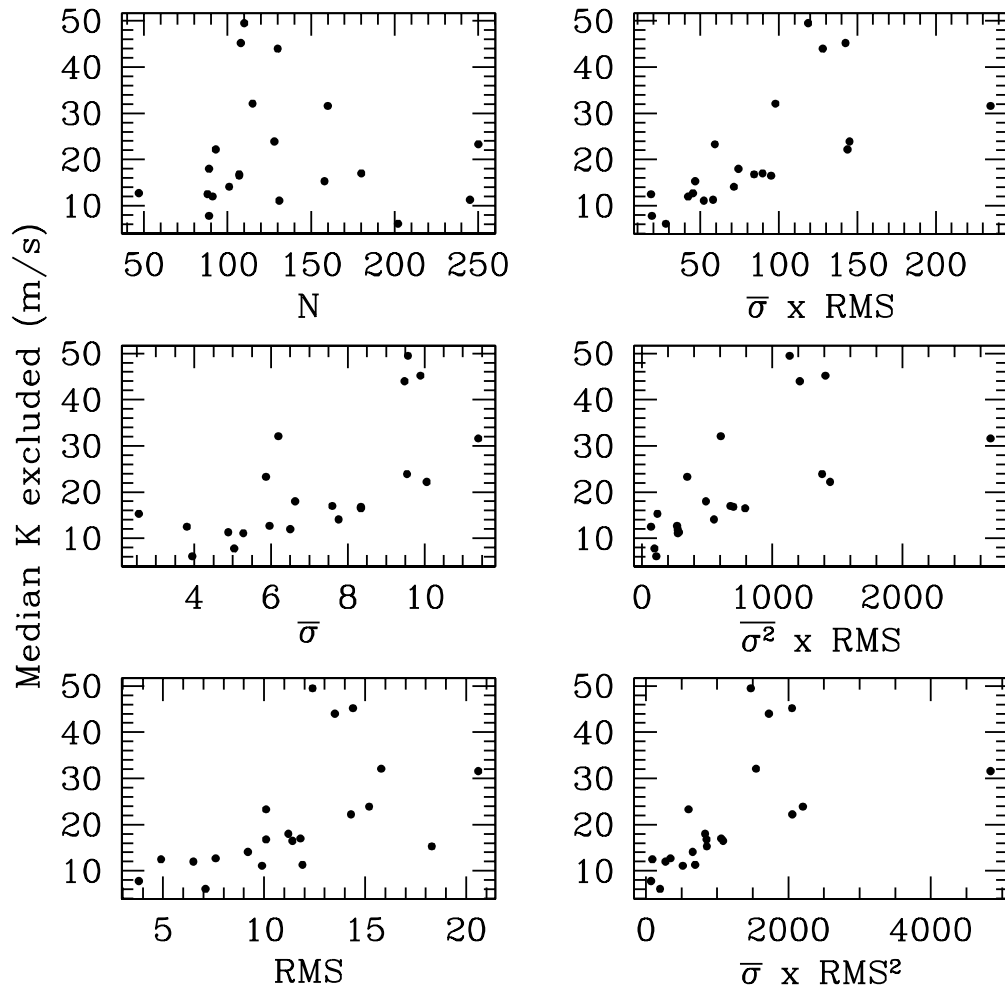


Figure 5.26 Median  $K$  for planetary companions which can be ruled out by these data, plotted against various combinations of the characteristics of the data.

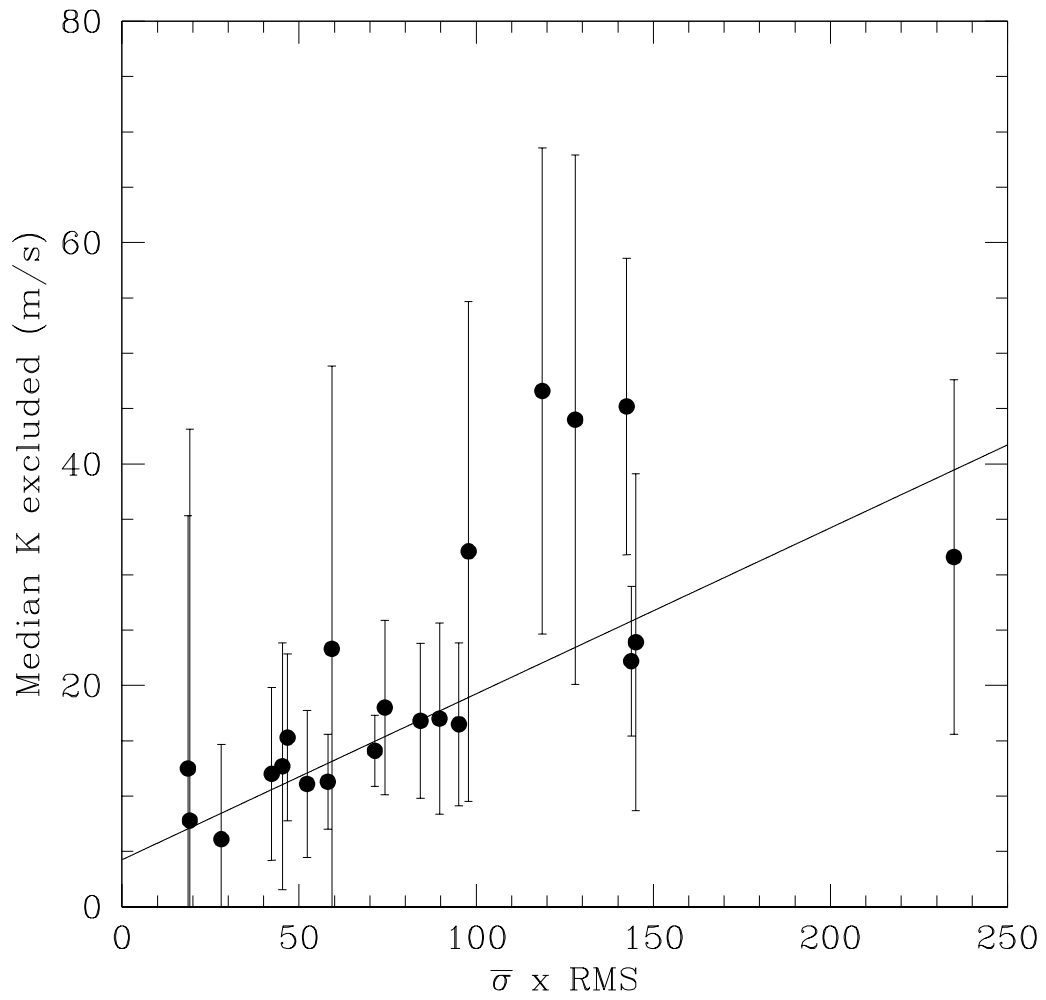


Figure 5.27 Linear fit of the median  $K$  which can be excluded versus the product  $\bar{\sigma} \times \text{RMS}$  of the input data.



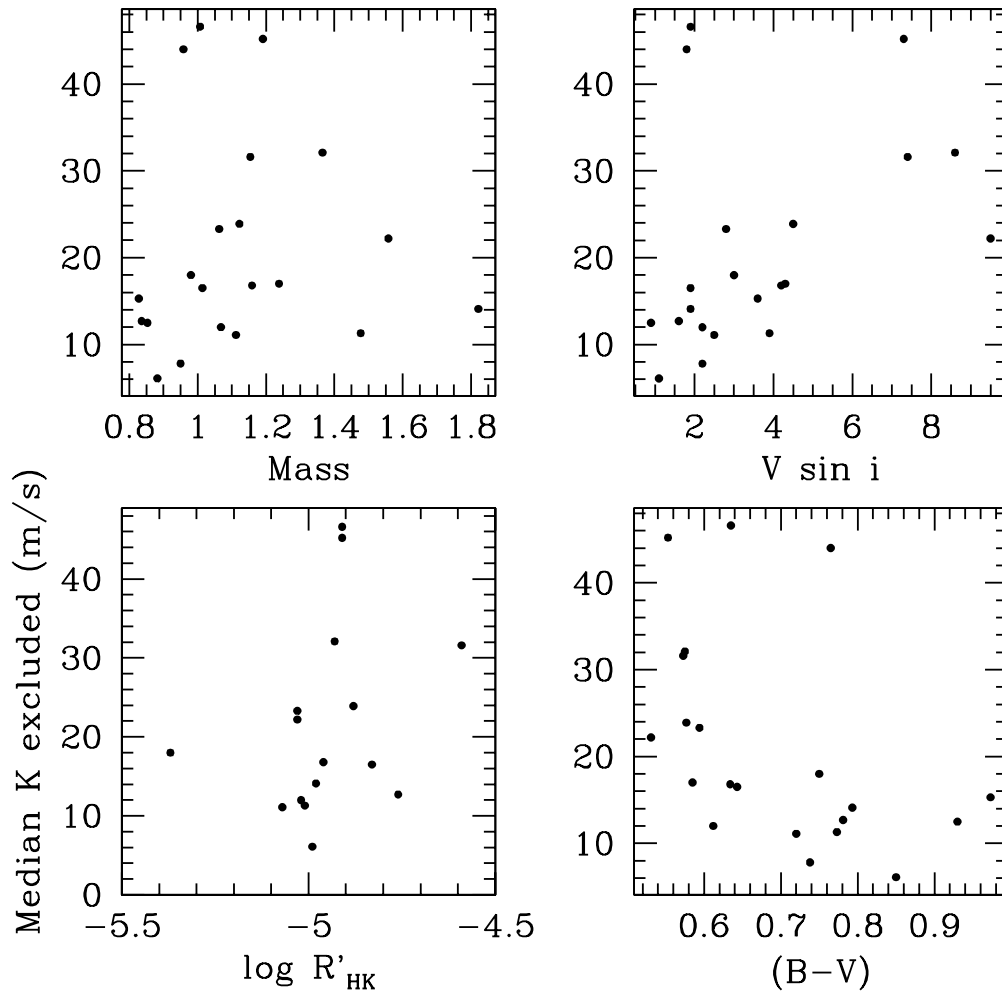


Figure 5.28 Median  $K$  as a function of various intrinsic stellar parameters.

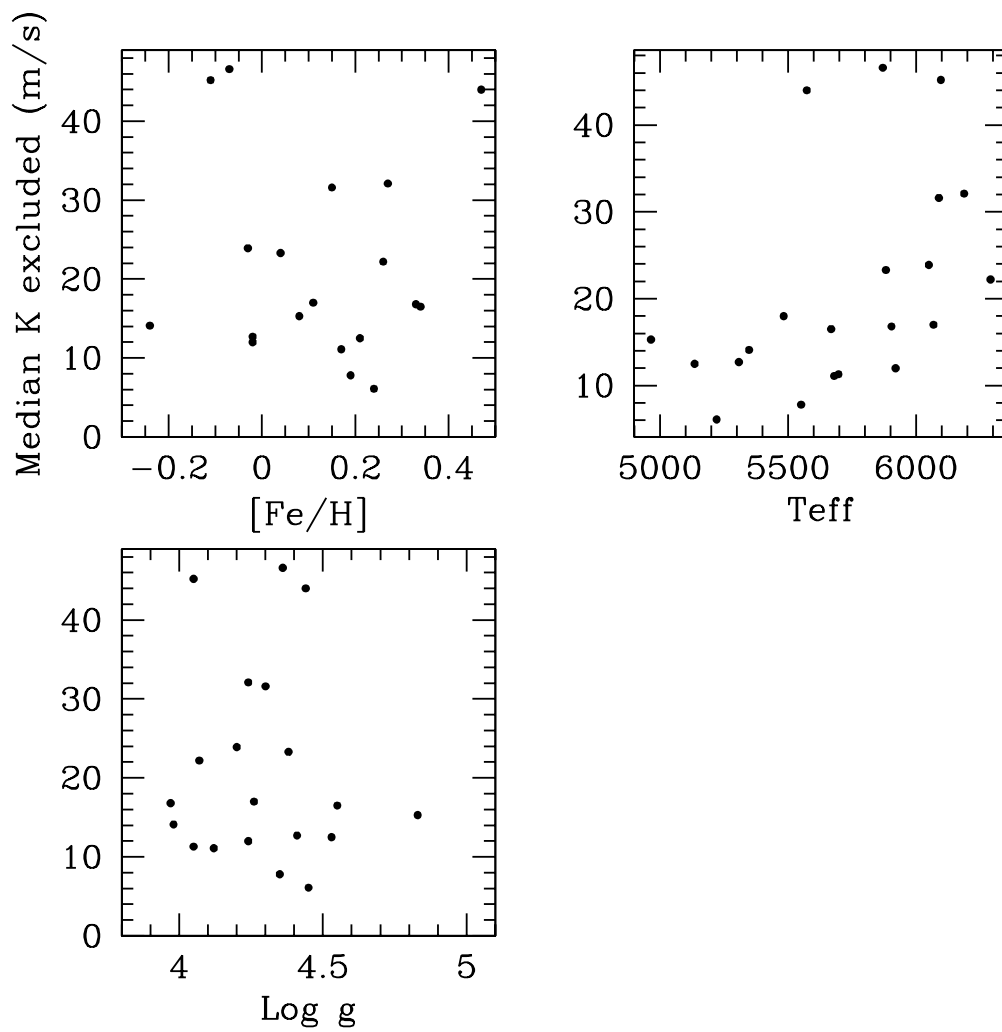


Figure 5.29 Median  $K$  as a function of various intrinsic stellar parameters.

conservative approach: where an unknown planet is allowed to have unlimited effect on the known planet’s radial-velocity signature. While conservatism is appealing in science, this particular example is not physically realistic. Examination of the values taken on by the parameters of 47 UMa b from this comparison immediately reveals some heinous iniquities: the period ( $P = 1077.2 \pm 2.1$  days) ranges from 500-2000 days, and the eccentricity ( $e = 0.027 \pm 0.023$ ) commonly takes on values greater than 0.5. Some injected trial periods caused the GaussFit model to crash, meaning that an eccentricity  $e > 1$  was reached in the iteration process, rendering the resulting residuals file meaningless. Holding the velocity offsets between each data set as fixed (dashed line in Fig. 5.30) gives similar results. The case where all of the parameters for the known planet are fixed (dotted line in Fig. 5.30) gives tight limits more consistent with expectations for a target as well-observed as 47 UMa. However, the underlying assumption that any undetected planet would have no effect on the fitted parameters for the known planet is too simplistic. The best method of determining limits, then, lies somewhere between the dotted and dashed lines in Fig. 5.30, and would be most easily accomplished by restricting the freedom of the free parameters in the Keplerian fits.

It is also important to note that the detection limits presented above represent the level at which 99% of planets could have been detected. The “blind spots” evident in these results may be due to only a few unfortunate configurations. A comparison of different detection criteria is shown in Figure 5.31 for 47 UMa. As expected, the level at which 50% of planets would have been detected is substantially lower, and indeed, relaxing the criteria alleviated the “blind spot” problem.

In considering how to improve the sensitivity of a survey, we can also look into the timing of the radial-velocity observations. The HET is a queue-scheduled telescope, allowing a degree of flexibility in the observations. In the course of this survey, the queue-scheduling feature was used at a basic level: stars with fewer observations were assigned higher priority. On occasion, stars which showed signs of an additional planetary signal were observed at key phases to test the veracity of such signals. Ford (2008) applies a Bayesian analysis to explore the use of adaptive scheduling to maximize the efficiency of planet searches. Monte Carlo simulations of radial-velocity planet search programs indicate that the adaptive scheduling algorithm made the simulated surveys much more sensitive to low-mass planets. Planets with velocity semiamplitude  $K$  near the detection threshold were found

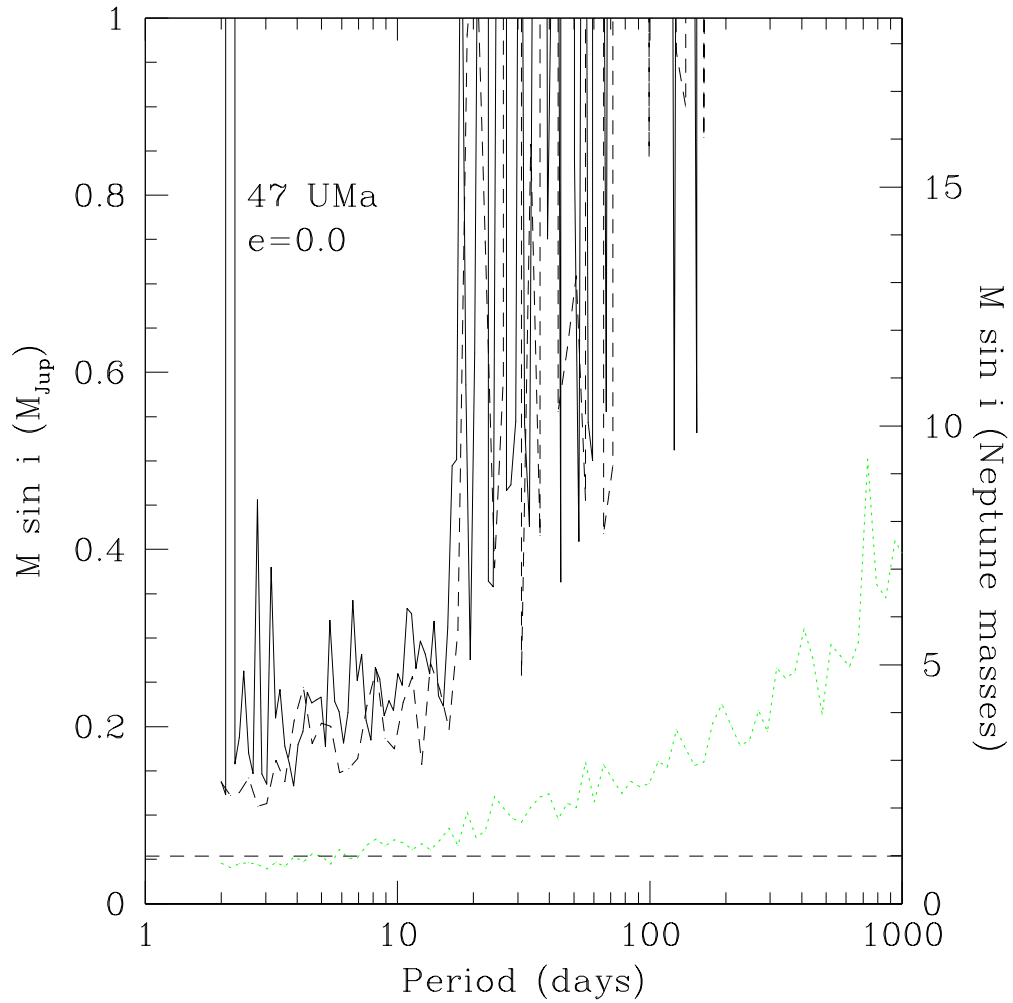


Figure 5.30 Detection limits for 47 UMa ( $e = 0.0$ ) by three different methods. Solid line: Keplerian method as described in § 5.2. Dashed line: Keplerian method, holding the offsets between data sets fixed. Dotted line: non-Keplerian method (“prewhitening”) method as described in § 5.1 and Wittenmyer et al. (2006).

about twice as often with the adaptive scheduling. Whereas regular scheduling resulted in each target being observed the same number of times (the strategy employed in this work), the adaptive algorithm resulted in a few stars being observed much more frequently while slightly reducing the number of observations of the remaining stars (Ford 2008). This sort of adaptive scheduling, in which the observing plan changes daily with each new datum, would be ideally applied to a survey on a queue-scheduled telescope such as the HET, and would likely have been quite useful for this work.

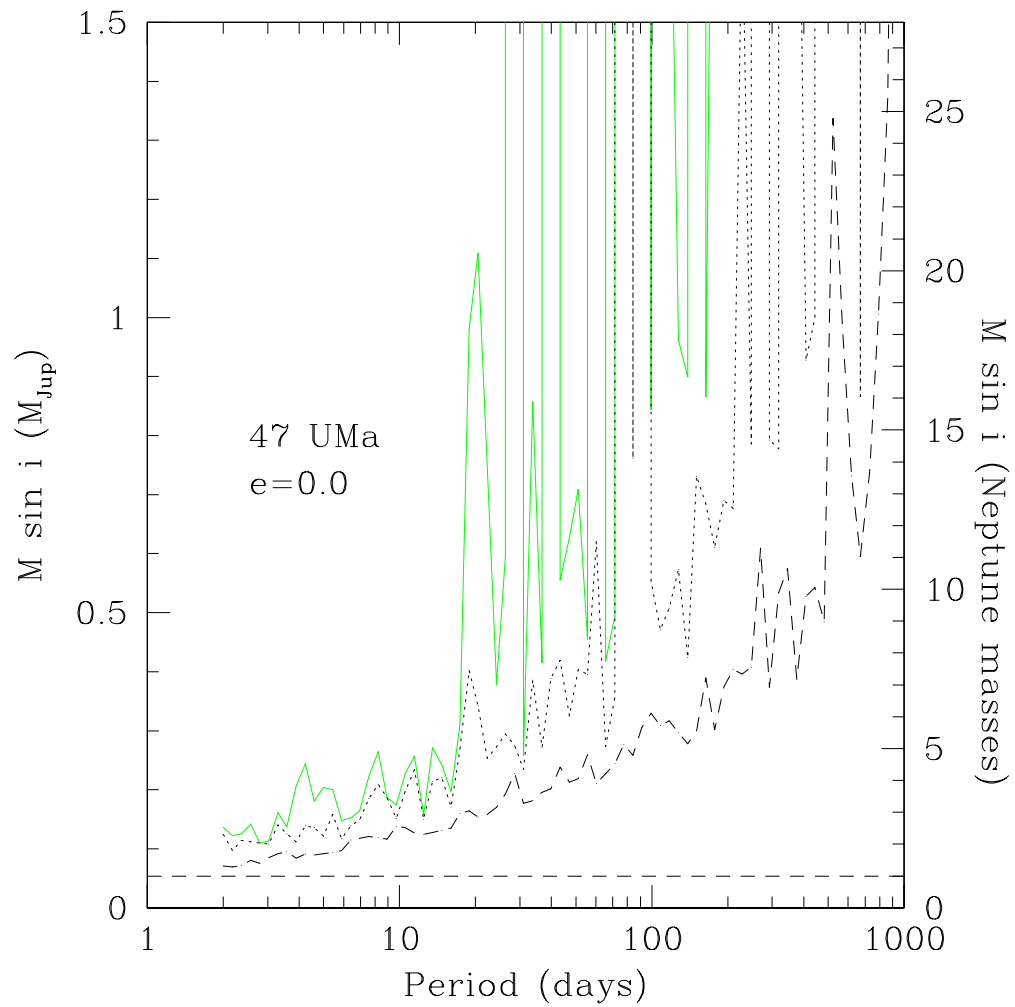


Figure 5.31 Detection limits for 47 UMa ( $e = 0.0$ ) using three different recovery criteria. Solid line: 99% of signals. Dotted line: 90% of signals. Dashed line: 50% of signals.

## Chapter 6

# Dynamical Simulations

To place constraints on the architecture of planetary systems, we would like to know where additional objects can remain in stable orbits in the presence of the known planet(s). In this section, I describe the results of dynamical simulations of the planetary systems under consideration. In Section 6.1, we map the regions of stability in each system by placing massless, non-interacting test particles in initially circular orbits in the presence of the known planet(s). In § 6.2, the stable regions are probed further, using massive bodies to test the long-term effects of gravitational interactions between the planets.

### 6.1 Massless Test Particles

#### 6.1.1 Numerical Methods

We performed test particle simulations using SWIFT<sup>1</sup> (Levison & Duncan 1994) to investigate the dynamical possibility of additional low-mass planets in each of the systems considered here. SWIFT is a numerical integration package which is designed to solve the equations of motion for gravitational interactions between massive bodies (star, planets) and massless test particles. Neptune-mass planets can be treated as test particles (1 Neptune mass =  $0.054 M_{\text{Jup}}$ ) since the exchange of angular momentum with jovian planets is small. We chose the regularized mixed-variable symplectic integrator (RMVS3) version of SWIFT for its ability to handle close approaches between massless, non-interacting test particles and planets. This

---

<sup>1</sup>SWIFT is publicly available at <http://www.boulder.swri.edu/~hal/swift.html>.

version is most efficient when the gravitational interactions are dominated by a single body (the central star). A symplectic integrator has the advantage that errors in energy and angular momentum do not accumulate. Particles are removed if they are (1) closer than 1 Hill radius to the planet, (2) closer than 0.01 AU to the star, or (3) farther than 10 AU from the star. A planetary-mass object passing within 1 Hill radius of another planet, or within 0.01 AU ( $2 R_{\odot}$ ) of the star’s barycenter, is unlikely to survive the encounter. Since the purpose of these simulations is to determine the regions in which additional planets could remain in stable orbits, we set the outer boundary at 10 AU because the current repository of radial-velocity data cannot detect objects at such distances.

The test particle simulations were set up following the methods used in Barnes & Raymond (2004), with the exception that only initially circular orbits are considered in this work. For each planetary system, 390 test particles were placed in initially circular orbits, spaced every 0.005 AU in the region between 0.05-2.0 AU. We have chosen to focus on this region because the duration of our high-precision HET data is currently 2-4 years for the objects in this study. The test particles were coplanar with the existing planet, which had the effect of confining the simulation to two dimensions. Input physical parameters for the known planet in each system were obtained from our Keplerian orbit fits described in Chapter 3 (Table 3.2). The planetary masses were taken to be their minimum values ( $\sin i = 1$ ). By choosing the minimum mass for the planets, the regions of dynamical stability are expected to be larger; hence, this results in a “best-case” scenario in terms of mapping the stable regions. The systems were integrated for  $10^7$  yr, following Barnes & Raymond (2004) and allowing completion of the computations in a reasonable time. We observed that nearly all of the test-particle removals occurred within the first  $10^6$  yr; after this time, the simulations had essentially stabilized to their final configurations.

### 6.1.2 Results and Discussion

The results of the dynamical simulations are shown in Figures 6.1-6.10. The survival time of the test particles is plotted against their initial semimajor axis. As shown in Figure 6.1, the short-period planet HD 3651b sweeps clean the region inside of about 0.5 AU. However, a small number of test particles remained in low-eccentricity orbits near the 1:3 and 2:1 mean-motion resonances (MMR). Since these regions lie within



the orbital excursion of HD 3651b, these appear to be protected resonances. The eccentricity of the test particles in the region of the 1:3 MMR oscillated between 0.00 and 0.31 with a periodicity of about  $1.2 \times 10^5$  yr, while those in the 2:1 resonance remained at  $e \lesssim 0.07$  throughout the simulation. Particles also remained in stable orbits beyond about 0.6 AU, which is not surprising given the low mass of the planet. Mandell et al. (2007) and Raymond et al. (2006) performed simulations of a Jupiter-mass planet migrating inward through a disk of planetesimals. In their simulations, the migrating giant planet captured planetesimals into low-order resonances, and these accreted into terrestrial planets during the 200 Myr run. The architecture of the HD 3651 system, with a  $0.2 M_{\text{Jup}}$  planet at 0.3 AU, is similar to the configuration modeled by Mandell et al. (2007). Given the stable regions evident near the 1:3 and 2:1 resonances for HD 3651b, it is possible that terrestrial-mass planets were captured into these regions during the migration process. The detection limits for HD 3651 complement the dynamics well, and the current data can place upper limits of  $\sim 3$  Neptune masses ( $\sim 48$  Earth masses) on such objects.

For most of the systems, the test-particle results give few surprises. Broad stable regions exist interior and exterior to HD 8574b, with the inner 0.47 AU retaining 100% of particles. For HD 10697 and HD 23596, particles remained in the inner 1.35 AU and 1.4 AU, respectively. The HD 19994 system, shown in Figure 6.2, proved to be quite interesting. One would expect any particles in orbits which cross that of the planet to be removed straightaway, but a strip of stability is evident at the 1:1 resonance with the planet, in the range 1.29-1.33 AU. Laughlin & Chambers (2002) investigated the possibility of planets in a 1:1 resonance, and concluded that such configurations are dynamically possible, but cannot be discerned by traditional least-squares Keplerian orbit fitting. They also demonstrated with synthetic data that the periodograms of a 1:1 resonant system and a single-planet system are indistinguishable, and that a dynamical fitting method is required to determine the correct parameters. This dynamical approach involves first using a genetic algorithm to create a population of 2-planet systems, which are then integrated to generate the radial-velocity response of the central star. In this way, each set of planetary parameters yields a stellar radial-velocity curve which can be compared to the data using the  $\chi^2$  statistic as a measure of fitness (cf. § 3.2). Unstable system configurations are thus excluded by this method. In one 1:1 configuration described by Laughlin & Chambers (2002), the “eccentric resonance,” one planet

is in a nearly circular orbit while the other is in a highly eccentric orbit. Though the orbits cross, the longitudes of pericenter are sufficiently different to avoid close encounters. Given the large scatter about the single-planet solution and the difficulty in fitting two planets, it would be most interesting to subject the HD 19994 data to the dynamical fitting method of Laughlin & Chambers (2002) to check for the 1:1 resonant situation.

In the HD 28185 system (Fig. 6.3), no stable regions exist exterior to the planet out to the maximum separation tested ( $a = 2.0$  AU). Figure 6.4 shows the results for the HD 38529 and HD 40979 systems. There is a broad region of stability between the widely-separated planets HD 38529b and c. The outer planet does not fall within the range of Fig. 6.4, but has an orbital excursion of 2.43–5.02 AU. For HD 74156, the recently-announced planet d (Bean et al. 2008), in a 346-day period between planets b and c, was not included in the simulation. Only those particles in a narrow strip near 1.25 AU survived the full 10 Myr; planet d would fall within the stable region. A run which included all three planets indicated that planet d remained stable, participating in a secular exchange of eccentricity with the inner planet on a timescale of about 3000 yr.

The  $4M_{\text{Jup}}$  planet orbiting HD 80606 removed all test particles to a distance of about 1.4 AU, and only beyond  $\sim 1.75$  AU did test particles remain in stable orbits for the duration of the simulation ( $10^7$  yr). Figure 6.6 shows that HD 89744b eliminated all test particles except for narrow regions at the innermost and outermost edges of the parameter space explored. Particles with  $a \sim 0.1$  AU remained stable, leaving open the possibility of short-period planets. The surviving particles oscillated in eccentricity up to  $e \sim 0.35$ , but these simulations treat the star as a point mass, and hence tidal damping of the eccentricity is not included. Our results are consistent with those of Menou & Tabachnik (2003), who investigated dynamical stability in extrasolar planetary systems and found that no test particles survived in the habitable zones of the HD 80606, HD 89744, and 16 Cyg B systems.

The 47 UMa system (Figure 6.7) included only the inner planet ( $a = 2.06$  AU) for this experiment; an outer planet, if present, would be too distant to affect the inner 2 AU explored here. A large region interior to the planet is stable for the full duration, including the habitable zone. This result is consistent with that of Jones et al. (2001), who also found the 47 UMa habitable zone to be stable for an Earth-mass planet at 1 AU. A strip of stability is also present in the range

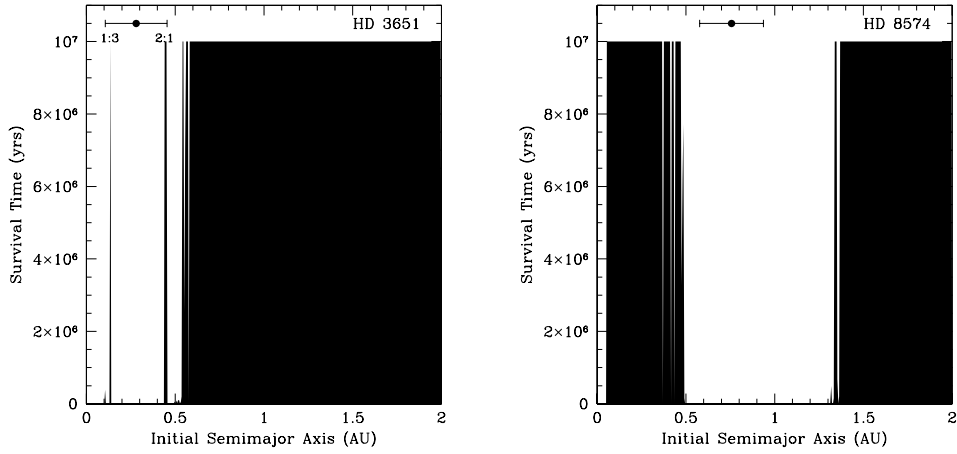


Figure 6.1 Left panel: Survival time as a function of initial semimajor axis for test particles in the HD 3651 system after  $10^7$  yr. The filled regions indicate test particles which survived. The orbital excursion of HD 3561b is indicated by the horizontal error bars at the top. Particles were placed on initially circular orbits with  $0.05 < a < 2.00$  AU. Right panel: Same, but for the HD 8574 system.

1.97-2.00 AU (the outer limit of the simulation). This region coincides with a 12:13 commensurability with the 47 Uma b ( $a = 2.06$  AU), but lies too close to the edge of the initial range of test particles (2 AU) to inspire confidence. With an  $M \sin i$  of  $6.9 M_{\text{Jup}}$ , HD 106252b clears out all particles outside of  $a \sim 0.7$  AU. For the HD 108874 system, no test particles survive between the two planets (Figure 6.8), but those in the innermost 0.3 AU remain stable. This region is considered in further detail in § 6.2, which describes massive-body simulations as well as nonzero eccentricities. As with 47 Uma, the HD 114783 system may contain a distant second body, but such an object was not considered in these simulations as its effect on the innermost 2 AU would be negligible. Particles interior to HD 114783b were stable to about  $a \sim 0.7$  AU. As expected for the HD 130322 hot-Jupiter system, all particles with  $a > 0.15$  AU survived. In the HD 178911B system, some particles remained in the inner 0.1 AU despite the large mass ( $M \sin i = 6.95 M_{\text{Jup}}$ ) and relative proximity ( $a = 0.34$  AU) of the planet.

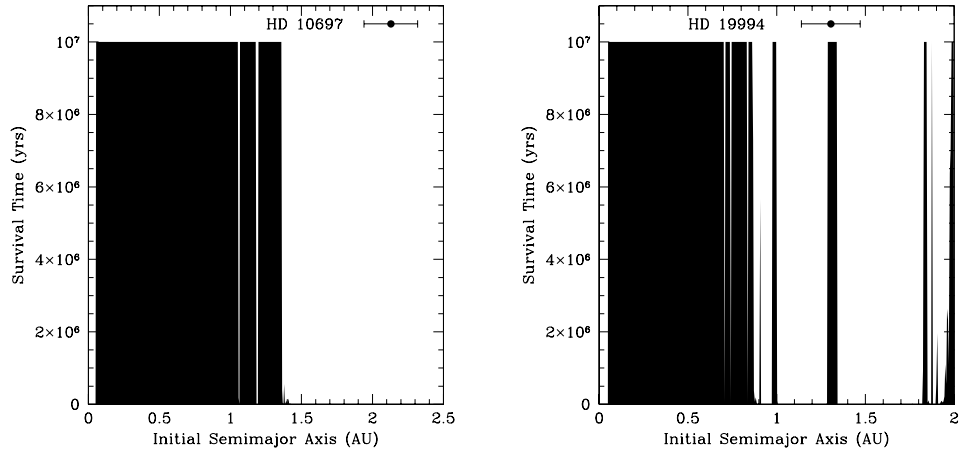


Figure 6.2 Same as Fig. 6.1, but for the HD 10697 (left) and HD 19994 (right) systems.

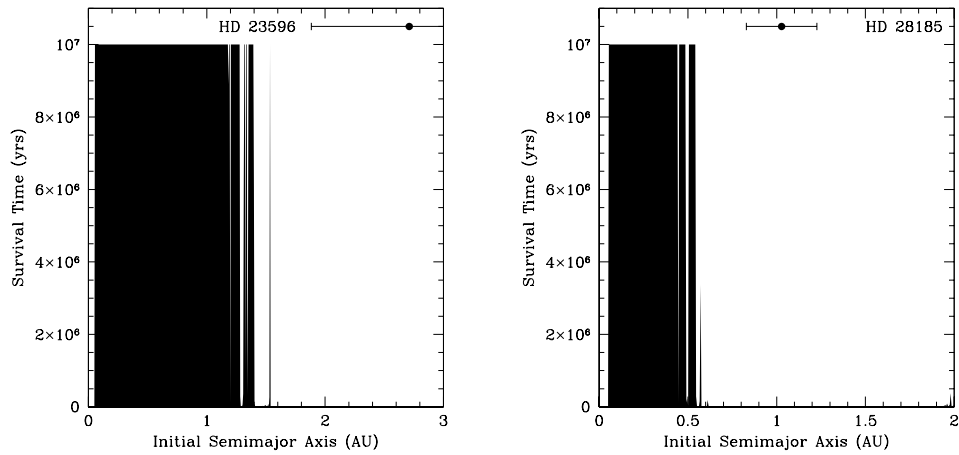


Figure 6.3 Same as Fig. 6.1, but for the HD 23596 (left) and HD 28185 (right) systems.

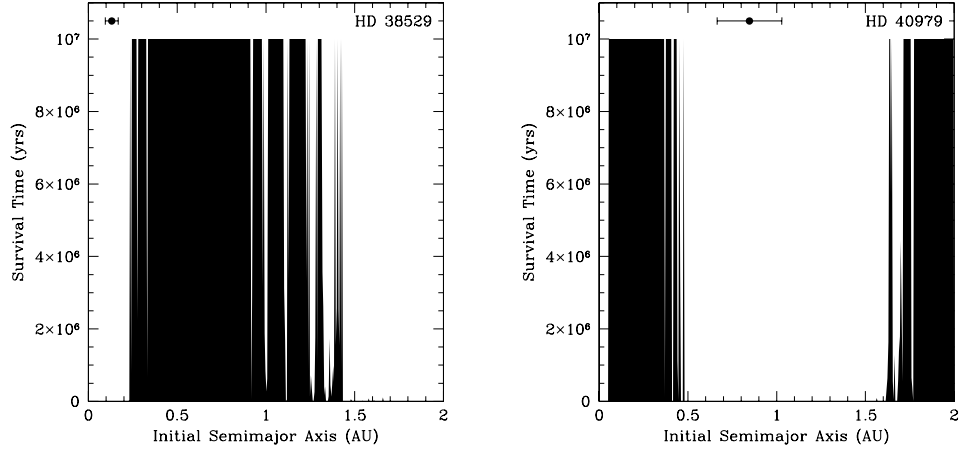


Figure 6.4 Same as Fig. 6.1, but for the HD 38529 (left) and HD 40979 (right) systems.

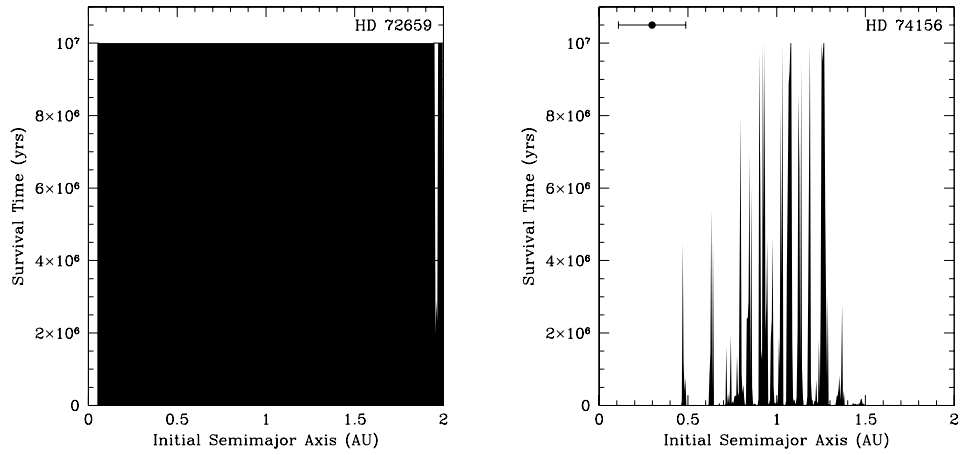


Figure 6.5 Same as Fig. 6.1, but for the HD 72659 (left) and HD 74156 (right) systems. HD 72659b, with an orbital excursion of 3.48-6.48 AU, is off the plot. The recently-announced planet HD 74156d, between planets b and c, was not included in the simulation, but would reside in the narrow stable strip.

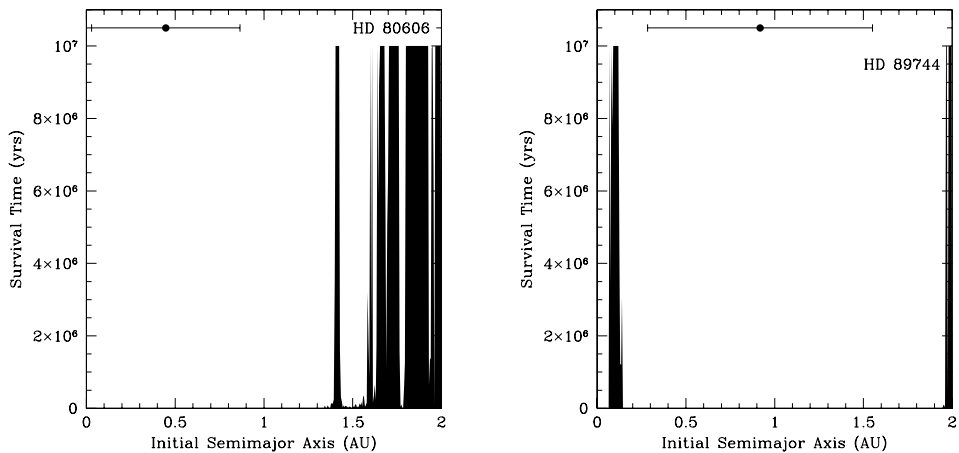


Figure 6.6 Same as Fig. 6.1, but for the HD 80606 (left) and HD 89744 (right) systems.

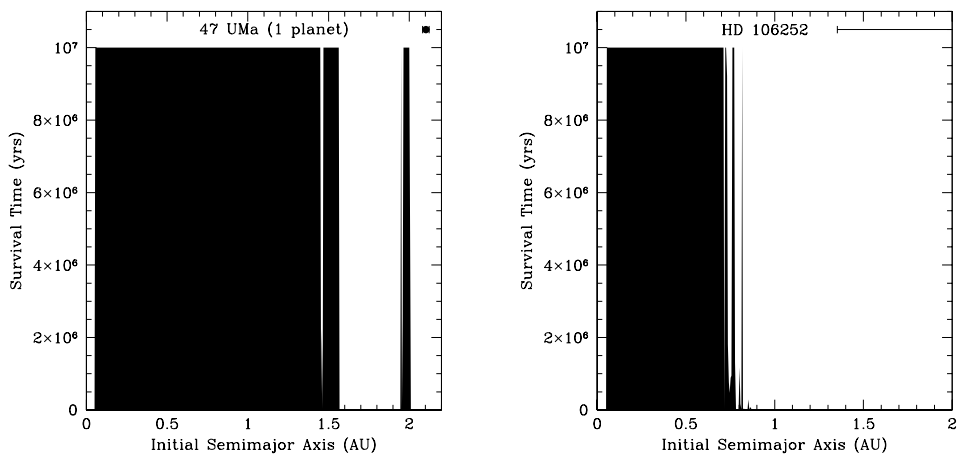


Figure 6.7 Same as Fig. 6.1, but for the 47 UMa (left) and HD 106252 (right) systems. Only 47 UMa b was considered in the simulations. An outer body, if present, would be too distant to affect the region under consideration.

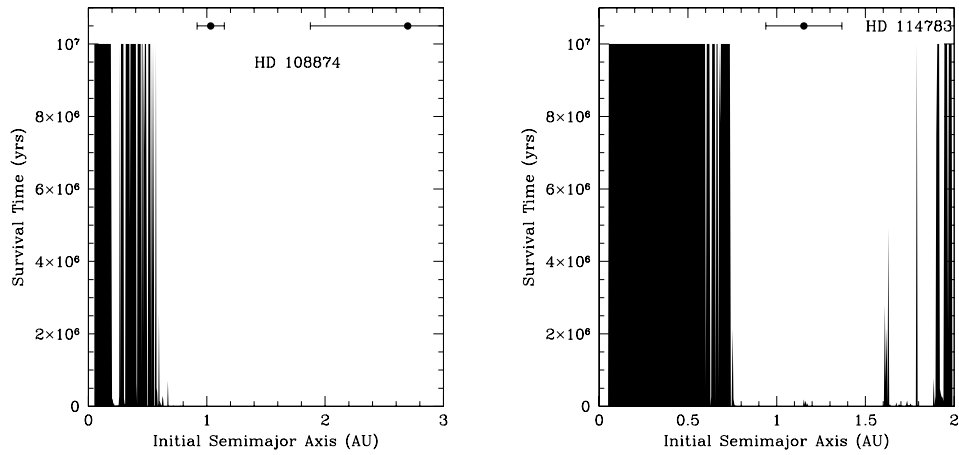


Figure 6.8 Same as Fig. 6.1, but for the HD 108874 (left) and HD 114783 (right) systems. Only HD 114783b was considered in the simulations. An outer body, if present, would be too distant to affect the region under consideration.

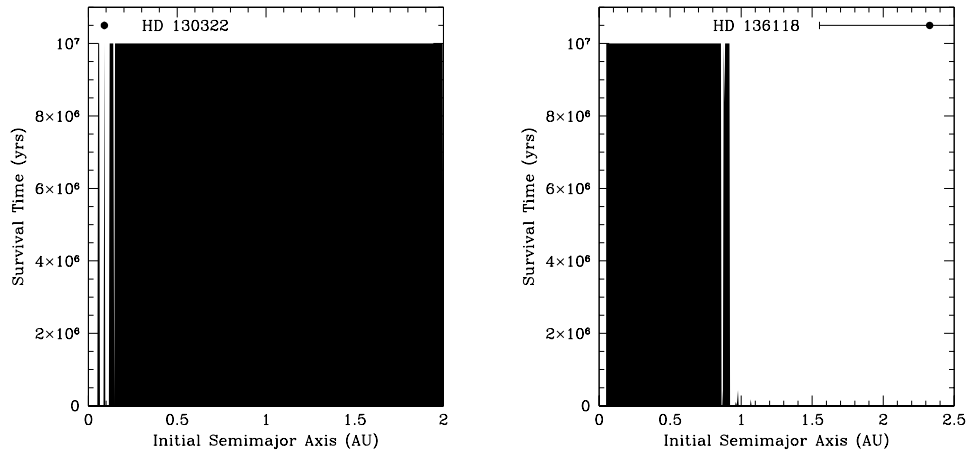


Figure 6.9 Same as Fig. 6.1, but for the HD 130322 (left) and HD 136118 (right) systems.

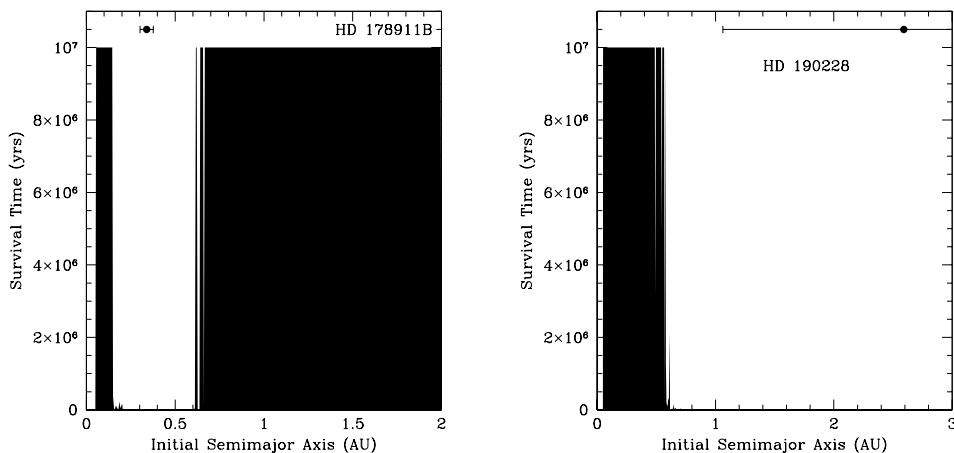


Figure 6.10 Same as Fig. 6.1, but for the HD 178911B (left) and HD 190228 (right) systems.

## 6.2 Massive Body Simulations

Regions stable for massless test particles may not be stable for massive bodies. Alternatively, regions unstable for test particles may be able to host a massive planet. In the latter case, the existing planet(s) may adjust their orbits in response to the perturbation induced by the introduced planet. For these reasons, it is important to also consider the effect of massive “test planets” in order to obtain a more complete dynamical picture of the systems under consideration. An additional complicating factor is the question of mutual inclination, a term used to describe systems in which the orbital planes of the planets are not coplanar, but rather inclined with respect to each other. Coplanarity is a convenient assumption which arises intuitively from the standard formation scenario of a flattened disk coalescing into planets. Observations of binary star systems by Hale (1994) indicate that for stellar systems with separations less than 30-40 AU, the orbital planes are generally aligned with the star’s equatorial plane. Hale (1994) uses this result to suggest that planetary systems should be essentially coplanar. Recently, however, McArthur et al. (2007) used *Hubble Space Telescope* FGS astrometry to constrain the inclinations of the Upsilon Andromedae planetary system, and found a  $35 \pm 6^\circ$  mutual inclination between the outer two planets (c and d). In this chapter, we explore the effect of inserting massive bodies into a known planetary system. Due to the extremely large parameter space



involved in such an undertaking, we restrict the analysis to one system, HD 108874. The HD 108874 system was chosen because of the relatively small size of the region found to be stable for test particles. This allowed for the timely completion of the additional tests described in § 6.2.1-6.2.3.

### 6.2.1 Numerical Methods

For these simulations, we use SWIFT in the same manner as in § 6.1, except that no test particles are included. For HD 108874, we consider a 3-planet system: the two known planets and a Saturn-mass “test planet.” The SWIFT test particle simulations described in § 6.1 indicate that objects could be stable in orbits with  $a \lesssim 0.6$  AU. The periastron of the inner planet is at 0.91 AU, and no particles survived at larger distances. For these tests, massive bodies were placed at 0.05 AU intervals from 0.05 AU to 0.90 AU. The masses of the bodies were set to a Saturn mass ( $=0.3 M_{\text{Jup}}$ ); this is about 3 times the average detection limit for HD 108874 shown in Chapter 5. Each massive-body simulation was run using SWIFT’s RMVS3 integrator in the same way as for the test-particle simulations. It should be noted that this method cannot handle close encounters, when massive bodies are closer to each other than 3 Hill radii. While the Mercury orbital integrator of Chambers (1999) has a hybrid feature with this capability, the loss in speed is a factor of 10-20, depending on the time step used. Due to this concession, we consider any approach within 3 Hill radii to result in the loss of the test planet. Simulations ran for  $10^6$  yr, and the time step was chosen to be  $\sim 1/20$  of the orbital period of the innermost body. This choice of time step, suggested by both H. Levison and J. Chambers, allows the orbit to be sufficiently resolved to prevent numerical errors which may arise during the periastron passage of eccentric objects. Wisdom & Holman (1992) tested the effect of stepsize on the stability of the symplectic integrator (Wisdom & Holman 1991) on which SWIFT and Mercury are based.

The first set of simulations placed a Saturn-mass planet in an initially circular orbit for each of 18 values of the orbital separation  $a$ , at 0.05 AU intervals from 0.05-0.90 AU. The 4-body systems (star and three planets) were integrated for  $10^6$  yr. Based on the criteria for removal described above, only those objects with  $a < 0.30$  AU remained for the full duration of the runs (Figure 6.11). Removals due to close encounters usually occurred within  $10^4$  yr.

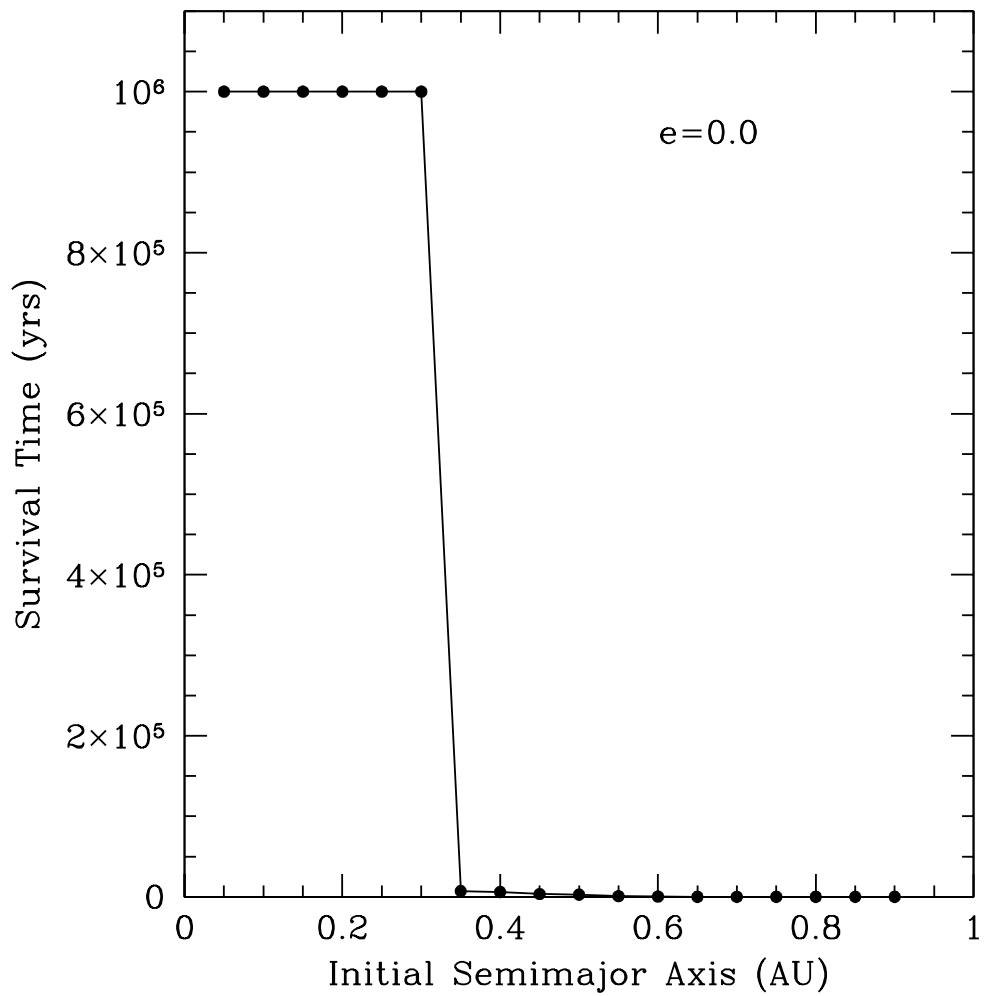


Figure 6.11 Survival time of Saturn-mass planets in the HD 108874 system on initially circular orbits.

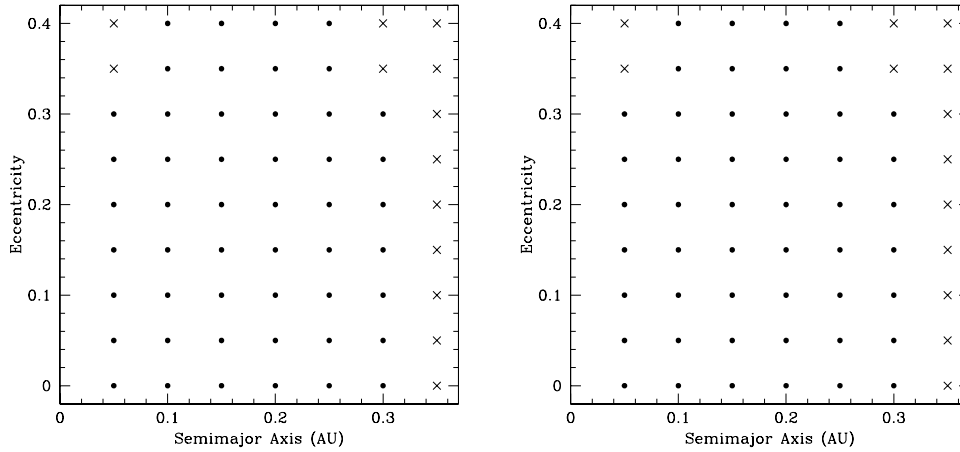


Figure 6.12 Results of dynamical tests inserting a Saturn-mass planet on an eccentric orbit into the HD 108874 system. Points indicate stability for the full  $10^6$  yr, crosses indicate unstable configurations. Left panel: Argument of periastron  $\omega$  aligned with that of HD 108874b. Right panel: Same, but  $\omega$  is anti-aligned with that of HD 108874b. All three bodies were coplanar.

### 6.2.2 Eccentric Orbits

The test runs were repeated for  $0.05 \leq a \leq 0.30$ , assigning a range of eccentricities to the added test planet. A grid of eccentricities was used from  $e = 0.05 - 0.30$  at intervals of 0.05. The argument of periastron  $\omega$  was treated in two ways: aligned and anti-aligned with the most massive planet. Ji et al. (2003) found that in most of the multi-planet systems,  $\Delta\omega = \omega_1 - \omega_2$  librated about  $0^\circ$ . However, in some systems the opposite appears to be occurring, e.g.  $\Delta\omega$  for HD 155358b and c librates about  $180^\circ$  (Cochran et al. 2007). For the HD 108874 system, the inner planet is most massive, and so  $\omega$  for the test planets was assigned a value of either  $231^\circ$  (aligned) or  $51^\circ$  (anti-aligned). These simulations were run for  $10^6$  yr, and the criteria for stability were the same as for the  $e = 0$  runs in § 6.2.1. The results for both cases are shown in Figure 6.12. There was no difference in stability between the aligned and anti-aligned cases. The region interior of  $a = 0.3$  AU seems to be stable for a wide range of planet eccentricities and orientations; repeating these tests with a random distribution of  $\omega$  for the test planet might be illuminating.

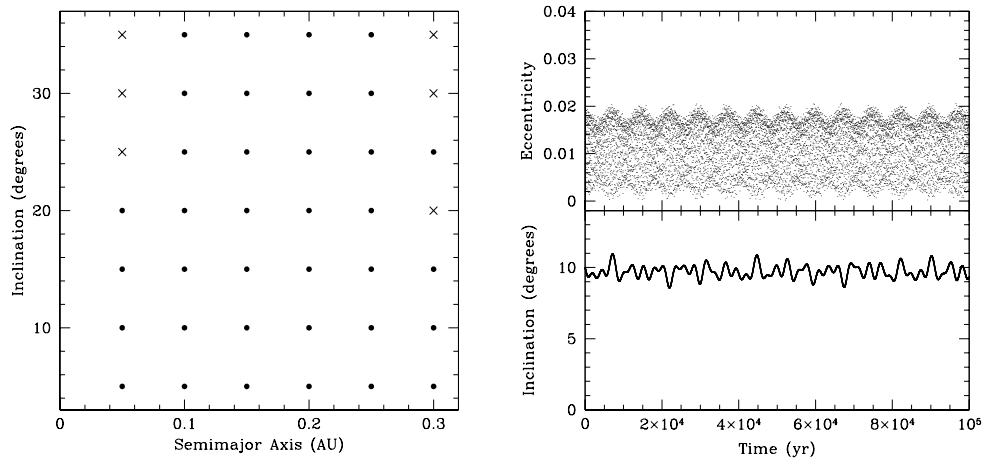


Figure 6.13 Left panel: Results of dynamical tests inserting a Saturn-mass planet on an inclined, circular orbit into the HD 108874 system. Points indicate stability for the full  $10^6$  yr, crosses indicate unstable configurations. Right panel: Evolution of eccentricity and inclination for a stable test body with initial  $e = 0$  and  $i = 10^\circ$ .

### 6.2.3 Mutual Inclinations

The experiments described above have restricted the three-planet test systems to be coplanar. In the interest of completeness, I performed additional tests in which the added Saturn-mass planet had a nonzero inclination with respect to the two existing planets in the HD 108874 system. Figure 6.13 shows the results for these tests, where the eccentricity of the added planet was initially zero. An example of the behaviour of a test body in this region is shown in Figure 6.13, for a test body with initial eccentricity  $e = 0$  and inclination  $i = 10^\circ$  with respect to HD 108874b. Even for inclinations much larger than found in our Solar system (Mercury:  $i = 7^\circ$ ), the test systems proved to be stable.

## Chapter 7

# Conclusions

The aim of this project has been to intensively monitor known planetary systems in search of additional planets. However, in the sample of 22 planet hosts, the results have been quite the opposite. These new data cast doubt on the existence of two of the previously known planets, HD 20367b and 47 UMa c. The announcement by Bean et al. (2008) of a third planet in the HD 74156 system, one of the targets of this study, prompted a detailed investigation; at present we cannot confirm this object. These results suggest that systems with multiple giant planets are considerably more rare, or harder to detect, than anticipated at the outset of this project.

### 7.1 Where are they?

In this section, we will explore some reasons why no new multiple-planet systems were detected by this study. Five possibilities are: 1) Biases in the target selection conspire against detection of weak signals, 2) There exist fundamental physical differences between single- and multiple-planet systems, 3) An insufficient quantity of high-quality data, 4) Mutual inclinations may be common, such that additional planets are present, but with nearly face-on orbits so that their radial-velocity signals are undetectable, and 5) Apparent single-planet systems may contain terrestrial-mass planets below the detection threshold.

Table 7.1. Comparison of Stellar Characteristics

Quantity	Targets	Non-Targets	Units
$[Fe/H]$ (mean)	$0.12\pm0.17$	$0.09\pm0.22$	dex
$[Fe/H]$ (median)	0.10	0.14	dex
$T_{eff}$ (mean)	$5741\pm361$	$5608\pm496$	K
$T_{eff}$ (median)	5697	5704	K
$(B - V)$ (mean)	$0.67\pm0.11$	$0.74\pm0.20$	mag
$(B - V)$ (median)	0.63	0.69	mag
$V \sin i$ (mean)	$3.72\pm2.50$	$2.75\pm1.72$	$\text{km s}^{-1}$
$V \sin i$ (median)	2.48	2.40	$\text{km s}^{-1}$

### 7.1.1 Biases in the Sample

As with any scientific experiment, it is important to determine whether the sample selection resulted in unforeseen biases which affected the results. The target-selection process for this study, described in § 2.1, included an intentional bias in favor of planet hosts with “large” ( $10\text{-}20 \text{ m s}^{-1}$ ) radial-velocity scatter about the orbital solution. The reasoning for this choice is straightforward: if a single planet can be fit with minimal scatter, there is little room for additional undetected planets to hide in the residuals. An unintended consequence of this selection criterion is that the excess scatter may be intrinsic to the star rather than indicative of additional planets. The achievable velocity precision improves with the number and strength of photospheric lines (Butler et al. 1996). Stars with higher temperatures or lower metallicities would have fewer and weaker lines, and result in lower velocity precision. In rapidly rotating stars, the spectral lines are broadened, which also degrades the radial-velocity precision. To check for this sort of bias, we can perform a Kolmogorov-Smirnov (K-S) test to determine the probability that two samples are drawn from the same distribution. Comparing our sample of 22 planet host stars with all other planet hosts, the K-S test shows no significant differences in  $T_{eff}$  ( $P = 0.698$ ),  $[Fe/H]$  ( $P = 0.969$ ), or  $V \sin i$  ( $P = 0.323$ ). A comparison of the mean and median values of these quantities is shown in Table 7.1. The uncertainties are too large to make meaningful comparisons, but the K-S test results indicate that there are no significant differences between the 22 planet hosts targeted here and those planet hosts not chosen.

### 7.1.2 Fundamental Differences

In this section, we ask the question, “Is there something special about the multi-planet systems”? Physical differences between single and multiple planet systems could arise either from the host star or from the processes of formation and dynamical evolution. Figure 7.1 plots the architecture of single- and multiple-planet systems, and Figure 7.2 examines the relation between planetary multiplicity and stellar parameters. Table 7.2 gives statistics on the planetary and stellar parameters for single and multiple-planet systems. Only those planets detected by radial-velocity with  $M \sin i < 13 M_{\text{Jup}}$  were considered in the compilation of these statistics. As evident from Table 7.2, the standard deviations of the means for the quantities of interest are too large to make any meaningful comparison. However, the Kolmogorov-Smirnov (K-S) test can be used to assess the probability that the two sets (single and multiple planet systems) are drawn from the same distribution. Table 7.3 shows the results of K-S tests on the planetary and stellar characteristics listed in Table 7.2. None of the parameters tested showed statistically significant differences between single and multiple planet systems. There are hints from the data in Tables 7.1–7.2 that planets in multiple systems have larger  $a$  and smaller  $M \sin i$  than those in single-planet systems. Both of these trends would work against the radial-velocity detection of planets in multiple systems. As the semimajor axis  $a$  increases by a factor of  $N$ , the velocity semiamplitude  $K$  decreases by  $\sqrt{N}$ , and as the planet mass decreases by a factor of  $N$ ,  $K$  also drops by a factor of  $N$ . It is also possible that a tendency toward lower mass and larger semimajor axis in multi-planet systems is the result of a selection effect. Once a single planet is found, follow-up observations may reveal longer-period (larger  $a$ ) planets, and intensive monitoring programs such as this work may find lower-mass planets. We can test whether a selection effect is at work by computing the statistics in Table 7.2 for the *first* planet discovered in the known multi-planet systems. These results are also given in Table 7.3; by comparing only the first planet found in the multiple systems with single planets, any hint of a difference between the distributions vanishes. While there is not a statistically significant difference between single and multiple-planet systems based on current data, there are hints of differences which may become significant with the detection of additional multiple-planet systems.

Table 7.2. Statistics of Single and Multiple Planet Systems

Quantity	Single	Multiple	Units
$a$ (mean)	$1.00 \pm 1.05$	$1.25 \pm 1.41$	AU
$a$ (median)	0.76	0.66	AU
$e$ (mean)	$0.25 \pm 0.23$	$0.20 \pm 0.16$	
$e$ (median)	0.20	0.18	
$M \sin i$ (mean)	$2.48 \pm 2.60$	$1.96 \pm 2.40$	$M_{\text{Jup}}$
$M \sin i$ (median)	1.50	1.08	$M_{\text{Jup}}$
Star mass (mean)	$1.10 \pm 0.30$	$1.00 \pm 0.25$	$M_{\odot}$
Star mass (median)	1.07	1.03	$M_{\odot}$
$[Fe/H]$ (mean)	$0.09 \pm 0.21$	$0.07 \pm 0.29$	dex
$[Fe/H]$ (median)	0.14	0.16	dex
$T_{\text{eff}}$ (mean)	$5640 \pm 473$	$5532 \pm 529$	K
$T_{\text{eff}}$ (median)	5724	5584	K
$(B - V)$ (mean)	$0.73 \pm 0.18$	$0.77 \pm 0.22$	mag
$(B - V)$ (median)	0.68	0.72	mag

Table 7.3. K-S Tests on Single and Multiple Planet Systems

Quantity	K-S Probability <sup>a</sup>
$a$	0.029 <sup>b</sup>
$a$ (1st planet)	0.249
$M \sin i$	0.057
$M \sin i$ (1st planet)	0.349
$e$	0.067
Star mass	0.388
$[Fe/H]$	0.795
$T_{\text{eff}}$	0.135
$(B - V)$	0.383

<sup>a</sup>Probability that the two samples are drawn from the same distribution.

<sup>b</sup>K-S tests were performed using T.W. Kirkman's online calculator at <http://www.physics.csbsju.edu/stats/>



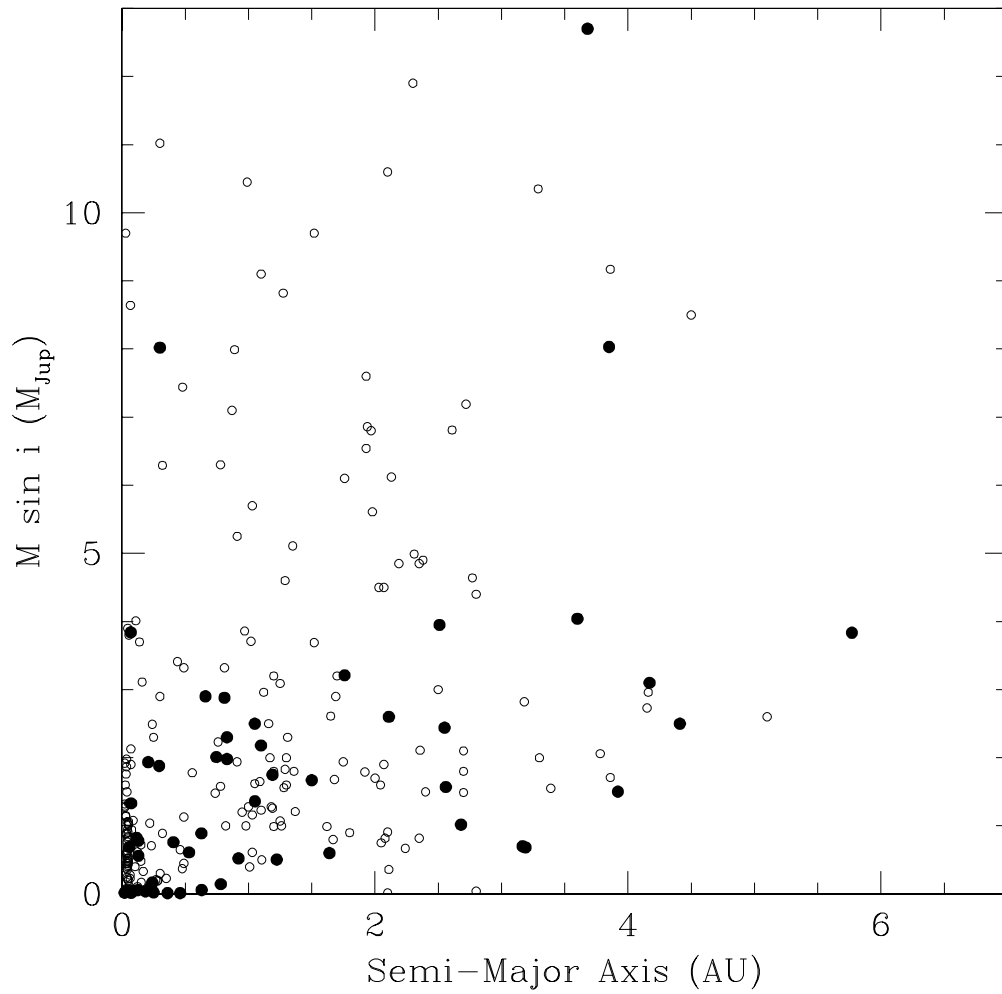


Figure 7.1 Projected planet mass  $M \sin i$  versus semimajor axis for all known exoplanets. Planets in multiple systems are shown as filled circles. Members of multiple-planet systems appear to tend toward lower masses. Planet data are from [exoplanet.eu](http://exoplanet.eu).

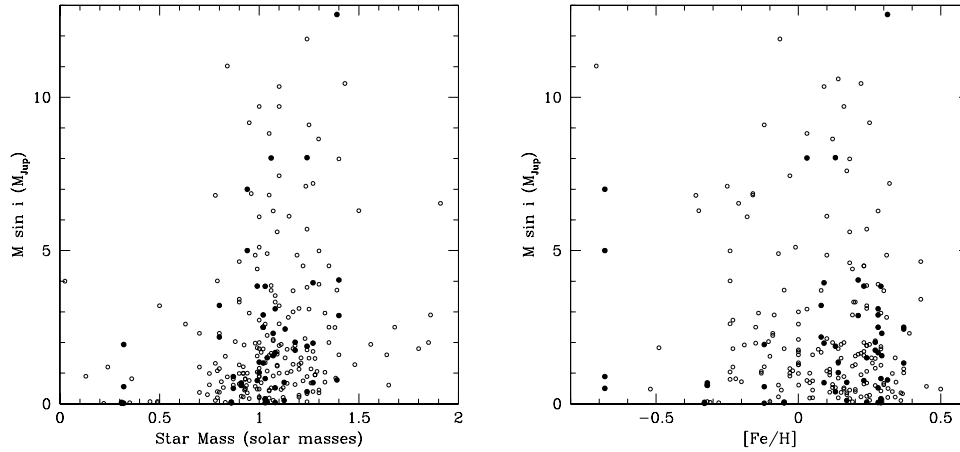


Figure 7.2 Planet mass plotted versus host star mass (left panel) and metallicity [Fe/H] (right panel). Planets in multiple systems are shown as filled circles. Planet data are from exoplanet.eu.

### 7.1.3 Observing Strategy

In considering whether there are important differences between the targets targeted in this work and known multi-planet systems, we can focus the comparison on the type of planetary system this survey was aimed at finding. The original motivation for this work (cf. Chapter 1) was to investigate the possibility that systems containing a jovian planet also contain Neptune-mass planets (1 Neptune mass=0.054  $M_{\text{Jup}}$ ). At this writing, there are four such systems: 55 Cnc, GJ 876,  $\mu$  Ara (=HD 160691), and GJ 777A (=HD 190360). With a sample size of only four, a meaningful statistical comparison of the host stars is not possible, but one can look at the characteristics of the body of radial-velocity data for these systems. In so doing, we ask whether those data are of exceptional quality or quantity which facilitated the detection of the additional low-mass planets in those systems. The recent detection of a fifth planet in the 55 Cnc system by Fischer et al. (2007) used 636 measurements, binned into 250 Lick visits and 70 Keck visits. The detection of the fourth planet by McArthur et al. (2004) used 138 HET observations combined with 143 Lick data points (Marcy et al. 2002) and 48 data points from Naef et al. (2004). For  $\mu$  Ara, the Neptune-mass planet was discovered using the HARPS spectrograph, which consistently delivers velocity precision of  $\sim 1 \text{ m s}^{-1}$  (Santos et al.

2004b; Pepe et al. 2007). The fourth planet in the  $\mu$  Ara system (Pepe et al. 2007) was discovered using a total of 86 HARPS measurements combined with data from CORALIE and the AAT. The  $18M_{\oplus}$  planet GJ 777Ac was discovered by Vogt et al. (2005) using 87 Keck velocities, and Rivera et al. (2005) found the  $7.5M_{\oplus}$  GJ 876d after 155 Keck observations. All four of these systems appear to have required an unusually large amount of the highest-quality data from Keck and HARPS, with a mean of 107 data points. By contrast, the targets in this work each received an average of 53 HET visits. It is possible that the number of visits required to detect a hot Neptune was underestimated.

#### 7.1.4 Just Unlucky

Here we consider the possibility that additional planets are present, but in orbits inclined so that their radial-velocity signatures are attenuated to a level below the detection threshold. For example, consider a planet with a true mass of  $0.3M_{\text{Jup}}$  (Saturn mass) at 0.1 AU. What inclination  $i_c$  is required so that the projected mass  $M \sin i$  is below the detection limits presented in Chapter 5? Assuming randomly distributed inclinations, we can then compute the probability that such an object would have that inclination or smaller:

$$\text{Prob}(i < i_c) = 1 - \cos(i). \quad (7.1)$$

The results of this thought experiment are shown in Table 7.4. If each system contained a planet with a true mass of  $0.3 M_{\text{Jup}}$  at an orbital distance of 0.1 AU, Table 7.4 gives the inclination below which that object would be undetectable by the current survey, and the probability of that inclination occurring by chance. From the test-particle simulations in Chapter 6, 15 of the systems considered here would be able to host an additional planet at  $a = 0.1$  AU. If planetary systems are truly “packed,” and every system contains the maximum number of planets dynamically possible, then the probability that none would have been detected is  $7.4 \times 10^{-8}$ . Of course, there are too many built-in assumptions to make this estimate scientifically useful; chief among them is the use of a Saturn mass ( $=0.30M_{\text{Jup}}$ ). If we repeat the exercise with Neptune-mass planets ( $=0.05M_{\text{Jup}}$ ), then such an object would only have been detectable in the HD 3651 system with  $i > 82^\circ$ . Even if all 22 systems contained a Neptune-mass planet at 0.1 AU, there is an 86% probability that they

Table 7.4. Inclinations for Undetectable Saturn-Mass Planets

Star	$i$ (degrees) $a = 0.1$ AU	Probability
HD 3651	10.2	0.016
HD 8574	69.0	0.642
HD 10697	27.4	0.112
HD 19994	... <sup>a</sup>	1.000
HD 23596	33.3	0.164
HD 28185	48.9	0.343
HD 38529	27.8	0.115
HD 40979	...	1.000
HD 72659	27.5	0.113
HD 74156	34.5	0.176
HD 80606	...	1.000
HD 89744	...	1.000
47 UMa	58.8	0.482
HD 106252	...	1.000
HD 108874	13.5	0.028
HD 114783	23.8	0.085
HD 128311	49.5	0.351
HD 130322	24.2	0.088
HD 136118	...	1.000
HD 178911B	42.5	0.263
HD 190228	62.5	0.538

<sup>a</sup>A Saturn-mass planet would not be detectable at any inclination.

would all have been missed. The extrasolar planet mass function (Figure 1.3) indicates that low-mass planets are considerably more common, so it is not unreasonable to expect that the systems are indeed “packed,” but with planets too small to detect at present. We will explore this further in the next section.

### 7.1.5 Swarms of Earths

Another possibility is that multiple-planet systems are indeed common, but, like our own Solar system, contain many terrestrial-mass objects which are undetectable by current radial-velocity surveys. Core-accretion simulations by Ida & Lin (2004a) predict a preponderance of 1-10 $M_{\oplus}$  planets inside of 1 AU, and a “planet desert” in the range of 10-100  $M_{\oplus}$ , arising due to rapid gas accretion by cores once they reach about 10  $M_{\oplus}$ . The current survey is not sensitive to the terrestrial-mass objects, but planets within the “desert” could have been detected. Of course, many

more than 22 systems need to be studied before conclusions can be made, but the characterization of hundreds of new systems by the *Kepler* spacecraft (Borucki et al. 2003) will help to define the upper and lower mass boundaries of the planet desert. Ida & Lin (2004a) note that the lower mass boundary would indicate the core mass required for rapid gas accretion, while the upper mass boundary would give insight into the mechanism by which gas accretion stops. *Kepler* discoveries of short-period super-Earths with masses 1-10 $M_{\oplus}$  would lend further support to the core-accretion mechanism.

Simulations of planetesimal formation and migration also provide support for the existence of terrestrial-mass planets in systems with a gas giant planet. The GJ 876 system (Rivera et al. 2005), which contains two giant planets and an interior “super-Earth” ( $M \sin i = 7.5 M_{\oplus}$ ), is thought to have originated by the shepherding of material as the giant planets migrated inward (Zhou et al. 2005). 200 Myr simulations by Raymond et al. (2006) and Mandell et al. (2007) (cf. Section 6.1.2) resulted in the formation of planets with 1-5 Earth masses interior and exterior to the migrating hot Jupiter. Those models included only Type II migration, in which the migrating giant planet opens a gap in the protoplanetary disk. The models of Fogg & Nelson (2007) consider the effects of Type I migration, in which the giant planet does not open a gap in the disk and inward drift is driven by differential torques on the planet. Inclusion of Type I migration did not alter the general outcome, that planets of several Earth masses are shepherded inward by the hot Jupiter, and some remain exterior to it. These models indicate that the inner regions of planetary systems may be populated with terrestrial-mass planets which would remain wholly undetectable by current radial-velocity surveys.

## 7.2 Broader Implications for Planetary Systems

We now take a step back and look at the bigger picture of planetary system formation and evolution. Based on the target selection and the resulting detection limits, this survey was most sensitive to systems with two giant planets (larger than Saturn mass). More specifically, our “key demographic” is a system with a “cold” Jupiter ( $a \sim 1$  AU) and a close-in planet with  $M \sin i \gtrsim 0.3 M_{\text{Jup}}$ . The detection limits given in Chapter 5 exclude such configurations at the 99% level for all of the planetary systems considered here. Systems containing a long-period, massive

planet could also have been detected by trends or curvature in the velocity residuals; no such trends were present for any of the targets. This survey was much less sensitive to planetary systems like our own, with multiple terrestrial-mass planets and long-period giants, for the reasons discussed in § 7.1.5. Planetary systems with architectures like our own Solar system may yet be common, but we will need to wait for the results from *Kepler* to begin making quantitative statements.

The results of this work are most useful in assessing the frequency of planetary systems in which extensive migration has occurred, to bring two gas giant planets interior to the “snow line.” In the core-accretion theory of giant planet formation (Pollack et al. 1996; Lissauer 1995), surface-density enhancement by ices facilitates the formation of  $\sim 10\text{--}15 M_{\oplus}$  cores. The snow line, beyond which ices are present in the protoplanetary disk, has been estimated to lie at 1.6–1.8 AU in a minimum-mass solar nebula (Lecar et al. 2006). Perhaps the extensive migration required to construct systems with multiple giant planets with  $a \lesssim 2$  AU is uncommon; the typical timescale in which a system is undergoing migration may be short. In other words, migration may be fast, a hypothesis which has led to theoretical scenarios in which the observed planets are the last of many “batches” of planets which migrated onto the host star (Trilling et al. 2002; Ida & Lin 2004a; Narayan et al. 2005). Type I migration, in which a net viscous torque on the protoplanet changes its orbit (Ward 1997), results in very fast migration with a timescale proportional to  $M_{planet}^{-1}$ . When a planet is massive enough ( $0.3\text{--}1.0 M_{Jup}$ ; Armitage 2007) to clear a gap in the disk, the slower Type II migration begins. The results of this work, showing a deficit of systems with multiple giant planets inside of 2–3 AU, suggest that these objects are dominated by Type I migration and rapidly accrete onto the star. Tanaka et al. (2002) showed that the Type I migration timescale is inversely proportional to the disk mass: planets in more massive disks migrate faster. If we make the reasonable assumption that multiple giant planets form from unusually massive disks, then Type I migration works against these planets surviving the migration if they remain below the gap-opening mass. To generate systems with multiple giant planets inside of 2–3 AU, migration should then be rapid enough to bring them there, but not so fast as to send the planets into the star. These results suggest that such a scenario is uncommon.

In addition to migration, the dynamical history of planetary systems is an important factor in producing the observed architectures. As discussed in Chapter 1

(5), the eccentricity distribution of extrasolar planets suggests that dynamically active histories are common. Interactions between giant planets can result in the ejection of one while imparting a significant eccentricity on the remaining planet (Rasio & Ford 1996; Ford et al. 2005). Systems containing a single giant planet on a moderately eccentric orbit may be the result of such encounters, and thus less likely to host the sort of planets this survey was seeking. The median eccentricity of the planets targeted in this work is 0.29, compared to a median  $e$  of 0.18 for all other planets. Comparing the distributions by the K-S test gives a probability of 0.322, indicating no significant difference between the two. Fischer et al. (2007) use the relatively low eccentricities ( $e < 0.2$ ) of the five 55 Cnc planets to suggest that a benign dynamical history allowed so many planets to remain. The GJ 876, HD 37124, HD 73526, and GJ 581 systems also have multiple planets with  $e < 0.2$ , but counterexamples are found in HD 160691, HD 74156, and HD 202206 ( $e_{max}=0.57, 0.64,$  and  $0.44$ , respectively). An uneventful dynamical history contributes to a planetary system's observed end state, but comprises only a part of the picture in combination with its formation history.

A primary goal of the search for extrasolar planets is to estimate how common the architecture of our own Solar system might be. If the processes of planet formation and migration form many systems similar to our own, it becomes more likely that Earth-like planets may be present. The results of this work indicate that planetary systems like our own may be common if 1) terrestrial-mass planets are present but undetected, or 2) Type I migration timescales are so short that multiple giant planets rarely end up within 2-3 AU. Conversely, our Solar system may be rare if 1) the dynamical history of most planetary systems results in many ejections and high eccentricities, or 2) planets with mutually inclined orbits are present but undetectable in most systems.

### 7.3 Future Investigations

As with any project, the constraints of time or computing resources force compromises to be made, balancing thoroughness with alacrity. Here I describe some extensions to the analysis presented in this work, which would contribute to a more complete picture of the sensitivity of this survey.

### 7.3.1 Other Approaches to Detection Limits

The wide-field genetic algorithm searches described in § 3.2 can also be used to determine companion limits by using different criteria than the recovery of an injected signal. The genetic algorithm, when used in this manner, attempts to fit an additional planet to the original data, generating a set of parameters and a  $\chi^2$  value for the multi-planet fit. As evidenced in Figures 3.45–3.54, the resulting  $\chi_\nu^2$  are usually quite large as the parameters evolve toward a best-fit solution. One could make use of this detritus in that the thousands of models cast aside can provide a measure of the degree to which an additional planetary signal affects the quality of the fit to the data. The matter of detection limits can then be approached by asking what sort of secondary signals would have been detected by the difference in the quality ( $\chi_\nu^2$ ) of the 2-planet fit compared to the single-planet fit. A significant disadvantage of this method is that the genetic algorithm “kills off” models with high  $\chi^2$ . For the purposes of detection limits, we would like a well-sampled set of parameters which would have been easily detected, i.e. where the 1-planet fit is exceedingly poor. A more systematic approach might be to modify the detection-limits routine described in § 5.2. Rather than attempt to recover the injected planet, we can record the  $\chi_\nu^2$  of the 1-planet fit to the data containing the added signal. A signal would then be considered as detectable if it increased the  $\chi_\nu^2$  by more than 9 ( $3\sigma$ ) over the  $\chi_\nu^2$  of the best single-planet fit. Figure 7.3 shows the results of such a test for 47 UMa. The detection limit line is the set of added planets with velocity semiamplitude  $K$  for which all orbital configurations resulted in a  $\Delta\chi_\nu^2 > 3$ . This method is about a factor of 10 faster in computing time, compared to the genetic algorithm.

### 7.3.2 Test Particles in Inclined Orbits

As shown in § 6.2, regions stable for test particles in orbits coplanar with the known planets can also be remarkably stable for bodies in inclined orbits. A more physically realistic set of test-particle simulations would allow the particles to take on inclined orbits. Previous investigations of dynamical stability in extrasolar planetary systems have restricted the test particles to the plane of the planets (Jones et al. 2001; Jones & Sleep 2002; Barnes & Quinn 2004; Barnes & Raymond 2004; Rivera & Haghhighipour 2007). Preliminary results from the massive-body tests in § 6.2.3 indicate that the effect of inclination is minimal. Test bodies inclined by up to



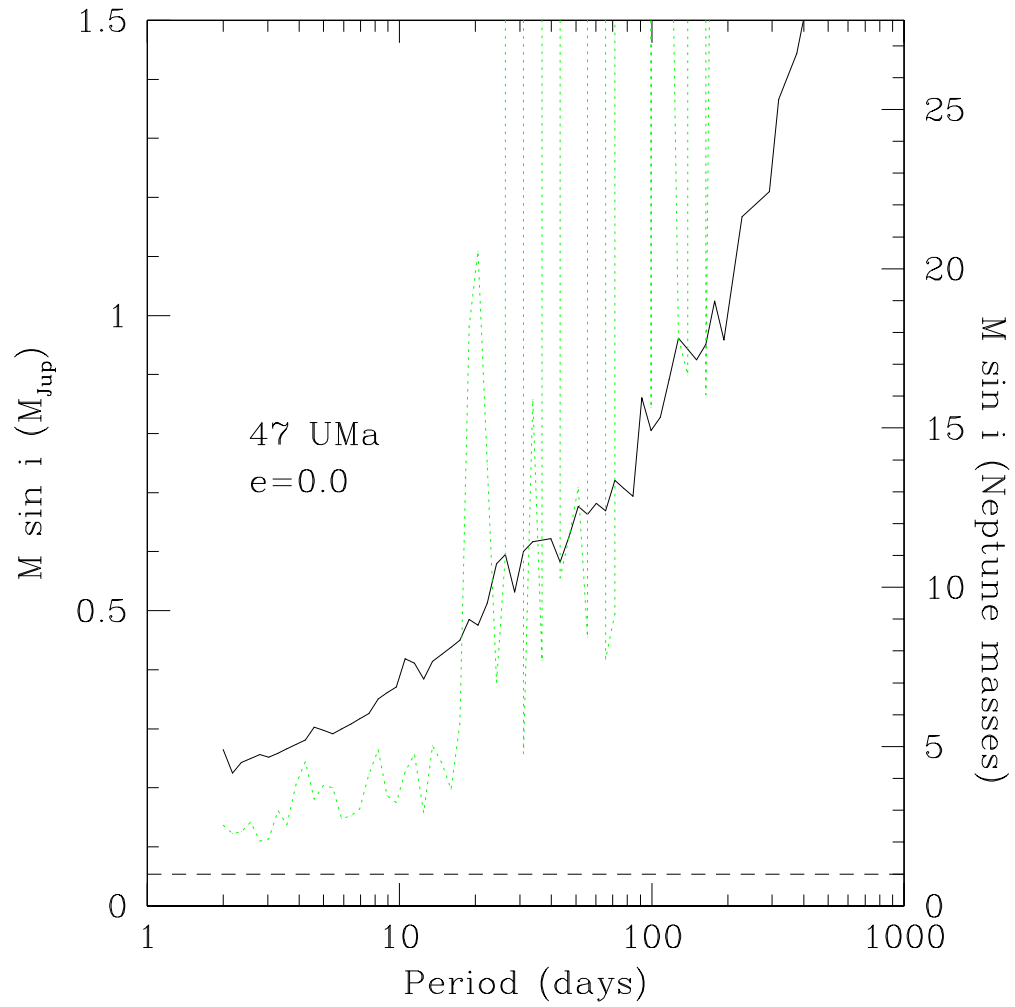


Figure 7.3 Detection limits for 47 UMa (black line), using the criterion that injected signals had to increase the reduced  $\chi^2$  by more than  $3\sigma$  to be considered as detectable. The grey line shows the detection limits obtained in § 5.2.

$15^\circ$  with respect to the known planets remained stable in the same regions as their coplanar counterparts (Figures 6.12, 6.13). For completeness, however, it would be interesting to see how the regions of stability are affected by allowing the test particles to have nonzero inclinations.

### **7.3.3 A Full Treatment of Massive Bodies**

In § 6.2, massive bodies were treated using the SWIFT RMVS3 integrator (Levison & Duncan 1994), which has the advantage of speed, but is unable to handle close encounters between planets. To account for this compromise, a test planet was considered as lost if it ventured within 3 Hill radii of the known planet. A more consistent approach would be to make use of the “hybrid” integrator in Mercury (Chambers 1999), which switches from MVS to a slower, but very accurate, Bulirsch-Stoer integration when objects are within 3 Hill radii of each other. In this way, the simulation may find interesting regions of parameter space where planets could survive repeated close encounters.

## Appendix A

# HET Radial-Velocity Data

Table A.1. HET Radial Velocities for HD 3651

JD-2400000	Velocity ( $\text{m s}^{-1}$ )	Uncertainty ( $\text{m s}^{-1}$ )
53581.87326	-10.8	2.7
53581.87586	-15.0	2.7
53581.87846	-14.0	2.6
53600.79669	-4.5	2.3
53600.79860	-7.3	2.9
53600.80050	-15.0	2.9
53604.79166	-9.2	1.8
53604.79356	-10.3	1.9
53604.79548	-15.7	2.2
53606.78169	-10.8	1.8
53606.78360	-6.4	2.1
53606.78551	-17.3	1.8
53608.77236	-12.1	1.8
53608.77426	-9.8	1.9
53608.77617	-12.5	1.7
53615.96280	-21.7	2.4
53615.96471	-25.7	2.3
53615.96662	-32.3	2.3
53628.74050	0.9	2.1
53628.74240	-5.8	2.2
53628.74431	2.4	2.1
53669.61012	-11.3	2.0
53669.61203	-9.5	2.2
53669.61394	-9.8	2.2
53678.78954	-3.8	2.3
53678.79141	-1.2	2.2
53678.79332	5.3	2.1
53682.78423	-6.7	2.2
53682.78609	-6.5	2.2
53682.78801	-3.9	2.2
53687.77684	19.6	2.2
53687.77875	17.3	2.2
53687.78066	24.5	2.1
53691.75967	20.8	2.2
53691.76158	28.8	2.1
53691.76349	24.7	2.0
53696.75837	24.5	1.8
53696.76028	28.5	1.8
53696.76220	29.2	1.8
53694.75275	25.1	2.1

Table A.1 (cont'd)

JD-2400000	Velocity (m s <sup>-1</sup> )	Uncertainty (m s <sup>-1</sup> )
53694.75466	22.6	2.0
53694.75656	25.9	2.0
53955.83401	9.0	2.0
53955.83593	9.8	2.1
53955.83785	9.5	2.0
53956.82850	9.4	2.0
53956.83046	7.6	2.0
53956.83236	4.0	2.2
53957.82201	5.1	2.0
53957.82392	7.4	2.0
53957.82583	6.1	2.0
53973.80721	18.4	7.1
53973.81020	10.9	2.2
53973.81200	4.4	1.9
53976.78393	-2.9	2.4
53976.78586	2.1	2.0
53976.78778	2.0	2.3
53978.97197	3.8	2.4
53985.95886	-2.6	2.1
53985.96079	10.4	3.0
53987.95335	-2.2	2.1
53987.95527	-2.0	2.0
53987.95719	-4.9	2.1
53989.73817	-6.0	2.0
53989.74009	-6.7	2.0
53989.74203	-11.8	1.9
54003.70719	9.8	2.1
54003.70915	12.1	2.2
54005.68297	13.2	2.4
54005.68488	18.0	2.0
54005.68690	16.8	2.2
54056.77919	2.3	2.1
54056.78110	-5.7	2.2
54056.78302	-1.8	2.3
54062.55119	27.8	1.8
54062.55312	30.7	2.0
54062.55505	29.5	2.0
54064.54710	20.5	2.0
54064.54902	26.0	2.0
54064.55094	26.9	2.0

Table A.1 (cont'd)

JD-2400000	Velocity (m s <sup>-1</sup> )	Uncertainty (m s <sup>-1</sup> )
54130.55316	26.9	2.3
54130.55508	21.3	2.5
54130.55701	22.8	2.5
54282.92589	4.8	2.0
54282.92782	1.4	2.0
54282.92976	-2.1	1.9
54285.92203	-4.6	2.2
54285.92396	-7.2	2.1
54285.92589	-9.2	2.2
54352.95992	-5.2	2.0
54352.96182	-2.0	2.1
54352.96374	-0.8	2.2
54394.64408	11.7	2.0
54394.64606	14.8	2.1
54394.64807	6.6	2.0
54399.61182	11.1	2.0
54399.61379	8.3	1.9
54399.61578	8.1	2.0
54414.77632	6.8	2.0
54414.77832	7.9	2.1
54414.78031	3.9	2.0
54423.75513	-0.4	1.9
54423.75717	-2.1	1.7
54423.75915	-7.4	1.8

Table A.2. HET Radial Velocities for HD 8574

JD-2400000	Velocity ( $\text{m s}^{-1}$ )	Uncertainty ( $\text{m s}^{-1}$ )
53601.81736	-86.5	2.2
53604.80314	-96.4	2.2
53605.82189	-104.1	2.3
53607.81271	-105.4	2.2
53609.79513	-106.4	2.3
53612.79858	-110.6	2.2
53633.96072	-96.3	2.1
53653.69022	-61.6	2.6
53663.88291	-67.3	2.3
53665.63806	-62.0	2.5
53668.64072	-59.6	2.3
53687.81363	-36.8	2.3
53696.78210	-29.5	2.5
53703.77271	-7.7	3.0
53695.79449	-30.1	2.7
53705.75396	-4.7	3.0
53936.90653	-11.4	2.2
53943.87924	18.8	3.6
53969.80550	37.2	2.1
53975.81126	23.4	2.9
53987.99307	18.5	2.1
53989.98424	9.6	2.0
53997.96536	-14.4	2.3
54000.73798	-31.8	2.5
54013.69475	-32.1	2.4
54018.90830	-41.2	2.5
54043.84966	-63.8	2.7
54046.60732	-76.9	2.9
54049.61516	-65.5	3.0
54057.78673	-58.4	2.8
54067.55166	-80.7	2.6
54071.76076	-71.6	3.0
54106.65631	-49.9	2.9
54110.66352	-61.2	2.9
54121.63331	-57.7	2.9
54306.89112	-103.1	2.9
54327.84853	-90.4	2.8
54344.80292	-83.3	2.5
54352.76329	-80.7	2.3
54367.73942	-44.9	2.3

Table A.2 (cont'd)

JD-2400000	Velocity (m s <sup>-1</sup> )	Uncertainty (m s <sup>-1</sup> )
54402.85369	10.4	2.3
54402.86084	17.6	1.9
54404.84838	19.6	2.1
54419.81583	44.1	2.1
54434.54809	37.5	2.7



Table A.3. HET Radial Velocities for HD 10697

JD-2400000	Velocity (m s <sup>-1</sup> )	Uncertainty (m s <sup>-1</sup> )
53581.90281	27.8	2.4
53606.84709	7.1	1.9
53653.91334	2.6	1.9
53663.69183	6.9	1.9
53665.67577	11.6	1.6
53681.83488	0.6	2.2
53681.83752	-0.2	1.9
53690.81667	-2.5	2.1
53696.79921	-14.0	2.2
53701.77012	-18.3	2.1
53703.79160	-12.8	2.1
53694.60078	-25.3	1.9
53923.95145	-16.2	1.9
53954.87796	-7.4	1.8
53956.86965	1.8	1.7
53958.88031	-0.4	1.9
53969.83080	-22.1	1.8
53971.83685	-21.8	2.1
53984.79870	11.2	1.8
53988.80905	14.0	1.8
53990.98655	5.9	1.7
53999.74552	29.6	2.0
54041.64127	41.8	2.2
54042.65929	34.3	2.0
54049.62382	45.9	2.0
54056.63399	60.1	2.1
54069.56942	59.0	2.0
54071.57888	57.2	1.9
54105.67044	92.5	2.1
54108.67092	89.9	2.2
54130.60755	96.2	2.1
54135.60424	118.0	2.2
54330.86457	165.2	2.1
54344.80964	149.8	2.3
54346.79984	163.6	2.0
54352.78595	167.5	1.9
54357.77232	160.3	1.9
54366.75077	166.2	1.8
54419.83538	175.2	2.0
54424.59411	172.7	1.7

Table A.3 (cont'd)

JD-2400000	Velocity ( $\text{m s}^{-1}$ )	Uncertainty ( $\text{m s}^{-1}$ )
------------	--------------------------------	-----------------------------------

Table A.4. HET Radial Velocities for HD 19994

JD-2400000	Velocity ( $\text{m s}^{-1}$ )	Uncertainty ( $\text{m s}^{-1}$ )
53605.94910	-73.9	1.9
53605.95050	-79.5	2.0
53605.95189	-65.4	2.0
53608.93911	-65.8	2.1
53608.94050	-66.8	1.9
53608.94188	-64.2	1.8
53612.92670	-59.9	1.9
53612.92809	-60.3	1.9
53612.92948	-67.6	1.6
53627.89533	-57.5	1.9
53627.89669	-53.6	1.8
53627.89807	-56.2	2.0
53633.88582	-58.9	2.0
53633.88721	-41.0	2.1
53633.88860	-57.4	2.0
53655.82268	-12.5	1.6
53655.82406	-21.5	1.7
53655.82545	-21.9	1.7
53663.80647	-21.5	2.0
53663.80786	-23.6	1.8
53663.80926	-22.2	2.1
53665.79867	-21.0	2.1
53665.80005	-15.7	2.1
53665.80144	-27.4	1.9
53669.87559	-7.0	2.0
53669.87722	-2.2	2.0
53669.87860	-8.4	2.1
53675.84648	-0.6	2.4
53675.84787	-17.6	2.2
53675.84926	-13.0	2.3
53680.83519	11.3	2.0
53680.83658	3.7	2.2
53680.83796	2.5	1.8
53685.73742	-12.1	1.9
53685.73881	-16.8	1.9
53685.74020	-11.9	2.0
53691.71994	6.8	1.6
53691.72150	7.1	1.9
53691.72307	4.5	1.9
53696.79097	17.3	2.0

Table A.4 (cont'd)

JD-2400000	Velocity (m s <sup>-1</sup> )	Uncertainty (m s <sup>-1</sup> )
53696.79236	13.6	2.0
53696.79375	0.6	2.0
53701.77764	19.5	2.4
53701.77903	19.6	2.9
53701.78042	18.9	2.4
53703.78296	14.5	2.5
53703.78434	11.1	2.8
53703.78574	15.4	2.7
53689.80978	4.6	1.8
53689.81169	17.7	1.8
53689.81360	7.4	1.9
53694.72833	-1.5	2.4
53694.72971	-2.3	2.3
53694.73110	-2.8	2.5
53743.59110	30.1	2.3
53743.59301	25.5	3.0
53743.59492	32.4	2.5
53749.65406	29.8	2.5
53749.65649	24.0	2.2
53749.65892	28.4	2.3
53771.60206	27.1	3.1
53771.60345	20.7	3.2
53771.60483	12.3	3.0
53964.96284	-24.4	2.6
53964.96483	-25.9	2.0
53964.96676	-34.8	2.3
53966.95796	-32.5	1.9
53966.95936	-30.2	1.9
53966.96076	-38.0	2.0
53985.91256	-35.8	2.1
53985.91398	-43.0	2.0
53985.91540	-40.0	2.0
53987.90507	-47.6	2.3
53987.90646	-47.6	2.5
53987.90786	-44.6	2.2
53989.91834	-47.2	2.0
53989.91975	-53.3	2.1
53989.92116	-53.6	2.0
53996.96469	-29.3	2.0
53996.96612	-33.4	2.1

Table A.4 (cont'd)

JD-2400000	Velocity (m s <sup>-1</sup> )	Uncertainty (m s <sup>-1</sup> )
53996.96756	-36.2	2.0
53998.88853	-29.8	2.2
53998.88994	-35.0	2.2
53998.89135	-41.4	2.5
54000.87446	-48.4	2.0
54000.87586	-41.8	2.2
54000.87727	-33.7	2.1
54003.87467	-36.9	2.1
54003.87611	-40.0	2.1
54003.87755	-33.5	2.1
54008.85510	-35.1	2.0
54008.85651	-37.8	2.1
54008.85792	-36.9	1.9
54018.91454	-39.1	2.2
54018.91597	-34.7	2.0
54018.91741	-39.5	2.2
54047.74739	-26.0	2.2
54047.74879	-13.8	2.1
54047.75019	-23.1	2.3
54050.73272	-36.5	2.6
54050.73464	-31.3	2.2
54050.73658	-23.0	1.9
54055.73677	-33.4	1.9
54055.73819	-41.1	2.1
54055.73959	-31.8	2.0
54061.71928	-47.4	2.2
54061.72068	-55.8	2.5
54061.72209	-42.5	2.2
54065.69746	-34.3	2.1
54065.69886	-28.0	1.9
54065.70026	-29.5	2.1
54067.70825	-28.3	2.3
54067.70982	-32.4	2.6
54067.71141	-29.2	3.0
54069.67573	-5.2	2.1
54069.67713	-4.7	2.4
54069.67854	-5.6	3.8
54071.69353	-20.5	2.6
54071.69494	-25.8	2.1
54071.69636	-30.9	2.2

Table A.4 (cont'd)

JD-2400000	Velocity (m s <sup>-1</sup> )	Uncertainty (m s <sup>-1</sup> )
54071.76916	-24.2	2.2
54071.77056	-21.9	2.2
54071.77197	-21.8	2.1
54084.64070	-20.9	2.6
54084.64261	-18.0	2.5
54084.64453	-15.3	2.5
54105.57988	10.9	3.1
54105.58129	11.3	3.1
54105.58269	11.5	3.0
54122.62032	8.7	5.2
54122.62276	-0.1	4.0
54130.61454	-0.4	2.9
54130.61594	-4.7	2.8
54130.61735	2.3	2.9
54330.97937	-19.5	2.9
54330.98078	-17.2	5.0
54330.98218	-32.6	3.0
54330.98365	-34.1	2.6
54330.98507	-32.1	2.3
54330.98647	-27.5	3.1
54352.90305	-28.8	1.9
54352.90449	-33.0	2.3
54352.90591	-34.8	2.0
54362.88474	-4.2	1.8
54362.88624	-6.2	1.6
54362.88773	-1.6	1.6
54374.94126	-4.5	1.6
54374.94279	-3.8	1.4
54374.94432	1.6	1.5
54391.80813	-14.1	2.0
54391.80959	-16.5	1.7
54391.81105	-6.8	2.0
54396.88708	-5.8	2.0
54396.88855	-3.7	1.8
54396.89002	-3.8	1.8
54400.86990	-2.6	1.6
54400.87136	10.7	1.7
54400.87282	9.6	1.6
54402.77607	-38.9	1.8
54402.77754	-21.7	1.8

Table A.4 (cont'd)

JD-2400000	Velocity ( $\text{m s}^{-1}$ )	Uncertainty ( $\text{m s}^{-1}$ )
54402.77905	-20.2	1.5
54415.83142	-13.5	2.5
54415.83289	-1.9	2.2
54415.83436	-7.2	2.6
54419.82768	-9.0	2.4
54419.82914	-23.9	2.4
54419.83062	-24.5	2.2
54425.79355	-24.8	1.9
54425.79502	-34.0	2.1
54425.79650	-31.5	2.0
54428.70157	-25.5	1.8
54428.70304	-17.1	1.9
54428.70451	-10.3	2.0

Table A.5. HET Radial Velocities for HD 20367

JD-2400000	Velocity ( $\text{m s}^{-1}$ )	Uncertainty ( $\text{m s}^{-1}$ )
------------	--------------------------------	-----------------------------------

Table A.6. HET Radial Velocities for HD 23596

JD-2400000	Velocity (m s <sup>-1</sup> )	Uncertainty (m s <sup>-1</sup> )
53581.96328	45.6	3.3
53592.92364	94.0	2.1
53593.94151	87.3	2.2
53594.92991	94.3	2.0
53605.89024	73.7	2.6
53607.89908	82.2	2.3
53608.88232	89.2	2.3
53609.89877	80.7	2.5
53627.84647	71.7	2.3
53629.84900	69.4	2.5
53636.81718	63.0	2.8
53668.74440	83.5	3.0
53677.71324	86.4	2.5
53677.71785	89.1	2.5
53680.71210	84.5	2.5
53682.70333	93.6	2.4
53691.89176	78.1	3.4
53696.66233	74.3	2.8
53701.64835	82.3	2.8
53703.87816	72.0	2.8
53694.67217	85.7	2.8
53708.84886	68.0	2.7
53710.83928	65.0	2.7
53712.85135	65.4	3.5
53712.85591	64.2	4.1
53734.78649	70.0	2.8
53741.76529	68.0	2.8
53748.74395	63.2	3.3
53800.58922	45.2	2.8
53956.94364	-12.0	2.3
53958.92009	-4.0	2.0
53960.92698	-8.7	2.3
53969.92325	-32.1	3.8
53973.90239	-13.1	3.5
53976.89466	-19.2	2.5
54057.66123	-29.7	2.7
54059.65849	-23.6	2.7
54064.88448	-17.9	2.7
54066.88228	-28.1	2.2
54068.65155	-43.6	3.0

Table A.6 (cont'd)

JD-2400000	Velocity (m s <sup>-1</sup> )	Uncertainty (m s <sup>-1</sup> )
54071.64397	-39.0	2.5
54073.86583	-21.2	2.6
54084.59010	-34.4	2.6
54092.57210	-52.9	3.0
54094.56514	-47.4	3.2
54130.71379	-38.9	2.8
54136.69786	-48.6	2.9
54147.66241	-61.1	2.9
54156.63332	-61.9	3.1
54159.61613	-59.2	2.6
54328.92108	-125.2	2.6
54370.81150	-112.8	2.1
54392.99377	-106.6	2.4
54394.74004	-108.0	2.8
54400.73405	-106.4	2.4
54403.72902	-103.8	2.6
54411.92379	-96.5	2.4
54419.91222	-109.4	3.1
54419.91687	-95.6	3.0
54419.92185	-102.6	2.7
54425.66281	-100.3	2.4
54427.65183	-96.5	2.5
54427.65648	-90.2	2.6



Table A.7. HET Radial Velocities for HD 28185

JD-2400000	Velocity ( $\text{m s}^{-1}$ )	Uncertainty ( $\text{m s}^{-1}$ )
53653.92112	-65.1	1.8
53663.89377	-47.2	2.0
53697.80395	23.0	1.5
53701.79069	34.6	1.6
53692.82400	13.0	1.5
53695.80664	18.6	1.6
53996.97502	-66.5	1.9
53998.99146	-64.6	1.8
54044.85384	-21.8	2.0
54047.83682	-11.4	1.9
54051.83487	-11.7	1.7
54053.83800	-14.1	1.8
54061.80571	-5.5	1.7
54063.79720	-8.7	1.6
54066.79837	2.0	1.7
54068.78387	12.0	1.6
54071.77898	24.3	1.6
54073.77510	22.1	1.7
54075.76724	32.0	1.9
54105.68544	89.7	2.1
54107.68662	97.5	1.9
54110.67889	100.2	2.0
54142.58869	188.5	1.8
54368.95856	-45.6	1.5
54370.96073	-49.5	1.4
54374.94882	-50.7	1.4
54376.93838	-50.0	1.5
54381.94035	-50.7	2.5
54390.90631	-64.8	1.6
54396.89578	-52.7	1.6
54402.86922	-46.9	1.5
54404.86865	-48.8	1.5
54418.82544	-30.6	1.4
54425.80631	-41.1	2.8
54433.79452	-11.3	1.6
54400.87895	-55.1	1.5

Table A.8. HET Radial Velocities for HD 38529

JD-2400000	Velocity (m s <sup>-1</sup> )	Uncertainty (m s <sup>-1</sup> )
53341.77928	-115.9	2.2
53341.78052	-105.3	2.1
53341.78177	-120.3	2.3
53341.89723	-113.9	2.0
53341.89849	-115.1	2.0
53341.89973	-124.9	2.2
53355.84447	-93.2	2.2
53355.84573	-89.3	2.0
53355.84699	-101.7	2.1
53357.85835	-86.3	2.3
53357.85963	-89.6	2.2
53357.86091	-85.0	2.5
53358.72346	-76.5	2.1
53358.72474	-69.8	2.3
53358.72602	-89.4	2.2
53359.72791	-73.0	2.6
53359.72919	-72.8	2.9
53359.73046	-76.0	2.6
53360.84824	-50.9	2.6
53360.84952	-55.2	2.4
53360.85079	-51.7	2.5
53365.81548	13.7	2.7
53365.81675	20.8	3.0
53365.81802	15.5	2.9
53367.81136	-6.4	3.0
53367.81263	-7.2	2.5
53367.81391	-11.4	2.4
53369.69940	-77.6	2.7
53369.70068	-78.2	2.4
53369.70195	-76.3	2.7
53371.68350	-94.5	2.6
53371.68476	-90.2	2.4
53371.68602	-85.3	2.3
53377.78519	-6.4	3.0
53377.78647	-22.1	2.4
53377.78774	-12.0	2.6
53379.67453	9.0	2.1
53379.67580	12.9	2.1
53379.67708	6.0	2.1
53389.75434	-40.0	2.2

Table A.8 (cont'd)

JD-2400000	Velocity (m s <sup>-1</sup> )	Uncertainty (m s <sup>-1</sup> )
53389.75562	-49.0	2.2
53389.75690	-41.3	2.1
53390.76196	-37.4	2.2
53390.76323	-33.0	2.0
53390.76452	-32.3	2.3
53391.75659	-25.0	2.1
53391.75788	-34.6	2.5
53391.75915	-27.0	2.5
53392.75078	-19.5	2.1
53392.75206	-19.1	2.5
53392.75332	-30.8	2.5
53395.73818	0.7	2.1
53395.73942	-8.8	1.9
53395.74067	-3.7	2.0
53414.69257	-78.0	4.4
53414.69383	-96.1	2.8
53414.69509	-89.8	3.1
53416.68239	-72.6	2.4
53416.68363	-65.3	2.3
53416.68488	-66.8	2.8
53708.89287	63.0	2.1
53708.89444	64.4	2.1
53708.89599	72.4	2.2
53709.88540	62.9	1.7
53709.88697	51.6	1.9
53709.88853	60.8	2.1
53711.76603	20.8	1.9
53711.76759	20.6	2.0
53711.76916	15.2	1.8
53712.87361	-21.0	2.2
53712.87586	-26.2	2.6
53712.87812	-26.9	3.0
53724.83978	71.3	2.1
53724.84134	76.2	2.0
53724.84290	69.3	2.1
53730.71611	-10.8	1.7
53730.71767	-17.6	1.9
53730.71923	-24.1	2.1
53731.70718	0.6	2.2
53731.70873	-0.7	2.3

Table A.8 (cont'd)

JD-2400000	Velocity (m s <sup>-1</sup> )	Uncertainty (m s <sup>-1</sup> )
53731.71029	-6.1	2.0
53733.70479	26.2	2.2
53733.70635	28.4	2.3
53733.70791	23.8	2.0
53735.71231	55.5	2.4
53735.71388	60.6	2.4
53735.71544	52.1	2.1
53739.69038	58.0	1.9
53739.69217	65.1	1.9
53739.69396	59.6	2.0
53742.68414	-36.5	2.0
53742.68570	-33.1	1.9
53742.68726	-39.8	2.0
53751.77420	85.4	1.9
53751.77576	80.1	1.9
53751.77733	87.8	1.9
53752.76115	86.3	1.8
53752.76272	79.3	1.8
53752.76428	91.3	2.2
53753.77130	80.1	2.1
53753.77304	69.0	2.0
53753.77477	77.9	2.1
53754.75836	37.3	1.9
53754.76015	47.8	2.0
53754.76194	42.7	2.1
53755.74977	-2.8	1.4
53755.75133	-3.8	1.7
53755.75289	3.3	1.7
53757.63469	-40.5	1.8
53757.63903	-30.8	1.8
53757.64337	-33.4	1.8
53758.75497	-29.2	1.9
53758.75653	-27.4	1.8
53764.74385	61.1	1.9
53764.74541	53.4	1.7
53764.74697	55.8	2.1
53989.99740	65.6	1.8
53989.99900	72.2	1.7
53990.00058	68.2	1.9
54020.92265	128.3	1.9

Table A.8 (cont'd)

JD-2400000	Velocity ( $\text{m s}^{-1}$ )	Uncertainty ( $\text{m s}^{-1}$ )
54020.92423	130.6	1.9
54020.92580	128.2	2.1
54021.92027	147.7	2.0
54021.92187	139.4	2.0
54021.92346	143.9	2.1
54022.92534	161.5	2.7
54022.92691	146.8	2.9
54028.90147	64.9	1.9
54028.90308	65.1	2.0
54028.90465	71.8	1.9
54031.88053	96.9	2.0
54031.88210	95.2	2.1
54031.88368	102.7	1.7
54031.99558	110.3	2.0
54031.99714	103.6	2.0
54031.99872	110.8	1.8
54035.00503	168.0	1.7
54035.00730	165.2	1.9
54035.01004	165.7	2.1
54035.88547	173.0	2.1
54035.88704	168.4	2.2
54035.88861	167.5	2.1
54036.99644	183.6	2.3
54036.99807	180.2	2.3
54036.99970	181.8	2.2
54037.87386	191.9	1.8
54037.87622	190.5	1.9
54037.87853	195.2	1.8
54039.86754	188.8	1.9
54039.86912	187.8	1.9
54039.87070	186.5	2.0
54040.97106	155.4	2.0
54040.97263	152.3	1.9
54040.97422	158.5	2.0
54043.85779	93.5	2.0
54043.85975	98.8	1.7
54043.86171	95.7	2.0
54045.96938	125.4	1.8
54045.97096	130.5	1.8
54045.97254	133.4	1.6

Table A.8 (cont'd)

JD-2400000	Velocity ( $\text{m s}^{-1}$ )	Uncertainty ( $\text{m s}^{-1}$ )
54046.96391	146.9	2.1
54046.96549	141.8	2.1
54046.96706	141.8	2.1
54048.84061	155.3	1.9
54048.84219	154.7	1.8
54048.84376	151.4	2.0
54048.93826	159.0	2.2
54048.94087	155.0	2.3
54048.94349	163.9	2.1
54051.84146	170.5	1.8
54051.84309	183.9	2.1
54051.84468	179.0	1.8
54052.83712	189.9	1.9
54052.83905	186.8	2.0
54052.84098	187.4	2.1
54053.84496	185.0	2.1
54053.84658	187.3	1.9
54053.84819	190.7	2.3
54054.82922	169.1	1.7
54056.92131	95.5	2.2
54056.92288	81.7	2.0
54056.92446	89.9	2.2
54060.91262	111.5	2.2
54060.91432	103.2	1.9
54060.91613	103.9	2.0
54061.91037	122.5	1.9
54061.91194	130.4	1.9
54061.91353	125.9	1.8
54062.80548	137.7	1.8
54062.80705	142.9	1.8
54062.80864	147.5	1.8
54063.80708	159.1	1.7
54063.80866	163.8	1.8
54063.81024	160.5	1.7
54071.88873	98.3	1.9
54071.89032	98.8	1.8
54071.89190	98.4	2.0
54072.77223	97.7	1.9
54072.77450	95.0	2.0
54072.77677	100.4	1.9

Table A.8 (cont'd)

JD-2400000	Velocity (m s <sup>-1</sup> )	Uncertainty (m s <sup>-1</sup> )
54073.89184	104.1	1.9
54073.89412	111.8	2.0
54073.89640	98.7	2.2
54075.75489	138.6	1.8
54075.75720	138.0	1.7
54075.75951	138.5	1.7
54081.86616	236.9	2.2
54081.86774	238.7	2.0
54081.86932	236.7	2.0
54100.83060	114.5	2.5
54100.83214	108.7	2.4
54100.83372	110.4	2.6
54105.80307	194.9	1.9
54105.80467	193.8	2.2
54105.80625	196.3	1.9
54109.79957	236.2	2.2
54109.80132	234.1	2.1
54109.80307	238.6	2.1
54110.68917	232.8	2.1
54110.69101	231.7	2.1
54110.69286	232.5	2.2
54128.72812	123.6	1.9
54128.72969	125.3	1.9
54128.73132	125.0	2.0
54132.72385	161.9	2.7
54132.72555	158.3	3.0
54132.72724	175.8	4.2
54133.71585	170.8	2.1
54133.71881	171.8	2.0
54133.72178	169.6	2.0
54163.63471	220.4	2.0
54163.63702	215.3	1.9
54163.63933	218.7	2.0

Table A.9. HET Radial Velocities for HD 40979

JD-2400000	Velocity (m s <sup>-1</sup> )	Uncertainty (m s <sup>-1</sup> )
53341.72130	106.0	2.4
53346.73432	99.9	2.4
53348.70934	109.7	2.7
53350.72298	102.3	2.3
53352.92178	90.0	2.2
53357.93997	134.2	2.5
53355.68899	134.7	2.3
53359.68105	134.9	2.7
53365.67253	142.8	2.2
53367.66116	164.8	2.5
53370.62842	187.3	2.7
53372.64584	130.4	10.2
53377.85739	185.4	4.8
53379.86067	220.6	2.2
53381.63007	236.1	2.3
53383.84999	247.6	2.1
53389.59831	232.4	2.4
53391.57735	251.7	2.8
53395.58085	275.5	2.4
53399.80045	258.1	2.3
53401.80944	287.7	2.5
53416.73452	275.0	2.9
53422.72494	279.3	1.4
53424.74945	265.1	1.6
53429.74027	255.4	1.7
53444.68952	252.2	1.7
53615.96771	69.1	2.1
53623.94032	113.6	2.1
53628.94576	107.7	1.8
53629.92910	127.4	1.6
53633.91493	141.0	1.9
53638.90545	144.3	1.9
53646.89729	176.0	6.0
53651.88585	213.3	1.5
53655.87437	210.2	1.5
53663.84616	217.7	1.7
53666.83032	252.1	2.0
53668.81351	251.0	2.0
53669.82586	234.4	2.0
53676.82778	226.0	2.1



Table A.9 (cont'd)

JD-2400000	Velocity (m s <sup>-1</sup> )	Uncertainty (m s <sup>-1</sup> )
53678.79984	245.8	1.8
53681.80384	241.3	1.9
53683.80383	228.9	1.9
53685.79896	252.9	1.7
53687.78847	214.8	1.8
53691.77056	237.0	1.9
53696.97730	232.9	1.8
53701.75161	197.9	1.9
53703.96738	213.1	2.2
53689.78041	243.8	1.6
53693.99550	216.2	1.7
53705.96824	201.6	2.0
53708.94157	168.2	2.3
53710.94020	175.5	2.1
53721.90230	153.7	2.3
53723.90854	181.1	2.1
53728.67332	155.0	2.2
53730.65950	155.3	2.3
53734.65127	164.9	2.1
53743.62390	164.9	2.8
53748.60983	157.5	2.2
53753.84141	102.8	2.3
53713.94615	212.7	1.8
53713.94937	204.2	2.1
53799.71352	65.2	2.5
53801.70827	77.4	2.3
53987.95684	143.2	1.7
54014.89116	74.5	1.9
54021.86435	73.4	1.8
54037.82927	55.1	2.3
54044.80399	33.6	2.2
54046.80429	59.4	2.0
54053.00792	26.8	1.8
54054.99336	64.3	1.8
54057.99292	49.5	1.8
54061.01007	66.2	2.0
54068.73628	53.0	2.2
54076.71914	51.9	2.0
54101.86096	37.5	2.2
54129.79577	58.0	2.4

Table A.9 (cont'd)

JD-2400000	Velocity (m s <sup>-1</sup> )	Uncertainty (m s <sup>-1</sup> )
54132.78782	82.1	2.7
54134.78060	86.3	2.5
54136.76258	75.5	2.8
54155.73508	134.3	2.3
54166.70337	179.3	2.5
54177.65753	198.7	2.1
54190.62821	272.0	1.9
54370.91031	35.4	1.6
54397.83722	101.1	1.5
54402.82966	78.2	1.8
54414.00568	102.3	1.6
54419.02519	131.5	1.5

Table A.10. HET Radial Velocities for HD 72659

JD-2400000	Velocity ( $\text{m s}^{-1}$ )	Uncertainty ( $\text{m s}^{-1}$ )
53342.98059	5.5	2.5
53346.89816	-10.1	2.7
53348.89792	-3.4	2.5
53351.88711	2.9	2.6
53355.85531	-3.6	2.6
53357.86778	-2.8	2.5
53359.86322	13.8	3.2
53366.92023	5.5	3.2
53370.82512	-0.2	2.8
53375.89102	9.4	4.1
53377.89403	-0.4	2.5
53379.88562	0.9	2.5
53383.88589	-4.8	2.5
53389.78303	-3.7	2.5
53391.78123	1.0	3.0
53395.75846	3.5	2.6
53399.83667	9.2	2.5
53401.82272	10.2	3.0
53408.71984	0.9	2.9
53416.69679	8.2	2.8
53422.69865	1.4	1.9
53424.76127	3.0	2.0
53429.75413	5.8	1.8
53439.64547	3.1	1.9
53446.69267	14.3	2.0
53447.69980	3.2	2.0
53448.70841	-0.9	1.9
53708.90029	-4.1	2.5
53710.89277	-11.8	2.1
53723.86387	-18.7	2.3
53728.92778	-16.7	2.7
53734.90001	-20.6	2.7
53742.80266	-8.1	2.4
53746.79841	-12.6	2.5
53751.79314	-18.2	2.7
53753.79398	-15.0	2.7
53755.85771	-15.9	2.5
53713.96630	-12.4	2.4
53764.75640	-8.3	2.6
53773.72893	-3.2	2.5

Table A.10 (cont'd)

JD-2400000	Velocity (m s <sup>-1</sup> )	Uncertainty (m s <sup>-1</sup> )
53780.78984	-4.8	2.5
53802.64977	5.2	2.3
54050.97483	-22.1	2.4
54053.02653	-19.7	2.2
54056.95675	-22.6	2.2
54061.02215	-14.2	2.4
54064.00548	-18.5	2.3
54127.75916	-26.5	2.9
54158.75638	-32.5	2.5
54161.66311	-16.8	2.2
54167.72203	-17.4	2.2
54420.02055	-39.9	2.7
54431.99247	-36.4	2.2

Table A.11. HET Radial Velocities for HD 74156

JD-2400000	Velocity ( $\text{m s}^{-1}$ )	Uncertainty ( $\text{m s}^{-1}$ )
53342.89404	-106.9	8.0
53342.89663	-99.5	9.3
53342.89922	-91.1	8.0
53346.99870	-91.0	6.3
53347.00129	-86.7	6.5
53347.00388	-96.8	6.6
53355.83119	-79.1	6.8
53355.83378	-81.1	6.8
53355.83637	-83.9	8.1
53357.84262	-87.2	7.1
53357.84522	-100.1	7.3
53357.84783	-93.4	7.7
53359.84782	-75.8	9.9
53359.85043	-69.1	10.9
53359.85303	-75.9	10.7
53360.97183	-82.0	7.5
53360.97444	-95.8	7.2
53360.97705	-86.3	6.5
53364.97336	-109.4	8.0
53364.97939	-112.3	8.9
53365.82337	-108.2	9.6
53365.82597	-98.9	8.4
53365.82857	-105.4	8.7
53367.81847	-131.4	7.5
53367.82107	-130.8	6.7
53367.82368	-129.5	8.1
53383.91802	-113.2	8.1
53383.92083	-121.1	8.1
53383.92345	-119.4	8.5
53390.74987	-98.8	8.1
53390.75247	-91.9	8.2
53390.75508	-84.9	6.8
53448.73454	-30.0	4.1
53448.73888	-33.6	4.2
53448.74322	-20.9	5.0
53451.72836	-20.1	5.7
53451.73096	-33.8	5.6
53451.73356	-36.3	5.7
53476.64639	-165.3	5.5
53476.64920	-158.8	5.7

Table A.11 (cont'd)

JD-2400000	Velocity ( $\text{m s}^{-1}$ )	Uncertainty ( $\text{m s}^{-1}$ )
53476.65179	-165.8	5.8
53480.63719	-147.9	12.2
53481.62931	-128.8	5.2
53481.63192	-141.4	4.7
53481.63452	-128.8	5.0
53482.62873	-106.5	5.2
53482.63133	-110.5	5.1
53482.63394	-109.4	5.1
53664.99322	60.4	4.7
53664.99582	65.9	5.2
53664.99842	54.4	4.8
53675.96847	44.4	4.5
53675.97107	42.8	5.0
53675.97368	41.7	5.4
53676.98182	42.8	7.0
53676.98443	44.5	8.0
53676.98703	52.4	5.8
53682.94929	-65.6	6.1
53682.95189	-70.2	6.0
53682.95450	-52.2	6.3
53687.92892	-60.3	5.9
53687.93153	-53.3	4.9
53687.93414	-64.2	6.2
53689.92662	-16.1	6.2
53689.92922	-24.5	5.7
53689.93183	5.9	5.6
53691.91245	24.8	7.6
53691.91679	23.3	6.6
53691.92113	29.2	6.1
53697.90966	60.7	5.2
53697.91227	63.6	5.7
53697.91487	63.2	5.7
53703.88356	69.6	9.7
53703.88617	70.1	9.2
53703.88876	80.2	9.0
53708.87919	82.7	6.8
53708.88180	73.8	7.3
53708.88441	87.1	7.0
53710.87673	90.7	5.9
53710.87934	92.5	6.8

Table A.11 (cont'd)

JD-2400000	Velocity (m s <sup>-1</sup> )	Uncertainty (m s <sup>-1</sup> )
53710.88194	103.6	6.8
53718.01094	83.9	9.8
53718.01348	66.6	9.3
53718.01603	81.6	9.1
53724.82733	71.4	7.1
53724.82993	73.1	7.2
53724.83254	67.5	7.0
53728.82225	44.1	6.5
53728.82486	50.6	6.2
53728.82746	56.1	7.3
53731.96515	25.0	9.8
53731.96775	24.9	8.3
53731.97035	4.6	9.3
53733.79926	-31.1	8.4
53733.80186	-23.1	7.4
53733.80446	-30.3	6.4
53734.80689	-64.6	6.8
53734.80949	-61.8	6.7
53734.81208	-66.1	6.5
53736.94060	-146.5	9.0
53736.94379	-138.5	9.2
53736.94697	-140.0	7.2
53741.78065	14.3	6.8
53741.78326	3.6	6.0
53741.78586	13.1	6.8
53742.78090	13.9	7.0
53742.78352	22.5	6.0
53742.78613	14.7	6.0
53743.78712	29.8	6.5
53743.79031	33.1	7.5
53743.79349	30.9	7.2
53748.77007	69.9	6.9
53748.77267	67.0	7.5
53748.77531	67.2	8.9
53751.76512	81.3	7.3
53751.76772	77.6	6.6
53751.77032	86.4	7.1
53753.75967	91.5	6.8
53753.76343	88.7	6.4
53753.76718	80.1	7.1

Table A.11 (cont'd)

JD-2400000	Velocity (m s <sup>-1</sup> )	Uncertainty (m s <sup>-1</sup> )
53754.74497	91.3	7.4
53754.74931	85.3	6.4
53754.75365	77.7	6.8
53756.74604	96.6	8.3
53756.74865	77.1	8.2
53756.75125	89.8	7.9
53764.73311	79.3	6.7
53764.73571	91.5	7.0
53764.73831	82.9	6.2
53832.67292	62.8	5.4
53832.67552	67.4	5.3
53832.67812	54.6	5.6
53833.69234	40.9	6.0
53833.69668	58.3	6.1
53833.70015	54.9	6.6
53834.67134	39.8	5.6
53834.67429	35.8	5.9
53834.67724	46.3	5.5
53835.66415	27.4	5.5
53835.66675	14.5	5.5
53835.66934	24.6	6.6
53838.66116	-78.2	5.6
53838.66377	-83.1	5.8
53838.66638	-85.6	5.0
53841.64194	-88.3	9.0
53841.64455	-95.2	10.7
53841.64715	-106.9	12.5
53845.62939	18.8	7.7
53845.63199	25.7	5.4
53845.63459	32.7	6.0
54029.98695	52.0	6.8
54029.98957	62.2	5.7
54029.99219	75.2	5.6
54035.98765	47.4	6.8
54035.99026	44.2	5.9
54035.99288	34.3	7.2
54037.97106	40.8	6.8
54037.97380	56.0	6.1
54037.97648	40.8	5.8
54038.97424	29.6	4.8



Table A.11 (cont'd)

JD-2400000	Velocity (m s <sup>-1</sup> )	Uncertainty (m s <sup>-1</sup> )
54038.97806	35.8	4.7
54038.98187	33.7	4.5
54039.96751	19.3	5.7
54039.97014	29.7	5.8
54039.97276	28.5	6.9
54040.95589	5.2	4.9
54040.95851	13.3	5.6
54040.96114	6.1	5.2
54043.95863	-53.5	4.4
54043.96476	-56.3	4.4
54043.97089	-53.8	5.2
54044.95125	-105.2	5.7
54044.95388	-97.0	5.3
54044.95651	-98.2	5.5
54045.95338	-145.8	4.7
54045.95600	-148.9	5.1
54045.95862	-145.5	4.7
54046.94885	-164.7	6.6
54046.95147	-168.2	6.9
54046.95409	-152.6	8.3
54047.93762	-110.1	9.0
54047.94023	-124.1	8.1
54047.94285	-117.0	8.1
54050.95005	-26.9	5.6
54050.95325	-26.0	5.6
54050.95646	-20.9	5.5
54051.94172	-12.5	6.7
54051.94628	-17.2	6.0
54051.95063	-19.1	6.1
54052.93495	0.9	4.6
54052.93930	-0.3	4.7
54052.94365	-3.2	4.8
54073.87656	74.2	5.8
54073.88022	72.5	5.3
54073.88389	65.5	6.3
54079.86154	85.5	7.1
54079.86418	77.1	7.0
54079.86679	90.0	6.1
54087.84125	39.8	5.3
54087.84388	43.3	5.2

Table A.11 (cont'd)

JD-2400000	Velocity (m s <sup>-1</sup> )	Uncertainty (m s <sup>-1</sup> )
54087.84650	53.9	5.2
54090.83393	33.6	6.1
54090.83844	31.2	6.1
54090.84280	20.3	5.5
54106.78149	22.2	6.7
54106.78411	17.8	7.0
54106.78672	24.1	6.8
54109.78526	24.2	7.1
54109.78788	31.2	7.3
54109.79079	20.7	7.0
54109.79410	34.4	6.8
54110.79650	31.7	7.0
54110.79981	34.7	6.5
54110.80336	32.8	6.6
54129.86616	51.2	6.6
54129.87051	48.3	6.6
54129.87490	49.6	7.0
54130.73774	53.7	6.7
54130.74036	40.0	6.8
54130.74299	46.6	7.1
54133.84308	25.3	7.7
54133.84698	11.2	7.0
54133.85087	21.3	6.9
54134.72342	19.5	6.9
54134.72603	32.1	7.2
54134.72865	27.5	7.3
54135.86349	36.2	7.5
54135.86669	39.5	7.3
54135.86989	33.4	7.2
54136.83851	22.7	8.2
54136.84112	28.3	8.2
54136.84376	37.9	7.7
54148.67505	-152.7	7.4
54148.67767	-147.2	8.3
54148.68029	-131.7	6.8
54156.65796	-14.9	7.5
54156.66058	-6.7	7.6
54156.66320	-7.2	7.3
54159.77718	8.8	7.3
54159.77984	13.6	6.7

Table A.11 (cont'd)

JD-2400000	Velocity (m s <sup>-1</sup> )	Uncertainty (m s <sup>-1</sup> )
54159.78249	10.7	6.4
54166.76062	42.8	6.5
54166.76336	42.8	5.9
54166.76610	38.5	6.3
54167.75347	39.0	6.2
54167.75867	45.8	5.9
54167.76389	44.3	6.2
54211.62592	19.6	6.3
54211.63030	28.9	5.9
54211.63469	15.6	6.8
54231.59552	78.9	6.9
54231.59849	44.6	5.0
54231.60146	48.8	5.4
54231.60460	50.3	5.1

Table A.12. HET Radial Velocities for HD 80606

JD-2400000	Velocity (m s <sup>-1</sup> )	Uncertainty (m s <sup>-1</sup> )
53346.88103	-20.8	3.0
53358.02089	-49.5	2.7
53359.82400	-60.4	3.0
53361.02985	-64.7	2.5
53365.03079	-77.4	2.4
53373.98282	-88.4	3.0
53377.80112	-105.5	2.4
53379.75230	-109.3	2.7
53389.74170	-115.3	2.5
53391.74400	-129.4	2.4
53395.72763	-146.4	2.3
53399.72518	-158.4	2.5
53401.72497	-174.7	2.7
53414.67819	-219.8	3.0
53421.85529	261.0	2.2
53423.86650	322.1	2.0
53424.85231	245.9	2.1
53432.87120	87.5	1.9
53433.60628	70.0	2.1
53446.79322	4.5	1.9
54161.85400	-109.5	2.8
54166.83797	-119.3	2.4
54186.76189	-184.2	2.3

Table A.13. HET Radial Velocities for HD 89744

JD-2400000	Velocity ( $\text{m s}^{-1}$ )	Uncertainty ( $\text{m s}^{-1}$ )
53709.89685	-14.5	2.9
53723.85188	-54.1	2.7
53723.85367	-62.3	3.0
53723.85546	-56.2	2.8
53727.84394	-67.6	3.0
53727.84573	-65.7	3.0
53727.84752	-62.3	3.0
53736.81887	-82.4	3.1
53736.82100	-77.8	3.2
53736.82315	-91.5	2.9
53738.03261	-60.9	3.4
53738.03441	-66.3	3.3
53738.03620	-60.8	3.1
53738.80860	-71.0	3.3
53738.81040	-80.9	3.2
53738.81219	-69.9	3.3
53734.81795	-77.6	3.1
53734.81973	-69.5	3.7
53734.82152	-78.4	3.1
53742.79119	-77.7	3.5
53742.79299	-81.5	3.1
53742.79479	-79.5	3.2
53751.78199	-78.0	3.5
53751.78378	-78.3	3.0
53751.78558	-83.4	3.0
53753.78155	-96.1	2.8
53753.78381	-96.6	3.3
53753.78607	-89.7	3.0
53755.76038	-104.4	3.5
53755.76218	-98.6	3.4
53755.76397	-105.9	3.3
53746.81506	-85.2	2.7
53746.81778	-78.1	3.0
53746.82051	-71.6	2.9
53757.77002	-109.3	3.1
53757.77181	-104.6	3.1
53757.77360	-125.0	3.0
53797.64609	-254.3	3.9
53797.64834	-278.8	3.4
53797.65059	-276.9	3.5

Table A.13 (cont'd)

JD-2400000	Velocity ( $\text{m s}^{-1}$ )	Uncertainty ( $\text{m s}^{-1}$ )
53809.62428	-482.8	2.9
53809.62700	-474.3	3.0
53809.62972	-482.8	3.2
53837.76359	-140.1	3.9
53837.76670	-155.8	3.5
53837.78731	-149.1	3.3
53837.79077	-130.0	3.2
53866.69987	-42.2	1.9
53866.70329	-37.7	2.2
53866.70670	-35.0	2.0
53868.68349	-59.7	5.3
53868.68562	-33.6	3.7
53868.68777	-64.8	13.3
53875.66956	-36.2	1.9
53883.65565	-31.4	2.0
53883.65837	-29.9	2.1
53883.66109	-16.3	2.0
53890.63776	-31.9	2.7
53890.63954	-25.5	2.0
53890.64134	-23.4	2.4
53893.62959	-29.8	2.7
53893.63139	-19.5	2.0
53893.63318	-24.0	2.4
54047.94811	-200.0	6.3
54047.94991	-176.5	6.2
54047.95172	-190.8	5.6
54050.96248	-237.4	3.2
54050.96453	-246.1	2.8
54050.96657	-253.3	2.9
54052.96488	-257.6	2.5
54052.96762	-263.2	2.9
54052.97035	-275.0	2.8
54056.94606	-305.0	2.7
54056.94786	-301.3	3.2
54056.94964	-309.9	3.0
54063.92981	-421.5	3.1
54063.93166	-431.0	2.7
54063.93348	-435.6	2.7
54073.91213	-518.0	3.7
54073.91476	-524.6	3.4

Table A.13 (cont'd)

JD-2400000	Velocity (m s <sup>-1</sup> )	Uncertainty (m s <sup>-1</sup> )
54073.91739	-526.7	3.6
54122.01039	-51.6	3.3
54122.01243	-51.0	3.3
54122.01447	-49.0	3.4
54129.74214	-54.6	3.3
54129.74491	-59.3	3.6
54129.74768	-48.6	3.3
54160.65850	-8.0	3.8
54160.66031	-1.5	3.5
54160.66212	-38.7	3.7
54163.66458	-39.2	3.8
54163.66643	-21.6	3.9
54163.66828	-28.4	3.9
54165.88148	-27.0	3.6
54421.94811	-24.6	2.3
54421.94997	-28.4	2.9
54421.95190	-26.9	2.7

Table A.14. HET Radial Velocities for 47 UMa

JD-2400000	Velocity (m s <sup>-1</sup> )	Uncertainty (m s <sup>-1</sup> )
53313.99226	23.4	2.0
53313.99417	22.0	2.2
53313.99608	19.8	2.2
53314.99013	16.5	1.6
53314.99204	16.7	1.7
53317.98892	11.4	2.0
53317.99083	4.6	1.9
53317.99274	4.6	1.9
53334.94874	14.7	1.7
53334.95296	13.6	1.8
53334.95591	14.5	1.9
53335.94414	17.9	1.7
53335.94709	15.9	1.7
53335.95003	16.1	1.5
53338.92570	18.8	2.4
53338.92757	18.8	4.0
53338.92947	5.7	2.8
53338.93800	7.0	2.4
53338.93991	15.6	2.2
53338.94181	21.7	2.4
53338.94426	20.8	2.4
53338.94617	6.6	2.4
53338.94808	11.1	2.6
53340.91533	18.2	2.1
53340.91724	16.9	2.0
53340.91915	15.3	1.8
53346.92016	13.2	1.9
53346.92207	8.3	1.9
53346.92399	17.0	1.7
53348.90749	14.3	2.3
53348.90940	17.5	2.3
53348.91131	17.4	2.0
53350.91700	8.6	2.0
53357.87818	2.7	2.4
53357.88009	16.0	2.4
53357.88200	11.0	2.0
53359.87352	10.4	2.7
53359.87543	14.0	2.9
53359.87734	11.3	3.0
53365.86302	5.9	3.0

Table A.14 (cont'd)

JD-2400000	Velocity (m s <sup>-1</sup> )	Uncertainty (m s <sup>-1</sup> )
53365.86489	13.7	3.1
53365.86680	10.8	2.7
53367.86199	14.1	2.3
53367.86390	8.7	2.5
53367.86581	9.3	2.0
53371.85542	0.2	2.3
53371.85734	5.4	3.1
53371.85925	9.2	2.5
53373.85760	6.3	2.9
53373.85951	-7.0	5.2
53377.83191	1.3	2.4
53377.83382	6.5	2.3
53377.83572	9.5	2.4
53379.84887	2.5	2.6
53379.85077	0.0	2.4
53379.85268	7.2	2.5
53389.79571	-3.3	2.4
53389.79762	-8.8	2.6
53389.79953	-6.1	2.4
53391.79095	-4.8	2.7
53391.79286	2.2	2.9
53391.79477	-1.5	2.3
53395.77630	4.8	2.3
53395.77820	-0.9	2.3
53395.78010	4.0	2.2
53400.99280	-7.3	2.3
53400.99471	-9.4	2.1
53400.99662	-11.3	2.4
53408.76777	-11.8	2.6
53408.76968	-9.6	2.9
53408.77159	-13.6	2.8
53414.72643	-5.6	2.5
53414.72833	0.1	2.6
53414.73024	-5.2	2.5
53416.70849	-13.4	2.6
53416.71039	-11.5	2.4
53416.71231	-8.8	2.7
53421.93925	-9.0	1.8
53421.94116	-5.4	1.8
53421.94307	-6.4	1.8



Table A.14 (cont'd)

JD-2400000	Velocity (m s <sup>-1</sup> )	Uncertainty (m s <sup>-1</sup> )
53423.70291	-5.9	1.7
53423.70482	-6.5	1.8
53423.70672	-12.5	1.9
53429.91362	-7.6	1.6
53429.91553	-2.0	1.6
53429.91744	-8.0	1.7
53432.90613	-8.0	1.7
53432.90803	-9.9	1.6
53432.90994	-8.8	1.7
53433.90512	-6.9	1.7
53433.90697	-5.9	1.6
53433.90836	-6.9	1.7
53437.65944	-5.4	2.3
53437.66101	-6.8	1.8
53437.66292	-6.4	1.7
53437.66489	-7.2	1.6
53439.65764	-2.4	1.7
53439.65955	0.0	1.7
53439.66146	-6.2	1.6
53440.89736	2.8	1.8
53440.90030	0.8	2.0
53440.90324	3.1	1.9
53476.80210	-15.5	1.6
53476.80401	-20.1	1.8
53476.80591	-19.3	1.7
53479.77654	-20.4	1.9
53479.77844	-18.5	1.7
53479.78035	-20.1	1.7
53481.76429	-24.7	1.6
53481.76620	-27.0	1.7
53481.76811	-26.7	1.7
53486.77539	-25.0	1.8
53486.77731	-23.2	1.8
53486.77922	-21.1	1.7
53488.76596	-28.8	1.8
53488.76788	-25.3	1.7
53488.76979	-25.8	1.6
53512.68994	-37.2	2.1
53512.69186	-39.1	1.8
53512.69377	-37.8	2.0

Table A.14 (cont'd)

JD-2400000	Velocity ( $\text{m s}^{-1}$ )	Uncertainty ( $\text{m s}^{-1}$ )
53526.63295	-55.3	2.0
53526.63493	-55.4	2.0
53526.63683	-57.1	2.0
53526.63848	-55.8	2.3
53526.63970	-59.4	2.6
53526.64091	-54.9	2.3
53539.63732	-63.4	2.3
53539.63923	-63.9	2.2
53539.64114	-69.2	2.2
53708.91866	-34.2	2.3
53708.92005	-30.0	2.0
53708.92143	-34.3	2.2
53709.92062	-31.1	2.3
53709.92254	-40.0	2.2
53709.92445	-33.4	2.0
53710.91178	-27.6	1.9
53710.91317	-31.3	2.0
53710.91457	-30.3	1.8
53711.92767	-24.4	3.0
53711.92906	-20.4	3.5
53711.93044	-27.1	3.4
53711.93510	-33.8	1.9
53711.93649	-32.9	1.9
53711.93788	-34.0	2.0
53721.87890	-28.7	2.5
53721.88029	-24.5	2.2
53721.88169	-28.7	2.2
53723.86895	-24.3	2.2
53723.87033	-28.7	2.3
53723.87172	-28.7	2.2
53725.86008	-23.4	2.5
53725.86147	-17.2	2.3
53725.86285	-18.0	2.4
53736.83987	-28.0	2.5
53736.84137	-29.5	2.4
53736.84288	-29.0	2.4
53738.82611	-20.0	2.3
53738.82750	-30.4	2.4
53738.82890	-23.7	2.4
53734.87673	-24.4	2.3

Table A.14 (cont'd)

JD-2400000	Velocity ( $\text{m s}^{-1}$ )	Uncertainty ( $\text{m s}^{-1}$ )
53734.87812	-29.5	2.3
53734.87951	-23.7	2.5
53742.81869	-24.1	2.5
53742.82008	-29.1	2.6
53742.82147	-18.7	2.4
53743.81885	-30.1	2.6
53743.82024	-29.6	2.3
53743.82163	-29.1	2.6
53744.82153	-26.8	2.2
53744.82292	-27.2	2.1
53744.82431	-26.5	2.1
53751.79848	-32.8	2.6
53751.79987	-30.6	2.9
53751.80126	-34.8	2.5
53746.80595	-27.4	2.4
53746.80758	-29.1	2.3
53746.80920	-21.1	2.2
53757.03611	-17.2	2.3
53757.03749	-15.4	2.2
53757.03887	-22.4	2.5
53771.75959	-24.7	2.5
53771.76109	-32.2	2.6
53771.76259	-26.3	2.6
53775.73900	-4.0	2.5
53775.74040	-20.8	2.4
53775.74179	-14.0	2.4
53777.96474	-7.1	2.8
53777.96664	-15.0	2.8
53777.96855	-10.6	2.8
53779.96267	-11.5	2.5
53779.96405	-13.8	2.6
53779.96543	-10.2	2.7
53786.70391	-27.7	2.9
53786.70737	-20.0	2.7
53786.71085	-17.5	2.9
53795.91621	-20.8	2.2
53795.91760	-16.7	2.3
53795.91899	-15.7	2.0
53795.92042	-16.4	2.3
53795.92181	-21.9	2.3

Table A.14 (cont'd)

JD-2400000	Velocity (m s <sup>-1</sup> )	Uncertainty (m s <sup>-1</sup> )
53795.92320	-22.6	2.5
53797.66582	-12.5	2.3
53797.66773	-25.4	3.1
53797.66964	-19.0	3.1
53894.65375	9.9	2.0
53894.65514	8.4	1.9
53894.65653	17.3	1.9
53901.63954	7.5	2.4
53901.64093	8.4	1.9
53901.64232	9.9	2.1
54047.98595	52.2	2.8
54047.98735	44.9	2.6
54047.98875	42.3	2.6
54050.99164	41.3	2.0
54050.99305	48.1	1.8
54050.99445	46.5	1.9
54052.99062	49.7	1.9
54052.99278	49.9	1.7
54052.99493	52.5	1.9
54054.97779	47.2	1.9
54054.97971	47.9	2.2
54054.98167	46.6	2.0
54056.96083	45.7	1.8
54056.96223	51.8	2.1
54056.96363	50.5	1.8
54121.80961	62.8	2.5
54121.81211	53.1	2.4
54121.81456	58.3	2.6
54129.77316	49.5	2.8
54129.77513	56.0	2.8
54129.77709	50.7	2.4
54157.69951	70.8	2.5
54157.70091	73.3	2.0
54157.70232	69.9	2.4
54160.68305	62.3	2.6
54160.68446	60.4	2.5
54160.68586	62.5	2.3
54165.91047	58.2	2.3
54165.91204	55.4	2.4
54165.91361	59.1	2.4

Table A.14 (cont'd)

JD-2400000	Velocity (m s <sup>-1</sup> )	Uncertainty (m s <sup>-1</sup> )
54419.99164	6.9	2.3
54419.99311	20.0	2.6
54419.99457	4.6	2.9
54419.99604	13.1	2.6
54419.99749	24.3	2.5
54419.99896	3.5	2.8
54431.94252	7.9	2.0
54431.94398	5.6	1.8
54431.94544	3.3	1.9

Table A.15. HET Radial Velocities for HD 106252

JD-2400000	Velocity (m s <sup>-1</sup> )	Uncertainty (m s <sup>-1</sup> )
53351.00010	-47.9	2.0
53392.87552	35.4	2.0
53396.02801	32.5	1.9
53399.86570	57.4	1.9
53422.81038	76.5	1.5
53423.95949	66.9	1.3
53424.95405	66.2	1.3
53429.93416	75.3	1.6
53436.93141	85.2	1.6
53439.93691	87.6	1.6
53440.93473	73.7	2.4
53448.72404	100.4	1.2
53449.71115	98.0	1.5
53450.72302	92.7	1.4
53451.72210	86.9	1.6
53452.88054	90.8	1.4
53454.86997	84.0	1.5
53455.86893	99.1	1.4
53457.70318	99.9	1.4
53480.62813	107.5	1.7
53487.78674	101.5	1.6
53498.76669	110.2	1.6
53543.64221	68.4	1.8
53736.92178	39.6	2.0
53736.92786	38.1	2.0
53743.93096	42.6	2.1
53744.90904	36.6	1.6
53745.89603	39.4	1.7
53753.89366	38.9	1.5
53755.88492	34.4	1.4
53758.87460	24.2	1.6
53765.02009	27.5	1.7
53779.82268	20.8	2.1
53796.76996	8.8	1.9
53866.75798	-1.0	1.9
53868.73636	4.4	1.4
53877.71039	-7.3	1.6
53891.67012	-9.0	1.6
54090.96158	-54.0	1.6
54110.90994	-47.6	1.7

Table A.15 (cont'd)

JD-2400000	Velocity (m s <sup>-1</sup> )	Uncertainty (m s <sup>-1</sup> )
54122.04519	-58.9	1.7
54161.76867	-78.5	2.0
54191.69138	-69.4	1.4

Table A.16. HET Radial Velocities for HD 108874

JD-2400000	Velocity (m s <sup>-1</sup> )	Uncertainty (m s <sup>-1</sup> )
53370.93479	12.9	2.0
53377.90734	12.4	2.3
53392.86111	21.1	2.4
53399.84978	20.3	2.3
53423.00572	17.5	1.6
53424.00026	16.9	1.6
53429.76827	13.6	1.7
53446.93347	20.1	1.9
53449.92196	19.3	1.6
53451.70786	17.7	1.7
53452.91476	12.3	1.6
53454.90261	11.5	1.8
53455.91231	6.7	1.8
53457.89845	6.3	1.6
53460.88699	10.8	1.8
53708.98585	-6.3	2.0
53723.95560	4.0	1.7
53730.92665	7.7	2.1
53751.89671	21.8	1.9
53753.88047	18.5	2.2
53755.87205	24.5	1.8
53773.81280	24.5	2.2
53806.96496	19.5	2.2
53847.61993	21.2	2.0
53866.78797	2.7	2.1
53868.77287	3.6	1.9
53880.76028	-4.8	2.3
53895.71194	-4.9	2.0
53897.70685	2.0	1.8
53912.66615	-15.8	2.1
54080.96833	-5.7	1.8
54084.96842	-2.4	1.9
54109.89738	15.4	1.9
54127.85761	25.1	2.2
54142.02401	30.0	2.2
54158.76779	38.3	2.3
54160.75929	40.5	2.2
54162.75513	31.4	2.1
54180.92025	41.5	2.0
54190.88453	42.0	2.2

Table A.16 (cont'd)

JD-2400000	Velocity (m s <sup>-1</sup> )	Uncertainty (m s <sup>-1</sup> )
------------	-------------------------------	----------------------------------

Table A.17. HET Radial Velocities for HD 114783

JD-2400000	Velocity (m s <sup>-1</sup> )	Uncertainty (m s <sup>-1</sup> )
53366.02839	-30.5	1.9
53368.02525	-28.4	1.8
53374.00882	-24.8	1.9
53378.99750	-29.2	1.6
53395.95201	-37.3	1.5
53399.94906	-31.2	1.5
53415.90535	-39.2	1.8
53416.96080	-40.3	1.9
53421.88527	-24.9	1.6
53423.88025	-34.7	1.5
53429.88531	-30.0	1.7
53436.92048	-31.2	1.4
53440.91862	-40.5	1.9
53446.81643	-32.2	1.5
53447.81352	-26.5	1.6
53448.81555	-22.9	1.6
53450.81211	-24.2	1.4
53451.82012	-23.2	1.4
53452.81032	-21.0	1.4
53455.78717	-19.6	1.5
53779.91198	-3.4	1.7
54106.00717	16.5	1.4
54121.96750	17.7	1.2
54127.95124	20.6	1.5
54130.94440	16.9	1.5
54140.98702	4.3	1.6
54143.92794	11.2	1.7
54156.87064	20.6	1.6
54158.87301	13.8	1.7
54163.85683	15.5	1.8
54168.83901	22.3	1.8
54186.78881	25.9	1.6
54191.77547	23.9	1.5
54097.02928	9.9	1.3



Table A.18. HET Radial Velocities for HD 128311

JD-2400000	Velocity (m s <sup>-1</sup> )	Uncertainty (m s <sup>-1</sup> )
53462.96527	-63.8	1.5
53479.73181	-89.5	1.4
53479.89952	-90.8	1.5
53480.91902	-74.1	1.6
53482.89103	-89.9	1.4
53486.72671	-105.4	1.4
53488.70965	-119.0	1.7
53509.81664	-113.4	1.6
53510.82254	-121.0	1.6
53511.80800	-121.7	1.7
53512.80394	-119.4	1.5
53539.74332	-161.3	1.7
53541.75416	-128.9	2.1
53541.75909	-120.6	3.0
53542.74601	-135.0	1.9
53544.73511	-150.5	1.9
53550.71539	-141.5	1.8
53554.69916	-143.2	1.7
53565.69081	-152.0	2.2
53570.66963	-120.2	2.2
53776.92892	10.8	1.6
53788.90110	-3.5	1.9
53816.97394	-13.5	1.8
53824.80309	-21.8	1.6
53837.91730	-46.6	1.7
53842.75039	4.6	1.7
53844.91973	-26.7	1.6
53846.91450	-54.4	1.4
53888.79633	-36.0	1.3
53895.75921	-103.3	1.7
53897.76919	-58.3	1.5
53899.76175	-20.6	1.5
53911.71053	-27.3	1.3
53926.66439	-86.9	1.8
53933.66149	-17.0	1.4
54107.99948	50.4	2.1
54108.00385	55.6	2.0
54108.00821	59.3	2.1
54110.00567	63.3	1.8
54110.00828	63.2	1.6

Table A.18 (cont'd)

JD-2400000	Velocity ( $\text{m s}^{-1}$ )	Uncertainty ( $\text{m s}^{-1}$ )
54110.01090	73.7	1.7
54110.99937	69.3	1.8
54111.00546	63.5	1.7
54111.01155	63.0	1.7
54130.95917	72.3	1.8
54130.96180	65.2	1.8
54130.96443	68.1	1.7
54133.93596	77.3	2.0
54133.93944	80.5	2.1
54133.94293	76.2	2.0
54135.93949	95.1	2.0
54135.94222	101.2	1.8
54135.94497	87.7	2.1
54138.92207	72.9	1.9
54138.92468	72.4	1.8
54138.92730	71.0	1.7
54139.92395	66.9	1.9
54139.92657	63.6	1.9
54139.92918	59.7	1.9
54141.92310	76.7	1.7
54141.92573	76.8	1.7
54141.92835	76.6	1.7
54161.87234	75.8	1.7
54164.85995	97.4	1.7
54168.84642	112.4	1.9
54173.99550	83.5	1.8
54174.99073	102.5	1.8
54156.87572	106.8	2.1
54156.87834	96.4	2.0
54156.88096	103.1	2.1
54157.88490	118.2	2.1
54157.88752	112.6	2.5
54157.89015	111.7	2.1
54158.87835	102.5	1.9
54158.88100	107.3	2.0
54158.88365	99.7	1.8
54160.87365	86.6	2.0
54160.87801	78.8	2.1
54160.88236	76.0	2.2
54161.86292	68.1	2.1

Table A.18 (cont'd)

JD-2400000	Velocity ( $\text{m s}^{-1}$ )	Uncertainty ( $\text{m s}^{-1}$ )
54161.86555	74.7	2.2
54161.86817	76.5	2.3
54163.86393	97.3	2.0
54163.86833	90.7	1.9
54163.87272	96.4	1.8
54173.82600	83.7	1.9
54173.82977	89.6	2.0
54173.83355	74.1	2.0
54177.00038	113.3	1.9
54177.00300	112.0	1.6
54177.00563	115.1	1.6
54191.79025	134.2	1.5
54191.95069	135.1	1.5
54186.79737	101.7	1.6
54186.80132	101.1	1.8
54186.80527	100.3	1.6
54190.79962	131.4	1.8
54190.80341	130.4	1.7
54190.80719	124.7	1.9
54249.78934	92.7	1.6
54211.91317	119.4	2.0
54211.91614	129.0	1.9
54211.91911	125.0	1.9
54214.71240	123.7	1.9
54214.71537	131.0	1.9
54214.71833	127.3	1.7
54216.71952	116.9	1.4
54216.72250	100.4	1.6
54216.72548	106.6	1.6
54217.87413	98.2	1.6
54217.87847	105.1	1.8
54217.88284	98.0	1.8
54221.69800	116.2	1.9
54221.70096	116.2	1.7
54221.70393	114.5	1.6
54222.71394	118.1	1.6
54222.71691	114.8	1.5
54222.72000	115.8	1.5
54223.87791	119.6	1.6
54223.88092	119.5	1.7

Table A.18 (cont'd)

JD-2400000	Velocity (m s <sup>-1</sup> )	Uncertainty (m s <sup>-1</sup> )
54223.88392	119.6	1.9
54231.84710	109.0	1.8
54231.85144	117.1	1.8
54231.85440	108.7	1.8
54232.84840	108.6	1.7
54232.85135	113.3	1.6
54232.85433	108.2	1.5
54249.79371	83.6	2.1
54249.79669	84.7	1.6
54249.79966	73.6	2.2
54250.78773	88.2	1.5
54250.79070	90.1	1.7
54250.79368	89.3	1.5
54251.62771	76.3	1.6
54251.63068	74.8	1.6
54251.63365	69.6	1.6
54253.78320	104.6	1.7
54253.78617	95.8	1.6
54253.78913	92.0	1.8
54254.79061	90.6	1.5
54254.79359	90.1	1.6
54254.79658	94.9	1.7
54255.77746	85.4	1.8
54255.78044	79.4	1.8
54255.78342	86.3	1.8
54279.73005	54.8	1.4
54318.61493	-46.1	1.9
54257.77545	102.3	1.7
54257.77841	105.2	1.8
54257.78137	99.2	1.7
54265.75050	65.2	1.6
54265.75347	72.4	1.8
54265.75644	72.0	1.6
54267.74562	68.9	1.7
54267.74859	76.1	2.0
54267.75156	79.2	1.8
54276.71609	51.0	1.7
54276.71906	48.2	1.9
54276.72203	52.5	1.7
54278.71057	50.3	1.9

Table A.18 (cont'd)

JD-2400000	Velocity (m s <sup>-1</sup> )	Uncertainty (m s <sup>-1</sup> )
54278.71354	49.2	1.7
54278.71651	49.7	1.5
54279.71973	52.8	1.7
54279.72271	56.7	1.7
54279.72568	60.0	1.7

Table A.19. HET Radial Velocities for HD 130322

JD-2400000	Velocity (m s <sup>-1</sup> )	Uncertainty (m s <sup>-1</sup> )
53471.80557	-33.0	1.2
53481.88526	-57.8	1.2
53486.85864	142.3	1.2
53488.75815	118.9	1.1
53509.79117	125.0	1.2
53512.78123	-41.7	1.1
53527.74971	33.2	1.2
53542.69985	58.7	1.3
53543.70614	6.5	1.1
53550.70420	111.3	1.3
53837.89677	44.9	1.2
53842.88880	80.7	1.1
53868.80896	-28.7	1.2
53882.78043	139.5	1.2
53897.72684	-5.5	1.2
53900.72079	-35.2	1.1
53936.63557	127.7	1.3
54122.01834	39.0	1.2
54128.00335	100.5	1.2
54135.98084	-52.5	1.1
54139.97029	143.3	1.3
54140.96840	146.7	1.0
54144.96962	-50.3	1.1
54157.01611	-62.9	1.2
54158.92425	18.4	1.2
54163.92465	90.4	1.4
54168.90656	-14.0	1.1
54173.98269	121.9	1.2
54176.87914	-37.1	1.1
54191.92631	77.6	1.1

Table A.20. HET Radial Velocities for HD 136118

JD-2400000	Velocity (m s <sup>-1</sup> )	Uncertainty (m s <sup>-1</sup> )
53472.82891	44.0	2.8
53472.83250	43.1	3.0
53480.89983	30.9	2.6
53482.87891	37.2	2.4
53482.88244	32.9	2.2
53486.86878	29.7	3.1
53487.88137	26.0	2.6
53487.88490	33.0	2.8
53509.80853	10.9	2.6
53527.76132	-15.6	3.2
53527.76486	-6.1	3.2
53544.72488	-28.4	3.5
53544.72840	-20.8	3.0
53575.62795	-63.4	3.9
53575.63150	-45.4	3.4
53758.03539	-61.6	3.7
53766.02403	-52.4	4.1
53766.02629	-71.4	4.1
53766.02855	-75.1	3.8
53767.02021	-52.9	3.8
53778.99248	-60.6	4.1
53779.98920	-62.7	3.9
53803.01595	-59.3	3.0
53805.98952	-79.5	3.1
53808.91057	-64.8	3.7
53820.88177	-77.3	3.4
53842.89836	-77.4	3.1
53757.03982	-82.9	4.5
53757.04207	-59.6	4.2
53757.04432	-53.5	4.3
53787.97854	-63.9	3.6
53787.98166	-73.2	3.3
53787.98484	-68.3	3.6
53808.90298	-48.7	4.0
53808.90523	-73.3	4.1
53808.90749	-68.3	3.7
53809.90641	-64.3	5.4
53809.90878	-73.5	4.1
53809.91116	-67.9	4.1
53815.88448	-60.1	4.1

Table A.20 (cont'd)

JD-2400000	Velocity ( $\text{m s}^{-1}$ )	Uncertainty ( $\text{m s}^{-1}$ )
53815.88767	-68.0	3.5
53815.89085	-71.1	4.0
53816.89525	-51.5	3.7
53816.89751	-73.6	3.6
53816.89979	-73.3	4.2
53816.96296	-57.7	3.7
53816.96521	-75.1	4.0
53816.96747	-51.5	4.2
53769.00657	-64.7	4.1
53769.01091	-46.6	4.1
53769.01525	-48.1	4.4
53818.87032	-75.9	4.2
53818.87257	-62.6	3.6
53818.87483	-79.1	4.1
53820.89306	-66.1	4.7
53820.89739	-71.8	4.8
53820.90173	-59.6	5.5
53868.75220	-54.3	2.5
53877.79422	-54.8	3.6
53832.83762	-67.8	3.8
53832.83987	-56.5	3.6
53832.84212	-59.6	3.9
53835.85020	-69.2	3.4
53835.85292	-59.0	4.0
53835.85563	-54.6	3.7
53836.85584	-63.8	5.2
53836.85839	-36.1	7.0
53836.86088	-79.7	7.5
53840.89125	-72.0	4.0
53840.89490	-75.0	3.4
53840.89854	-69.2	3.5
53844.90638	-62.1	3.7
53844.90864	-78.0	3.4
53844.91090	-64.2	3.5
53866.76990	-54.1	3.8
53866.77342	-52.7	3.8
53866.77750	-69.3	3.9
53867.75148	-50.2	3.2
53867.75385	-53.9	3.0
53867.75621	-57.5	3.5

Table A.20 (cont'd)

JD-2400000	Velocity ( $\text{m s}^{-1}$ )	Uncertainty ( $\text{m s}^{-1}$ )
53877.72181	-42.1	3.1
53877.72409	-39.9	2.7
53877.72634	-56.2	3.0
53883.77349	-63.5	2.4
53883.77783	-56.6	2.5
53883.78217	-59.5	2.6
53888.69754	-61.3	2.9
53888.69980	-57.2	2.8
53888.70206	-59.5	2.8
53890.67675	-45.2	3.8
53890.67902	-30.5	3.1
53890.68127	-42.6	3.6
53891.68022	-50.7	3.1
53891.68247	-54.8	2.9
53891.68472	-50.3	2.6
53892.68678	-54.6	2.9
53892.68903	-52.9	3.5
53892.69128	-65.8	3.0
53893.76585	-54.2	2.7
53893.76811	-55.8	2.9
53893.77036	-61.1	3.0
53895.74381	-33.5	3.0
53897.74667	-46.7	3.1
53897.74893	-48.5	3.3
53897.75119	-52.6	3.0
53898.67519	-42.5	2.8
53898.67744	-53.7	2.9
53898.67970	-43.0	3.2
53901.73789	-35.9	2.8
53901.74015	-48.8	3.3
53901.74241	-52.6	3.4
53905.73143	-63.9	3.7
53905.73367	-50.4	3.8
53905.73593	-53.2	3.6
53755.04853	-55.2	5.0
53755.05078	-66.3	5.9
53755.05303	-53.7	6.4
53917.68891	-44.8	3.4
53937.64758	-47.0	2.9
53939.63048	-55.6	2.9



Table A.20 (cont'd)

JD-2400000	Velocity (m s <sup>-1</sup> )	Uncertainty (m s <sup>-1</sup> )
53911.72776	-63.2	3.8
53911.73001	-44.2	4.2
53911.73226	-40.1	4.0
53880.80537	-56.4	3.0
53880.80832	-54.9	3.7
53880.81127	-51.2	3.7
54144.99774	232.4	3.4
54164.01886	274.5	3.5
54129.03484	209.3	3.9
54129.03715	209.1	3.8
54129.03946	197.7	4.1
54131.02150	204.9	4.3
54131.02378	199.4	4.5
54131.02605	203.8	4.3
54176.99062	284.3	3.6
54176.99295	300.3	3.0
54176.99523	299.8	3.0
54190.87336	316.0	3.2
54180.88720	299.9	3.3
54180.88948	298.9	3.7
54180.89172	296.1	2.9
54186.88364	313.6	2.8
54186.88695	304.8	2.9
54186.89027	311.3	2.9
54211.80835	329.3	4.4
54211.81131	328.3	3.5
54211.81521	344.4	3.4
54221.78703	343.3	3.7
54221.78930	336.9	4.0
54221.79163	340.0	3.5
54253.69685	365.5	3.1
54253.69912	365.5	2.8
54253.70139	369.5	2.7
54282.62851	341.7	3.7
54282.63079	329.2	3.7
54282.63306	326.1	3.6

Table A.21. HET Radial Velocities for HD 178911B

JD-2400000	Velocity ( $\text{m s}^{-1}$ )	Uncertainty ( $\text{m s}^{-1}$ )
53653.66528	-61.4	1.6
53801.00302	-169.6	1.4
53803.02412	-225.9	1.6
53837.93570	285.5	1.8
53846.89693	347.4	1.6
53866.83649	-6.5	1.5
53868.81760	-70.4	1.5
53883.79325	-319.4	1.3
53954.82320	-328.0	1.6
53955.82606	-316.1	1.5
53956.82027	-309.6	1.4
53958.81704	-270.6	1.4
53960.80356	-236.7	1.4
53965.80164	-92.9	1.4
53966.78694	-67.9	1.5
53971.77135	74.0	1.6
53976.76788	189.1	1.4
53979.76859	250.1	1.6
53988.72794	326.2	1.4
53988.73584	330.2	1.4
53993.71885	312.2	1.7
54014.66291	-167.0	1.4
54016.65503	-230.5	1.5
54035.60988	-126.7	1.5
54039.58877	-7.9	1.5
54055.55127	316.8	1.4
54063.54556	344.6	1.5
54165.01752	-303.4	1.6
54167.00332	-313.9	1.7
54190.93933	214.4	1.8
54251.77451	-79.4	1.5
54323.81680	-85.3	1.5
54332.79368	162.2	2.2
54335.79347	212.4	1.7
54338.78881	261.6	1.5
54340.77677	289.9	1.6
54344.77039	320.2	1.6
54365.69757	39.6	1.4
54396.61972	-19.2	1.3
54400.59558	94.4	1.3

Table A.21 (cont'd)

JD-2400000	Velocity (m s <sup>-1</sup> )	Uncertainty (m s <sup>-1</sup> )
------------	-------------------------------	----------------------------------

Table A.22. HET Radial Velocities for HD 190228

JD-2400000	Velocity (m s <sup>-1</sup> )	Uncertainty (m s <sup>-1</sup> )
53581.89473	-90.7	2.8
53589.86259	-78.7	2.0
53605.81074	-77.3	1.9
53606.81111	-74.2	2.0
53607.80141	-71.7	2.1
53609.80786	-75.1	2.0
53628.75754	-69.6	2.2
53635.71968	-66.2	2.3
53653.67654	-60.2	2.0
53655.68369	-56.4	2.0
53686.58579	-51.6	2.0
53844.93852	-15.6	2.1
53867.88496	-13.0	2.0
53877.84874	1.0	1.8
53883.82777	15.3	1.9
53888.81145	19.1	2.1
53897.79760	9.3	2.1
53935.90970	12.1	2.0
53956.84836	8.9	1.9
53966.81728	15.1	1.9
53976.79349	9.8	2.2
53996.75947	30.5	2.0
53998.73191	26.1	2.0
53998.73697	21.1	1.9
54008.70583	25.3	1.8
54013.70146	25.5	1.8
54019.66975	25.1	1.9
54032.62480	42.7	2.2
54217.92567	59.3	2.1
54265.79082	51.9	2.1
54284.96126	74.5	2.1
54326.62326	53.5	2.0
54328.62216	53.0	2.0
54331.61953	56.8	2.0
54336.59244	66.8	2.3
54344.79398	68.2	2.1
54352.77160	69.0	2.1
54368.71625	82.0	1.9
54370.72492	84.5	1.7
54377.68917	92.9	2.0

Table A.22 (cont'd)

JD-2400000	Velocity ( $\text{m s}^{-1}$ )	Uncertainty ( $\text{m s}^{-1}$ )
54401.62808	96.4	1.9
54428.57314	107.9	2.0

## Appendix B

# 2.7m Radial-Velocity Data

Table B.1. 2.7m Radial Velocities for HD 3651

JD-2400000	Velocity ( $\text{m s}^{-1}$ )	Uncertainty ( $\text{m s}^{-1}$ )
53633.86853	-3.3	5.0
53654.79777	6.6	6.6
53690.69920	-3.4	6.5

Table B.2. 2.7m Radial Velocities for HD 8574

JD-2400000	Velocity ( $\text{m s}^{-1}$ )	Uncertainty ( $\text{m s}^{-1}$ )
52116.95398	24.0	9.6
52141.96262	70.0	8.0
52219.89758	-10.8	10.0
52249.70181	-30.2	9.6
52331.61330	1.7	7.7
52493.90858	-17.4	9.7
52540.91557	-13.9	8.9
52658.62787	-18.5	9.3
52932.83883	-45.8	8.9
53015.71309	29.6	9.2
53564.94976	2.1	10.8
53632.92472	-62.8	8.6
53635.90969	-22.1	8.4
53691.75684	-4.6	10.4
53970.92894	95.0	13.5
54018.87142	3.7	9.9

Table B.3. 2.7m Radial Velocities for HD 10697

JD-2400000	Velocity (m s <sup>-1</sup> )	Uncertainty (m s <sup>-1</sup> )
51066.97570	76.4	6.0
51152.79209	108.3	6.3
51211.61496	98.3	6.5
51239.60083	105.0	12.8
51449.91000	-20.3	5.2
51503.72131	-69.6	10.7
51529.67754	-72.8	7.6
51558.57566	-97.3	6.7
51775.92530	-83.4	5.6
51811.88858	-86.5	6.8
51859.67414	-64.9	5.8
51917.68431	-19.2	7.0
51946.64764	3.0	7.5
51987.56487	10.3	8.8
52116.96710	84.9	6.7
52247.79070	109.6	5.9
52306.67720	101.0	5.7
52493.92186	3.3	6.2
52539.87531	-31.9	5.7
52577.87821	-63.3	6.2
52897.88453	-68.5	8.2
52932.87904	-69.5	6.8
53017.69801	4.1	6.5
53215.85694	99.7	15.3
53215.87160	89.8	6.7
53320.75657	129.6	10.1
53564.96191	3.4	8.1
53566.91539	16.1	6.8
53635.89769	-51.9	8.8
53690.71397	-94.3	7.5
53968.92927	-88.3	10.9
54018.85867	-61.1	6.9

Table B.4. 2.7m Radial Velocities for HD 19994

JD-2400000	Velocity (m s <sup>-1</sup> )	Uncertainty (m s <sup>-1</sup> )
53635.94301	-4.1	9.7
53655.86581	-35.7	18.0
53690.87053	32.5	8.0
53747.67357	50.7	10.1
54020.88376	-36.1	8.5
54310.93898	20.1	10.4
54346.88504	0.6	11.4
54377.85942	-21.9	9.6
54404.79890	-6.3	8.9
54404.80349	-11.9	10.1
54460.79143	12.1	12.5

Table B.5. 2.7m Radial Velocities for HD 20367

JD-2400000	Velocity (m s <sup>-1</sup> )	Uncertainty (m s <sup>-1</sup> )
53632.00290	-0.1	7.2
53635.96984	4.6	7.8
53691.80381	-4.4	8.2
53808.62780	3.2	6.7
53967.90828	5.9	7.0
53968.90725	12.6	9.2
54018.98018	-8.1	6.5
54158.59352	-5.0	7.4
54189.59664	1.8	6.7
54189.61001	6.0	8.0
54190.61247	-2.8	7.2
54191.60150	-2.2	5.9
54192.60131	5.4	5.6
54345.84686	4.1	8.5
54377.85210	-19.4	6.0
54402.79239	-10.2	6.2
54460.80432	8.6	12.5

Table B.6. 2.7m Radial Velocities for HD 23596

JD-2400000	Velocity (m s <sup>-1</sup> )	Uncertainty (m s <sup>-1</sup> )
53636.88979	73.6	7.1
53692.83650	48.7	7.6
53787.66076	11.9	6.0
53808.63976	13.0	7.1
54020.93260	-51.4	8.2
54158.60541	-95.8	6.1



Table B.7. 2.7m Radial Velocities for HD 28185

JD-2400000	Velocity (m s <sup>-1</sup> )	Uncertainty (m s <sup>-1</sup> )
52600.88444	65.9	5.7
52660.76836	134.9	6.3
52933.83603	-68.7	5.8
52958.78444	3.6	8.0
53017.72283	138.4	7.2
53038.72649	153.0	9.2
53632.98850	-161.3	7.3
53692.85380	-58.2	8.4
53747.72300	74.1	7.9
53808.61690	168.0	6.3
53970.97858	-140.2	6.3
54017.94034	-145.1	7.3
54067.77664	-83.4	6.6
54068.87312	-80.9	7.3

Table B.8. 2.7m Radial Velocities for HD 38529

JD-2400000	Velocity (m s <sup>-1</sup> )	Uncertainty (m s <sup>-1</sup> )
53633.96726	-44.5	5.7
53636.91593	-19.0	4.9
53691.91356	-24.9	5.8
53746.78728	-51.1	5.7
53809.64793	47.7	5.5
53984.94973	-1.4	5.1
54020.90382	93.2	6.4

Table B.9. 2.7m Radial Velocities for HD 40979

JD-2400000	Velocity (m s <sup>-1</sup> )	Uncertainty (m s <sup>-1</sup> )
53636.00527	78.9	8.9
53787.77595	-46.2	8.3
53864.61096	-23.4	7.6
54020.94453	-9.2	6.7

Table B.10. 2.7m Radial Velocities for HD 72659

JD-2400000	Velocity (m s <sup>-1</sup> )	Uncertainty (m s <sup>-1</sup> )
53392.77671	18.4	9.7
53745.88712	-12.3	9.7
53806.77417	-21.8	9.1
53843.65099	13.6	12.1
53861.65749	4.3	9.6
54067.96590	-2.1	10.2

Table B.11. 2.7m Radial Velocities for HD 89744

JD-2400000	Velocity (m s <sup>-1</sup> )	Uncertainty (m s <sup>-1</sup> )
53690.03080	262.2	7.7
53805.87856	-129.3	7.1
53806.73923	-130.0	8.9
53807.83562	-188.4	10.8
53809.79691	-198.1	7.8
53840.78664	168.0	9.8
53864.76543	203.8	8.9
53911.61226	252.5	9.3
54068.94214	-240.7	8.7

Table B.12. 2.7m Radial Velocities for 47 UMa

JD-2400000	Velocity ( $\text{m s}^{-1}$ )	Uncertainty ( $\text{m s}^{-1}$ )
51010.62898	49.7	6.4
51212.97474	-12.7	5.5
51240.81250	-9.2	6.2
51274.78993	-13.1	5.4
51326.70558	-24.3	6.2
51504.95996	-44.1	6.0
51530.01978	-31.3	6.9
51555.94972	-27.4	5.8
51655.74023	3.9	5.8
51686.75156	-8.6	6.5
51750.60418	0.1	6.6
51861.01895	51.8	6.9
51917.93086	45.6	7.1
51987.85527	45.9	8.5
52004.83235	57.8	6.0
52039.77936	53.0	7.5
52116.60554	37.5	7.6
52249.00010	7.6	7.6
52303.89238	-11.5	5.5
52305.84757	-13.7	6.1
52327.86285	10.5	16.6
52353.85949	-14.8	7.7
52661.95399	-26.8	5.4
53017.93695	59.6	7.5
53069.76686	58.8	6.4
53692.03243	-51.6	8.1
53748.89147	-49.8	6.0
53787.91198	-37.1	6.3
53805.88756	-31.2	5.6
53809.80777	-32.7	6.1
53805.88756	-31.2	5.6
53809.80777	-32.7	6.1
53787.91198	-37.1	6.3
53861.74397	-19.0	6.1
53909.61977	12.0	7.0
54280.64401	35.6	7.9
54280.64893	30.7	6.8

Table B.13. 2.7m Radial Velocities for HD 106252

JD-2400000	Velocity (m s <sup>-1</sup> )	Uncertainty (m s <sup>-1</sup> )
52116.61921	46.4	11.5
52307.00335	16.9	9.8
52328.89167	-32.1	11.8
52357.80730	-40.7	9.6
52743.85538	-129.6	9.1
53465.74189	55.7	10.4
53504.65833	73.1	9.8
53564.63133	73.7	10.5
53566.62685	84.6	10.8
53808.85919	-23.7	10.3
53842.77638	-24.6	10.9
53861.78041	-35.8	10.2

Table B.14. 2.7m Radial Velocities for HD 130322

JD-2400000	Velocity (m s <sup>-1</sup> )	Uncertainty (m s <sup>-1</sup> )
53585.64900	83.7	7.5
53843.89253	-18.0	7.5
53863.78301	75.5	8.6
53910.78043	-68.5	8.1
54251.84318	-72.8	9.4

Table B.15. 2.7m Radial Velocities for HD 136118

JD-2400000	Velocity (m s <sup>-1</sup> )	Uncertainty (m s <sup>-1</sup> )
53585.66699	13.5	11.4
53805.93741	-1.7	9.1
53863.76953	-12.0	13.8
53911.75165	0.2	10.0

Table B.16. 2.7m Radial Velocities for HD 178911B

JD-2400000	Velocity (m s <sup>-1</sup> )	Uncertainty (m s <sup>-1</sup> )
53632.70820	584.2	6.8
53636.67681	541.6	6.8

Table B.17. 2.7m Radial Velocities for HD 190228

JD-2400000	Velocity (m s <sup>-1</sup> )	Uncertainty (m s <sup>-1</sup> )
53584.82785	-47.3	6.2
53585.80785	-27.8	8.9
53635.70876	-42.5	6.9
53636.74761	-41.8	5.5
53691.63145	-16.2	7.9
53862.94967	14.5	6.4
53927.85541	43.2	6.8
54403.65001	118.0	7.1

# Bibliography

- Allende Prieto, C., & Lambert, D. L. 1999, *A&A*, 352, 555
- Angel, J. R. P., & Woolf, N. J. 1997, *ApJ*, 475, 373
- Armitage, P. J. 2007, *ArXiv Astrophysics e-prints*, arXiv:astro-ph/0701485
- Barnes, R., & Quinn, T. 2004, *ApJ*, 611, 494
- Barnes, R., & Raymond, S. N. 2004, *ApJ*, 617, 569
- Barnes, R., Raymond, S. N., Bean, J. L., McArthur, B. E., Greenberg, R., & Benedict, G. F. 2007, *American Astronomical Society Meeting Abstracts*, 211, #17.06
- Batten, A. H., Fletcher, J. M., & Campbell, B. 1984, *PASP*, 96, 903
- Baranne, A., et al. 1996, *A&AS*, 119, 373
- Bean, J. L., McArthur, B. E., Benedict, G. F., & Armstrong, A. 2008, *ApJ*, 672, 1202
- Bean, J. L., McArthur, B. E., Benedict, G. F., Harrison, T. E., Bizyaev, D., Nelan, E., & Smith, V. V. 2007, *AJ*, 134, 749
- Bean, J. L., McArthur, B. E., Benedict, G. F., & Armstrong, A. 2008, *ApJ*, 672, 1202
- Beckers, J. M. 1976, *Nature*, 260, 227
- Beichman, C. A., Woolf, N. J., & Lindensmith, C. A. 1999, *The Terrestrial Planet Finder (TPF) : a NASA Origins Program to search for habitable planets / the TPF*

- Science Working Group ; edited by C.A. Beichman, N.J. Woolf, and C.A. Lindensmith. [Washington, D.C.] : National Aeronautics and Space Administration ; Pasadena, Calif. : Jet Propulsion Laboratory, California Institute of Technology, [1999] (JPL publication ; 99-3)
- Benedict, G. F., et al. 2006, *AJ*, 132, 2206
- Binnendijk, L. 1960, Philadelphia, University of Pennsylvania Press [1960]
- Bodenheimer, P., Hubickyj, O., & Lissauer, J. J. 2000, *Icarus*, 143, 2
- Bodenheimer, P., Lin, D. N. C., & Mardling, R. A. 2001, *ApJ*, 548, 466
- Bonfils, X., et al. 2005, *A&A*, 443, L15
- Borucki, W. J., et al. 2003, *Proc. SPIE*, 4854, 129
- Boss, A. P. 2003, *ApJ*, 599, 577
- Boss, A. P. 1998, *ApJ*, 503, 923
- Boss, A. P. 1995, *Science*, 267, 360
- Brown, T. M., Charbonneau, D., Gilliland, R. L., Noyes, R. W., & Burrows, A. 2001, *ApJ*, 552, 699
- Butler, R. P., et al. 2006, *ApJ*, 646, 505
- Butler, R. P., Vogt, S. S., Marcy, G. W., Fischer, D. A., Wright, J. T., Henry, G. W., Laughlin, G., & Lissauer, J. J. 2004, *ApJ*, 617, 580
- Butler, R. P., Marcy, G. W., Vogt, S. S., Fischer, D. A., Henry, G. W., Laughlin, G., & Wright, J. T. 2003, *ApJ*, 582, 455
- Butler, R. P., Marcy, G. W., Fischer, D. A., Brown, T. M., Contos, A. R., Korzennik, S. G., Nisenson, P., & Noyes, R. W. 1999, *ApJ*, 526, 916
- Butler, R. P., Marcy, G. W., Williams, E., Hauser, H., & Shirts, P. 1997, *ApJ*, 474, L115
- Butler, R. P., Marcy, G. W., Williams, E., McCarthy, C., Dosanji, P., & Vogt, S. S. 1996, *PASP*, 108, 500

- Campbell, B., Walker, G. A. H., & Yang, S. 1988, ApJ, 331, 902
- Campbell, B., & Walker, G. A. H. 1979, PASP, 91, 540
- Chambers, J. E. 1999, MNRAS, 304, 793
- Charbonneau, D., Brown, T. M., Noyes, R. W., & Gilliland, R. L. 2002, ApJ, 568, 377
- Charbonneau, D., Brown, T. M., Latham, D. W., & Mayor, M. 2000, ApJ, 529, L45
- Cochran, W. D. 1988, ApJ, 334, 349
- Cochran, W. D., Endl, M., Wittenmyer, R. A., & Bean, J. L. 2007, ApJ, 665, 1407
- Cochran, W. D., Hatzes, A. P., Butler, R. P., & Marcy, G. W. 1997, ApJ, 483, 457
- Cochran, W. D., Hatzes, A. P., & Hancock, T. J. 1991, ApJ, 380, L35
- Cochran, W. D., Hatzes, A. P., & Paulson, D. B. 2002, AJ, 124, 565
- Cochran, W. D., Smith, H. J., & Smith, W. H. 1982, Proc. SPIE, 331, 315
- Cochran, W. D., et al. 2004, ApJ, 611, L133
- Connes, P. 1985, Ap&SS, 110, 211
- Cumming, A., Marcy, G. W., & Butler, R. P. 1999, ApJ, 526, 890
- Deming, D., Brown, T. M., Charbonneau, D., Harrington, J., & Richardson, L. J. 2005, ApJ, 622, 1149
- Deming, D., Harrington, J., Laughlin, G., Seager, S., Navarro, S. B., Bowman, W. C., & Horning, K. 2007, ApJ, 667, L199
- Desidera, S., & Barbieri, M. 2007, A&A, 462, 345
- Desidera, S., et al. 2003, A&A, 405, 207
- do Nascimento, J. D., Canto Martins, B. L., Melo, C. H. F., Porto de Mello, G., & De Medeiros, J. R. 2003, A&A, 405, 723



- Eaton, J. A., Henry, G. W., & Fekel, F. C. 2003, in *The Future of Small Telescopes in the New Millennium II. The Telescopes We Use*, ed. T. Oswalt (Dordrecht: Kluwer), 189
- Endl, M., Cochran, W. D., Wittenmyer, R. A., & Boss, A. P. 2007, ArXiv e-prints, 709, arXiv:0709.0944
- Endl, M., Cochran, W. D., Wittenmyer, R. A., & Hatzes, A. P. 2006, *AJ*, 131, 3131
- Endl, M., Cochran, W. D., Hatzes, A. P., & Wittenmyer, R. A. 2005, *Revista Mexicana de Astronomia y Astrofisica Conference Series*, 23, 64
- Endl, M., Hatzes, A. P., Cochran, W. D., McArthur, B., Allende Prieto, C., Paulson, D. B., Guenther, E., & Bedalov, A. 2004, *ApJ*, 611, 1121
- Endl, M., Kürster, M., Els, S. H. A. P., Cochran, W. D., Dennerl, K., Döbereiner, S. 2002, *A&A*, 392, 671
- Endl, M., Kürster, M., Els, S., Hatzes, A. P., & Cochran, W. D. 2001, *A&A*, 374, 675
- Endl, M., Kürster, M., & Els, S. 2000, *A&A*, 362, 585
- Erskine, D. J., & Ge, J. 2000, *Imaging the Universe in Three Dimensions*, 195, 501
- Fischer, D. A., Butler, R. P., Marcy, G. W., Vogt, S. S., & Henry, G. W. 2003, *ApJ*, 590, 1081
- Fischer, D. A., et al. 2003, *ApJ*, 586, 1394
- Fischer, D. A., et al. 2007, ArXiv e-prints, 712, arXiv:0712.3917
- Fischer, D. A., Marcy, G. W., Butler, R. P., Laughlin, G., & Vogt, S. S. 2002, *ApJ*, 564, 1028
- Fischer, D. A., Marcy, G. W., Butler, R. P., Vogt, S. S., Walp, B., & Apps, K. 2002, *PASP*, 114, 529
- Fischer, D. A., Marcy, G. W., Butler, R. P., Vogt, S. S., Frink, S., & Apps, K. 2001, *ApJ*, 551, 1107

- Fischer, D. A., Marcy, G. W., Butler, R. P., Vogt, S. S., & Apps, K. 1999, *PASP*, 111, 50
- Fogg, M. J., & Nelson, R. P. 2007, *A&A*, 472, 1003
- Ford, E. B. 2008, *AJ*, 135, 1008
- Ford, E. B., Lystad, V., & Rasio, F. A. 2005, *Nature*, 434, 873
- Gaudi, B. S., et al. 2008, *Science*, 319, 927
- Ge, J., et al. 2006, *ApJ*, submitted
- Ge, J. 2002, *ApJ*, 571, L165
- Gillon, M., et al. 2007, *A&A*, 471, L51
- Gillon, M., et al. 2007, *A&A*, 472, L13
- Goldreich, P., & Soter, S. 1966, *Icarus*, 5, 375
- Goździewski, K., & Konacki, M. 2006, *ApJ*, 647, 573
- Goździewski, K., Konacki, M., & Maciejewski, A. J. 2006, *ApJ*, 645, 688
- Gray, D. F., & Hatzes, A. P. 1997, *ApJ*, 490, 412
- Griffin, R., & Griffin, R. 1973, *MNRAS*, 162, 255
- Hale, A. 1994, *AJ*, 107, 306
- Hatzes, A. P., et al. 2006, *A&A*, 457, 335
- Hatzes, A. P., Guenther, E. W., Endl, M., Cochran, W. D., Döllinger, M. P., & Bedalov, A. 2005, *A&A*, 437, 743
- Hatzes, A. P., et al. 2000, *ApJ*, 544, L145
- Hatzes, A. P., Cochran, W. D., Endl, M., McArthur, B., Paulson, D. B., Walker, G. A. H., Campbell, B., & Yang, S. 2003, *ApJ*, 599, 1383
- Hauser, H. M., & Marcy, G. W. 1999, *PASP*, 111, 321

- Heintz, W. D. 1988, JRASC, 82, 140
- Henry, G. W. 1999, PASP, 111, 845
- Henry, G. W., Marcy, G. W., Butler, R. P., & Vogt, S. S. 2000, ApJ, 529, L41
- Holman, M., Touma, J., & Tremaine, S. 1997, Nature, 386, 254
- Horne, J. H., & Baliunas, S. L. 1986, ApJ, 302, 757
- Ida, S., & Lin, D. N. C. 2004, ApJ, 616, 567
- Ida, S., & Lin, D. N. C. 2004, ApJ, 604, 388
- Jefferys, W. H., Fitzpatrick, M. J., & McArthur, B. E. 1987, Celestial Mechanics, 41, 39
- Ji, J., Liu, L., Kinoshita, H., Zhou, J., Nakai, H., & Li, G. 2003, ApJ, 591, L57
- Jones, B. W., & Sleep, P. N. 2002, A&A, 393, 1015
- Jones, B. W., Sleep, P. N., & Chambers, J. E. 2001, A&A, 366, 254
- Kasting, J. F., Whitmire, D. P., & Reynolds, R. T. 1993, Icarus, 101, 108
- Knutson, H. A., et al. 2007, Nature, 447, 183
- Koch, A., & Woehl, H. 1984, A&A, 134, 134
- Korzennik, S. G., Brown, T. M., Fischer, D. A., Nisenson, P., & Noyes, R. W. 2000, ApJ, 533, L147
- Kozai, Y. 1962, AJ, 67, 591
- Kürster, M., et al. 2003, A&A, 403, 1077
- Kürster, M., Endl, M., Els, S., Hatzes, A. P., Cochran, W. D., Döbereiner, S., & Dennerl, K. 2000, A&A, 353, L33
- Kürster, M., Schmitt, J. H. M. M., Cutispoto, G., & Dennerl, K. 1997, A&A, 320, 831

- Latham, D. W., Stefanik, R. P., Mazeh, T., Mayor, M., & Burki, G. 1989, *Nature*, 339, 38
- Laughlin, G., & Chambers, J. E. 2001, *ApJ*, 551, L109
- Laughlin, G., & Chambers, J. E. 2002, *AJ*, 124, 592
- Laughlin, G., Butler, R. P., Fischer, D. A., Marcy, G. W., Vogt, S. S., & Wolf, A. S. 2005, *ApJ*, 622, 1182
- Lecar, M., Podolak, M., Sasselov, D., & Chiang, E. 2006, *ApJ*, 640, 1115
- Léger, A., Mariotti, J. M., Mennesson, B., Ollivier, M., Puget, J. L., Rouan, D., & Schneider, J. 1996, *Ap&SS*, 241, 135
- Lehmann-Filhés, R. 1894, *Astronomische Nachrichten*, 136, 17
- Levison, H. F., & Duncan, M. J. 1994, *Icarus*, 108, 18
- Levison, H. F., Lissauer, J. J., & Duncan, M. J. 1998, *AJ*, 116, 1998
- Libbrecht, K. G. 1988, *IAU Symp. 132: The Impact of Very High S/N Spectroscopy on Stellar Physics*, 132, 83
- Lin, D. N. C., & Ida, S. 1997, *ApJ*, 477, 781
- Lissauer, J. J. 1995, *Icarus*, 114, 217
- Lomb, N. R. 1976, *Ap&SS*, 39, 447
- Lovis, C., et al. 2006, *Nature*, 441, 305
- Luhman, K. L., et al. 2007, *ApJ*, 654, 570
- Luhman, K. L., & Jayawardhana, R. 2002, *ApJ*, 566, 1132
- Malmberg, D., Davies, M. B., & Chambers, J. E. 2007, *MNRAS*, 377, L1
- Mandell, A. M., Raymond, S. N., & Sigurdsson, S. 2007, *ApJ*, 660, 823
- Mao, S., & Paczynski, B. 1991, *ApJ*, 374, L37

- Marcy, G., Butler, R. P., Fischer, D., Vogt, S., Wright, J. T., Tinney, C. G., & Jones, H. R. A. 2005, *Progress of Theoretical Physics Supplement*, 158, 24
- Marcy, G. W., et al. 2001, *ApJ*, 555, 418
- Marcy, G. W., Butler, R. P., Fischer, D. A., Laughlin, G., Vogt, S. S., Henry, G. W., & Pourbaix, D. 2002, *ApJ*, 581, 1375
- Marcy, G. W., Butler, R. P., Vogt, S. S., Fischer, D., & Liu, M. C. 1999, *ApJ*, 520, 239
- Marcy, G. W., & Butler, R. P. 1992, *PASP*, 104, 270
- Martioli, E., McArthur, B. E., Benedict, G. F., Bean, J. L., & Armstrong, A. 2007, *American Astronomical Society Meeting Abstracts*, 211, #134.18
- Mayor, M., et al. 2003, *The Messenger*, 114, 20
- Mayor, M., Udry, S., Naef, D., Pepe, F., Queloz, D., Santos, N. C., & Burnet, M. 2004, *A&A*, 415, 391
- Mayor, M., & Queloz, D. 1995, *Nature*, 378, 355
- Mazeh, T., Krymolowski, Y., & Rosenfeld, G. 1997, *ApJ*, 477, L103
- McArthur, B., Benedict, G. F., Bean, J., & Martioli, E. 2007, *American Astronomical Society Meeting Abstracts*, 211, #134.17
- McArthur, B. E., et al. 2004, *ApJ*, 614, L81
- McMillan, R. S., Smith, P. H., Frecker, J. E., Merline, W. J., & Perry, M. L. 1985, *IAU Colloq. 88: Stellar Radial Velocities*, 63
- McMillan, R. S., Smith, P. H., Perry, M. L., Moore, T. L., & Merline, W. J. 1990, *Proc. SPIE*, 1235, 601
- McMillan, R. S., Moore, T. L., Perry, M. L., & Smith, P. H. 1994, *Ap&SS*, 212, 271
- Menou, K., & Tabachnik, S. 2003, *ApJ*, 583, 473
- Mugrauer, M., Seifahrt, A., Neuhäuser, R., & Mazeh, T. 2006, *MNRAS*, 373, L31

- Mugrauer, M., Neuhäuser, R., Mazeh, T., Guenther, E., & Fernández, M. 2004, *Astronomische Nachrichten*, 325, 718
- Murdoch, K. A., Hearnshaw, J. B., & Clark, M. 1993, *ApJ*, 413, 349
- Naef, D., et al. 2007, *A&A*, in press, arXiv:0704.0917
- Naef, D., Mayor, M., Beuzit, J. L., Perrier, C., Queloz, D., Sivan, J. P., & Udry, S. 2004, *A&A*, 414, 351
- Naef, D., Mayor, M., Pepe, F., Queloz, D., Santos, N. C., Udry, S., & Burnet, M. 2001, *A&A*, 375, 205
- Naef, D., et al. 2001, *A&A*, 375, L27
- Narayan, R., Cumming, A., & Lin, D. N. C. 2005, *ApJ*, 620, 1002
- Nelson, A. F., & Angel, J. R. P. 1998, *ApJ*, 500, 940
- Nordström, B., et al. 2004, *A&A*, 418, 989
- Noyes, R. W., Hartmann, L. W., Baliunas, S. L., Duncan, D. K., & Vaughan, A. H. 1984, *ApJ*, 279, 763
- Paulson, D. B., Cochran, W. D., & Hatzes, A. P. 2004, *AJ*, 127, 3579
- Paulson, D. B., Saar, S. H., Cochran, W. D., & Henry, G. W. 2004, *AJ*, 127, 1644
- Paulson, D. B., Sneden, C., & Cochran, W. D. 2003, *AJ*, 125, 3185
- Paulson, D. B., Saar, S. H., Cochran, W. D., & Hatzes, A. P. 2002, *AJ*, 124, 572
- Patience, J., et al. 2002, *ApJ*, 581, 654
- Pepe, F., et al. 2007, *A&A*, 462, 769
- Perrier, C., Sivan, J.-P., Naef, D., Beuzit, J. L., Mayor, M., Queloz, D., & Udry, S. 2003, *A&A*, 410, 1039
- Perryman, M. A. C., et al. 1997, *A&A*, 323, L49
- Pollack, J. B., Hubickyj, O., Bodenheimer, P., Lissauer, J. J., Podolak, M., & Greenzweig, Y. 1996, *Icarus*, 124, 62

- Pourbaix, D. 2000, A&AS, 145, 215
- Press, W. H., Teukolsky, S. A., Vetterling, W. T., & Flannery, B. P. 1992, Cambridge: University Press, 1992, 2nd ed.
- Queloz, D., et al. 2000, A&A, 354, 99
- Raghavan, D., Henry, T. J., Mason, B. D., Subasavage, J. P., Jao, W.-C., Beaulieu, T. D., & Hambly, N. C. 2006, ApJ, 646, 523
- Rasio, F. A., & Ford, E. B. 1996, Science, 274, 954
- Raymond, S. N., Mandell, A. M., & Sigurdsson, S. 2006, Science, 313, 1413
- Redfield, S., Endl, M., Cochran, W. D., & Koesterke, L. 2008, ApJ, 673, L87
- Rivera, E., & Haghighipour, N. 2007, MNRAS, 374, 599
- Rivera, E. J., et al. 2005, ApJ, 634, 625
- Rupprecht, G., et al. 2004, Proc. SPIE, 5492, 148
- Santos, N. C., Israelian, G., & Mayor, M. 2004, A&A, 415, 1153
- Santos, N. C., et al. 2004, A&A, 426, L19
- Santos, N. C., Mayor, M., Naef, D., Pepe, F., Queloz, D., Udry, S., & Burnet, M. 2001, A&A, 379, 999
- Scargle, J. D. 1982, ApJ, 263, 835
- Seager, S., Kuchner, M., Hier-Majumder, C. A., & Militzer, B. 2007, ApJ, 669, 1279
- Silvotti, R., et al. 2007, Nature, 449, 189
- Smith, P. H., McMillan, R. S., & Merline, W. J. 1987, ApJ, 317, L79
- Sozzetti, A. 2005, PASP, 117, 1021
- Takeda, G., Ford, E. B., Sills, A., Rasio, F. A., Fischer, D. A., & Valenti, J. A. 2007, ApJS, 168, 297
- Takeda, G., & Rasio, F. A. 2005, ApJ, 627, 1001

- Tanaka, H., Takeuchi, T., & Ward, W. R. 2002, *ApJ*, 565, 1257
- Tinney, C. G., Butler, R. P., Marcy, G. W., Jones, H. R. A., Penny, A. J., Vogt, S. S., Apps, K., & Henry, G. W. 2001, *ApJ*, 551, 507
- Tokovinin, A. A., Griffin, R. F., Balega, Y. Y., Pluzhnik, E. A., & Udry, S. 2000, *Astronomy Letters*, 26, 116
- Trilling, D. E., Benz, W., Guillot, T., Lunine, J. I., Hubbard, W. B., & Burrows, A. 1998, *ApJ*, 500, 428
- Trilling, D. E., Lunine, J. I., & Benz, W. 2002, *A&A*, 394, 241
- Tull, R. G. 1998, *Proc. SPIE*, 3355, 387
- Tull, R. G. 1969, *Appl. Opt.*, 8, 1635
- Tull, R. G., MacQueen, P., Sneden, C., & Lambert, D. L. 1994, *ASP Conf. Ser.* 55: *Optical Astronomy from the Earth and Moon*, 55, 148
- Tull, R. G., MacQueen, P. J., Sneden, C., & Lambert, D. L. 1995, *PASP*, 107, 251
- Udry, S., et al. 2007, *A&A*, 469, L43
- Udry, S., Mayor, M., & Queloz, D. 2003, *Scientific Frontiers in Research on Extrasolar Planets*, 294, 17
- Udry, S., Mayor, M., Naef, D., Pepe, F., Queloz, D., Santos, N. C., & Burnet, M. 2002, *A&A*, 390, 267
- Udry, S., et al. 2000, *A&A*, 356, 590
- Valenti, J. A., & Fischer, D. A. 2005, *ApJS*, 159, 141
- Valenti, J. A., Butler, R. P., & Marcy, G. W. 1995, *PASP*, 107, 966
- van Eyken, J. C., Ge, J. C., Mahadevan, S., DeWitt, C., & Ren, D. 2003, *Proc. SPIE*, 5170, 250
- Vogt, S. S. 1987, *PASP*, 99, 1214
- Vogt, S. S., Marcy, G. W., Butler, R. P., & Apps, K. 2000, *ApJ*, 536, 902



- Vogt, S. S., Butler, R. P., Marcy, G. W., Fischer, D. A., Henry, G. W., Laughlin, G., Wright, J. T., & Johnson, J. A. 2005, *ApJ*, 632, 638
- Vogt, S. S., Butler, R. P., Marcy, G. W., Fischer, D. A., Pourbaix, D., Apps, K., & Laughlin, G. 2002, *ApJ*, 568, 352
- Walker, G. A. H., Walker, A. R., Irwin, A. W., Larson, A. M., Yang, S. L. S., & Richardson, D. C. 1995, *Icarus*, 116, 359
- Ward, W. R. 1997, *Icarus*, 126, 261
- Wilson, J. C., Kirkpatrick, J. D., Gizis, J. E., Skrutskie, M. F., Monet, D. G., & Houck, J. R. 2001, *AJ*, 122, 1989
- Wisdom, J., & Holman, M. 1991, *AJ*, 102, 1528
- Wisdom, J., & Holman, M. 1992, *AJ*, 104, 2022
- Wittenmyer, R. A., Endl, M., Cochran, W. D., Hatzes, A. P., Walker, G. A. H., Yang, S. L. S., & Paulson, D. B. 2006, *AJ*, 132, 177
- Wittenmyer, R. A., Endl, M., & Cochran, W. D. 2007, *ApJ*, 654, 625
- Wittenmyer, R. A., Endl, M., Cochran, W. D., & Levison, H. F. 2007, *AJ*, 134, 1276
- Wittenmyer, R. A., Endl, M., Cochran, W. D., Ramirez, I., & Shetrone, M. 2008, in prep.
- Wolszczan, A., & Frail, D. A. 1992, *Nature*, 355, 145
- Worley, C. E., & Heintz, W. D. 1995, *VizieR Online Data Catalog*, 5039, 0
- Wright, J. T. 2005, *PASP*, 117, 657
- Wright, J. T., et al. 2007, *ApJ*, 657, 533
- Wright, J. T., Butler, R. P., Marcy, G. W., Vogt, S. S., Fischer, D. A., Rinney, C. G., & Jones, H. R. A. 2005, *Protostars and Planets V*, 8605
- Wright, J. T., Marcy, G. W., Butler, R. P., & Vogt, S. S. 2004, *ApJS*, 152, 261

Wu, Y., & Murray, N. 2003, ApJ, 589, 605

Zhou, J.-L., Aarseth, S. J., Lin, D. N. C., & Nagasawa, M. 2005, ApJ, 631, L85

Zucker, S., et al. 2002, ApJ, 568, 363

# Vita

Robert Andrew Wittenmyer was born in Newport News, Virginia on 1976 April 1 to Larry and Susan Wittenmyer. He received the Bachelor of Arts degree in Astronomy, Biology, and Environmental Studies from Williams College with honors in June 1998. He taught at SCICON, the Tulare County (California) outdoor science school, from August 1998 until June 1999, then he taught 7th grade math and science at Alta Vista Elementary School in Porterville, California from August 1999 to July 2000, finishing a teaching credential at Fresno Pacific University in June 2000. He obtained a Master of Arts in Biology at Boston University's Marine Program in Woods Hole, Massachusetts in May 2001, then entered the Astronomy master's program at San Diego State University in January 2002, graduating with a Master of Science in Astronomy in December 2003. After working as a Research Associate for the Antarctic Research Center in San Diego from May 2003 until July 2004, he began the PhD program at the University of Texas Department of Astronomy in August 2004. At the University of Texas, he worked with Bill Cochran and Mike Endl on the topics described in this dissertation. He married Gretchen Rhinehart on June 30, 2007 in Austin, Texas. From 2008 to 2011, he will be at the University of New South Wales in Sydney, Australia to pursue postdoctoral research with the Anglo-Australian Planet Search team.

Permanent Address: 2012 Burnie Bishop Place  
Cedar Park, TX 78613

This dissertation was typeset with  $\text{\LaTeX} 2_{\epsilon}$ <sup>1</sup> by the author.

---

<sup>1</sup> $\text{\LaTeX} 2_{\epsilon}$  is an extension of  $\text{\LaTeX}$ .  $\text{\LaTeX}$  is a collection of macros for  $\text{\TeX}$ .  $\text{\TeX}$  is a trademark of the American Mathematical Society. The macros used in formatting this dissertation were written by Dinesh Das, Department of Computer Sciences, The University of Texas at Austin, and extended by Bert Kay, James A. Bednar, and Ayman El-Khashab.